D2.1 Good practice criteria for multi-hazard forecasting (including a multidisciplinary calibration) and application limits, as enablers for risk reduction through restoration, exportable to other coasts

12/07/23

WP2

Lead beneficiary: LIM/UPC

Author/s: M. Espino, L. Garrote, D. Santillan, X. S.-Artús, V. Gracia, M. Liste, M. Mestres, M. Grifoll, M. Balsells, J. Staneva, B. Jacob, W. Chei, J. Pein, L. Villa, P. Dissanayake, M. de Vries, I. Federico, S. Causio, O. Boutron, C. Briere, R. Caillibote & A. S-Arcilla.

REST-COAST

Large Scale RESToration of COASTal Ecosystems through Rivers to Sea Connectivity

This project receives funding from the European Union's Horizon 2020 research and innovation programme, under Grant Agreement 101037097

Prepared under contract from the European Commission
Grant agreement No. 101037097
EU Horizon 2020 Coordination and Support Action

Project acronym:	**REST-COAST**
Project full title:	**Large Scale RESToration of COASTal Ecosystems through Rivers to Sea Connectivity**
Start of the project:	01.10.2021
Duration:	54 months
Project coordinator:	Prof. Agustín Sánchez-Arcilla, Universitat Politècnica De Catalunya (UPC)
Type:	Restoring biodiversity and ecosystem services
Call:	H2020-LC-GD-2020-3
Deliverable title	Good practice criteria for multi-hazard forecasting (including a multidisciplinary calibration) and application limits, as enablers for risk reduction through restoration, exportable to other coasts
Deliverable n°	D2.1
Nature of the deliverable:	Report
Dissemination level:	Public
WP responsible:	WP2
Lead beneficiary:	LIM/UPC
Citation:	Espino, M., L. Garrote, D. Santillan, X. S.-Artús, V. Gracia, M. Liste, M. Mestres, M. Grifoll, M. Balsells, J. Staneva, B. Jacob, W. Chei, J. Pein, L. Villa, P. Dissanayake, M. de Vries, I. Federico, S. Causio, O. Boutron, C. Briere, R. Caillibote & A. S-Arcilla (2023). *Good practice criteria for multi-hazard forecasting (including a multidisciplinary calibration) and application limits, as enablers for risk reduction through restoration, exportable to other coasts*. Deliverable D2.1. EU Horizon 2020 REST-COAST Project, Grant agreement No 101037097
Due date of deliverable:	Month n°21
Actual submission date:	Month n°21

Deliverable status:

Version	Status	Date	Author(s)
0.0	Template	15 March 2023	Manuel Espino (UPC)
1.0	First Draft	30 June 2023	M. Espino, X. S.-Artús, V. Gracia, M. Liste, M. Mestres, M. Grifoll, M. Balsells, A. S-Arcilla (UPC), L. Garrote, D. Santillan (UPM), J. Staneva, B. Jacob, W. Chei, J. Pein, L. Villa (HZG), P. Dissanayake, M. de Vries (DEL), I. Federico, S. Causio (CMCC), O. Boutron (TDV), C. Briere, R. Caillibote (EGIS)
2.0	Reviwed Final Document	02 June 2025	M. Espino, X. S.-Artús, V. Gracia, M. Liste, M. Mestres, M. Grifoll, M. Balsells, A. S-Arcilla (UPC), L. Garrote, D. Santillan (UPM), J. Staneva, B. Jacob, W. Chei, J. Pein, L. Villa (HZG), P. Dissanayake, M. de Vries (DEL), I. Federico, S. Causio (CMCC), O. Boutron (TDV), C. Briere, R. Caillibote (EGIS)

Table of Contents

Preface

The REST-COAST project (Large-scale RESToration of COASTal ecosystems through rivers to sea connectivity) is a Horizon 2020 research initiative funded by the European Commission under Grant Agreement No. 101037097. Its overarching aim is to restore coastal ecosystems across Europe by advancing science-based approaches to hazard mitigation and resilience, with a strong emphasis on nature-based solutions (NbS) and the sustainable delivery of ecosystem services (ESS).

To meet this objective, the project adopts a multidisciplinary approach that combines modelling, monitoring, restoration, governance, and finance. Scientific development is tightly linked to practical implementation through a network of pilot sites representing diverse coastal typologies and pressures. These sites serve as laboratories for testing and validating coupled hydro-morpho-eco models capable of simulating the role of natural ecosystems in reducing risks such as coastal flooding, erosion, and saline intrusion.

This deliverable, D2.1, documents the modelling work conducted under Task 2.1, focusing on present-day storm conditions. It presents the model configurations, validation procedures, and simulation outcomes used to evaluate the risk reduction potential of NbS across seven pilot sites. The work includes detailed analysis of hydrodynamic and morphodynamic processes, sediment transport, and vegetation interactions, as well as the derivation of site-specific ESS indicators. The models are tailored to local physical settings and restoration goals, and have been validated against real storm events using field and remote sensing data.

D2.1 provides a robust technical foundation for assessing the effectiveness and operational relevance of ecosystem-based approaches to coastal risk management. The methods and results presented here contribute to the broader REST-COAST objective of supporting adaptive, transferable, and evidence-based coastal restoration strategies throughout Europe.

Summary

Deliverable D2.1 presents the modelling frameworks developed and applied across seven REST-COAST pilot sites to evaluate the role of nature-based solutions (NbS) in reducing multi-hazard risks under present-day storm conditions. The work focuses on coastal hazards such as erosion, flooding, salinisation, and hydro-saline imbalances, and on the delivery of key ecosystem services (ESS) including sediment retention, wave attenuation, water quality improvement, and habitat support.

The coupled hydro-morpho-eco models developed within Work Package 2 integrate circulation, wave dynamics, sediment transport, and vegetation effects using tools such as COAWST, Delft3D, SHYFEM, TELEMAC, XBeach, and SCHISM. These models have been calibrated and validated with site-specific field data, including discharge measurements, sediment fluxes, topographic and bathymetric surveys, and extreme storm observations. Each pilot has adapted the modelling strategy to its geomorphological context, restoration stage, and technical objectives.

In the Ebro Delta, the model chain combines riverine and coastal processes to assess sediment fluxes and NbS performance during recent high-energy storms. In the Wadden Sea, multi-partner models quantify the contribution of seagrass and saltmarshes to wave and current attenuation, with robust validation under storm conditions. The Venice Lagoon models explore the effects of submerged vegetation and wetlands on storm surge and circulation, offering insights for NbS planning in interaction with the MOSE barrier system.

In the Rhone Delta, coupled hydro-saline and morphodynamic simulations evaluate overwash, breaching, and salinity regulation in restored lagoons. The Arcachon Bay team has implemented a vegetation-sensitive morphodynamic model to assess the protective function of seagrass meadows under wave forcing. In Sicily, SWAN-XBeach simulations quantify the impact of dune vegetation and Posidonia oceanica meadows on wave energy reduction. In the Vistula Lagoon, hydrodynamic models assess the stability and by-effects of a newly constructed artificial island as a hard-structure NbS in a physically constrained lagoon system.

Across all pilots, the models have been used to test NbS versus no-NbS configurations, allowing a clear quantification of their contributions to hazard mitigation. ESS indicators were derived for each site, including wave height reduction, sediment trapping, water level changes, and habitat feedbacks. The outcomes confirm that ecosystem-based approaches can play a substantial role in enhancing coastal resilience, provided they are adapted to local physical conditions and restoration potential.

This deliverable provides a consolidated, validated reference for the operational use of coupled modelling in support of risk reduction and coastal restoration, offering transferable methodologies that are grounded in site-specific evidence.

List of abbreviations

AEMET: Agencia Estatal de Meteorología (Spain)
AR5: IPCC Fifth Assessment Report
AR6: IPCC Sixth Assessment Report
ASCE: American Society of Civil Engineers
ASCEJ: ASCE Journal

BLENDER: Open-source 3D creation suite used for grid generation
BRGM: Bureau de Recherches Géologiques et Minières (France)
BSH: Bundesamt für Seeschifffahrt und Hydrographie
BSS: Brier Skill Score

CDS: Climate Data Store (CDS).
CEH: Coastal Erosion Hazard Model
C3S: Copernicus Climate Change Service
CMCC: Centro Euro-Mediterraneo sui Cambiamenti Climatici
CMEMS: Copernicus Marine Environment Monitoring Service
CNR: Consiglio Nazionale delle Ricerche (Italy)
COR: Consorzio coordinamento delle ricerche al Sistema lagunare di Venezia (CORILA)
CORE-PLAT: COastal REstoration PLATform
COAWST: A Coupled-Ocean-Atmosphere-Wave-Sediment Transport Modeling System.
COR: Consorzio per il Coordinamento delle Ricerche sul Sistema Lagunare di Venezia

D: Deliverable
D2M: 2 m dew point temperature
DEL: Deltares
DEM: Digital Elevation Model
DFM: Delft3D Flexible Mesh
DGM: Digitales Geländemodell
DIA: Discrete Interaction Approximation
DSAS: Digital Shoreline Analysis System
DTM: Digital Terrain Model
DW600: Sensor of the Optech Titan Multispectral Lidar System.
D-Waves: Delft3D Wave Model Component
DWD: Deutscher Wetterdienst (German Weather Service)

ECMWF: European Centre for Medium-Range Weather Forecasts.
EDOM: Field Campaign
EFWS:
EGIS: EGIS Water and Maritime
EMODnet: European Marine Observation and Data Network
EMS: Ems-Dollard Estuary
EPSG: European Petroleum Survey Group (spatial reference codes)
ERA5: ECMWF Reanalysis v5
ESS: Ecosystem Services
EU: European Union
EUNIS: European Nature Information System
EUNIS2019: Habitat Maps Classification

EVA: Extreme Value Analysis
EWS: Early Warning System

FH: Flooding Hazard Model
FM: Flexible mesh
FSK: Forschungsstelle Küste (NLWKN, Germany)

GARR: Italian Academic and Research Network
GEO-TUBES: Geotextile Tubes
GHG: Green Hous Gases
GIS: Geographic Information System
GMSH: Gmsh Mesh Generator
GOTM: General Ocean Turbulence Model
GPS: Global Positioning System

HEREON: Helmholtz-Zentrum Hereon (formerly HZG)
HF: HF Radar (Puertos del Estado, Spain)
HIRLAM: High Resolution Limited Area Model
HZG: Helmholtz-Zentrum Geesthacht (now HEREON)

IBW: Institute of Hydro-Engineering of the Polish Academy of Sciences.
ICAM: International Conference on Alpine Meteorology
ICGC: Institut Cartogràfic i Geològic de Catalunya
IFS: Integrated Forecasting System dataset produced by ECMWF
INTERREG: European Territorial Cooperation Programme
IOWAGA: Innovative Ocean Wave for Assessing Global Applications
IPBES: IPBES report (2019)
IPCC: Intergovernmental Panel on Climate Change
IPCC AR6: Intergovernmental Panel on Climate Change Sixth Assessment Report

JOIN-SEA: JOIN-SEA approach
JONSWAP: Joint North Sea Wave Project

LiDAR: Laser imaging detection and ranging
LIFE: EU Financial Instrument for Environment and Climate Action
LIM: Laboratori d'Enginyeria Marítima /Univ. Politècnica de Catalunya

MARS3D: Coastal Hydrodynamical Model
MATLAB: Matrix Laboratory (numerical computing environment)
MEDSEA: Med MFC physical multiyear product from Copernicus Marine Data.
MFC: Monitoring Forecasting Centre (MED MFC)
MOSE: Modulo Sperimentale Elettromeccanico
MPI: Message Passing Interface
MSL: Mean Sea Level
MST: Milestone
MWL: Mean Water Level
NLWKN: Niedersächsischer Landesbetrieb für Wasserwirtschaft, Küsten- und Naturschutz

NASA: National Aeronautics and Space Administration
NBS: Nature-Based Solutions

NbS: Nature-based Solutions
NN: NetworkNature
NOAA: National Oceanic and Atmospheric Administration
NTU: Nephelometric Turbidity Unit
NATURA 2000: Network of protected Areas covering Europe's.
NEMO: Nucleus for European Modelling of the Ocean
NEWS: INTERREG Italia-Malta Project
NLWKN: Ley-Bay model

OEMS: Oster-Ems (subdomain in Ley Bay)

PHREEQC: Geochemical Modeling Software
PL: Poland (used as ISO country code)
PLB280010: NATURA 2000 area for birds.
PLH280007: NATURA 2000 area for habitats.
POT: Peak Over Threshold
PROVV: Provveditorato Interregionale per le Opere Pubbliche per il Veneto, Trentino Alto Adige e Friuli Venezia Giulia
PSI: Positive Streamwise Invariant

R^2: Coefficient of Determination (used in model validation)
RAMSAR: Convention on Wetlands of International Importance
RCE: Reduction of Coastal Erosion
RCP: Representative Concentration Pathways
RCPs: Representative Concentration Pathways (RCPs)
RCP4: RCP scenario
RCP8: RCP scenario
REF: Reference configuration without NbS
REF_MOSE: Reference configuration with MOSE closed
REST: Restoration configuration with NbS
REST-COAST: Large scale RESToration of COASTal ecosystems through rivers to sea connectivity Project
REST_MOSE: Restoration configuration with MOSE closed
RFR: Reduction of Flood Risk
RMSE: Root Mean Square Error
ROMS: Regional Ocean Modeling System

SAIH: Ebro Automatic Hydrological Information System
SAW: ECMWF's Wave Model
SCHISM: Semi-implicit Cross-scale Hydroscience Integrated System Model
SED3D: 3D Sediment Transport Model (within SCHISM framework)
SHYFEM: Sistema Idrodinamico Finito ad Elevata Risoluzione
SHOM: Service Hydrographique et Océanographique de la Marine
SHOWEX: Formulations from Ardhuin et al., 2003
SIBA: Syndicat Intercommunal du Bassin d'Arcachon
SLR: Sea level rise
SPM: Suspended Particulate Matter
SS: Storm surge
SSP: Socioeconomic Pathways
SSP2: SPP2 scenario
SSP5: SPP5 scenario

SWAN: Simulating WAves Nearshore model
SWE: Shallow-Water Equations
SWH: Significant Wave Height

T: Task
T2M: 2-m air temperature
TA: Tidal Anomaly
TCC: Total cloud cover
TDV: Tour du Valat
TELEMAC: Telemac Modelling System for Hydrodynamics and Sediment Transport
TELEMAC-2D: Two-dimensional module of the TELEMAC Modelling System
TKE: Turbulent Kinetic Energy
TOMAWAC: Telemac-based Model for Wave Propagation in Coastal Areas
TOMAWAV: Software for sea state modelling on unstructured grids over oceans and coastal seas
TP: Total precipitation
TR: Return period
TVD: Total Variation Diminishing

U10M: Meridional wind components at 10-m height
UAS: Unmanned aircraft system
UC: University of Catania
UNESCO: United Nations Educational, Scientific and Cultural organization
UPC: Universitat Politècnica de Catalunya
UPM: Universidad Politécnica de Madrid
USGS: United States Geological Survey
USGS: United States Geological Survey
UTM: Universal Transverse Mercator (coordinate system)

V10M: Zonal wind components at 10-m height

WAM: Wave Model (used for ocean wave prediction)
WAVEWATCH: NOAA Wave Model
WES: Westerland
WFD: Water Framework Directive
WP: Work Package
WP1: Work Package 1
WP2: Work Package 2
WP4: Work Package 3
WP6: Work Package 4
WSS: Willmott Skill Score
WT-NBS: without NBS
WW3: WAVEWATCH III
WWM III: Wind Wave Model III

XBEACH: eXtreme BEACH Behaviour Model

Z. marina / Z. noltii: Seagrass species

List of Figures

1. General introduction

WP2 is preparing a risk assessment simulation tool for multi-hazard forecasting, based on calibrated hydro-morpho-eco coupled models with ESS parameterised as a function of restoration scale and climatic conditions. The coupled models, calibrated for present conditions and critically analysed for future climates, notably relative sea-level-rise and changes in storminess, are being used to consistently simulate impacts across timescales (from storms to decades), considering the socio-economic data and projections available at the Pilots to co-design limits for alarm levels. Here the partners have agreed on the future scenarios (RCPs 4.5 and 8.5), horizons, and storm return periods (5, 50 and 100 years) to be used, in order to produce comparable analyses (Mst 8). The resulting risk estimations, with explicit error intervals based on in-situ/satellite data, aim to provide:

1. Warnings for present conditions (Task 2.1) and future scenarios (Task 2.2) with model application limits and co-designed thresholds for the dashboard being developed in WP6. This work is the basis of the ongoing work to prepare good practice criteria for multi-hazard forecasting, with application limits (D2.1) for the Pilots.
2. Maps displaying risk levels in space, considering existing infrastructures and ESS to modulate risk propagation (Task 2.3) and suited to incorporate adaptation pathways (WP4) for assessing risk reduction with/without ESS to promote a proactive approach to restoration.
3. Probabilistic characterizations of main drivers and responses in the risk assessment to estimate hazards for single and multi-variable combinations, considering existing knowledge plus conventional/conditional statistics (Task 2.4).

Pilot analyses will enrich the global assessment of risk reduction through wetland restoration, improving the model calibration for the coastal archetypes considered in the Pilots. From the combined results, WP2 will provide simulated data to derive good practice criteria for multi-hazard forecasting, exportable to any coastal site.

REST-COAST modelling encompasses a number of state-of-the-art models already calibrated for the Pilots and which are being further validated within the project. These models comprise unstructured and structured meshes for waves, currents, morphodynamics and nutrient /pollutant dispersion and transport. The bathymetries for the pilots are based on improved combinations of aerial photographs, lidar data and EMODNET bathymetry. The model runs are driven by CMEMS products and include, at different levels depending on the Pilot, some of the ecosystem services considered. The simulation of what-if scenarios has been harmonised for the Pilots and comprise present and future conditions (RCP 8.5 and RCP 4.5 scenarios and storms with commonly agreed 5, 50 and 100 year return periods).

2. Multi-hazard forecasting (including a multidisciplinary calibration) and application limits Ebro Delta Pilot (LIM, UPM)

2.1. Introduction

The Ebro River is the second largest river in the Iberian Peninsula and generates a deltaic system in the southern area of Catalonia, on the Spanish Mediterranean coast, which extends around 25 kilometres offshore and forms two enclosed bays (Fangar to the north and Alfacs to the south). The Ebro valley was a closed basin until its opening to the Mediterranean Sea ca. 5.3 M years ago (transition between the Miocene and Pliocene). During the 20th and 21st centuries there has been a relative stabilization of the deltaic morphology, largely caused by the anthropic hydrological modifications carried out in the basin.

Nowadays we can distinguish three types of sedimentary environments in the Ebro Delta: the deltaic plain, the coastal environments and the marine environments.

- The deltaic plain comprises most of the emerged lands and includes two types of sedimentary environments: river environments and lake and marsh environments. The former are represented by the river channels and the natural specks that surround them (dykes), formed by soils of medium granulometry and for silt. The lacustrine and marshy environments are located in the regular or permanently flooded wetlands.

- Coastal and transitional environments are sedimentary environments with fluvial influence in which there is a more or less intense retreat of sediments by marine agents (waves and storms). These environments are basically represented by the deltaic front, formed by the crescent-shaped sand bars and associated with the deltaic progression. The materials which form them have a fairly homogeneous granulometry, basically sandy. The beaches, the coastal bars and the arrows are holomarine coastal formations, originated from the deltaic river front, which are removed by the sea, or from the erosion of the ancient deltaic lobes.

- Marine environments can be classified into bay, beach and platform environments.

  - The beach environment develops in the bodies of sea water that are confined by the coastal fringe, even though they are connected in accordance with the open sea by the permanent rivers.

  - The prodelta environment is located in coastal submerged environments and constitutes the transition between fluvial-marine and marine sediments. It is mainly made up of terrestrial materials with a significant content of organic matter of terrestrial origin.

  - The continental shelf environment is located in the open sea, at a depth of more than 100 m, and is a relict sedimentary environment, associated with the last post-glacial eustatic descents.

All aquatic ecosystems of the delta are influenced by water coming from rice fields. About 65% of the delta's area is dedicated to rice cultivation. From April to October, a quantity of 45 m3·s-1 of river water is diverted to the irrigation canals for continuous irrigation (Ibàñez et al., 1997). The river water is rich in nutrients (Ibàñez et al., 1995), but farmers add large amounts of fertilizer to enhance rice production, as well as several types of pesticides, mainly during spring and early summer (Ibàñez et al., 1997). Water coming from the rice fields is carried by drainage canals to the sea through the bays.

The Ebro river and deltaic plain are the main focus of UPM, while LIM is working on Coastal and Marine environments, currently focusing on the Trabucador barrier beach (South hemidelta).

2.2. Ebro river and deltaic plain simulation domain

We simulate the erosion process, sediment transport, and sediment deposition in the Ebro Delta pilot case through numerical modeling, using the freely-available two-dimensional (2-D) Iber code (Cea et al., 2007; Bladé et al., 2014), which solves the 2-D hydrodynamic equations coupled to the sediment transport equations, amongst others. In the following sections, we first describe the hydrodynamic equations and the erosion model, followed by a description of the Pilot site in terms of model configuration data (topography, hydrodynamic parameters, and boundary conditions) and, finally, we calibrate the hydrodynamic numerical model with controlled flood observations.

2.3. Description of the numerical model for fluvial simulation (Iber)

Iber solves the 2-D Depth-Integrated Shallow-Water Equations (SWE) using a finite volume scheme. This scheme can handle unstructured meshes, irregular topographies, friction losses, and wet-dry fronts (Cea et al., 2007). The 2D SWEs are derived from the Navier–Stokes equations by assuming quasi-hydrostatic flow and incompressibility of water. The 2D mass conservation equation in a Cartesian coordinate system is given by:

$$\frac{\partial \mathrm{h}}{\partial \mathrm{t}} + \frac{\partial \mathrm{hU_x}}{\partial \mathrm{x}} + \frac{\partial \mathrm{hU_y}}{\partial \mathrm{y}} = 0, \tag{2.1}$$

and the momentum balance equations in conservative form with source terms in a Cartesian coordinate system are:

$$\begin{aligned} &\frac{\partial}{\partial \mathrm{t}}(\mathrm{hU_x}) + \frac{\partial}{\partial \mathrm{x}}\left(\mathrm{hU_x^2} + \mathrm{g}\frac{\mathrm{h}^2}{2}\right) + \frac{\partial}{\partial \mathrm{y}}\left(\mathrm{hU_xU_y}\right) \\ &\qquad = -\mathrm{gh}\frac{\partial \mathrm{z_b}}{\partial \mathrm{x}} + \frac{\tau_{\mathrm{s,x}}}{\rho} - \frac{\tau_{\mathrm{b,x}}}{\rho} + \frac{\partial}{\partial \mathrm{x}}\left(\nu_\mathrm{t}\mathrm{h}\frac{\partial \mathrm{U_x}}{\partial \mathrm{x}}\right) + \frac{\partial}{\partial \mathrm{y}}\left(\nu_\mathrm{t}\mathrm{h}\frac{\partial \mathrm{U_x}}{\partial \mathrm{y}}\right), \end{aligned} \tag{2.2}$$

and

$$\begin{aligned} &\frac{\partial}{\partial \mathrm{t}}(\mathrm{hU_y}) + \frac{\partial}{\partial \mathrm{y}}\left(\mathrm{hU_y^2} + \mathrm{g}\frac{\mathrm{h}^2}{2}\right) + \frac{\partial}{\partial \mathrm{x}}\left(\mathrm{hU_yU_x}\right) \\ &\qquad = -\mathrm{gh}\frac{\partial \mathrm{z_b}}{\partial \mathrm{y}} + \frac{\tau_{\mathrm{s,y}}}{\rho} - \frac{\tau_{\mathrm{b,y}}}{\rho} + \frac{\partial}{\partial \mathrm{x}}\left(\nu_\mathrm{t}\mathrm{h}\frac{\partial \mathrm{U_y}}{\partial \mathrm{x}}\right) + \frac{\partial}{\partial \mathrm{y}}\left(\nu_\mathrm{t}\mathrm{h}\frac{\partial \mathrm{U_y}}{\partial \mathrm{y}}\right). \end{aligned} \tag{2.3}$$

In the previous equations, h is the water depth, $\mathrm{U_i}$ is the depth average velocity along the i direction, ρ is the density of the water, $\mathrm{z_b}$ is the channel-bottom height, g is the acceleration of gravity, $\tau_{\mathrm{b,i}}$ is the bed friction along the i direction, $\tau_{s,\mathrm{i}}$ is the free-water surface friction along the i direction (i.e., wind traction), and ν_t is the turbulent eddy viscosity. In the following simulations, we neglect molecular and eddy viscosities, wind traction, as well as Coriolis acceleration. The bed friction terms, $\tau_{\mathrm{b,i}}$, read:

$$\tau_{\mathrm{b,i}} = \rho \mathrm{gh}\frac{\mathrm{n}^2\mathrm{U_i^2}}{\mathrm{h}^{4/3}} \tag{2.4}$$

where i = x, y, and n is the Manning coefficient.

The Iber erosion and sediment transport module solves the non-cohesive sediment transport equations with uniform granulometries, in a non-stationary regime. The hydrodynamics, sediment transport processes, and river morphology interplay in mobile-bed simulations. Iber software couples these three processes. Iber simulates sediment transport as bedload and suspended load.
The sediment transport process is simulated through the 2D Exner equation (Anderson 2002; Mudd & Furbish 2004; Paola & Voller 2005). The equation provides the bed elevation evolution in response to the erosion and sedimentation and is given in the form of bedload and suspended load:

$$(1-\phi)\frac{\partial z_b}{\partial t}+\frac{\partial q_{b,x}}{\partial x}+\frac{\partial q_{b,y}}{\partial y}+(E-D)=0, \tag{2.5}$$

where ϕ is the porosity, $q_{b,i}$ is the bedload discharge along the i direction, E is the entrainment deposition term of suspended sediment on the bed, and D is the deposition term of suspended sediment on the bed.

We simulate the bedload solid flow rate due to the bedload transport using the van Rijn equation (Van Rijn 1984a), as it provides satisfactory results compared with laboratory experiments (Santillan et al., 2020). The equation reads:

$$q_b^*=\frac{0.053}{D^{*0.3}}\left(\frac{\tau^*}{\tau_{crit}^*}-1\right)^{2.1}, \tag{2.6}$$

where q_b^* is the dimensionless bedload solid volumetric flow rate, D^* is the dimensionless diameter of solid particles, τ^* is the dimensionless shear stress acting on the particles, and τ_{crit}^* is the dimensionless critical shear stress. The dimensionless bedload solid volumetric flow rate, q_b^*, is:

$$q_b^*=\frac{q_b}{\sqrt{(s-1)gD^3}}, \tag{2.7}$$

where q_b is the bedload solid volumetric flow rate, s is the ratio between the densities of the particles and water, $s=\rho_S/\rho$, and D is the characteristic diameter of sediments, usually taken as the median diameter $D=D_{50}$.

The dimensionless diameter of solid particles is given by:

$$D^*=D\left(\frac{g(s-1)}{\nu^2}\right)^{1/3}, \tag{2.8}$$

being ν the kinematic viscosity of water, and the dimensionless shear stress is:

$$\tau^*=\frac{\tau_b}{\rho(s-1)gD}, \tag{2.9}$$

being τ_b the bed friction shear stress, given by Eq. (4).

The dimensionless critical shear stress τ_{crit}^* is given by the Soulsby-Whitehouse equation (Soulsby & Whitehouse 1997), based on the experiments of Shield (1936). It is given by:

$$\tau_{crit}^*=\frac{0.3}{1+1.2D^*}+0.055\left(1-e^{-0.02D^*}\right). \tag{2.10}$$

Iber simulates the suspended sediment transport with the depth-averaged convection-diffusion equation for the sediment concentration. The model accounts for the turbulent diffusion and the equilibrium suspended concentration, and is given by:

$$\frac{\partial hC}{\partial t}+\frac{\partial hU_xC}{\partial x}+\frac{\partial hU_yC}{\partial y}=\frac{\partial}{\partial x}\left(\left(\Gamma+\frac{\nu_t}{S_c}\right)h\frac{\partial C}{\partial x}\right)+\frac{\partial}{\partial y}\left(\left(\Gamma+\frac{\nu_t}{S_c}\right)h\frac{\partial C}{\partial y}\right)+\frac{\partial D_{s,x}}{\partial x}+\frac{\partial D_{s,y}}{\partial y}+(E-D), \quad (2.11)$$

where C is the depth-averaged concentration of suspended solids, Γ is the molecular diffusion coefficient for suspended solids, S_c is the Schmidt number, which relates the moment turbulent diffusion coefficient with the suspended turbulent diffusion coefficient, and $D_{s,i}$ is the suspended sediment dispersion along the i direction due to the non-homogeneous vertical velocity profile and sediment concentration.

The Entrainment/Deposition term, $(E-D)$, models the bedload grains that become suspended (entrainment) and deposited from suspended sediments to the bed layer. We simulate the Entrainment/Deposition term with the Van Rijn formula (van Rijn, 1987), given by:

$$E-D=\alpha\omega_s(C^*-C), \quad (2.12)$$

where α is a coefficient that relates the mean suspended particle concentration and the river bedload concentration, ω_s is the fall velocity of the suspended sediments, C^* is the depth-averaged suspended load concentration at equilibrium conditions, and C is the depth-averaged suspended load concentration.

The fall velocity of the suspended sediments for sand particles is computed using Van Rijn (1984b) recommendations. For particles smaller than about 0.1 mm, ω_s is given by:

$$\omega_s=\frac{(s-1)gD_{50}^2}{18\nu}, \quad (2.13)$$

for suspended sand particles in the range 0.1 to 1 mm, the fall velocity is:

$$\omega_s=10\frac{\nu}{D_{50}}\left\{\left(1+\frac{0.01(s-1)gD_{50}^3}{\nu^2}\right)^{0.5}-1\right\}, \quad (2.14)$$

and for particles larger than 1 mm, the following equation is used:

$$\omega_s=1.1[(s-1)gD_{50}]^{0.5}. \quad (2.15)$$

The depth-averaged suspended load concentration at equilibrium conditions, C^*, reads (Van Rijn 1984b):

$$C^*=\frac{1}{\alpha}0.005\frac{T^{1.5}}{D^{*0.3}}, \quad (2.16)$$

where T is the transport stage parameter given by:

$$T=\frac{(U^*)^2-(U^*_{crit})^2}{(U^*_{crit})^2}, \quad (2.17)$$

in which U^*_{crit} is the critical bed-shear velocity, that according to Shields (1936) is:

$$U^*_{crit}=\sqrt{\frac{\tau^*_{crit}}{\rho}}, \quad (2.18)$$

and bed-shear velocity, U^*, reads (Van Rijn 1984b):

$$U^* = \frac{\sqrt{g}}{C'}\overline{U}, \tag{2.19}$$

in which $C' = 18\log(12R_b/3D_{90})$ is the Chézy-coefficient related to grains, R_b is the hydraulic radius related to the bed according to Vanoni-Brooks (1957), and $\overline{U}$ is the mean flow velocity.

The system of Partial Differential Equations are solved using a first-order finite volume scheme based on the Monotonic Upwind Scheme for Conservation Laws (Van Leer 1979).

2.4. Description of model configuration data: topography, hydrodynamic parameters, boundary conditions

The Ebro River is strongly regulated with dams, of which the Mequinenza-Ribarroja-Flix reservoir system retains a large part of the sediment flow in the Ebro River (Figure 2.1). Therefore, this reservoir system must be included in the numerical domain to model the sediment transport to the Delta site. The modelling objectives are: (1) to study the alternatives to restore, at least in part, the sediment flow, (2) to estimate the quantity of sediments that can be mobilized, (3) to determine how long the sediments would take to research the Delta site, and (4) to know how the sediment would be delivered to the Delta system.

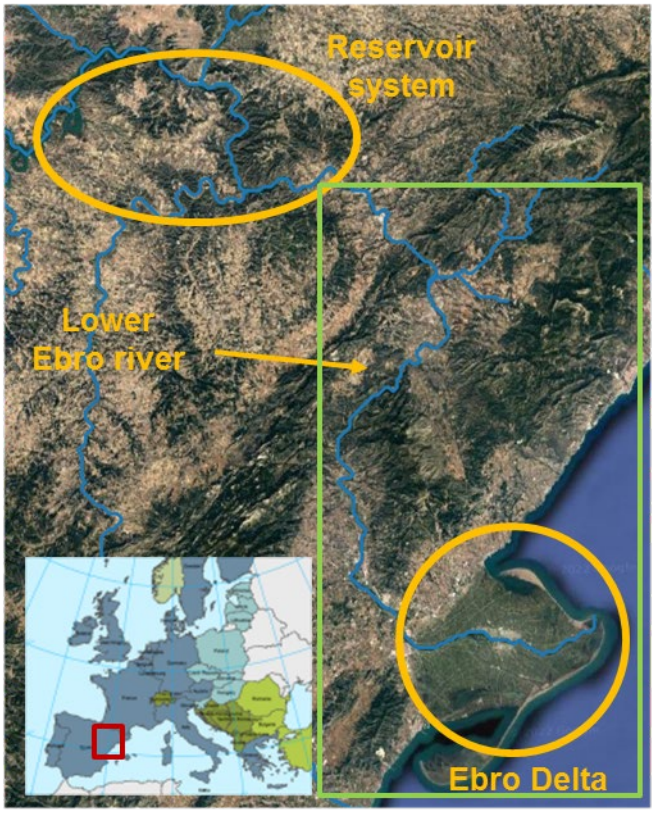

Figure 2.1. Ebro Delta pilot site

The topography of the simulated stretch is depicted in Figure 2.1. The fluid flow and sediment transport from the Flix reservoir, located about 100 km from the river mouth and 41.1 meters above the mean sea level, up to the Delta site, was simulated. This dam is the last barrage in the Ebro River.

A Triangulated Irregular Network (TIN) model of the river with 0.4-meter tolerance, maximum side of 300 meters, and minimum side of 15 m was generated using a 1 m-resolution Digital Terrain Model (DTM) of the Ebro basin provided by the Spanish National System for Flood Risk. This TIN includes 100 km of the Ebro River

topography and is composed of about 2,489,643 triangles (Figure 2.2, left). Figure 2.2, right shows two snapshots of the topography. The TIN was used to generate a coincident unstructured mesh composed of about 2,489,643 triangular elements, in which each triangle of the TIN model is a finite volume in the numerical model.

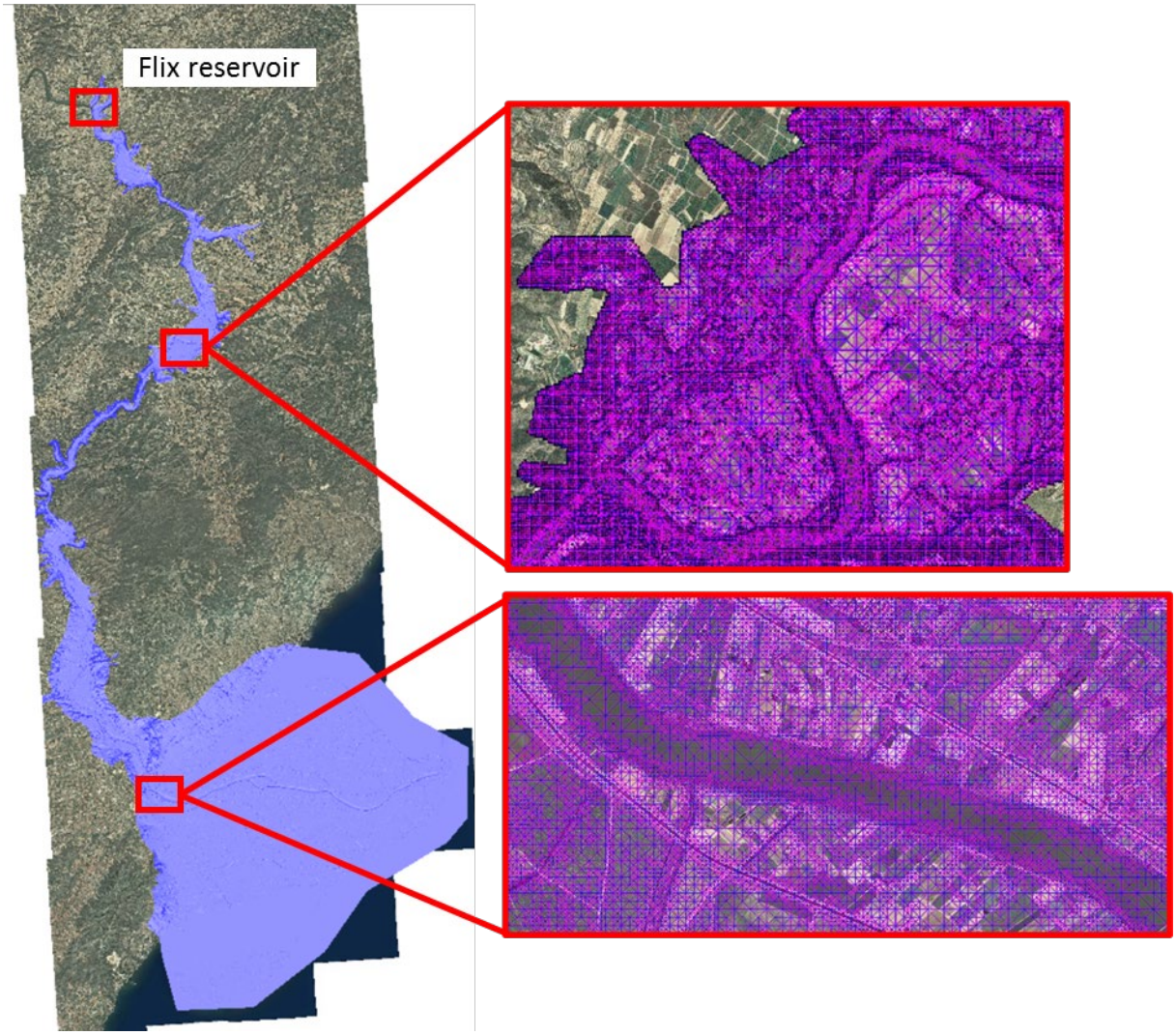

Figure 2.2. Domain of the numerical simulations in the Ebro Delta pilot site.

The boundary hydrodynamics conditions of the numerical model are (1) imposed flow rate in Flix in subcritical regime, and (2) outlet boundary condition in critical regime imposed on the sea.

2.5. Hydrodynamic calibration of the model with controlled flood observations

The rugosity of the model, given by Manning's coefficient, has been calibrated with the observed flood event on May 5th, 2022. This event also allows testing the performance of the hydrodynamic module. The Ebro Automatic Hydrological Information System (SAIH) provides 30-minute flow rate observations at two points of the river: Ascó and Tortosa -see Figure 2.3 (a). Moreover, during the flood event, 180 m^3/s were abstracted from the river in Xerta through an irrigation channel. The observed flow rate in Ascó and Tortosa gauge stations are plotted in Figure 2.3 (b) and Figure 2.3 (c), respectively.

(a) Location of Ascó and Tortosa flow-rate gauge stations

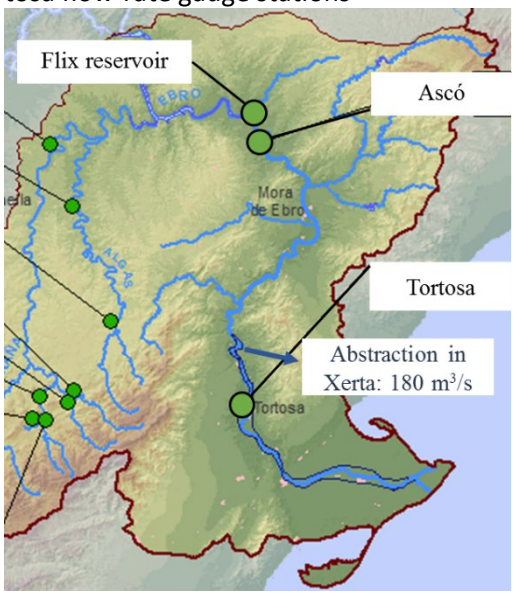

(b) Observed flow rate in Ascó flow-rate gauge station

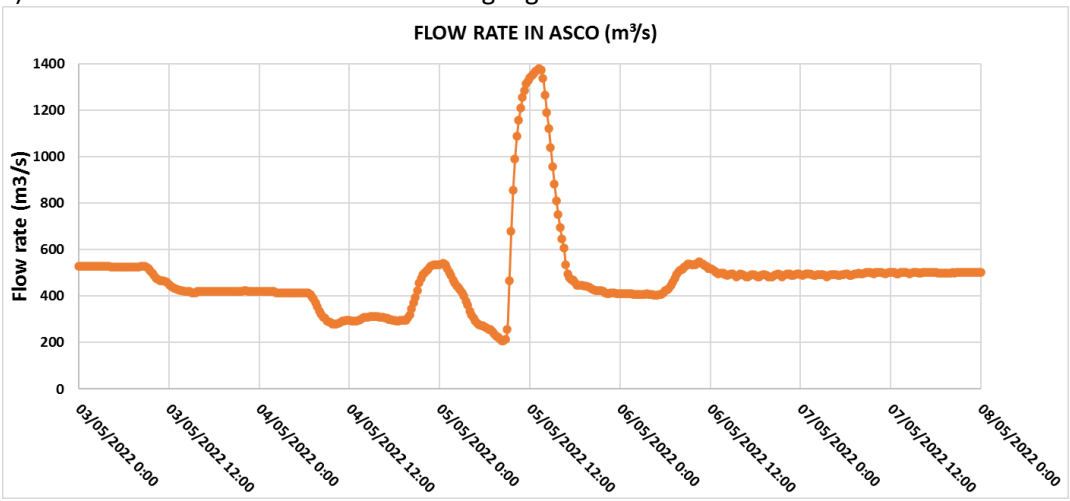

(c) Observed flow rate in Tortosa flow-rate gauge station

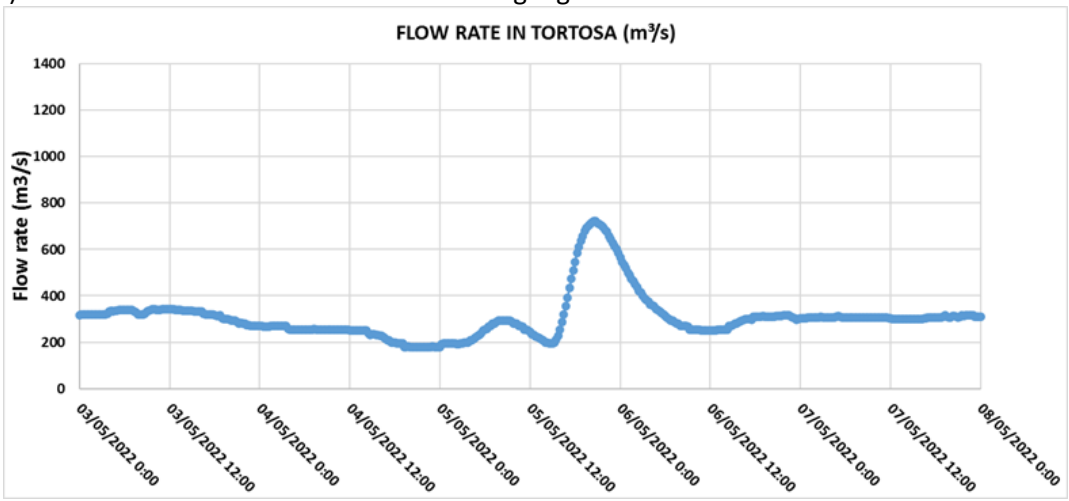

Figure 2.3. River Ebro flow-rates at the Ascó and Tortosa gauge stations.

The boundary conditions of the numerical model are, thus, (1) imposed flow rate in Ascó in subcritical regime given by the observed data plotted in Figure 2.3 (b), and (2) outlet boundary condition in critical regime imposed on the sea. Several numerical simulations were run with different values of Manning's coefficient, and the modelled flow rate in Tortosa was compared to the measured rates. The best agreement between the simulated and the observed flow rates were obtained with a Manning's coefficient of 0.027. The results are depicted in Figure 2.4. The model can capture the flood-wave propagation along the river in terms of time and flood peak downstream of the inlet. Figure 2.5 shows the river's water depth at 5:30 p.m. on 5th May 2022.

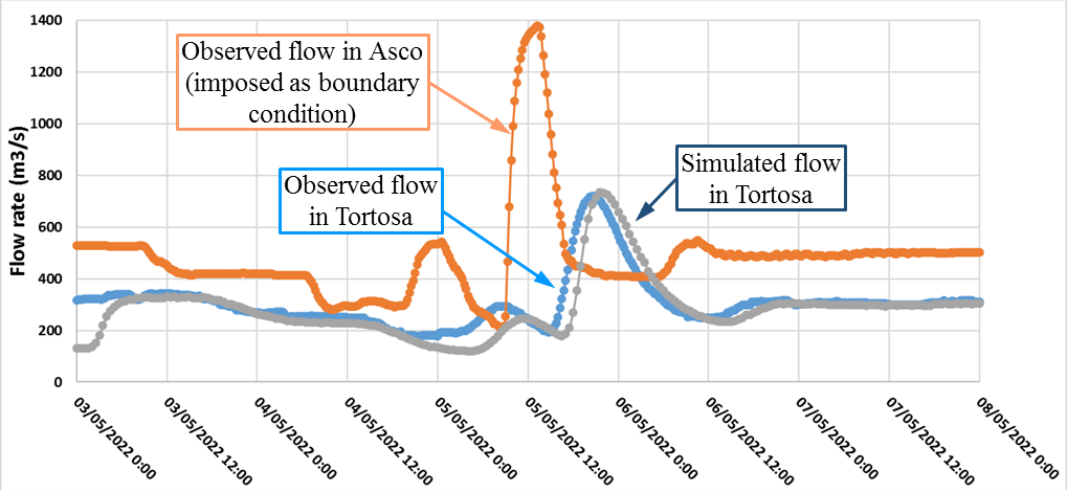

Figure 2.4. Observed and simulated flow rate in Tortosa.

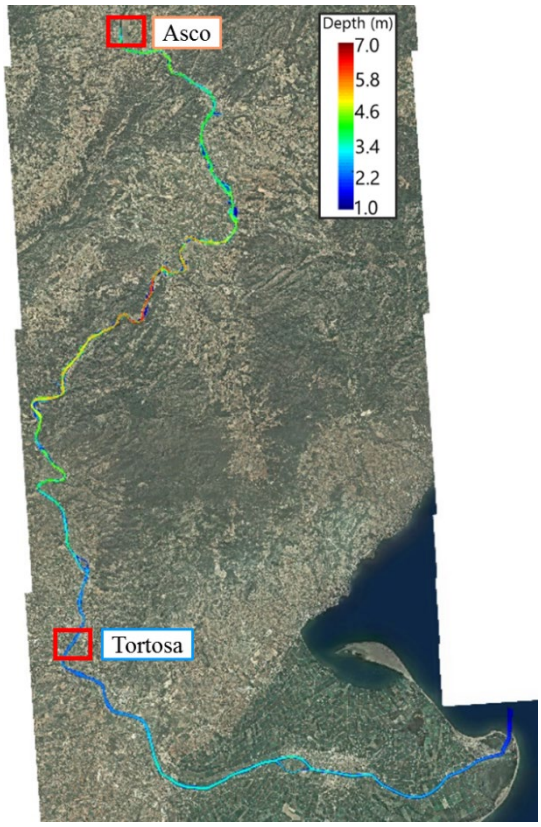

Figure 2.5. Water depth at 5:30 p.m. on 5th May 2022.

2.6. Approach to the characterization of sediment transport (based on historical observations)

Ibañez et al., (1996) studied the changes in the hydrological and sediment transport produced by large dams on the lower Ebro River and its estuary. They provided estimates of annual suspended sediment transport for several mean river flows, based on the data obtained from Gorria's experiments (Gorria, 1877), and listed in Table 2.1. Two flow regimes were adopted, i.e., the mean water flow, with high frequency over the hydrological year, and the annual flood regime, with low frequency over the hydrological year.

Table 2.1. Annual suspended sediment transport from Gorria's data (Gorria, 1877) and Ibañez et al., (1996).

Flow regime	Mean flow (m^3/s)	Frecuency (days/year)	Concentration of suspended sediment (g/l)
Mean water	710	256	0.9
Annual flood	1764	11	7.2

The performance of the model was assessed by simulating both flow regimes, and evaluating whether the code can reproduce the data in Table 2.1. In the following section, the parameters of the sediment transport model are included, the concentration of suspended sediments at several time steps are presented, and the performance of our model is analyzed.

2.7. Numerical analysis of sediment transport

Two numerical simulations are performed for both flow regimes included in Table 2.1, modelling the river-flow hydrodynamics and the suspended sediment transport for each one. The hydraulic boundary conditions of the model are (1) imposed constant flow rate at the outlet of Flix reservoir in subcritical regime given by the data in Table 2.1, and (2) outlet boundary condition in critical regime imposed at the sea. Moreover, water at the inlet has a suspended sediment concentration given by the data in Table 2.1. These numerical simulations are aimed at analyzing whether or not the Ebro River can transport those sediment concentrations down to the Ebro Delta.

The sediment used is characterized by a relative density of 2.65, a friction angle of 30 degrees, a median diameter of 0.0001 mm –clay–, a suspended sediment dispersion of 0.001 m^2/s, and a Schmidt number of 1.1.

The first simulation considered the mean water flow regime, starting from an initially dry river (i.e., water depth is 0), into which water was introduced through the inlet at the Flix reservoir. The flow at the inlet was 710 m^3/s and the concentration of sediments was 0.9 g/l. The flow propagated through the river until a steady-state regime was reached.

Figure 2.6 depicts the suspended sediment concentration at three different times. After 2 hours –Figure 2.6(b)– the flow had advanced 11 km and reached Ascó. The concentration of suspended sediments was 0.9 g/l along the whole stretch of Ebro River. After 12 hours, the flow was close to Xerta –Figure 2.6(b)–, and the concentration of suspended sediments was still 0.9 g/l along the whole stretch. The sediment deposition at this time step was zero (not shown), which means the flow can transport the given sediment concentration along the river.

The steady-state regime is shown in Figure 2.6(c). The concentration of suspended sediments is constant at 0.9 g/l, and the sediment deposition is zero. Under these simulated conditions, the flow can transport that sediment concentration from Flix reservoir to the Delta without deposition.

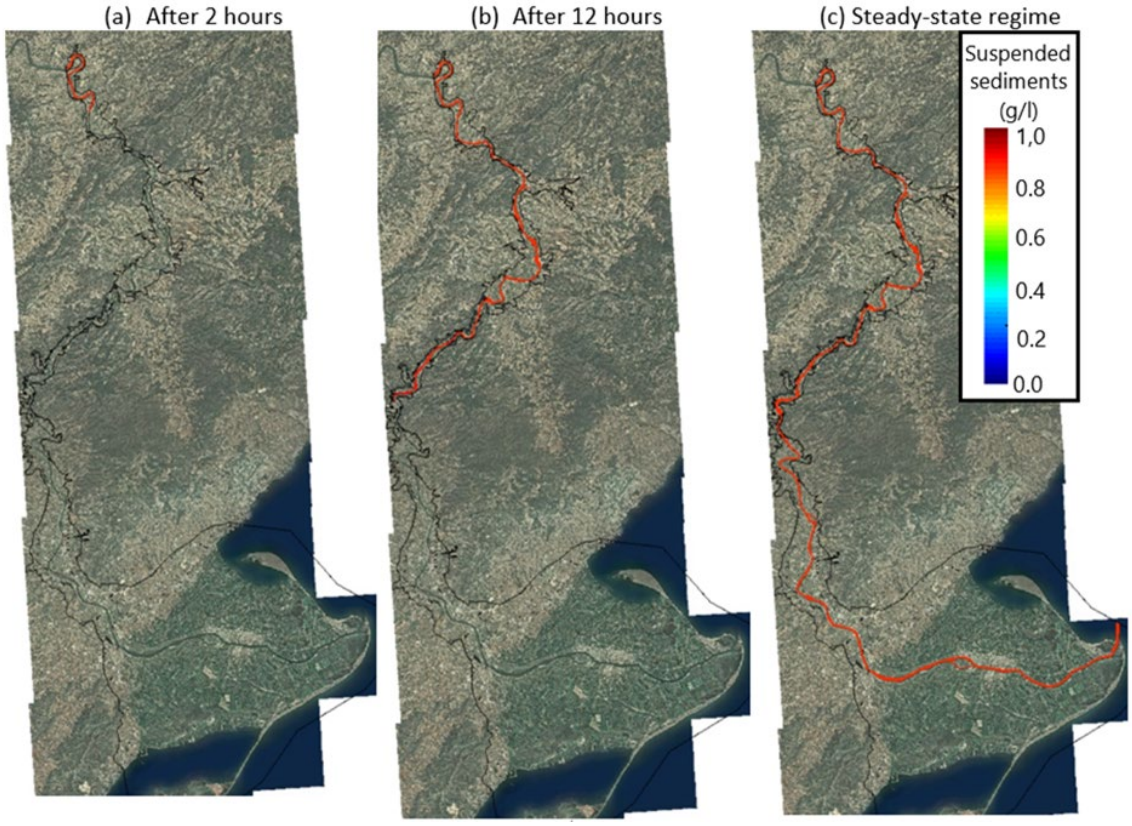

Figure 2.6. Suspended sediment concentration for the mean water regime given in Table 2.1. Flow water is 710 m3/s and suspended sediment concentration at the inlet is 0.9 g/l. We depict the contour plots of the concentration of suspended sediment after 2 h in a panel, after 12 hours in b panel and under the steady-state regime in c panel.

The annual flood conditions –Table 2.1– were also simulated, following the same procedure as in the previous case. Now, the flow at the inlet was 1760 m^3/s and the sediments concentration was 7.2 g/l. The flow propagated through the river until a stationary state was reached after several time-steps. Figure 2.7 depicts the suspended sediment concertation at three different times.

After 2 hours –Figure 2.7(b)– the flow had advanced further than during the mean flow regime. The concentration of suspended sediments was 7.2 g/l along the whole stretch of Ebro River, and the deposition was zero (not shown). After 12 hours, the flow was close to Tortosa –Figure 2.7(b)–, and the concentration of suspended sediments was still 7.2 g/l along the whole stretch. Finally, Figure 2.7(c) shows the steady-state regime. The concentration of suspended sediments was constant at 7.2 g/l, and sediments did not deposit along the river, except in some areas of the Delta (not shown). The river can transport the given sediment concentration to the Delta during the annual flood with the given concentration.

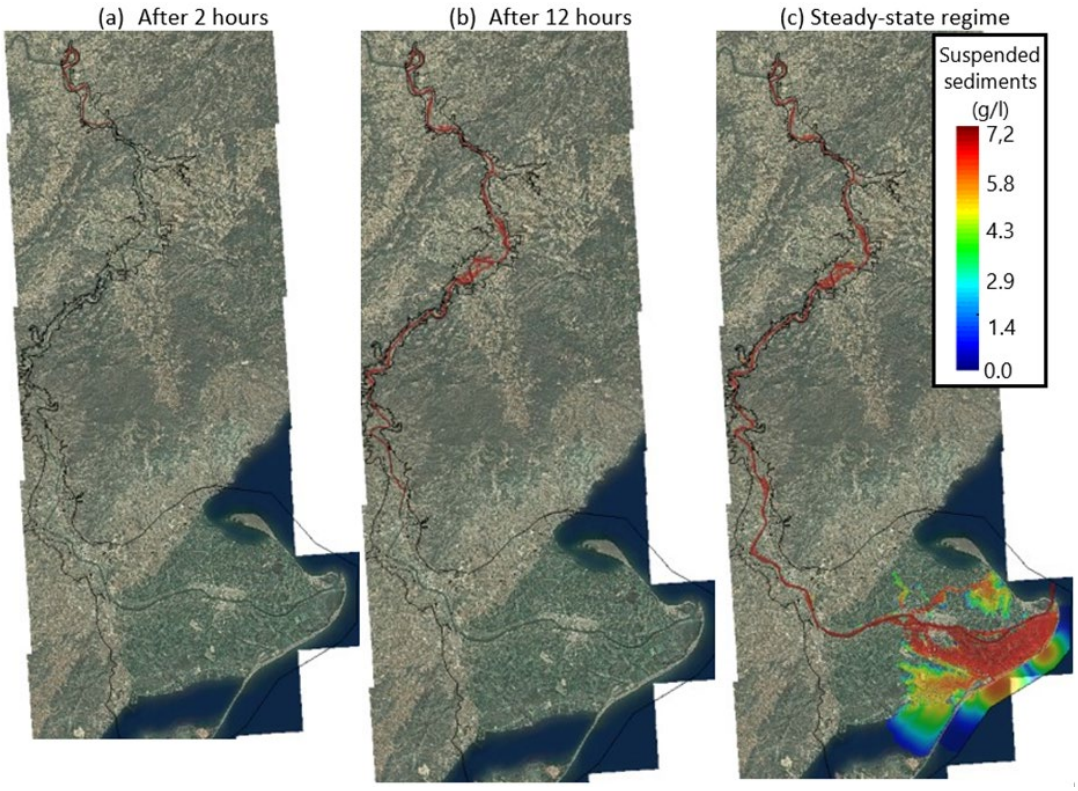

Figure 2.7. Suspended sediment concentration for the mean water regime given in Table 2.1. Flow water is 1760 m3/s and suspended sediment concentration at the inlet is 7.2 g/l. We depict the contour plots of the concentration of suspended sediment after 12 hours in (b), and under the steady-state regime in (c).

2.8. Simulation of realistic scenarios of sediment transport under current water management strategy

The scenarios of sediment transport analyzed in section 2.2.5 are not realistic, because they assume constant discharge over a sufficiently long period of time to achieve steady state. In practice, flows vary according to the natural water availability and management strategy.

To evaluate sediment transport under current water management strategy, flow and turbidity data were compiled from the available measuring stations in the lower Ebro River. Flow data were compared with turbidity data in the sites where data are available for both variables, which are the stations of Ascó and Tortosa. The availability of turbidity data is very low. The series show numerous gaps and the years without failure are exceptional. The Ascó series includes data since 1996, but Tortosa only began measuring in 2011. Therefore, the periods of overlap of flow and turbidity data are intermittent and do not allow continuous analysis. For these reasons, the available data is analyzed globally, regardless of the date to which they correspond.

Figure 2.8 presents the relationship between flow (in m^3/s) and turbidity (in NTU units) at the two analyzed stations. The graphs on the left present the relationships in natural values and those on the right on a logarithmic scale. A linear fit line has been added in both cases. It can be seen that there is a certain tendency to increase turbidity when the flow rate is increased, but there is a great dispersion in the data and the trends are not clear. The R^2 coefficients of the correlations are very low, indicating that a linear relationship between the NTU and Q variables cannot be established. The station where the relationship is most evident is Tortosa on a logarithmic scale, although the law between variables is not linear, but seems to correspond to a logistic function. The Ascó station shows a similar trend, although the greater abundance of data produces a much greater dispersion.

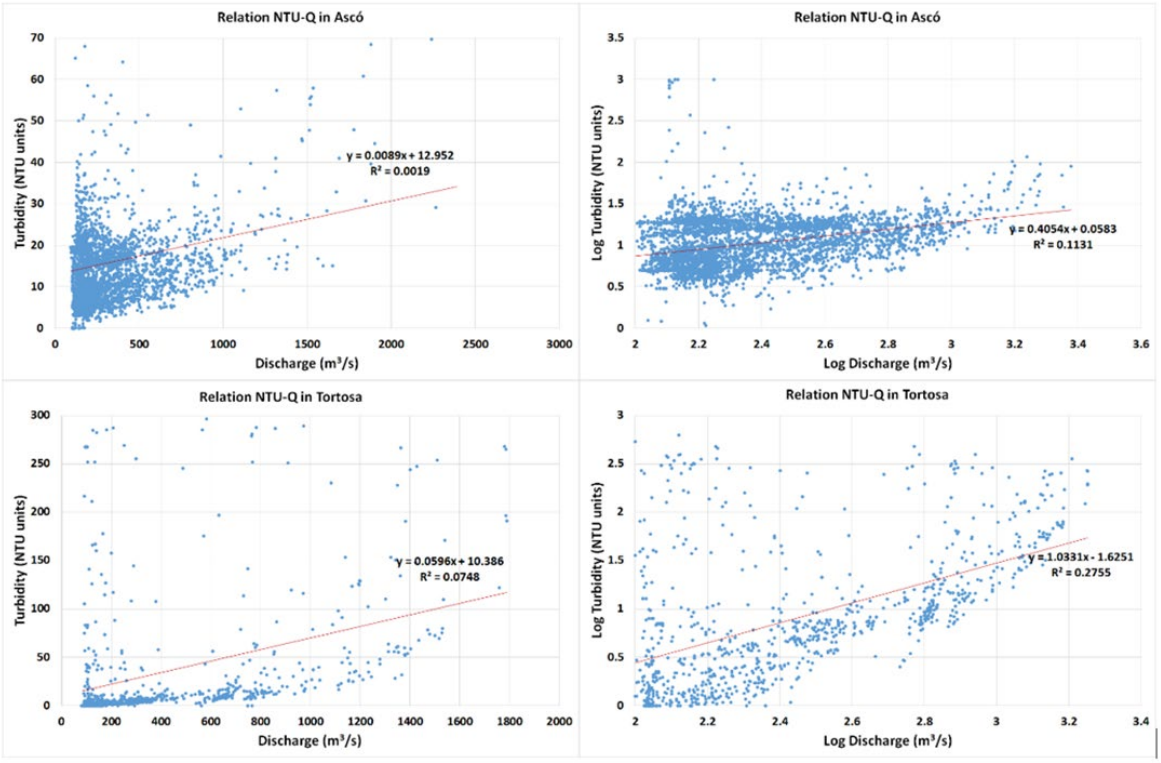

Figure 2.8. Relationship between flow and turbidity for the stations of Ascó (top) and Tortosa (bottom). The graphs on the left are in natural scale and those on the right are in a logarithmic scale.

The data compiled will be used to perform simulations of realistic scenarios of sediment transport under current management strategies. These data are conditioned by the fact that there is no sediment source for transport, although the influence of this factor can be explored with the help of numerical simulations.

2.9. Coastal and Marine environments of the Ebro delta simulations

The Ebro Delta coast is highly vulnerable against high-energetic events as well as to the rising MWL, specially in the Trabucador barrier beach that links the mainland with the southern arrow. The necessity to maintain this environment due to its value has led UPC to focus efforts in the implementation of NBS in order to reduce the ESS, in this case coastal erosion and flooding.

To test the viability of such approaches,the COAWST and XBeach models are used to simulate the best hydrodynamic conditions and the most accurate response of the coast to these extreme events. Following the literature, together with the expertise and conclusions extracted from the field, the implementation of dunes is selected in the area as the most optimal NBS.

2.10. High-resolution coupled coastal models

To reach the proposed objectives, the framework synthesized in Figure 2.9 is developed. The final goal is to use this methodology in operational mode to create an EWS able to alert of possible hazards during storm events. First, meteorological and oceanographic forcings from CMEMS forecast products are gathered and processed to feed COAWST, which is a combination of SWAN + ROMS models. The obtained results serve as inputs for the XBeach model that is capable of reproducing the effect of flooding and erosion in the study area with high-resolution. The nesting is done through the passing of the COAWST-modelled wave spectra at several points along the open boundaries of the Xbeach domain. Routines are prepared to ease the

transition from pre-operational to operational phases when required. Some tests have been made to check the viability of the operational approach, in which XBeach directly takes data daily from CMEMS and computes the flooded area for a three-day forecast period. Once the validation and calibration of the COAWST model for the Ebro Delta as well as the nesting with XBeach are completed, COAWST will be included in the operational chain to fill the presented framework.

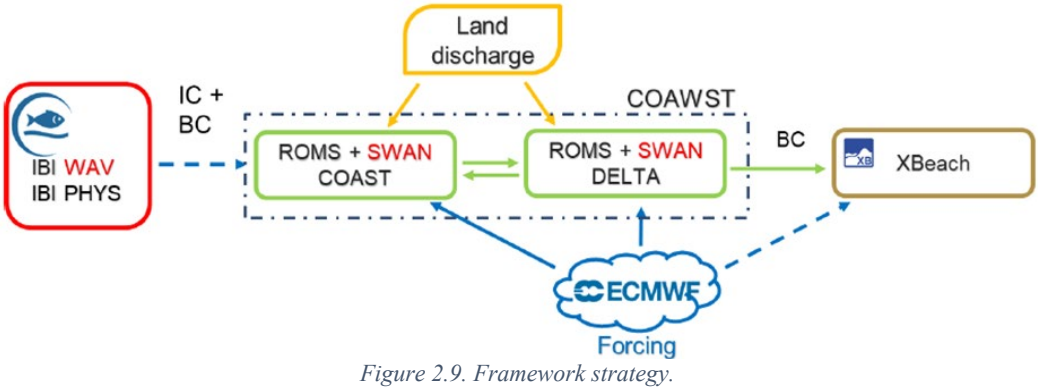

Figure 2.9. Framework strategy.

To evaluate the efficiency of the dune implementation in the Trabucador barrier beach, only XBeach has been used due to computational constrains, since both the calibration and validation of the model need a huge number of runs. Meanwhile, parallel validations of COAWST are being performed. When both models have been assessed individually, they will be combined to work together to provide an improvement of the results presented separately.

The computational grid of the COAWST model covers the Ebro Shelf with a horizontal resolution of 350m, which finally produces a 160x150 cells mesh at the area where XBeach is run. The vertical discretization has 8 sigma levels, which resolve both surface and bottom boundary layers over the continental shelf. The XBeach grid is focused on the Trabucador barrier beach reaching a resolution of 5x10m, with higher resolution in the cross-shore direction (Figure 2.10). As it is, the model is able to simulate 1 day in approximately 5 hours, although this configuration, used for the NBS viability test, will be changed to a coarser resolution mesh when running in operational mode, reducing the simulation time to adapt to operationality needs.

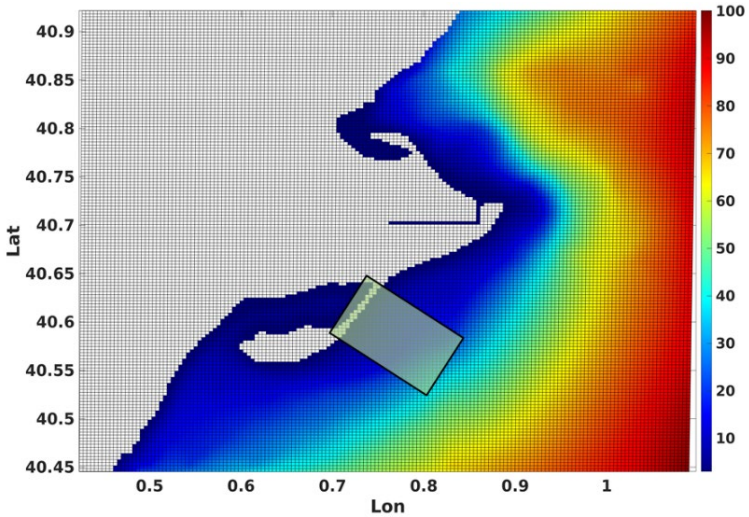

Figure 2.10. COAWST and XBeach grids location. The green rectangle represent the area of the XBeach mesh inside the COAWST mesh.

2.11. Parameterization of hydro-morpho-eco interactions to simulate ESS.

The Ebro Delta pilot site, specially the Trabucador barrier, frequently suffers breaching events during storms. The barrier connects the mainland with salt pans, and its breaching leads to productivity and economic losses due to the inability of the trucks to reach the pans. Besides, mostly during summer, the beach is used for recreational use. These factors ensure a dependency of the local economy on the correct preservation of the barrier. An improvement of the stability of the barrier directly enhances the ESS to coastal erosion and coastal floading. For extreme events, is thought to be reached through the incorporation of embrionary dunes.as NBS.

The first necessity was to built the most realistic grid with the available data. The barrier's topobathymetry has been changing for years due to the sedimentary transport caused by wind, currents and waves. In order to use the most accurate mesh corresponding to the selected time scenarios, UPC used the best available sources. The bathymetry was generated with a digitization of the Navionics nautical chart using GIS sofware, combined with the existing topographies created by merging DTMs provided by the ICGC (Institut Cartogràfic i Geològic de Catalunya) and LiDAR data from 2021 done by Costas de Tarragona. The final grid, Figure 2.11, was done by coalescing both the bathymetry and the topography, checking for any incompatibilies and comparing the result with orthophotos to verify its correct fittin with reality.

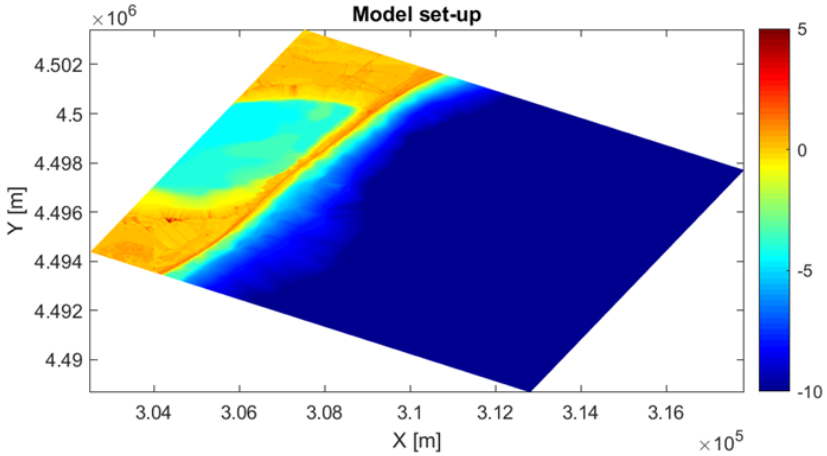

Figure 2.11. XBeach mesh.

In addition, during the beginning of 2023, the UPC was involved in a real test in which embrionary dunes were created on the Trabucador beach. These dunes were characterised on a DTM which was used to create a new grid to simulate events with the ESS strategy (Figure 2.12). During the time when the dunes were generated, storm Isaak hit the Trabucador beach (specifically on the first half of February 2023). The expertise of the UPC team, that saw the effects of the storm on the barrier and the level of mitigation provided by the dunes, jointly with drone flights allowed to see the resistance of the barrier to breaching. The gathered information helped to correctly characterise the event and validate both the XBeach model and the NBS mitigation strategy. In this case, the forcing wave data were taken from the "Puertos del Estado" observational network, but in the future they will be provided by the CMEMS + COAWST framework presented before to see that the strategy provides similar results.

Figure 2.12. Left: Alternate embrionary dunes placed on the Trabucador barrier beach. Right: DTM obtained previously to the Isaak storm event with the dunes placement.

2.12. Target operational period for testing the EWS nested into CMEMS products

Testing was done using two storms for calibration and validation. Since the LiDAR data used to generate the first topobathymetry was close in time to the Filomena storm, this event was the first one selected for the XBeach simulations. The storm, one of the most important meteo-oceanic events in Catalonia in the past years, hit the study area from 7th January to 12th January 2021, causing significant wave heights of up to 5 m of in some areas, being. The second storm, selected as a validation scenario and to test the linking between COAWST and XBeach, was Gloria. This was the most intense storm recorded in the last decades in Catalonia, from 18th January to 24th January 2020. Ortophotos show that this event completely breached the Trabucador barrierm so it is a good indicator of the maximum type of storm this beach is going to face.

Regarding the COAWST inputs, the open boundaries of the Ebro Delta Shelf ROMS domain were forced by a Mediterranean-scale circulation model (Med MFC) with a horizontal grid resolution of 1/24˚ (ca. 4-5 km) and 141 unevenly spaced vertical levels (Escudier et al., 2021). The Med MFC physical multiyear product (MEDSEA_MULTIYEAR_PHY_006_004) is generated by a numerical system composed of a hydrodynamic model, supplied by the Nucleus for European Modelling of the Ocean (NEMO) and a variational data assimilation scheme (OceanVAR) for temperature and salinity vertical profiles and satellite Sea Level Anomaly along track data. The SWAN open boundary conditions were provided by the MEDSEA_ANALYSISFORECAST_WAV_006_017 wave product of the Mediterranean Sea Forecasting system, composed by hourly wave parameters at 1/24˚ horizontal resolution covering the Mediterranean Sea and extending up to 18.125W into the Atlantic Ocean. The Med-WAV system is based on the WAM Cycle 6, and resolves the prognostic part of the wave spectrum with 24 directional and 32 logarithmically distributed frequency bins, correcting the solution with an optimal interpolation data assimilation scheme of all available along track satellite significant wave height observations. Atmospheric forcing (hourly heat and freshwater fluxes, and wind stress) was obtained from the European Centre for Medium-Range Weather Forecasts (ECMWF; www.ecmwf.int) and, alternatively, hourly winds from AEMET (Spanish Meteorological Agency) were also used. The Ebro River discharge was included in the model as a daily freshwater source with flow rates provided by the Confederación Hidrográfica del Ebro (CHE, Ebro River Basin Regulator). With these forcings, COAWST was used to simulate the Gloria storm from 18/01/2020 14:00h to 24/01/2020 22:00h. Figure 2.13 shows the comparison between the surface currents measured by the Ebro HF Radar (Puertos del Estado) and the ROMS model output for the Gloria storm simulation. Figure 2.14 shows the bottom currents obtained in the Marquesa (north of the Ebro Delta) and Trabucador (area of study) beaches during the peak of the storm.

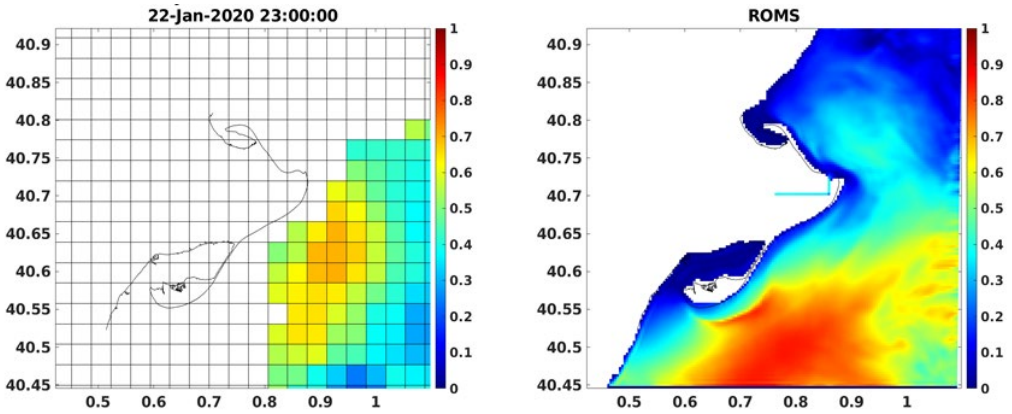

Figure 2.13. Comparison of the numerical results and HF-Radar from Puertos del Estado in terms of surface currents.

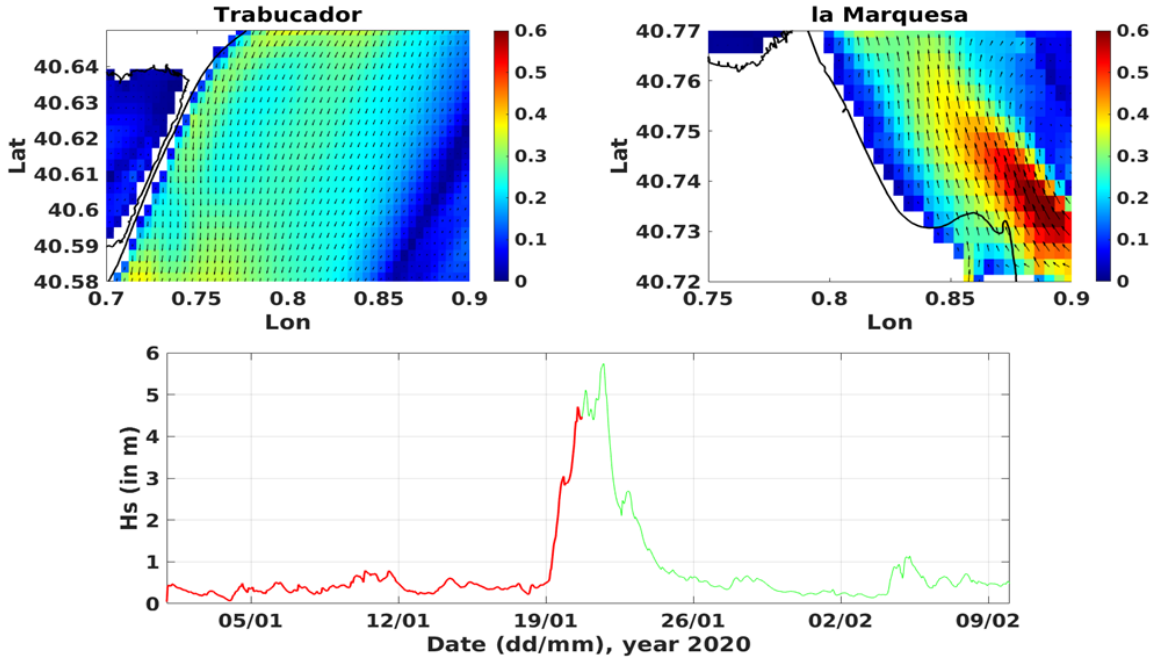

Figure 2.14. Bottom currents obtained during the peak of Gloria storm

Previous to the validation of Xbeach using Gloria , the Filomena storm was used to calibrate and validate the model because the topobathymetries available for the Filomena period was of better quality. Table 2.2 summarizes the model parameters that best reproduce the behaviour of the beach under storm conditions as compared with ortophotos, after performing nearly 65 runs. Generally, it was seen that morfac (morphological acceleration) was a parameter that helped the model to run faster rather than introducing significant changes in the model output (when ranging within reasonable values), whereas fallvelred, cmax, facua and gammax were the parameters that affected most in terms of erosion, which leads to breaching problems.

It has been observed that barrier breaching during a storm event leads to the formation of small sand islands, instead of only breaking the barrier continuity. To reproduce this, UPC has tried a novel strategy to validate the erosion outputs instead of using the Brier Skill Score (BSS), which is the most usual approach. In this case, the Goodness of Fit computing the similarity between polygons from two different sources was the selected methodology. As it can be seen in Figure 2.15, the comparison of the polygons obtained from the real scenario (taken from orthophotos at the end of the event) and the polygons produced by Xbeach for the

same event yielded a similarity larger than 50%, plus the additional fact that the observed polygons fully match and the number of breaches coincide. It is also important to understand that this methodology is very strict, and results of more than 50% similarity rely on a very accurate reproduction of the observed behaviour.

Using the same optimal parameters obtained from the calibration and validation using Filomena storm, simulations for the Gloria and Isaak events were done, and the response of the beach was also checked by comparing ortophotos with the outputs of the model. Good correlations between modelling and reality were observed, confirming the capability of XBeach to reproduce the behaviour of the Trabucador barrier under storm events.

Table 2.2. XBeach calibration parameters. The box colour represents parameters that do not affect the results (white), parameters that slighty affect the results (light green), and parameters that strongly affect the results (dark green).

Parameter	Impact on the model	Storm Filomena
morfac	Speed-up model	10
	Bed Slope related parameters	
wetslp	Increasing it reduced off-shore bar formation during initial runs	1.2
dryslp	Increasing it reduced off-shore bar formation during initial runs	0.8
dilatancy	Reduce critical Shields number due to dilatancy (reduced and off-shore bar formation)	1
bdslpeffdir	Modify the direction of the sediment transport based on the bed slope (no Significant impact)	talmon
	Sediment Transport related parameters	
fallvelred	Switch to reduce fall velocity for high concentrations	1
cmax	Maximum allowed sediment concentration	1
facua	Reduced erosion over-estimation cross-shore transport and increased on-shore but during calibration process increasing it more than 0.2 produced over accretion and bars	0.15
	Wave Dissipation related parameters	
gammax	Reduced erosion-overestimation greatly	1.5
	Others	
wci	Initially enabled produced good results at barrier but every time model blow-out during calm period post storm with high degree of accretion in bay side (several meters)	0
lws	Long wave Stirring – no Significant impact	0
gwflow	Ground water flow - no Significant impact	1

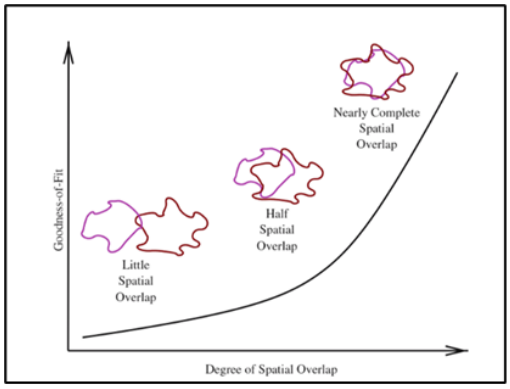

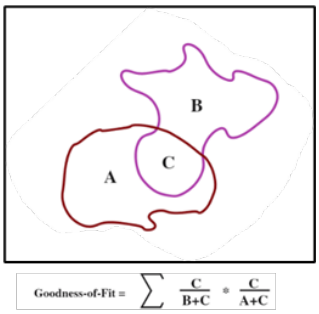

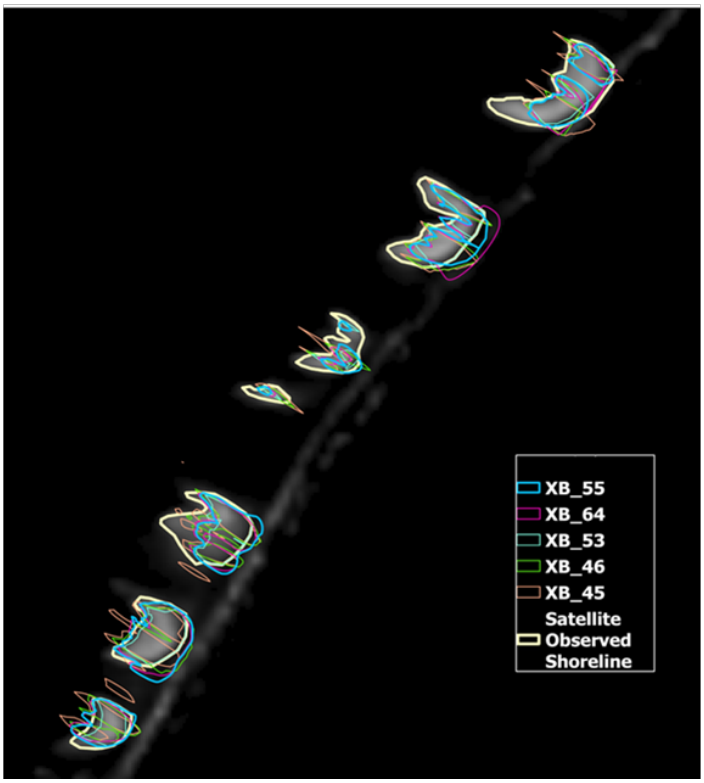

Model run	Goodness of fit
XB_45	0.3
XB_46	0.38
XB_53	0.36
XB_55	**0.52**
XB_64	0.44

Figure 2.15. XBeach validation. Top explains the concept of Goodness of Fit. Middle presents the results for the best runs from the calibration. Table at bottom shows the results from the index for each run.

2.13. Hazard reduction from ESS as a function of restoration scale.

Considering that the model reproduces the barrier beach for the studied storm scenarios, it was possible to generate the so-called ”like-scenarios”, in which the introduction or removal of dunes was tested. As stated in Section 2.3.2, during the passing of the Isaak storm a series of alternate embrionary dunes were built along the barrier beach to test their effectiveness in reducing the ESS, in this case erosion in form of breaching, and flooding of the area. Since XBeach reproduced correctly the behaviour of the beach with these dunes, the same exercise was repeated but using a new mesh without the dunes. Figure 2.16 shows how the absence of the dunes clearly favours the breaching problem and leads to some breaking of the barrier during the storm, while their presence preserves the continuity of the beach and reduces the ESS, validating thus the NBS strategy used at this site.

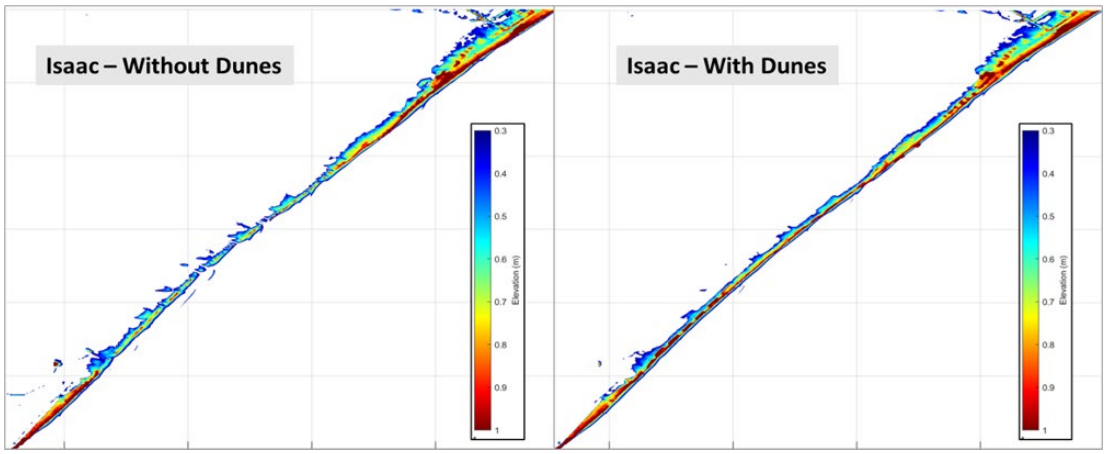

Figure 2.16. XBeach results for the Isaak storm with the dunes (right) and what could have happened if the dunes had not been placed (left).

To better understand the role of the dunes in the hazard reduction, the same test was done under the Filomena and Gloria storms. In this case, the beach faced the events without any protection measure and the new grid included the same dune configuration as for the Isaak storm. Figure 2.17 shows how for the Filomena storm the dunes reduced significantly the breaching processes and only small breaks are registered, mantaining the continuity of the barrier and allowing the pass of the trucks if necessary with few sand recoveries. By contrast, the Gloria storm produces a similar destruction for both cases and no big mitigations are observed at first sight. This event, as already described previously, was the strongest storm registered in Catalonia for the past decades and is highly infrequent. This test allows to see that there is a limit above which the dune strategy does not work as expected, enhancing the necessity to look for the tipping points in the future.

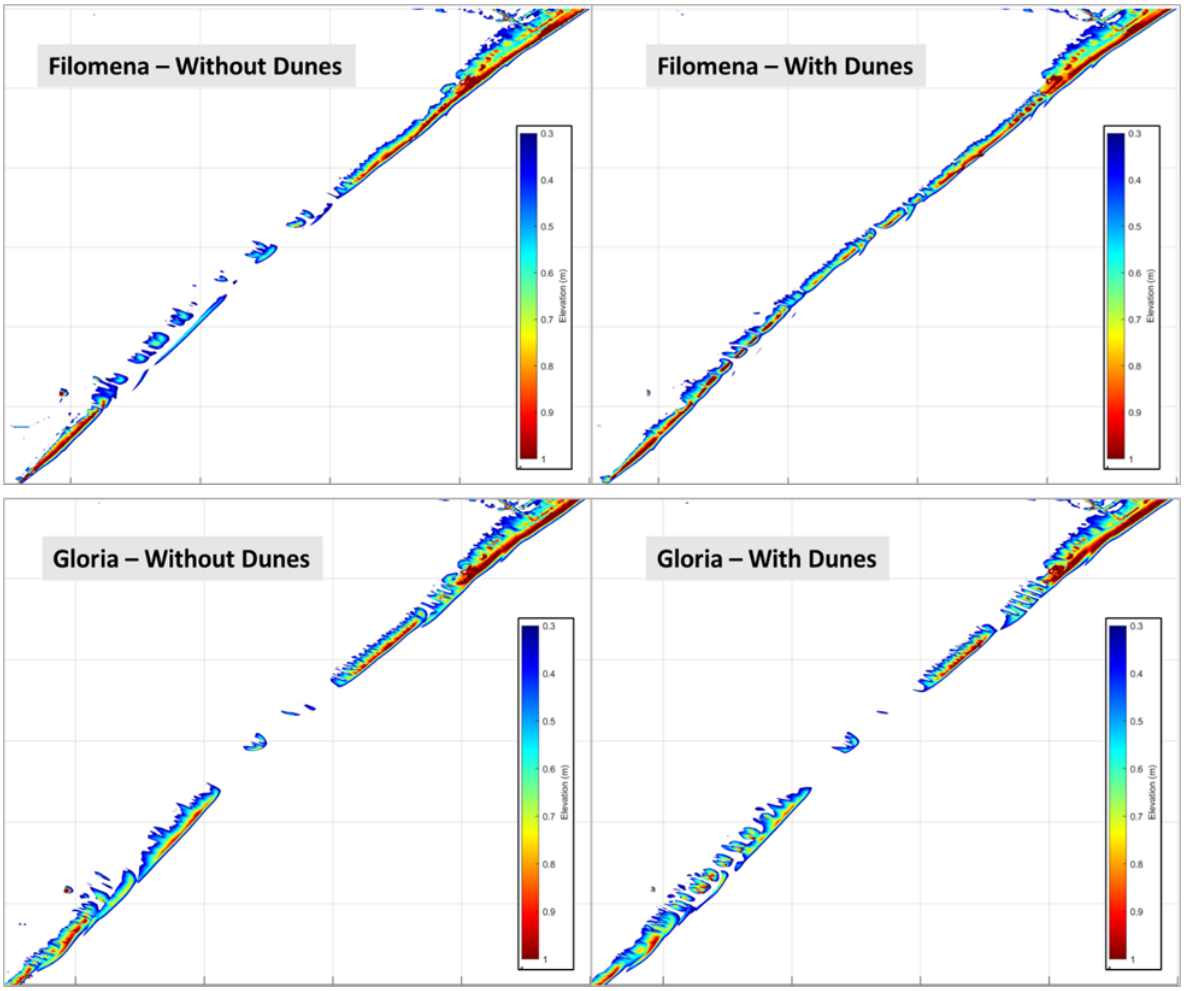

Figure 2.17. XBeach results for the Filomena and Gloria storms and what could be happened if the duned were placed.

Although the response of the beach under the storms with and without the dunes can be seen visually in Figures 2.16 and Figure 2.17, some metrics have been developed in order to quantify the reduction of the breaching. First, in order to check the magnitude, percentage of volume breached was computed as the total volume submerged at the end of the simulation from +0.3m (avoiding the storm surge effects) with respect to the total volume of the beach before the storm. ure 2.18 shows that for all cases, there is an important mitigation of the volume breached, even for the Gloria storm, although this was not apparent from the figures. This enhances the usefulness of dunes to protect the beach from these problems. Even so, this metric does not account for the possibility in which many small barrier breaches have more volume than a single big breach and, in this case, it could be seen that the strategy works but the continuity of the barrier is on risk. For the trucks, it is better to have small breaches that are easier to restore than a larger one. In order to solve this problem, the percentage of breached area was also computed, to see if a truck would be able to progress along the barrier. Figure 2.18 also shows that, except for the Gloria storm, the area breached is highly reduced for Filomena and Isaak, thus strengthening the selection of the NBS. More metrics are under development to improve the interpretation of the results.

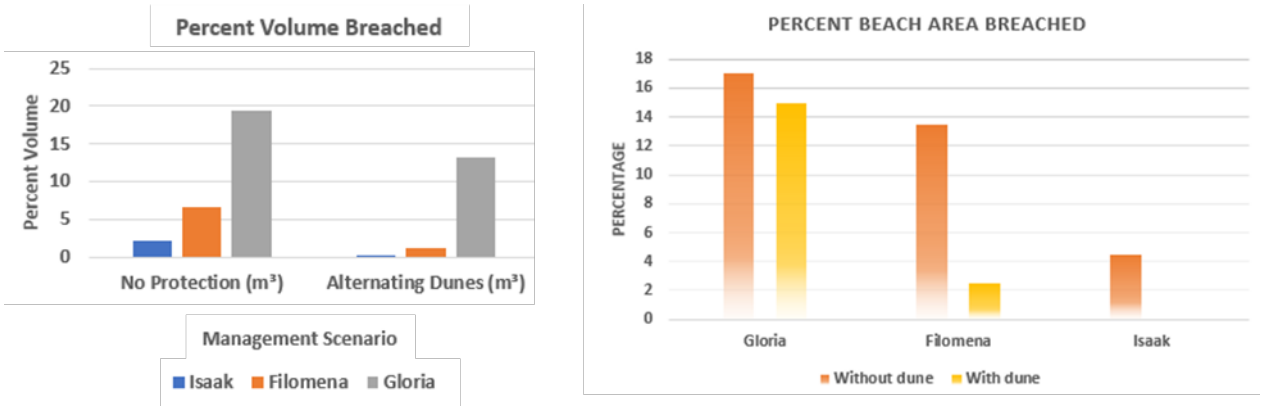

Figure 2.18. Metrics for breaching effects. Left: Percentage of volume breached for each storm scenario with and without dunes. Right: Percentage of area breached for each storm scenario with and without dunes.

2.14. Conclusions

XBeach is able to correctly simulate the evolution of the Trabucador barrier beach under storm scenarios with good accuracy after an exhaustive calibration. A novel validation of the erosion outputs has been used according to the needs and limitation of the available data, achieving high similarity between reality and model results. The incorporation of the COAWST model into the modelling chain will improve the performance of the whole framework since the capacity of this model to reproduce the waves and current dynamics of the Ebro Delta shelf has been also proved.

Based on both field tests and numerical modelling, it seems that dune seeding works effectivey as a hazard mitigator strategy in terms of breaching. A large reduction in both the volume and the area of breaching have been found for all the simulated scenarios when dunes are introduced as compared to the same scenarios without dunes.

The Gloria storm has helped to understand that there is a threshold above which the dunes do not work as expected, and that the tipping points for the strategy have to be found. Improvements on this problematic jointly with the study of new metrics to better represent the performance of the NBS will be tested in the future.

Operationality is starting to be implemented and working for the direct nesting between CMEMS and XBeach and it is planned that COAWST enters as a link between them to increase the accuracy of the results.

3. Multi-hazard forecasting (including a multidisciplinary calibration) and application limits Wadden Sea Pilot (DEL, FSK, HZG)

3.1. Introduction

The Wadden Sea is one of the most valuable areas of shoreline in the world. The Dutch and German areas have been listed as World Heritage Sites since 2009 (Common Wadden Sea Secretariat, 2008). It is a very dynamic tidal region where water column heights change depending on season, tide, and the weather conditions. Its tidal inlets are high-energy zones that are continually shifting in response to environmental influences.

The Ems-Dollard estuary of the Wadden Sea is the main focus of the Dutch partners, while the German partners are working on the Wadden Sea section along the coast of Niedersachsen with spatial focus on the Ems and Weser estuaries, as well as the tidal basins behind Borkum, Juist and Norderney barrier islands.

3.2. High-resolution coupled coastal models

For the quantification of ecosystem services, the partners involved have further developed and applied different high-resolution model systems for different focus areas.

3.2.1. Ems-Dollart model (Deltares)

With the thematic focus of modelling morphodynamics of the Ems estuary, Deltares has developed a new morphological model within the Delft3D flexible mesh software. This model builds on earlier morphological models developed in Delft3D4 by Deltares in 2016-2017 and the Delft3D FM hydrodynamic model developed by Schrijvershof et al., (2023). The shift towards the flexible mesh software is motivated by (1) its ability to flexibly expand or locally refine the numerical model domain, in order to flexibly implement ecosystem services and (2) the more advanced methodologies to model the morphodynamic impact of vegetation. The hydrodynamic model includes reduced tidal boundary conditions (see Schrijvershof et al., 2023) and wind-driven flow nested in the Dutch operational system, with a major point of attention during calibration being the alongshore water flux as this drives sediment supply (see details hereafter). Waves are computed with SWAN, using a wave climate schematization fitting the tidal input reduction. Sea level rise and changes in storm conditions will be derived from larger-scale CMEMS models.

Grid and bathymetry

The morphodynamic model consists of two models (Figure 3.1), a larger model covering the Wadden Sea and part of the North Sea as in Schrijvershof (2023) (A) and a smaller model nested within it covering the Ems-Dollard (B). The purpose of the large model is to characterize the alongshore sediment fluxes and to provide boundary conditions for the smaller model domain. The smaller domain is computationally more efficient allowing predictions up to the year 2100. The bathymetry used is a composite of vaklodingen (a dataset of bathymetries of the Dutch coast) by the Dutch authority Rijkswaterstaat between the years 2017 and 2020, with preference given to the latest dataset during compositing. Offshore bathymetry in the North Sea was obtained from EMODnet while bed levels of the Ems River are derived from the Digitales Geländemodell (DGM).

Hydrodynamic forcing

Hydrodynamic boundaries (waterlevels and velocities) at the North Sea are obtained from the Dutch Continental Shelf model (Zijl, Groenenboom, Laan & Zijlker, 2022) and reduced into a cyclic synthetic spring-neap tide (Schrijvershof, 2023). In this approach, the harmonic components of the tide are reduced into signals that repeat every spring-neap cycle. The approach ensures a tidal boundary forcing that is appropriate for morphodynamic up-scaling, while conserving the amplitude and phase variance in the original signal. With reduced inter-annual variability in the forcing, the morphodynamics are accelerated by a factor 24, such that each hour in the simulation effectively equates to one day of morphodynamic development. The applied river discharge is taken from the winter of 2018-2019 (time period of the EDOM campaign) and repeated for subsequent years.

Meteorological forcings are obtained from the HIRLAM Weather model (https://registry.opendata.aws/hirlam). Waves at the offshore boundaries are based on observed wave heights, periods, and directions near the island of Schiermonikoog (https://rijkswaterstaatdata.nl/waterdata/). The wave time-series are implemented directly in the storm scenarios. The long-term morphological simulations require a reduced forcing. The Method by Scheel (2017) was applied to derive 12 representative wave and meteo classes from the 30 years of wave data (Figure 3.2).

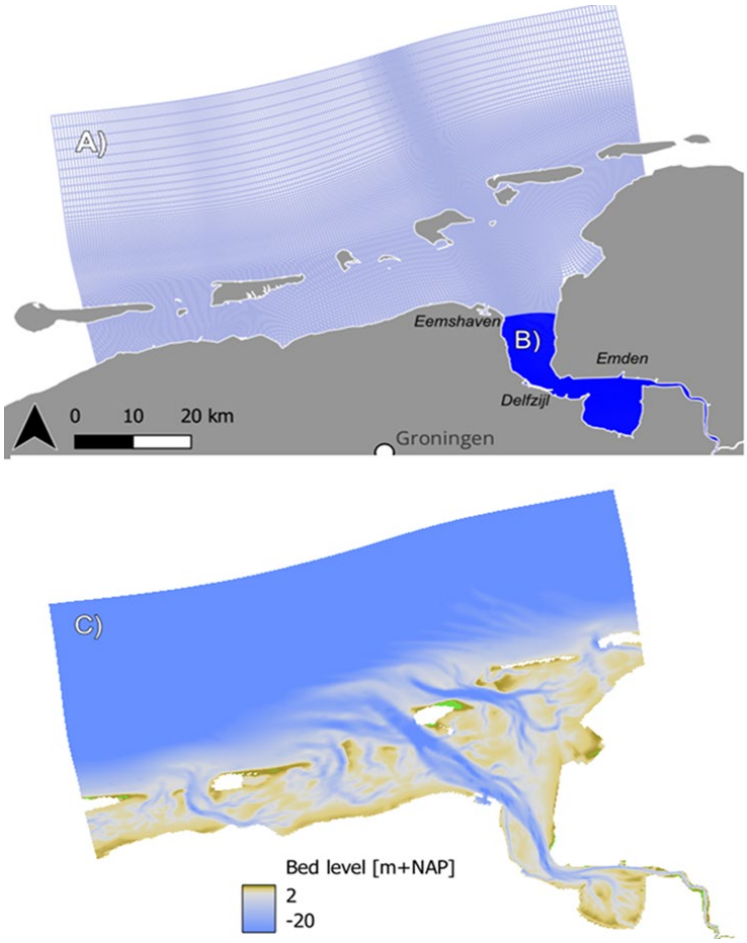

Figure 3.1. A) the outer modelling domain covering the Ems Estuary and Wadden Sea, B) the inner modeling domain covering the Ems-Dollart. C) the bathymetry composited from vaklodingen by Rijkswaterstaat (2017-2020), DGM (2015) for the Ems river, and EMODnet bathymetry for offshore bathymetry (http://data.europa.eu/88u/dataset/EMODnet_bathymetry.

The wave-meteo classes are ordered in a random sequence to synchronize the wave forcing with the consecutive repetitive tidal spring-neap cycles (Figure 3.3).

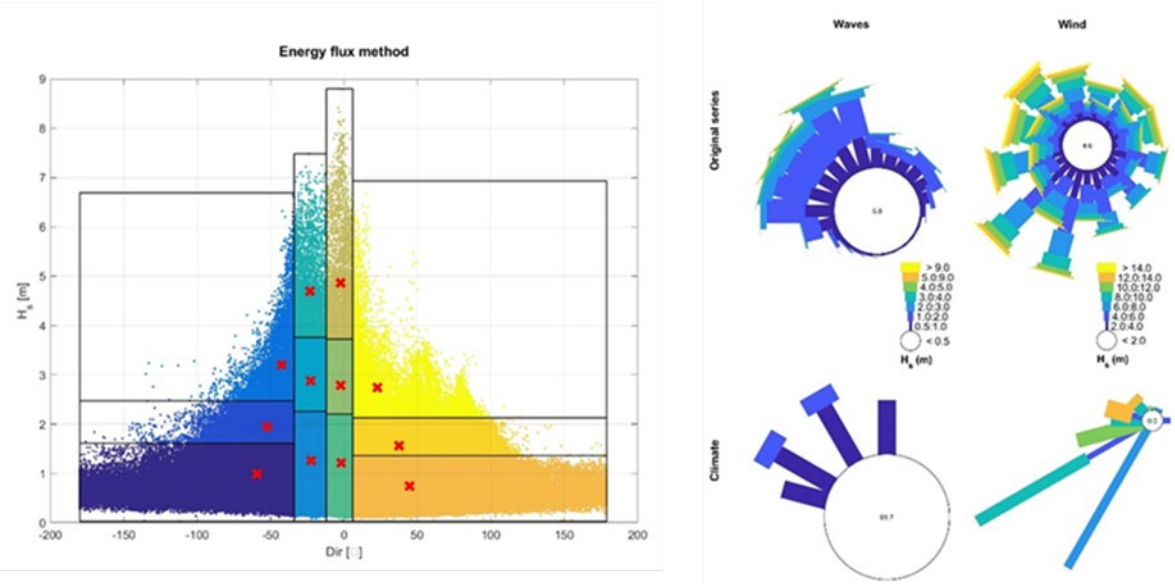

Figure 3.2. Reduction of the wave- and wind climate into representative 12 representative classes. A) wave climate (significant wave height Hs versus mean direction) classes represented against data points at Schiermonikoog, B) Wind and wave rose from the from the station at Schiermonnikoog versus the schematized climate.

Tidal asymmetry driven sediment transport is the main import mechanism for sediment into the Dollard. The model by Schrijvershof (2023) was further calibrated to improve and validate tidal propagation in the Ems estuary. A varying manning roughness ranging from 0.019 s m-1/3 in the Wadden sea, to 0.017 s m-1/3 in the Dollard, and 0.015 s m-1/3 decreasing to 0.010 s m-1/3 in the Ems was found to best reproduce the tidal signal in the overall modelling domain (Figure 3.4) and the tidal water level fluctuations and velocity patterns in the Emder Fahrwasser in particular (Figure 3.5).

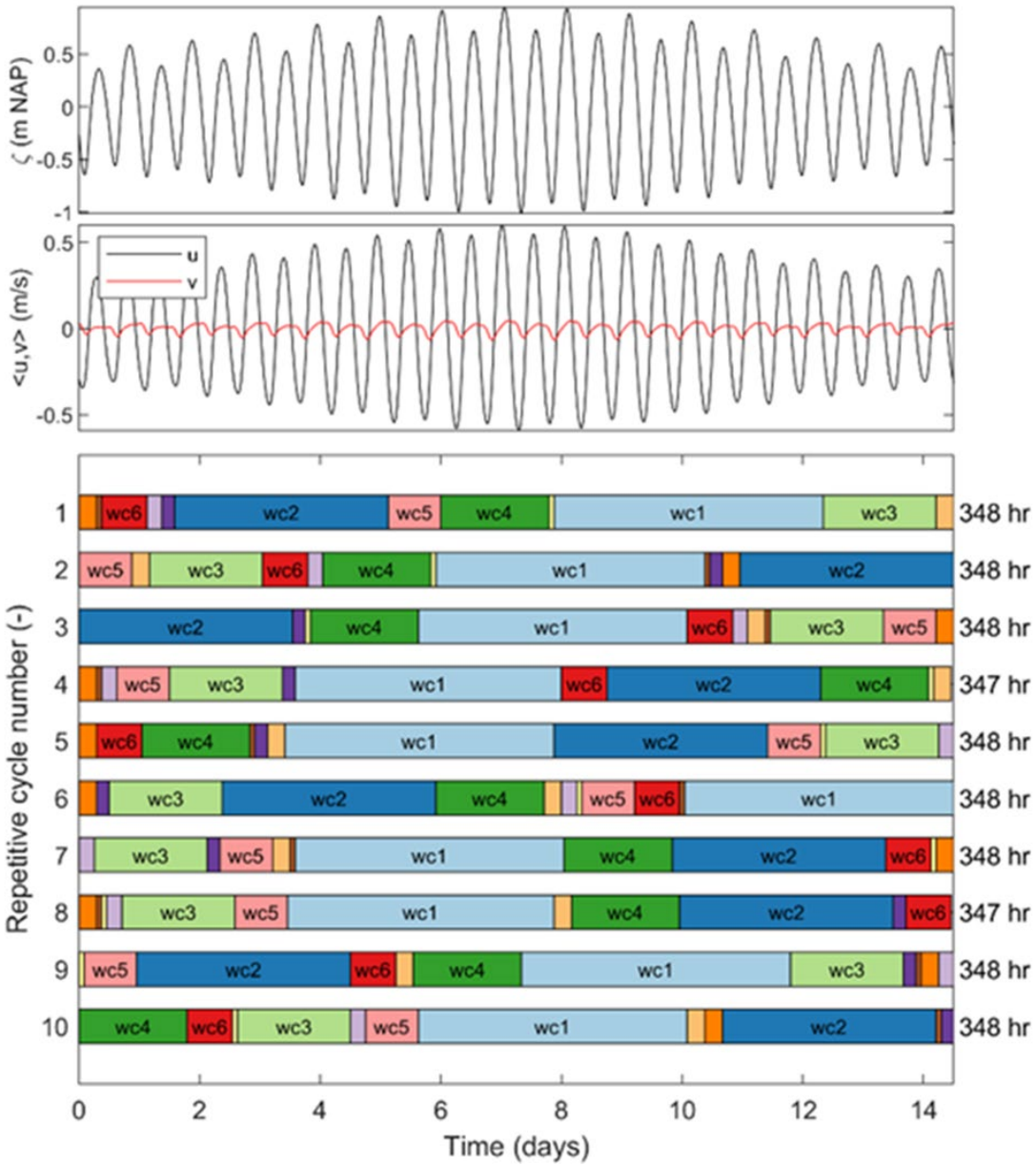

Figure 3.3. Example of a single synthetic representative spring-neap cycle for waterlevels (top), flow velocities in the u and v direction (middle), and sequencing of the wave and meteo climate conditions.

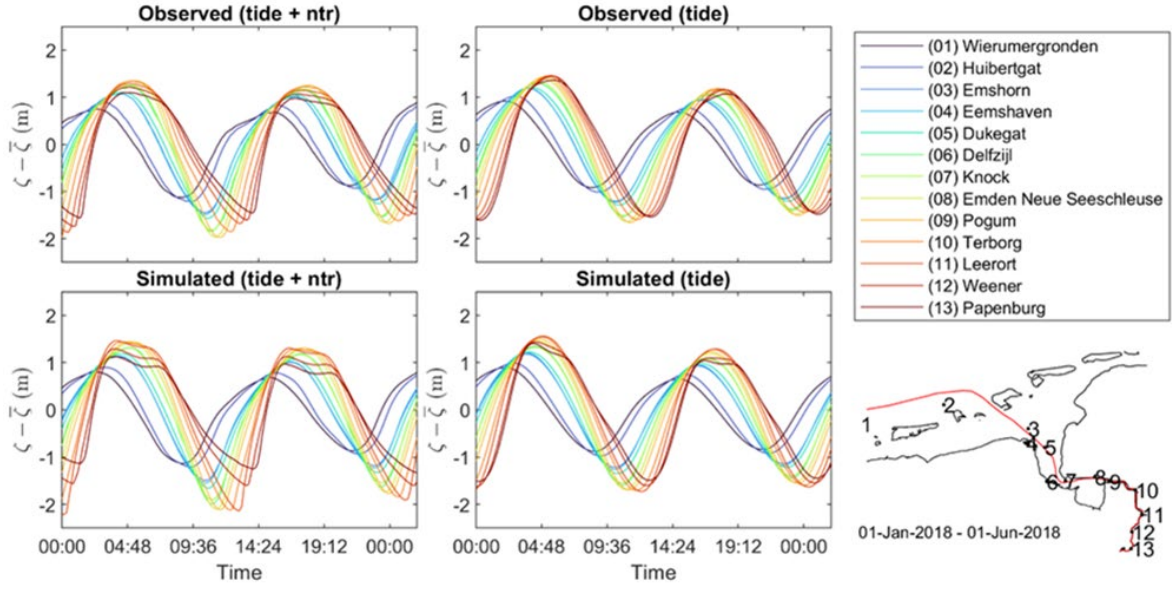

Figure 3.4. Tidal curves of observations (top) and the roughness-calibrated model

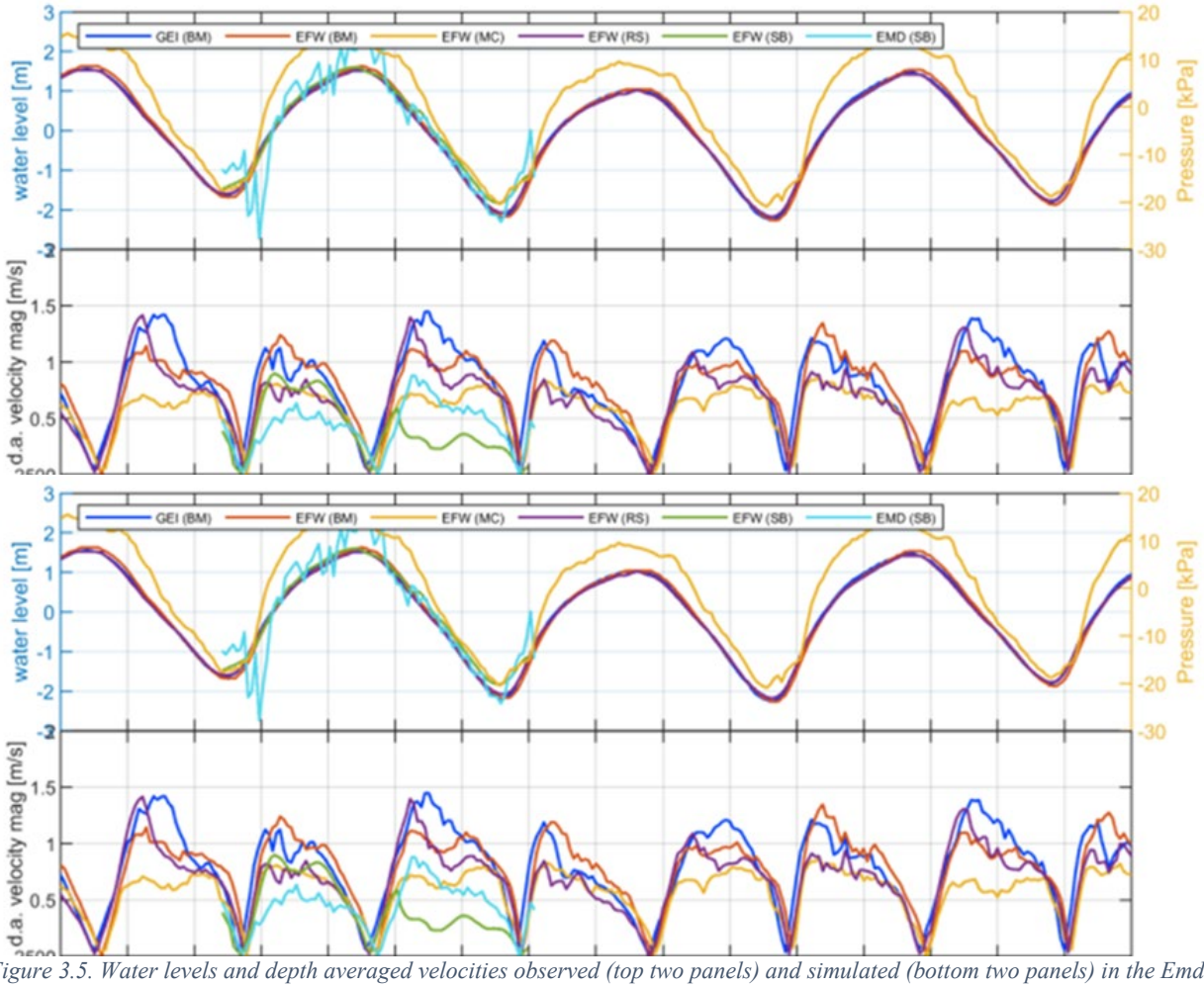

Figure 3.5. Water levels and depth averaged velocities observed (top two panels) and simulated (bottom two panels) in the Emder Fahrwasser in the winter of 2018-2019 during the EDOM campaign.

The wave model was calibrated by forcing the model with wave information from the three observation stations Borkum, Schiermonnikoog Noord, and F3 platform. Based on a comparison of wave simulation results using these three boundary forcings and in-situ wave observations at various stations in the Ems estuary mouth, Schiermonnikoog Noord produced the best fit for simulating wave heights within the estuary (Table 3.1).

Storms Xaver (December 2013) and Herwart (October 2018) are used as scenarios for evaluating flood risk reduction in the Wadden Sea pilot. These specific storms were validated using the boundary conditions derrived at Schiermonnikoog Noord. In Figure 3.8 the observed and modelled waves are plotted for station Randzelgat Noord at seaward end of the estuary and station oude Westereems zuid as the most landward station available. The model can reasonably reproduce the wave heights during the storm events but does suffer in predicting the duration of the high waves during the event, possibly due to the lower time resolution (1 hour) for updating waves in the hydrodynamic simulation.

Table 3.1. Error statistics for one-year from Schiermonnikoog BC.

Wave parameter	Statistic	
Hm0	Bias (m)	0.02
	RMSE (m)	0.23
Tm02	Bias (s)	-0.72
	RMSE (s)	1.08
Th0	Bias (°)	5.17
	RMSE (°)	42.28

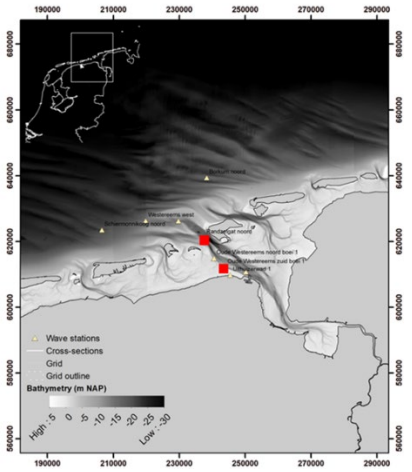

Figure 3.6. Locations of wave stations. The red squares represent the stations Randzelgat noord (top) and Oude Westereems zuid boei 1 in Figure 3.11 and Figure 3.12.

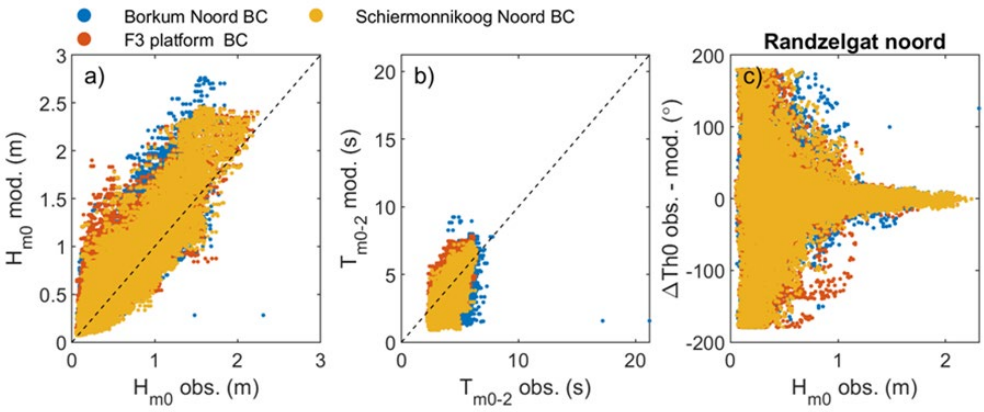

Figure 3.7. Scatter plot of wave heights at wave stations using wave boundaries calibrated on Borkum Noord (blue), Schiermonnikoog Noord (yellow), and F3 platform (orange).

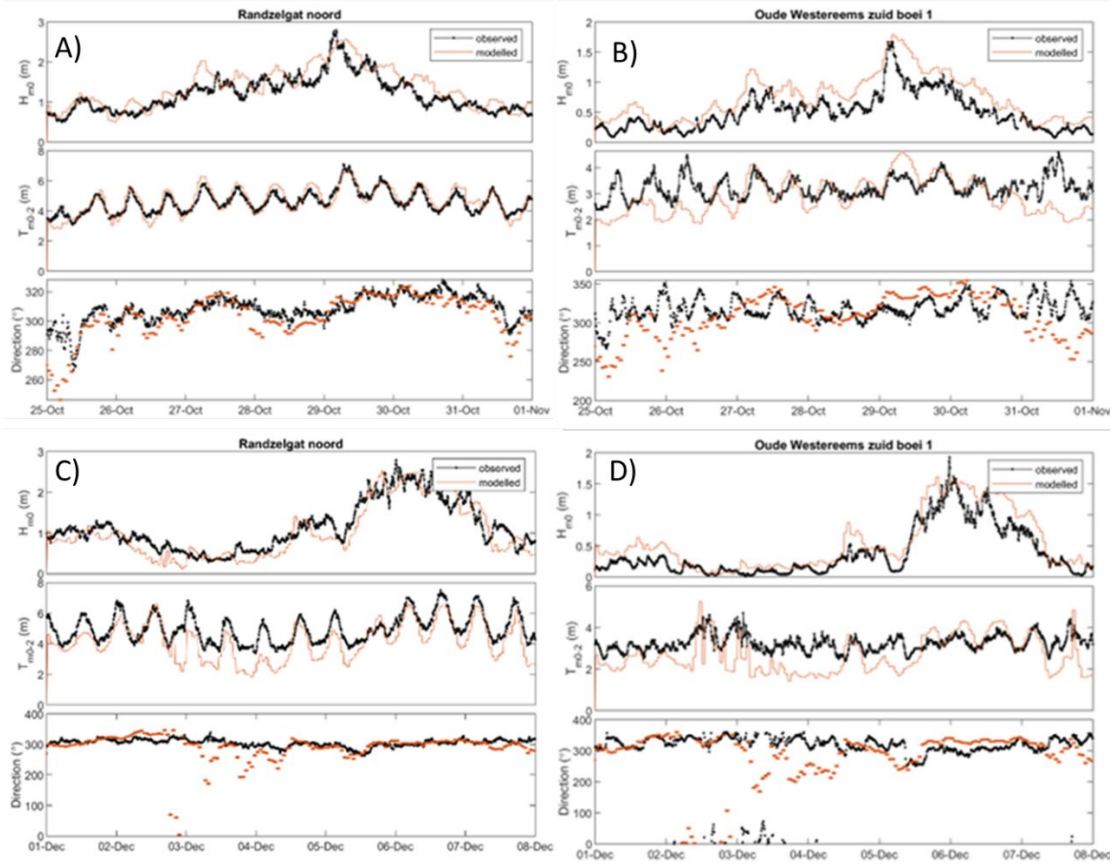

Figure 3.8. Comparison of modelled and observed wave heights during storm Herwart (2018), panels A and B, and Xaver (2013), panels C and D.

3.2.2.Ley-Bay model (NLWKN)

The focus of NLWKN is on modelling saltmarsh impacts on the decrease of hydrodynamic forcing and subsequently enhancement of sedimentation in the Oster-EMS (OEMS) using a Delft3D configuration for the eastern part of the Ems-Dollard estuary. The key aspect is to investigate the contribution of saltmarshes to sediment trapping, and hence to morphological evolution.

The main objective is to investigate the potential use of saltmarsh as a nature-based-solution (NBS) for coastal protection. The present work focused on the evaluation of hydrodynamics, sediment transport and bed evolution during extreme events. The contribution of NBS to these processes was analyzed by comparing the hydromorphodynamic results without NBS (WT - NBS) and with NBS (NBS) applications.

Grid and bathymetry

Our study area is Ley Bay, which is located at the landward end of the tidal basin between Borkum and Juist barrier islands, and spans an area of about 5 km x 5 km. A high resolution grid (OEMS: Figure 3.9b) and bathymetry (Figure 3.9c) were developed within the present project to investigate the potential effect of NBS on hydrodynamics and morphological evolution. The OEMS domain consists of parts from both North Sea and Wadden Sea to provide a good interaction between North Sea and Wadden Sea processes, and covers an area of about 920 km2. The highest resolution in the Ley Bay is 30 m x 80 m, which is sufficient to represent the existing channel and shoal pattern and to optimize the computational cost. The bathymetry was

developed using the LiDAR data, which was measured in 2015 by the field measurement department of NLWKN.

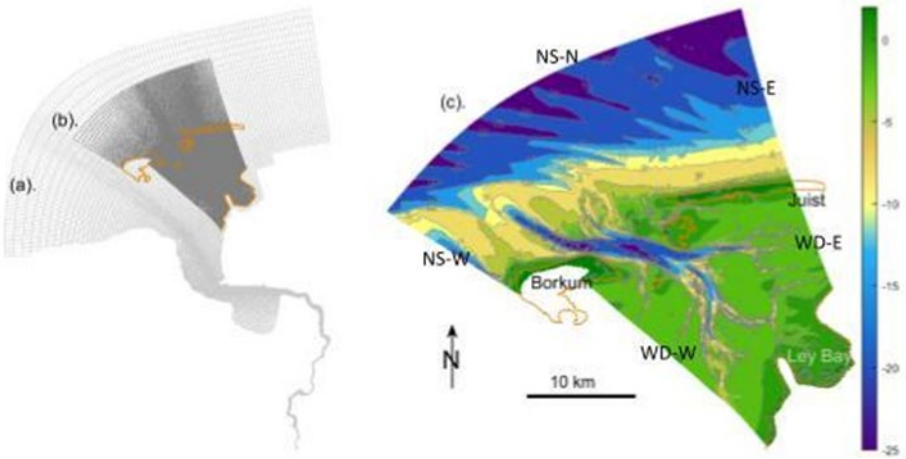

Figure 3.9. EMS-grid (a), OEMS-grid (b) and OEMS-bathymetry (c). For clarity, only every other gird is shown. The orange-line indicates the land boundary, and the investigation area is Ley Bay. Color bar indicates water depths with respect to MSL. There are 5 open boundaries: 2 at Wadden Sea, East (WD-E) and West (WD-W), and 3 at North Sea, East (NS-E), North (NS-N) and West (NS-W).

Model boundary forcing

The OEMS model was simulated by force with tide, wave and wind. Both tide and wave were developed for the OEMS by coupling with the EMS model (Figure 3.9a). The OEMS model has 5 open boundaries: 3 at the North Sea side (i.e., NS_E, NS_N and NS_W) and 2 at the Wadden Sea side (i.e., WD_E and WD_W) (Figure 3.9c). All 4 lateral boundaries were implemented as velocities, while the north boundary (NS_N) is water level. Water level and current boundaries were set up based on the predicted values of the EMS model. For waves, both models were simulated simultaneously applying the offshore wave boundary for the EMS model. Based on a sensitivity analysis, the optimal wave prediction around the Ley Bay area was found, when the EMS model is forced with spatiotemporal wind fields (DWD, 2023) and the OEMS is forced with uniform wind measured at the station of Norderney: the next island to the east of Juist (DWD, 2023). For the sorm events, Xaver and Herwart, the boundary forcing for the EMS model was obtained from a North Sea model of HEREON SCHISM.

3.2.3.German Bight model (Hereon)

Hereon (former HZG) investigates the impact of seagrass on coupled hydro-, wave- and sediment dynamics of the Wadden Sea using the SCHISM and Xbeach model systems. In order to quantify the ecosystem services of seagrass restoration in the entire Wadden Sea region, Hereon´s SCHISM (Zhang et al., 2016) configuration for the German Bight (Stanev et al., 2019) was further upgraded incorporating the multi-physics coupling, involving waves, sediments, and the vegetation module. The wave component is contributed by the state-of-the-art 3D generation wind wave model WWM III (Roland et al., 2012), which solves the wave action balance action equation on an unstructured triangular mesh, corresponding to the core model, and involves shallow water wave breaking.

For the simulation of sediment dynamics, the 3D sediment model SED3D is coupled, which is an unstructured grid portation of the community Sediment Transport Model (Warner et al., 2008). The sediment model resolves the processes of erosion, deposition, bed load transport and suspended load transport. It was

configured analogously to Stanev et al. (2019), using eight sediment classes with median grain sizes (D50) of 0.06 mm, 0.07 mm, 0.1 mm, 0.125 mm, 0.24 mm, 0.5 mm, 1.0 mm, and 2.0 mm.

To represent the Nature-based Solutions (NbS) /ESS for hazard reduction, vegetation effects are represented using SCHISM´s Vegetations module, which can simulate the first order vegetation effects approximating the plants as rigid cylinders. The vegetation model of SCHISM has been demonstrated to generally replicate vegetation effects at lab and field scales in good correlation with observation data (Zhang et al., 2020).

The German Bight model is hydrodynamically forced by the regional CMEMS product at the open boundaries (yellow line Figure 3.10); the resolution of the unstructured grid model is downscaled from 1.5 km at the open boundaries to 200-300 m in the Wadden Sea areas. The spectral wave forcing for the German Bight model is generated in-house applying a WaveWatch3 -based configuration for the North Western European shelf.
Hourly atmospheric forcing is derived from the operational model of the German Weather Service (DWD).

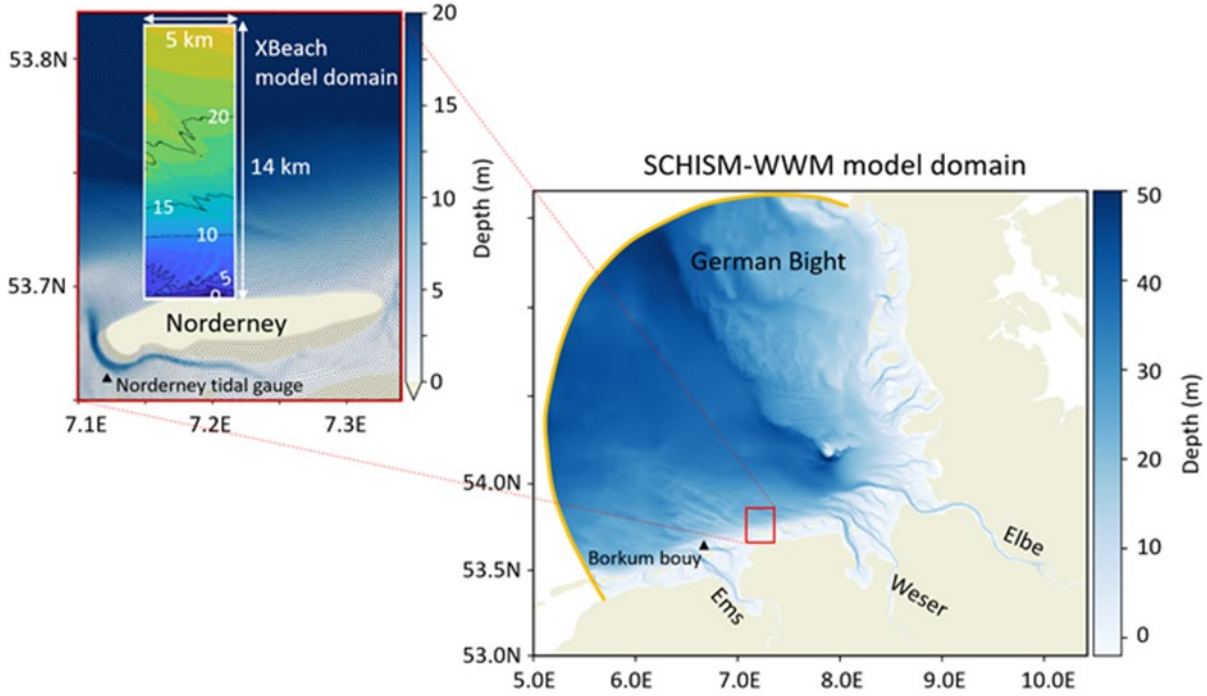

Figure 3.10. Domain and bathymetry of the SCHISM-WWM model (right) and the magnified box showing the study site Norderney (left, red box). The white box indicates the domain and bathymetry of the XBeach model. The open boundary of the SCHISM-WWM model is illustrated with an orange curve.

The model was applied to selected high-intensity storm events of the past, with the year 2017 and the storm Herwart being the main reference case for present-day storm conditions.

The model was successfully validated against tide gauge stations and wave buoys along the regional coast, and is generally able to simulate sea level during the calm and stormy phases. The performance of the model was assessed by comparing the simulations with different tide gauge stations in the German Bight for the period September and October (Figure. 3.11). The overall correlation between the model and observations is between 0.95 and 0.99%, with a root mean square error mostly between 0.2 and 0.3m. The relative standard deviation is around 0.9. In general, the model reproduces the tidal amplitudes and timing

accurately. Storm surge peaks during Herwart are correctly timed, but slightly underestimated in the EFWS (about 20-30 cm).

At Cuxhaven, the highest tide station in the German Bight, the peak of about 3.6 m on the south coast was underestimated by about 20%. The model predicted a peak of about 2.9 m (Figure. 3.11b)). This underestimation was attributed to insufficient energy in the wind forcing, resulting in an underestimation of the wind-driven rise of the south coast water level (EFWS) in the hydrodynamic model.

Validation of the significant wave height at the Fino3 (FN3) and Westerland (WES) buoys (Figure. 3.12), focusing on the week before and during the Herwart storm, shows that the model significant wave height is in good agreement with observations in terms of timing and general trends for HS. However, there is a tendency to underestimate the maximum significant wave height prior to the 29 October storm event at station Fino3. The measured (simulated) maximum significant wave heights during Herwart are about 6.9 (6.2) m at Fino3 and about 5.2 (4.8) m at Westerland. The correlation between model and observations is about 0.959 at FN3 and 0.963 at WES. The mean squared error is 0.322 m and 0.252 m respectively. The bias at these stations is about 0.115 and -0.06 m, respectively.

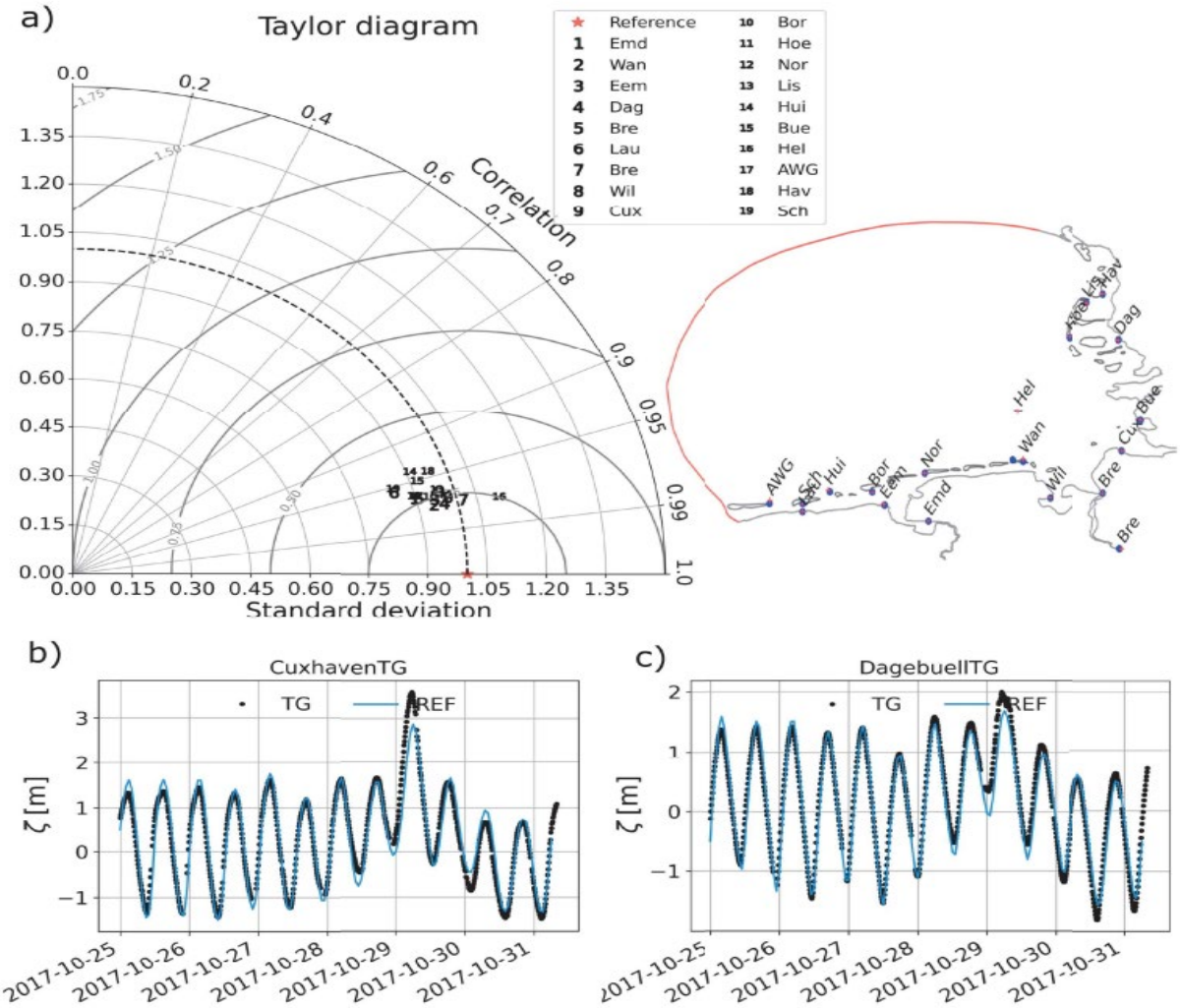

Figure 3.11. Validation of sea surface height against tide gauge stations within the German Bight in a Taylor diagram (a) for the period September-October 2017 and as time series comparison for the stations Cuchaven (b) and Dagebuell (c). The location of the tide gauge stations is indicated by the map in a).

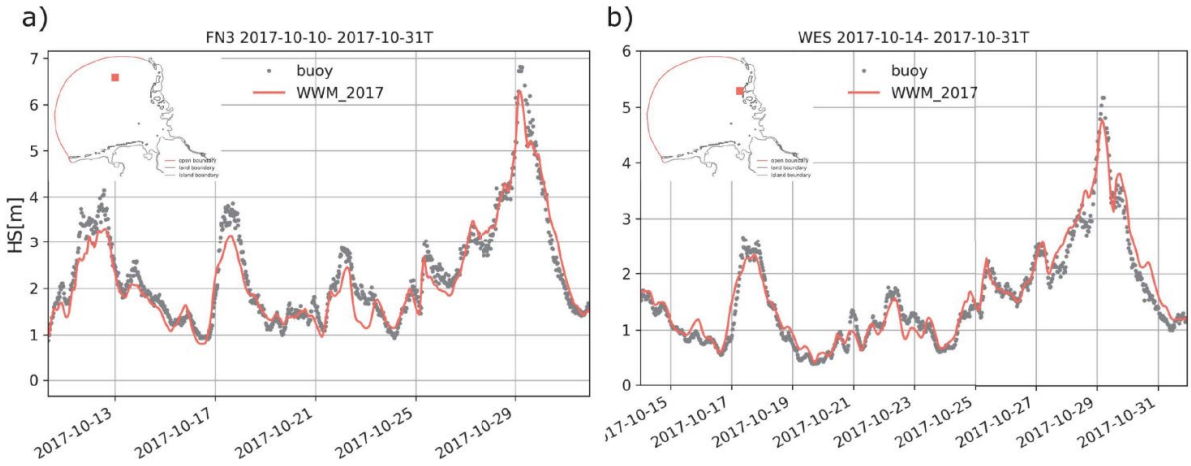

Figure 3.12. Validation of significant wave height against wave buoys Fino 3 (FN3, a) and Westerland (WES,b). The buoy location is indicated by the red square of the map in the upper left corner.

In the next derivable 2.2, sea level rise and changes in storm conditions will be derived from larger regionalized RCP8.5 sea level data.

The research focus is on the potential risk reduction for coastal flooding and erosion as enhanced ESS for extended coastal vegetation in different scenarios. Therefore, the SCHISM setup is used morphostatically, and the impact of seagrass on hydrodynamic variables and sediment concentration has been evaluated.

For direct erosion protection assessments due to enhanced coastal vegetation, an integrated framework is developed that contains two levels of simulation packages. The first level is the regional scale coupled hydro-dynamic model that simulates the processes of a specific storm and provides boundary forces to apply the morphodynamic model XBeach at the next level, simulating nearshore morphological evolution. The framework is applied at the open coast of Norderney (Figure. 3.10) in the German Bight of the North Sea. A series of what-if scenarios is designed for different features of seagrass meadow (see Figure. 3.14). The results demonstrate that optimizing the location and size of seagrass meadows is important to increase the efficiency of onshore sediment erosion mitigation.

3.3. Parameterization of hydro-morpho-eco interactions to simulate ESS

Deltares will quantify the four Ecosystem Services as follows through a scenario-based approach (simulations with and without climate change and with/without NbS sediment management strategies). The reduction of erosion risk will be assessed with the morphodynamic model directly. The reduction of flood hazard is computed by simulating storms Hewart and Xaver using the within the hydrodynamic model (see section 3.2.1 and 3.4.1.1) for the predicted bed topographies computed with the morphodynamic model. Changes in coastal water quality are computed by comparing the long-term changes in turbidity predicted by the model with and without implenting NbS sediment management strategies. Blue carbon benefits are quantified by estimating changes in carbon storage resulting from changes in sedimentation rates due to the implementation of a NbS sediment management strategy. Finally, the model predictions are transferred to biotopes based on the selected parameters using the established classification EUNIS (Baptist et al., 2019). In this respect, all three partners (Deltares, HEREON and NLWKN) work together to develop a common list of biotopes. In addition, work is done to establish principles that link maintaining ecosystem quality to managing sediment balances in the estuary, since those relations should be quantified based on numerical model results.

3.3.1.Design of what-if scenarios for seagrass configurations

Beyond the extra coupled physical modules, Hereon has advanced their modeling system accounting for the effect of coastal vegetation. The vegetation model of SCHISM (Zhang et al., 2020) physically involves the extra 3D drag introduced by the plants, as well as the generation of turbulence. The impact of seagrass is accounted for within both the hydrodynamic core and the wave model WWM III. The ESS provided by seagrass in the context of coastal flooding and erosion protection is evaluated.

Both SCHISM and Xbeach account for the first order impact of vegetation on hydro and wave dynamics, in which seagrass is represented as rigid cylinders (e.g. Zhang et al., 2020). The dampening by seagrass is accounted for as additional drag term in the momentum equation:

$$\frac{D\boldsymbol{u}}{dt} = \boldsymbol{f} - g\nabla\eta + \boldsymbol{m_z} - \alpha|\boldsymbol{u}|\boldsymbol{u}L(x, y, z) \tag{3.1}$$

f encompasses the numerically explicitly treated terms

$$\boldsymbol{f} = f(v, -u) - \frac{g}{\rho_0}\int_z^\eta \nabla\rho d\zeta - \frac{\nabla p_A}{\rho_0} + \boldsymbol{F_m} + \boldsymbol{R} \tag{3.2}$$

The seagrass drag term alpha

$$\alpha(x, y) = D_v N_v C_{Dv}/2 \tag{3.3}$$

parameterizes the vegetation density-related frictional scaling as the product of the individual's stem diameter (Dv), the vegetation density (Nv, given as number of stems per m2), and CDv, the bulk form drag coefficient, typically ranging between values of 0 and 3 (Nepf and Vivoni 2000; Tanino and Nepf 2008) and, in our case, chosen as 1. In the 3D configuration of SCHISM, also the vegetation term is regulated active in the vegetated part of the water via L

$$L(x, y, z) = \begin{cases} \mathcal{H}(z_v - z), 3D \\ 1, 2D \end{cases}$$
$$\mathcal{H}(x) = \begin{cases} 1, x \geq 0 \\ 0, x < 0 \end{cases} \tag{3.4}$$

with H being the Heaviside step function and zv the z-coordinate of the canopy height. The turbulence induced by vegetation is represented in the model as an additional source for turbulent kinetic energy. Further the wave damping is taking into account a sink term in in the wave action equation of the wave model:

$$\frac{DN}{Dt} = S_{total} = S_{in} + S_{nl4} + S_{ds} + S_{nl3} + S_{br} + S_{bf} + S_{d,veg} \tag{3.5}$$

with the source function Stot including the wind energy input, Sin, the nonlinear interactions in deep water (Snl4) and shallow, water (Snl3), and the energy dissipation in deep and shallow water due to white capping (Sds) and wave breaking (Sbr). Furthermore, it encompasses the dissipation due to bottom friction (Sbf) and vegetation (Sd,veg).

The model systems, which were developed as coupled model chains within Rest-Coast are used to explore the impact of restoration scenarios in different experiments (Figure. 3.14 Flowchart).

The experiments using SCHISM were constructed as academic 'what-if scenarios' evaluating the hypothetical dampening effect of seagrass at different extents and in different regions of the Wadden Sea. The scenarios explore the uppermost ceiling of seagrass expansion, as well as the distinguished effect of having seagrass in highly energetic zones where it would interact with stronger currents and wave energy, and analogously the effect of seagrass recovery taking place in the low energetic zone (Jacob et al., 2023, Figure 3.6, Table 3.4).

For those experiments the vegetation drag alpha was configured, setting the plant geometry/property-related drag coefficient CDv=1, the individual's stem diameter Dv, is generalized to Dv = 1.99mm for Z. marina dominated regions, Dv = 0.8mm for Z. noltei dominated regions, and in places of mixed occurrences (i.e., the majority of E1 and all areas in E3-E5) was set to the average value. The canopy height Hz, which influences the part of the water column that is influenced by seagrass interaction, was set to – Hz = 19cm for Z. marina dominated regions, – Hz = 9.8cm for Z. noltei dominated regions, – and in places of mixed occurrences (i.e., the majority of E1 and all areas in E3-E5) of both species Hz = 14.4 cm was set to the average value. Finally, Nv represents the areal coverage given as the number of shoots (cylinders) per m2, which was derived for E1 from the areal coverage estimates according to Table 3.3.

Table 3.2. Interval of seagrass areal coverage in data, and corresponding shoot density (Nv) provided to the model.

Areal coverage (%)	Shoots (1/m2)
5-19.9	450
20-39.9	1130
40-59.9	1530
60-79.9	3540
80-100	7360

Table 3.3. Different Scenarios

Experiment	Name	Seagrass cover
E1	Ref	Present-day (data) coverage
E2	Blank	No Seagrass (control)
E3	Vegmax	Entire WS between -1 and 4m
E4	VegLE	Shallowest 10% of Vegmax
E5	VegHE	Deepest 10% of Vegmax

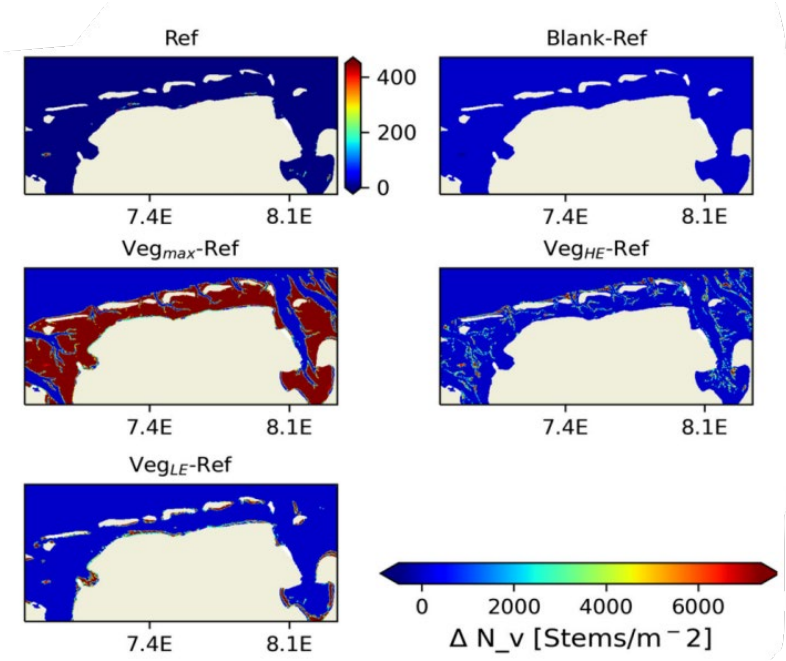

Figure 3.13. Seagrass coverage and shoot density in the different seagrass scenarios within the German Bight setup the EFWS: op left: shoot density in reference run (corresponding to the sparse seagrass coverage derived from observations), followed by differences of E2-E5 (Table 3.3) minus reference run.

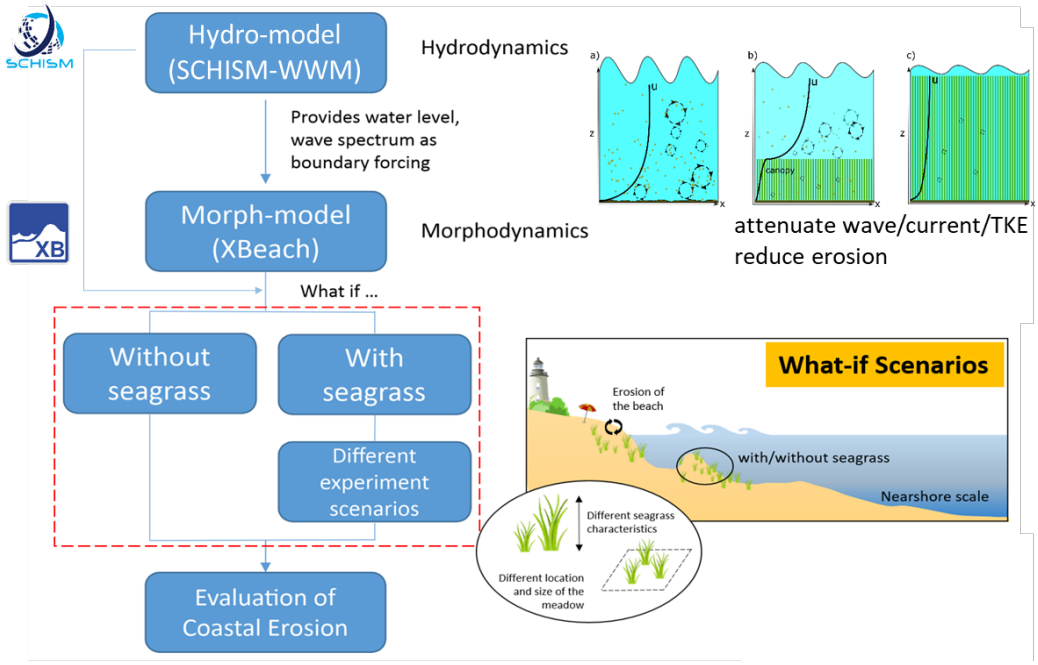

Figure 3.14. Flowchart showing the process applied when evaluating the impact seagrass has on coastal erosion.

Moreover, the numerical experiments are conducted systematically in order to identify the effectiveness of various seagrass planting techniques in reducing coastal erosion and increasing coastal resilience to storm events.

The Xbeach code, forced by the coupled SCHISM-WWM model, applied the model domain of high-resolution bathymetry measured by NLWKN. The seagrass meadow size, shape and location of the seagrass domain is

further controlled by two introduced parameters: hs and hr (Figure. 3.15). The first one initializes the depth where the seagrass meadow starts and the second measures the range of the depth covered by the seagrass meadow. Moreover, seagrass is characterized by stem height ah, diameter bv, and density Nv.

As illustrated in Figure. 3.15, the depth start planning seagrass hs and the range in depth hr control the location and size of the seagrass meadow. Area of all experiments are normalized with respect to the experiment that hs-hr combination reaches the largest seagrass meadow, which is assigned to 1. The normalized area A for all experiments with different combinations of hs and hr in the prototype XBeach modeling domain are plotted in Figure. 3.16(a). Figure. 3.16(b) and (c) show two examples of seagrass layouts for different combination of hs and hr. In general, a wider range of depths requires a larger area of seagrass. However, since the slope of the shoreface varies in the alongshore direction, the area and distribution of seagrass change when the plantings start at different depths and have different sizes. The height of the seagrass and density of seagrass stem per square are determined by ah and bv. Varying the two parameters as well as hs and hr describe different characteristics of the seagrass meadow and seagrass at different phase of lifetime. Details of all experiments are listed in Table 3.4.

Table 3.4. Overview of all what-if model simulations.

What-if	Run	Abbr.	No.Exp.	Description
no seagrass	Reference scenario	Ref.	1	----
with seagrass	Default scenario	Default	4	Seagrass characteristics: ah=50 cm; bv=1 cm; Nv=1000/m2; Rectangular seagrass meadow places at different across-shore locations from the coast;
with seagrass	Scenario I	S-I	42	Seagrass characteristics are the same as Default runs, but with the meadow size and location depends on hr and hs.
with seagrass	Scenario II	S-IIa	33	bv=1 cm; Nv=1000/m2 , but ah= varies from 0 to 50 cm; Three hr-hs combinations are selected such that meadow size and location represents different typical meadow distributions; determined after S-I.
		S-IIb	30	as S-IIa, but for Nv varies from 0 to 1000;

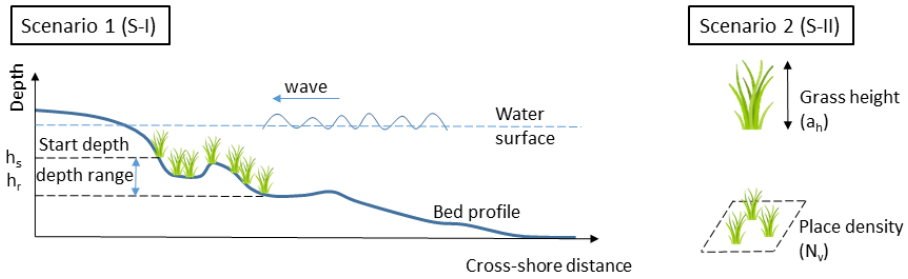

Figure 3.15. Experimental design of the scenario for different combinations of seagrass parameterizations.

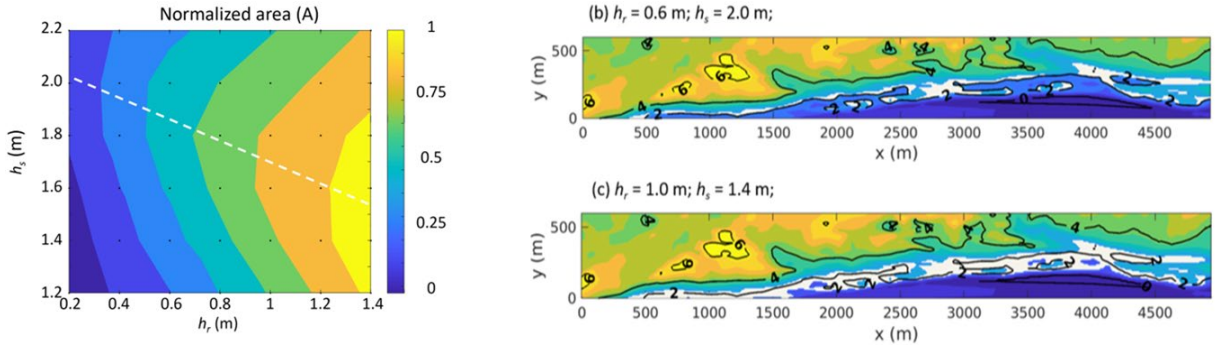

Figure 3.16. (a) Seagrass meadow in normalized area A for experiments as a function of hr and hs. The black dots indicate experiments with different hr and hs combinations. The seagrass area reaches an extreme when the combination of the two parameters intersects the white dashed line; (b) and (c) are two examples of seagrass layouts (white blank zones) for different 'hs' and 'hr' combinations. The x and y are along-shore and across-shore directions and the contour values indicate the water depth.

For the assessments of the ESS of biodiversity, we follow the joint habitat mapping approach agreed upon by the Wadden Sea partners.

3.4. Target operational period for testing the EWS nested into CMEMS products

3.4.1. Baseline risk reduction under present day conditions and seasonal variability

3.4.1.1. Ems-Dollart model (Deltares)

Storm hazards in the Ems-Dollart model are assessed by simulating storms Herwart (October 2017) and Xaver (December 2013). The wave data for these storm events (wave heights, periods, and directions) are obtained from observations at the island of Schiermonikoog, the Netherlands. Meteorological forcing is provided by the HIRLAM Weather model. The Copernicus data EMODnet was used to obtain the appropriate offshore bathymetry. In order to assess the effects associated with the long-term morphological changes resulting from the different sediment management strategies at this pilot site, EWS can only be considered on long time scales considering the effects of climate change and sea-level. Results of this model are therefore presented in D2.2.

3.4.1.2. German bight model (Hereon)

The evaluation of the risk reduction potential of the applied Nature Based Solutions is conducted under present day conditions. To assess the vegetation ESS, the year 2017 was chosen as the reference year to establish the baseline of expected merit from the restoration scenarios. Due to significant intra-annual variability in the study area, simulations and analysis are conducted separately for the summer and winter seasons.

The study compares seagrass during the summer and winter seasons using data from the 2017 simulation to examine seasonal differences. To represent seasonal variability in computationally heavy morphological simulations with Delft3D, which evaluate the impact of salt marsh development on erosion, the Hereon SCHISM simulations were extended to a two-year period. The simulations were then subjected to harmonic analysis to derive the seasonal variation of tidal constituents, which are implicitly modulated by meteorological variability. Based on the analysis data, we conducted time-compressed (scaling) simulations using SCHISM and Delft3D to perform coherent hydro and morphodynamic runs. We contrasted the summer and winter periods to obtain an indication of the range within one year.

3.4.2. Risk reduction under extreme weather conditions

The second part of the baseline analysis takes an event-based approach. Simulations were conducted for realistic historic storm events, rather than using a synthetic event construction. This approach allows for a coherent forcing across the multi-parameter hydrodynamic and meteorological forcing.

The first storm event analysed is Herwart, which is an example of a severe storm surge that occurred on 29 October 2017. Peak velocities of 120 to 140 km/h were recorded along the North Sea coast. This resulted in the highest water level in the North Frisian Wadden Sea, specifically on the west coast of Büsum, where it reached 2.06 m above mean high water. In Bremerhaven, on the coast of Lower Saxony, the water level reached its highest point at 2.60 m above mean high water. In Hamburg St.-Pauli, the water level rose to 3.34 m above mean sea level on the morning of 2017 (Pegelonline, BSH).

On December 5 and 6, 2013, the storm 'Xaver' caused peak gusts of 150 to 160 km/h (BSH) on the German North Sea coasts and in Denmark, classifying as a hurricane. The long persistence of north-westerly winds of force 9 - 10 Bft over the German Bight allowed a series of three consecutive storm surges to build up, one of which reached the 'very severe storm surge' category (Sturmflut 2013_bm1101 (bsh.de)). The water level in Hamburg St. Pauli reached a peak of 3.98 m above the mean high tide or 6.09 m above sea level, similar to the storm surge in February 1962.

These events can be classified with return periods of 2 years (Herwart) and 125 years (Xaver), respectively, when considering the combined variation of tidal anomaly and wave height.

A set of ESS restoration experiments were conducted for this period in addition to the vegetation observation based reference scenario (REF). Those further restoration scenarios were constructed by variation of the stem density and seagrass location (Figure. 3.17) and an increase of the stem density to the maximum observed value of about 7600 shoots per m^2. In addition to a control run without seagrass (Blank), other simulations involved restoration in the eintere for seagrass potentially habitable depth range (Vegmax), as well as on the shallowest (VegLE) and deepest (VegHE) 10% of the Vegmax area, to see the effect of restoring the low energy area vs restoring the high energy area.

Exploring seagrass as a nature-based storm buffer to mitigate beach erosion, the erosion assessment with Xbeach focuses on a short period during the Herwart storm event. Different series of what-if scenarios were conducted for testing the EWS. In total, 110 experiments were performed, including a reference case without seagrass, 4 default runs with square seagrass domain being placed at different cross-shore locations, 42 simulations with different depth range and start depth combinations, 33 simulations for different planting densities, and 30 simulations for different stem heights (Table 3.5).

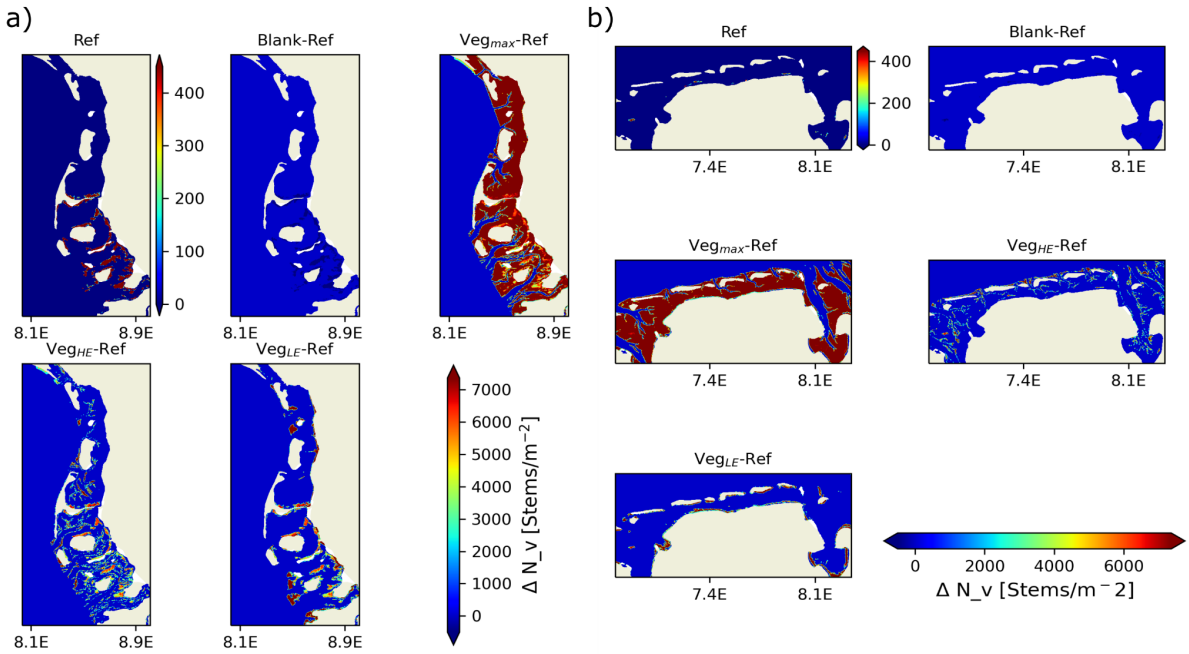

Figure 3.17. Restoration design via Seagrass coverage and shoot density in the different seagrass scenarios (a) in the NFWS and (b) in the EFWS. In (a)/(b) top left: Shoot density in reference run, followed by differences minus reference run.

3.5. Hazard reduction from ESS as a function of restoration scale

The key aspect within the approach followed with the morphodynamic model of the Ems estuary is not so much to focus on the direct impact of vegetation on hazard reduction, but on its impact via morphological changes (with the main reduction realized by these morphological changes). At this point, the Deltares partners are still in the process of improving the morphological model. The model does not yet include vegetation and is also not yet applied for hazard reduction.

3.5.1. Ley bay model (NLWKN)

Similar to the approach of Deltares, the main focus of NLWKN is to understand the contribution of saltmarsh in erosion risk reduction, by evaluating the saltmarsh effect on morphological changes. The main objective is to investigate the potential use of saltmarsh as a NbS for coastal protection. The present work focused on the evaluation of hydrodynamics, sediment transport and bed evolution during extreme events. The contribution of NbS to these processes was analyzed by comparing the hydromorphodynamic results without NbS (WT - NBS) and with NbS (NBS) applications.

Scenarios

Occurrence of three events was selected for the analysis representing two scenarios, Base-case (1) and extreme events (2). The base-case extends from 26-Jul-2017 23:00 to 31-Jul-2017 13:00 covering a 110 h of summer period, in which the occurrence of wave heights represents fair weather conditions (e.g., maximum Hs at 20 m depth < 2 m). The first extreme event (Xaver) occurred in December 2013 (max. Hs ~ 7.5 m at 20 m depth), while the second (Herwart) was in October 2017 (max. Hs ~ 6.0 m at 20 m depth). Storm periods of each event were selected following the statistical approach of Dissanayake et al. (2019). They combined the variation of tidal anomaly (TA=total water level-astronomical tide) and wave height (Hs) and classified that TA+Hs > 3.4 m as a storm event in the study area. Accordingly, Xaver occurred from 04-December-2013

16:30 to 09-December-2013 09:00, which covers a 112.5 h period (Figure 3.20a). Herwart spanned from 28-October-2017 09:00 to 30-October-2017 08:00 for a period of 47 h (Figure 3.20b).

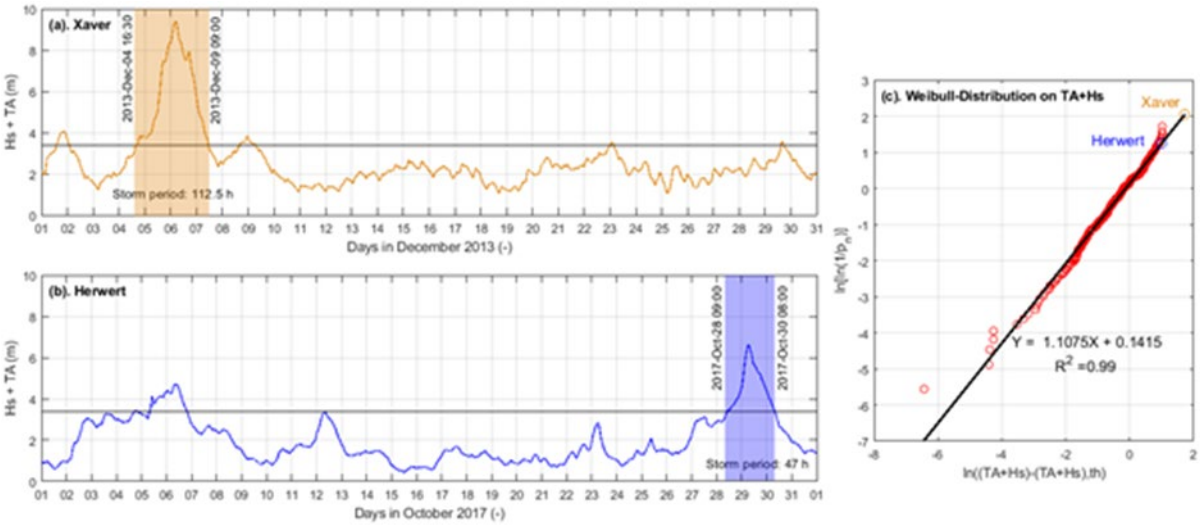

Figure 3.18. Variation of wave height (Hs) and tidal anomaly (TA) with the selected extreme events, Xaver in December 2013 (a) and Herwart in October 2017 (b). Colour-window indicates the identified storm period following the storm classification of Dissanayake et al. (2019) (black-line). Severity of storm events is shown with the agreement of Hs+TA with the theoretical extreme value distribution: Weibull (c).

Severity of each storm event was analyzed by comparing the sample data with an extreme value distribution, Weibull (Figure 3.9c and Eq. 3.1: Probability density function) (Coles, 2009). The comparison indicates a good agreement between the sample data and the theoretical distribution (R2=0.99). Accordingly, Xaver is a very extreme event (return period 125 years) than Herwart (2 years).

$$f(x;\lambda_0,k) = \{\frac{k}{\lambda_0}(\frac{x}{\lambda_0})^{k-1} e^{-(\frac{x}{\lambda_0})^k}, x \geq 0\ 0, x < 0 \quad (3.6)$$

where, x = Hs+TA (m); , k, shape parameter (-); , λ_0 scale parameter (-)

Using the aforementioned two scenarios, 6 simulations were carried out applying WT-NBS (3) and NBS (3) (Table 3.5). Each model was forced with tide, wave and wind and simulated with the modelling tool Delft3D (Lesser et al., 2004) to investigate hydrodynamics, sediment transport and morphological changes, and to analyze the effect of NBS.

Table 3.5. Model simulations with Tide+Wave+Wind and morphology for the selected two extreme events, Xaver and Herwart. Derived return levels of the events by comparing Hs+TA with the extreme value distribution Weibull.

Scenario	Without NBS (WT-NBS)	With NBS (NBS)	Return period comparing Hs+TA with the Weibull-distribution (years)
Base-Case	Fair-weather	Fair-weather	-
Extreme events	Xaver	Xaver	125
	Herwart	Herwart	2

Bed sediment composition

In any sediment transport and morphological simulation, it is of utmost importance to implement the bed sediment composition as accurately as possible. Therefore, we used spatial varying 6 sediment fractions based on the NLWKN measured data covering littoral and eulittoral areas (e.g., grab sampling, sediment cores) (Mascioli et al., 2021). These data represent the bed sediment composition in 2015 (Figure 3.19). For the modeling purpose, they were implemented in two layers, in which the top layer has a maximum thickness of 1 m and the second layer represents the rest of the sediment thickness down to the Holocene layer. Initially, a quasi-equilibrium sediment distribution of each fraction was established by simulating the model for the sediment distribution without bed level change (Dissanayake and Wurpts, 2013). These sediment maps were then used as the initial bed sediment composition of the model to simulate the scenarios.

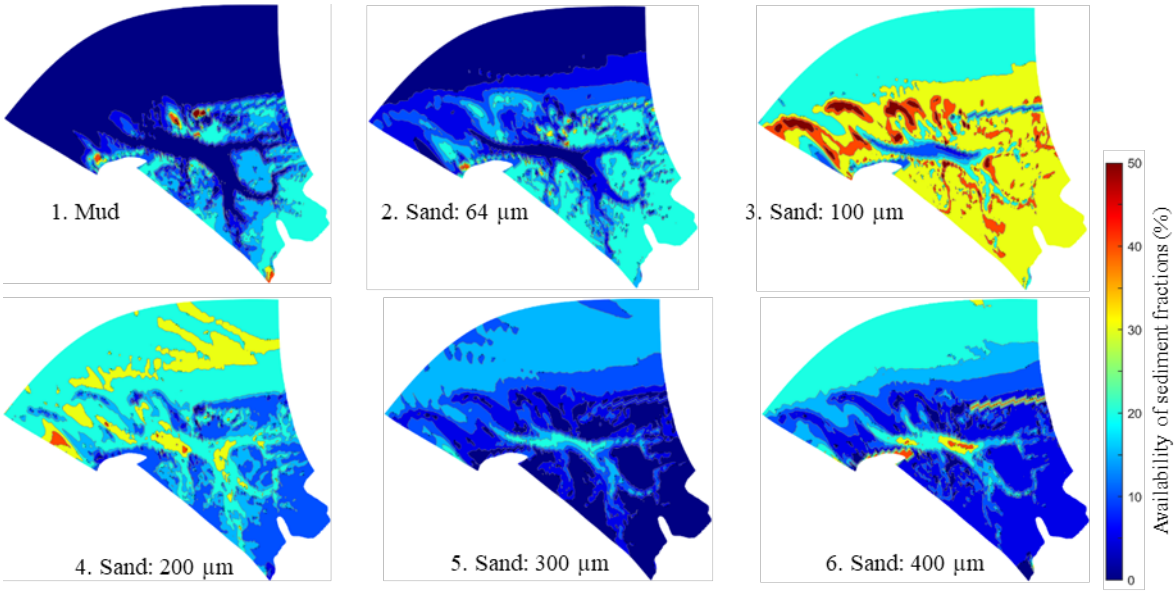

Figure 3.19. Bed sediment composition of the OEMS-domain. Color indicates the spatial availability of the adopted sediment fraction at the top layer: Mud (1), Sand 64 µm (2), Sand 100 µm (3), Sand 200 µm (4), Sand 300 µm (5) and Sand 400 µm (6).

Implementation of Saltmarsh

Saltmarshes are vegetated coastal wetlands that are flooded and drained as a result of fluctuations of sea level. In tidal systems, saltmarshes are populated at the upper part of intertidal zone: sea-land interface. The entire saltmarsh area of Wadden Sea accounts for about 400 km2 (3%) (Esselink et al., 2017), while it is about 12 km2 (38%) in Ley Bay.

In this study, the models were simulated in the 2DH-mode (depth-averaged). Therefore, the presence of Saltmarsh was implemented using a Trachytope approach (Delft3D, 2023), which has been developed following Baptist (2005), to estimate the vegetation exerted drag force to flow considering submerged and non-submerged plants. According to these formulations, the presence of vegetation leads to higher bed roughness and thus higher bed shear resulting in higher sediment transport, which is unrealistic, because the presence of vegetation tends to decrease sediment transport. Therefore, he has further introduced a reduction factor f considering the overall bed roughness: background roughness (i.e., situation without saltmarsh) + roughness generated due to saltmarsh, flow resistance (Chap. 4 in Baptist, 2005). However, in Delft3D, this issue is resolved by adding an additional term in the momentum equation: - /2 〖^2〗 (λ, flow

resistance due to vegetation and u: velocity) (Delft3D, 2023). Therefore, the two roughness components are separately computed in the area of the saltmarsh: background roughness (Cb in Eq. 7 for the case of submerged vegetation: h>hv) and saltmarsh roughness (second term in right-hand of Eq. 7). The first is used to estimate bed shear stress, which determines the sediment mobility, while the second is used to estimate the vegetation exerted drag force on flow.

$$C = C_b + \frac{\sqrt{g}}{\kappa} ln\left(\frac{h}{h_v}\right)\sqrt{1 + \frac{C_D n h_v C_b^2}{2g}} \quad (3.7)$$

$$\lambda = C_D n \frac{h_v}{h}\frac{C_b^2}{C^2} \quad (3.8)$$

where, C, net bed roughness $(m^{1/2}/s)$; κ is Von Kámán constant (-); n = mD, Vegetation density (m); h, water depth (m); g, gravitational acceleration (m^2/s)

At the transition region h=hv, the second term of Eq. 3.7 goes to zero. For the non-submerged h<hv, the flow resistance and bed roughness are explicitly separated.

$$C = C_b \quad (3.9)$$

$$\lambda = C_D n \quad (3.10)$$

Few parameters need to be provided into the model to set up the saltmarsh configuration: number of cross sections stems/branches per m^2 (m), diameter of branches/stems (D), plant height (h_v), drag coefficient (C_D) and background roughness (C_b). Multiple bifurcations can be applied to implement a more realistic plant structure considering different depth layers, whereas only in the 3D applications. According to our study area (Figure 3.20), these values were applied as 100 (m), 0.008 m (D), 0.5 m (hv), 1.65 (C_D) and 45 $m^{1/2}/s$ (C_b). The saltmarsh area (green-polygon in Figure 3.12c) is located above the high-water line (~ 1.5 m + MSL) along the land boundary. Therefore, it can be expected that this area is hardly submerged during fair weather conditions.

It should be noted that the present configuration of saltmarsh does not allow vertical variation of plants and the adjustment of plants based on flow velocity (i.e., 2DH approach). Furthermore, in a long-term morphological simulation, the growth of the plant configuration needs to be updated off-the-shelf. These

demand improvements of the saltmarsh implementation in the model, which would be undertaken in the cause of the project upon the time allowance.

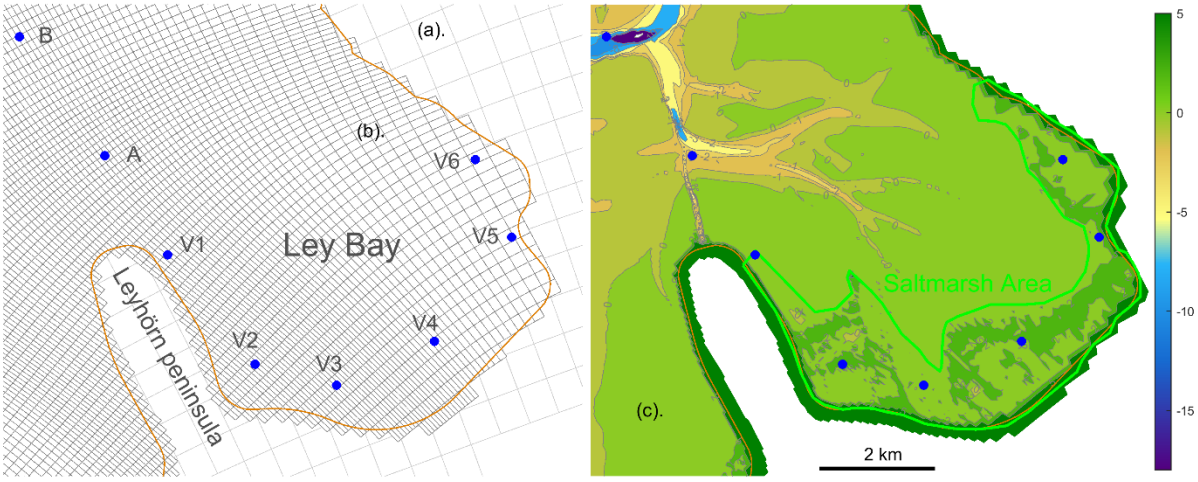

Figure 3.20. EMS-grid (a), Grid in the Ley Bay area from the OEMS-grid (b) (for clarity every other grid is shown) and bathymetry in the Ley Bay area (c). Salt marsh coverage is indicated with the green-polygon. Analysis points A (Depth: -1.4 m), B (-8.4 m) (see Figure 3.13), and V1 (1.3 m), V2 (2.0 m), V3 (1.9 m), V4 (1.0 m), V5 (1.9 m) and V6 (2.0 m). Color bar indicates water depths with respect to MSL.

Calibration and validation

The model calibration was carried out for the period of October 2015 applying different bed roughness schemes (Table 3.6). The accuracy of the model predicted water levels was compared with the measured data at the station A (Figure 3.19a). In general, it is found that there is no significant variation among the different schemes (R2 in Figure 3.20a). However, the most optimal prediction resulted with M2-roughness-scheme, in which the bed roughness is similar to an existing Ley Bay model (Dissanayake and Wurpts, 2013). Note that this existing model restricts to the Wadden Sea area only, and does not cover North Sea, and thus the new model setup was required and developed for the present project. The validity of the M2 roughness was then investigated simulating two independent periods: November 2015 (Figure 3.20b) and December 2015. Statistical comparison indicates a reasonable agreement between measured and predicted water levels (R2 = 0.95 and rmse = 0.22 m).

Performance of the wave propagation in the Ley Bay area was analyzed using different bed frictions, breaker parameters and wind fields for the wave model. The optimal wave prediction at B (Figure 3.19a) is shown in Figure 3.20d applying a bed friction of 0.07, a breaker parameter of 0.73 and uniform wind fields from the station Norderney (DWD, 2023). Generally, there is a reasonable agreement of wave heights between the measurements and the model prediction (R2 = 0.82 and rmse = 0.05 m). The observed variations are expected mainly due to the applied wind fields (i.e., spatial constant), in which they are not able to capture local scale small variations.

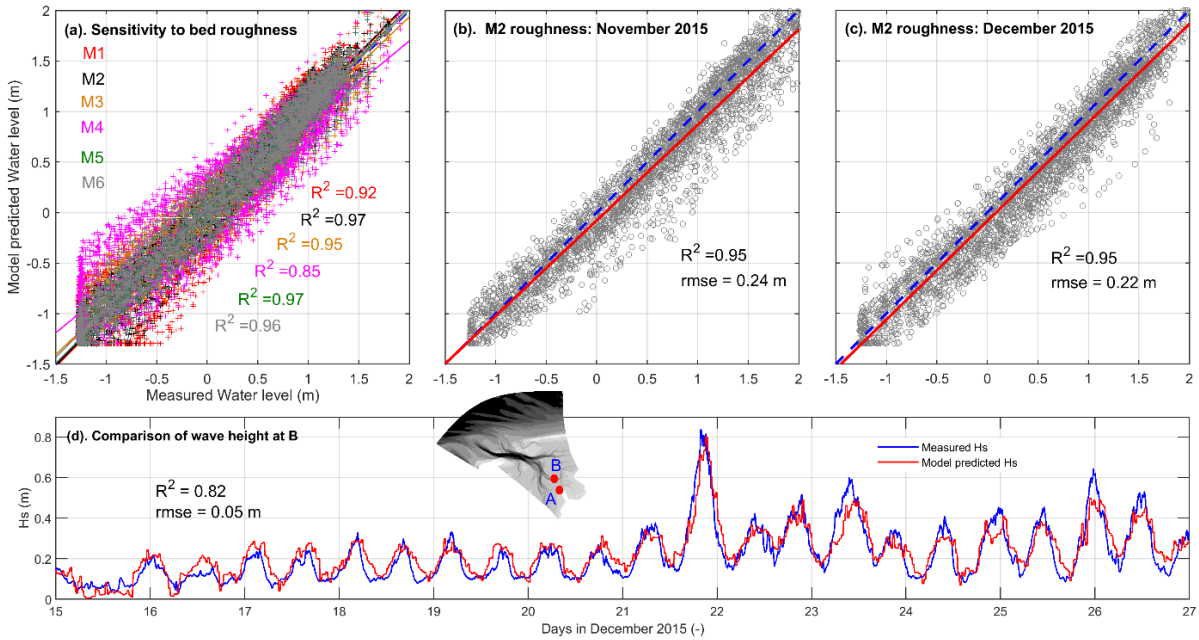

Figure 3.21. Calibration and validation of water level prediction at A (see on the OEMS-bathymetry: insert view). Comparison of predicted water levels for October 2015 with different bed roughness schemes (see Table 2) (a), validation using the optimum roughness (M2) for two independent periods; November 2015 (b) and December 2015 (c). Dash-line indicates the perfect agreement, while solid-line shows the agreement between measured and predicted water levels. Comparison of wave height prediction at B (d). For clarity, only the final result is shown through different wind fields and roughness values in the wave model were investigated.

Selected bed roughness schemes for the model calibration are summarized in Table 3.6.

Table 3.6. Sensitivity simulations applying different bed roughness schemes to calibrate the OEMS model. z0 is bed roughness length, where z0 = ks/30, ks: Nikuradse roughness length.

Model	**Description of bed roughness scheme**
M1	White-Colbrook from the EMS model (Oberrecht, 2020): spatial varying z0
M2	Different Mannings as in the existing Ley Bay model (Dissanayake and Wurpts, 2013): depth-class specific values
M3	Chèzy = 50 m1/2/s: spatial constant
M4	Chèzy = 40 m1/2/s: spatial constant
M5	Chèzy = 60 m1/2/s: spatial constant
M6	Different z0 in White-Colbrook: open coast z0=0.0002, tidal basin z0 = 0.006 (WMO, 2008)

Effects of NBS on water level, wave height, velocity and bed shear stress were analyzed at the stations from V1 to V5 (Figure 3.20). Spatial effects of NBS in the Ley Bay were then investigated with respect to bed shear stress, sediment transport and morphological changes during the three events.

Water level

For clarity, water level comparison only for three stations V2, V4 and V5 is shown in Figure 3.22. Additionally, the offshore water level variation (at 20 m depth of the boundary of EMS, see Figure 3.9a) of the respective event is added to the right y-axis (gray-line) for a better comparison with the local changes.

Three events indicate different trends of water level in the saltmarsh area. During the fair weather condition, the maximum water level rise is lower than 1.5 m, while the saltmarsh area is located at around the level of 1.5 m + MSL. Therefore, the saltmarsh area remained dry during this period. In Xaver, the offshore maximum water level is about 2.7 m, which resulted in a similar water level rise at V4. Both V2 and V5 have low water levels than V4, but they are similar (maximum ~1.7 m). These indicate that the furthest location along Ley Bay experienced high water levels due to reflection of tidal wave from the surrounding dykes. NBS has delayed both rising and draining of water, and thus resulting low water levels before the storm peak and high water levels (red-line) after the storm peak than WT-NBS (blue-line). Herwart had lower water levels (max. 1.6 m) than Xaver. Therefore, all locations submerged only during the storm peak. However, such water level rise in NBS is completely damped at the stations in the middle of the saltmarsh (e.g., V2, V4), and showed increase of water levels only at V5, which is located at the seaward edge of saltmarsh. These results suggest that there is a considerable water level variation within the saltmarsh area, and NBS delays rising and draining of water levels.

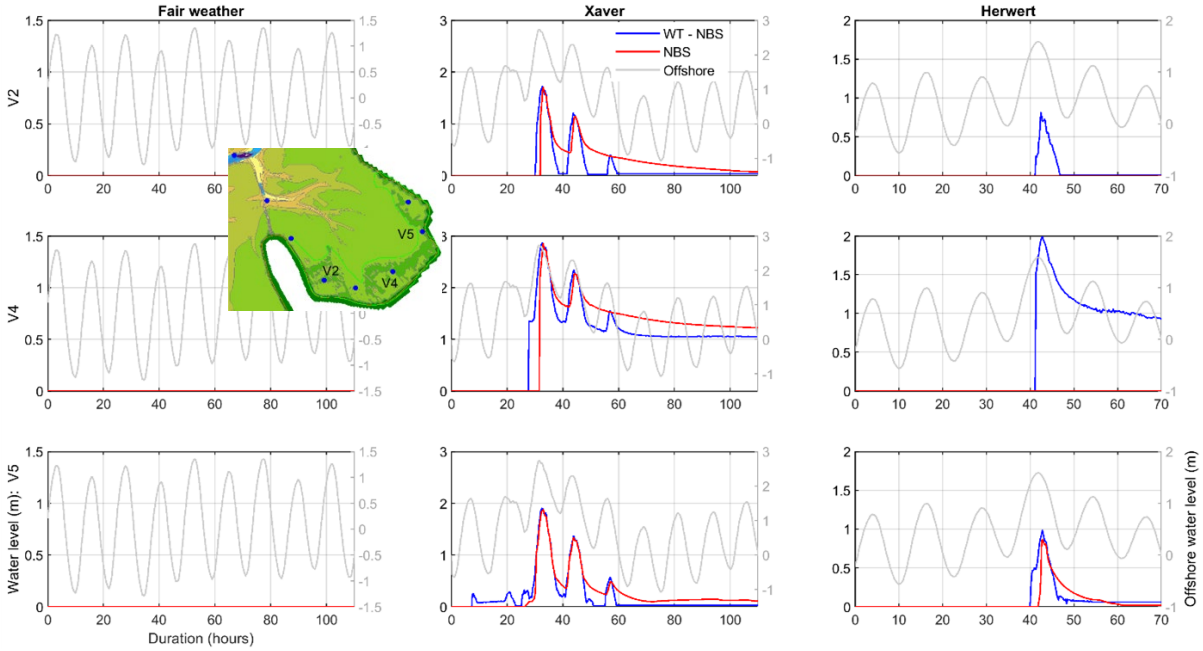

Figure 3.22. Comparison of water levels at the selected locations V2, V4 and V5 (see on Ley Bay bathymetry: insert view), without NBS (WT – NBS: blue-line) and with NBS (red-line) for fair weather, Xaver and Herwart events. Respective offshore water levels (20 m depth) are shown with the gray-line. For clarity, y-axises in a row of events have different scales.

Bed shear stress

Spatial variability of the maximum bed shear stress at each grid-cell during the events was then analyzed for the two scenarios (Figure 3.23). In the fair weather, high bed shear stresses are generally found along the channels. During flood and ebb, the maximum velocities occur at mid-tide. Therefore, high bed shear is concentrated at channels, which are submerged at mid-tide. There is no difference between WT – NBS and NBS applications due to the occurrence of low water levels (see Figure 3.22). High water levels in Xaver (maximum 2.7 m) together with high waves (0.7 m) in Ley Bay resulted in high bed shear stresses in the channels as well as at the shallow areas, particularly in the saltmarsh area. In the NBS application, the bed

shear stresses in the saltmarsh area are significantly decreased. For example, the maximum value is about 0.1 N/m2, while it is over 1 N/m2 in WT – NBS. Furthermore, it is shown a remarkable decrease at seaward side along the saltmarsh edge. In Herwart, the bed shear stresses are lower than Xaver due to low water levels and wave heights. It should be noted that some locations along the channels experienced lower bed shear than even the fair weather condition. This could be due to the fact that the velocities in the flooding and ebbing processes within the channels are counteracted during this weak storm event. However, as in Xaver, a significant decrease of bed shear is found within the saltmarsh area as well as along the edge. These results clearly indicate that NBS significantly decreases bed shear stresses not only within the saltmarsh area but also at the seaward side close to the saltmarsh edge, and that directly affects on the potential bed sediment transport.

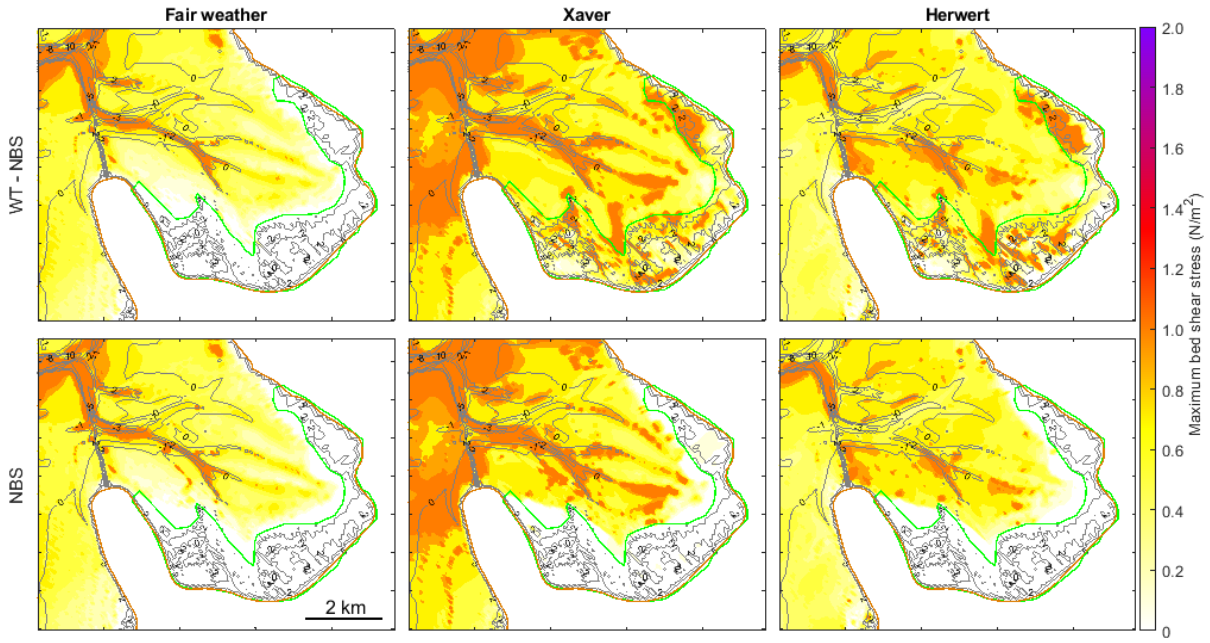

Figure 3.23. Comparison of the maximum bed shear stress (color-bar) in the Ley Bay area during fair weather, Xaver and Herwart events for the scenarios applying no salt marsh (WT-NBS) and with salt marsh (NBS). Salt marsh area is indicated by the green-polygon. Initial bed topography is shown by depth contours.

Sediment transport and bed evolution

Similar to the maximum bed shear stress, sediment transport was estimated during the events for the two scenarios. Suspended and total sediment transports (both bed and suspended together) were separately analyzed in order to investigate the effect of NBS on each component separately.

In the fair weather condition, both suspended and total transports are generally strong in the channels, and they indicate a sediment transport pattern away from Ley Bay. In the saltmarsh area, no sediment transport occurred due to low water levels (see Figure 3.22), and thus no difference is found between WT – NBS and NBS. Xaver resulted in the strongest transport within the entire area, in which the orientation of the total transport is still similar to that of the fair weather condition. In the NBS application, there is a considerable decrease of transport compared with that of WT – NBS. The transport within the saltmarsh area in NBS is predominantly driven by the suspended transport (see Figure 3.24: no bed shear stress). Furthermore, it is shown that lower transport in Ley Bay compared with WT – NBS. This indicates a reduction of sediment contribution from the saltmarsh area to Ley Bay in NBS. At the east part of the saltmarsh area, NBS caused strong suspended transport, which can be occurred due to the flow diversion from the rest of saltmarsh. The

entire Ley Bay experienced a similar sediment transport pattern in Herwart albeit lower than Xaver. Particularly, there is very weak transport within the saltmarsh area in NBS due to low water levels and wave heights. Therefore, NBS decreases sediment transport. However, suspended transport can be increased depending on the severity of a storm event.

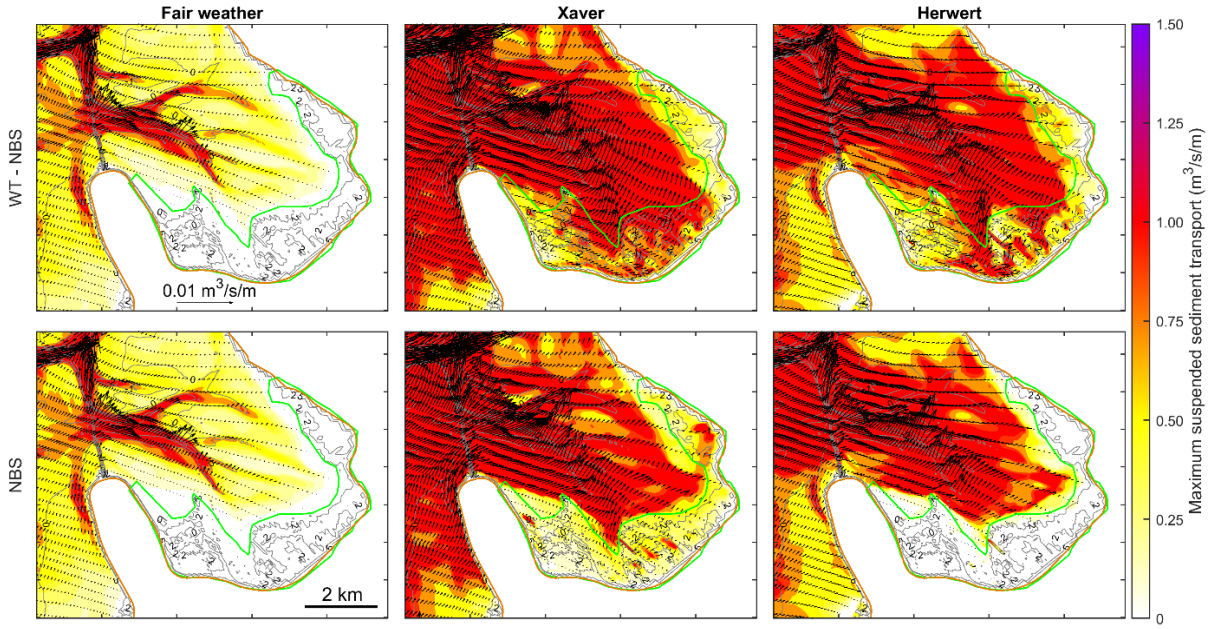

Figure 3.24. Comparison of the maximum suspended sediment transport (color-bar) and the maximum total transport (vectors: for clarity every 8th vector is shown) in the Ley Bay area during fair weather, Xaver and Herwart events for the scenarios applying no salt marsh (WT-NBS) and with salt marsh (NBS). Salt marsh area is indicated by the green-polygon. Initial bed topography is shown by depth contours.

Bed evolution during the events was compared by analyzing erosion and sedimentation patterns for the two scenarios (Figure 3.25). In all cases, the maximum erosion and sedimentation occurred at channels, which vary between -0.2 m to 0.3 m. In fair weather, the bed evolution above MSL (0 m depth contour) is very small and the saltmarsh area is not affected. The patterns indicate, there is no difference between WT – NBS and NBS. Xaver caused strong erosion at the channel banks and sedimentation in the channels. Furthermore, strong erosion and sedimentation occurred within the saltmarsh area, which depend on the location, and they considerably decreased in NBS. In Herwart, similar patterns are found for erosion and sedimentation, whereas they are not prominent as in Xaver. Particularly, saltmarsh area in NBS has experienced very weak bed evolution.

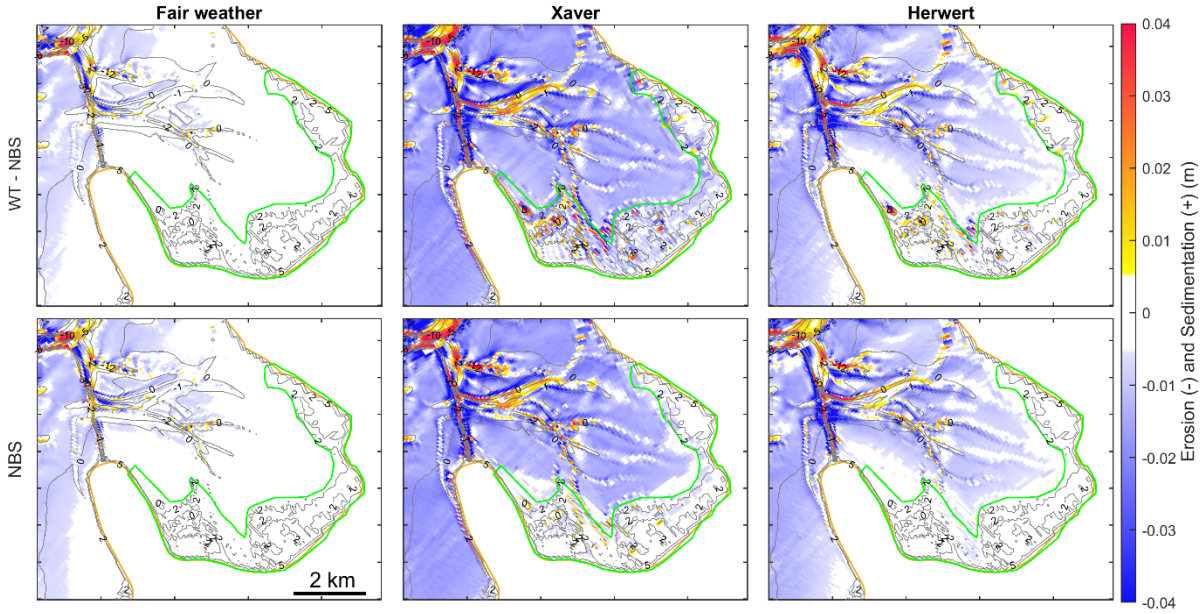

Figure 3.25. Comparison of the bed evolution pattern (color-bar) in the Ley Bay area during fair weather, Xaver and Herwart events for the scenarios applying no salt marsh (WT-NBS) and with salt marsh (NBS). Salt marsh area is indicated by the green-polygon. Initial bed topography is shown by depth contours.

Volume of bed evolution within the saltmarsh area was estimated for erosion and sedimentation during the events (Figure 3.26a). Positive values in relative reduction imply a higher volume change in WT – NBS than NBS, and the higher the value the lower the effect of NBS (Figure 3.23). Negative values indicate a higher volume change in NBS than WT – NBS, and the lower the value the higher the effect of NBS. Zeros occur, when both are similar. As found earlier, the saltmarsh area experienced no bed evolution in the fair weather condition irrespective to the NBS applications (a). In Xaver, maximum erosion (-75×103 m3) and sedimentation (15×103 m3) occurred. Both decreased more than 60% in NBS (b). Similar trend is found in Herwart. However, the sedimentation volume in NBS is very small (0.4×103 m3). Therefore, the relative reduction increased up to 96%. These indicate that strong erosion in the saltmarsh area resulted in strong

sedimentation and vice versa. Furthermore, the eroded sediments from the saltmarsh area escape into Ley Bay rather sedimentation therein.

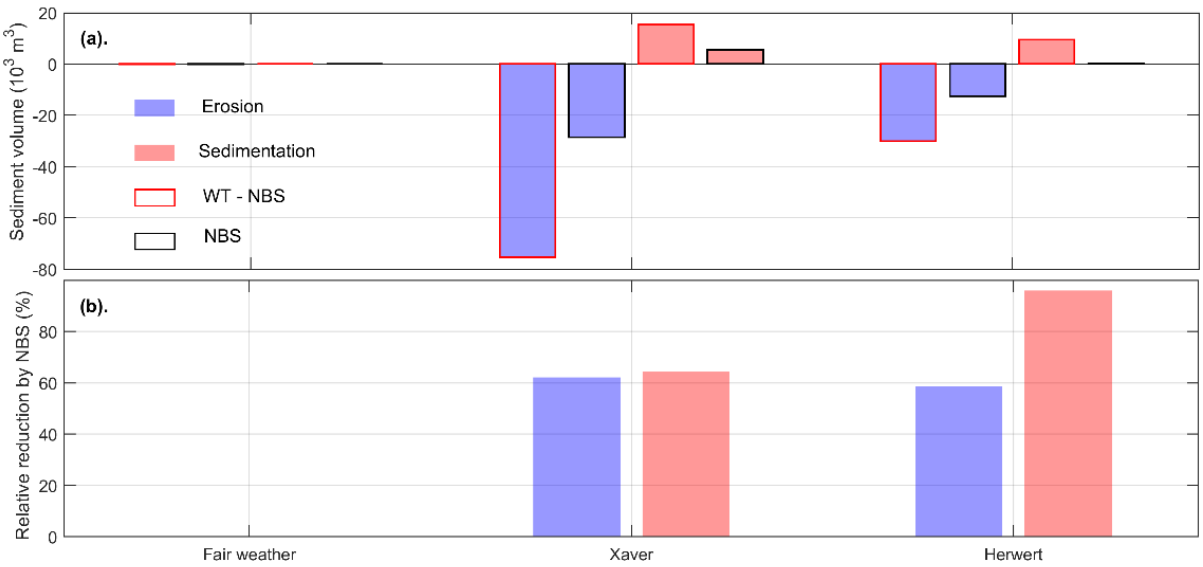

Figure 3.26. Erosion and sedimentation volumes within the salt marsh area without NBS (WT - NBS) and with NBS (NBS) applications (a) and the relative reduction of volume in erosion and sedimentation with respect to the WT - NBS application: (([WT - NBS] – [NBS])/[WT- NBS]×100%) (b).

Sensitivity of the saltmarsh configuration to the bed evolution was finally investigated applying different plant density, plant diameter and height (see section 3.3.1). The most extreme event Xaver was simulated with three different values for each parameter, and the relative reduction of volume with respect to WT-NBS was estimated and compared.

Both plant density (i.e., number of plants per square meter) and plant diameter indicate a relative reduction of volume about 60% in erosion and sedimentation though the value of each parameter is increased by a factor of 2 and 4 (Figure 3.27a and b). Therefore, these two parameters have less sensitivity to the bed evolution within the saltmarsh area. The plant height shows increased effects of NBS as the value increases (Figure 3.27c). The erosion volume within the saltmarsh area in NBS increases up to -16×103m3, -28×103m3 and -86×103m3 while sedimentation decreases down to 7.8×103m3, 5.5×103m3 and 2.3×103m3 as the plant height increases from 0.25 m, 0.50 m to 1.00 m respectively. The erosion and sedimentation of WT - NBS are -75×103m3 and 15×103m3. Therefore, the relative reduction of volume decreases in erosion and increases in sedimentation. As found earlier, the sedimentation decreases though the erosion increases with increasing plant height, which indicates that the eroded sediment escaped from the saltmarsh area. Accordingly, only plant height is sensitive to the bed evolution rather than plant density and diameter.

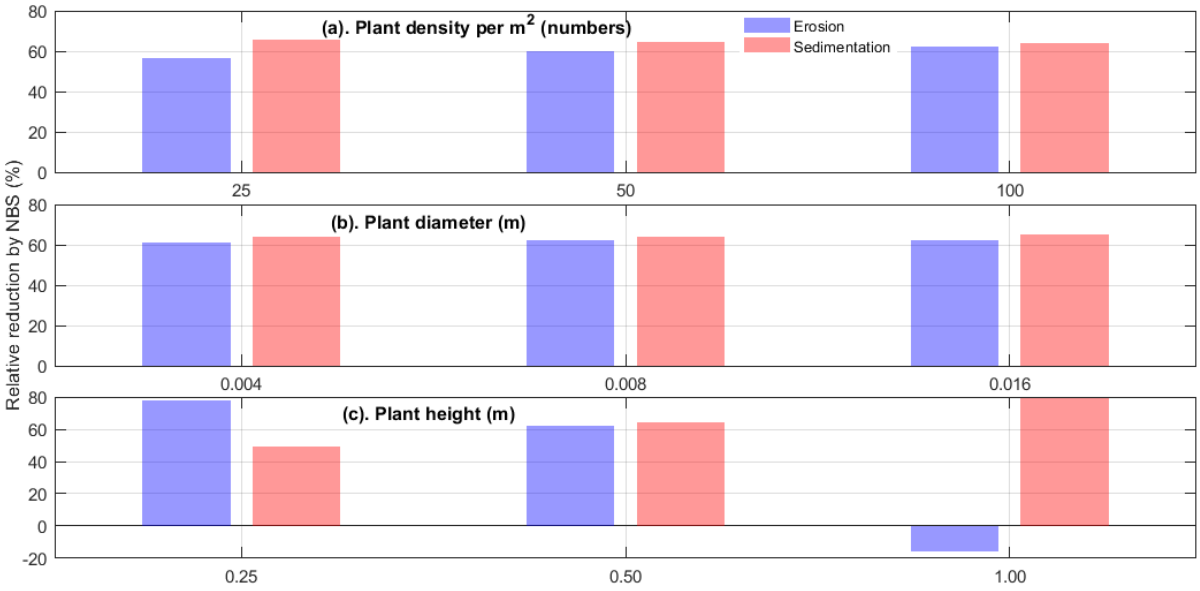

Figure 3.27. Relative reduction of volume change in erosion and sedimentation with respect to the WT - NBS application, (([WT - NBS] – [NBS])/[WT - NBS]×100%), for different salt marsh configurations: Plant density per square-meter (a), Plant diameter (b) and Plant height (c).

Summary

<u>High resolution domain needs to investigate saltmarsh effects</u>

A high-resolution model setup was developed within this project to investigate the effects of saltmarsh on hydrodynamics and bed evolution. Small channel and shoal patterns in Ley Bay can be accurately represented with a high-resolution model grid. However, applying very fine grids (e.g., O (10 m)) increases the number of grid cells over the OEMS area (920 km2) exploding the computational time. Therefore, we applied a maximum resolution of 30 m x 80 m as this model setup will be used for the long-term morphological simulations. In the initial phase, the sensitivity of the grid resolution was investigated by lowering and increasing the resolution by a factor of 2. This analysis revealed that the increased resolution can represent the channel and shoal configuration as similar as in the measured data. However, the present resolution is sufficient to represent the main channel and shaol structure without missing the main features.

The model domain has a direct connectivity between Wadden Sea and North Sea, in which offshore North Sea boundary is located at about 20 m depth. This facilitates to accurately represent the influence of nearshore processes into Wadden Sea. For example, it is very important to consider the contribution of sediments from the ebb-tidal delta and the adjacent coasts, while simulating extreme events (as in the present study) and long-term morphodynamics (e.g., sea level rise).

<u>Saltmarsh has an unique vertical structure</u>

The model was simulated in the 2DH mode, and thus the saltmarsh configuration needs to be provided as averaged values over the water column: density, diameter and height. The drawbacks of this approach are twofold. First, it is required to estimate the roughness to the bed shear and the saltmarsh induced flow resistance separately. Second, there is no change of the plant structure along the water column, and that is a high schematisation of saltmarsh in general, and Ley Bay in particular. Applying different vertical layers (i.e., full 3D model) allows providing vertical variation of the plants and the effect of vegetation on the 3D flow and turbulence (Houwing et al., 2000). However, such an approach demands high computational time, which

could not be completed by the time of this report albeit under progress now. In the 2DH approach, the model bed had 6 spatial varying sediment fractions and the forcing from tide and wave together with wind. These however support the increase in the accuracy of the hydromorphodynamic processes in Ley Bay.

Sensitivity analysis of plant parameters indicated, both erosion and sedimentation considerably vary only with the plant height. Furthermore, it was found that erosion increases and sedimentation decreases as the plant height increases. Increasing the density by a factor of 2 and 4 caused decreasing erosion only by 8% and 11%, and increasing sedimentation only by 3% and 5% respectively. Similarly, increasing the plant diameter by a factor of 2 and 4 resulted in decreased erosion only by 2% and 3%, and decreased sedimentation by 0% and 2%. The vegetation – flow interaction approach after Baptist (2005) is well validated and implemented in the model. The tendencies observed here have to be further investigated though. This work is in progress at the time of this report. It is assumed that 3D model runs will further improve the sedimentation. Also, the consideration of the stabilization of the sediment bed by the plant roots could contribute here. This ongoing work will determine whether it is required to improve the model formulation to provide better interactions between plants and flow, and between plants and sediment movements.

Selected NBS has a potential application for coastal protection

In this study, application of saltmarsh was selected as NBS, and its effects for coastal protection were investigated during extreme events. Two extreme events, Xaver and Herwart, which have different severity levels (i.e., occurrence of TA+Hs has 125 and 2 years return levels respectively) were simulated. Therefore, it can be expected to have different effects with the application of NBS. Furthermore, the saltmarsh area in Ley Bay is located above the High-Water line (~1.5 m + MSL), and thus it is hardly submerged during fair weather conditions.

Results indicated that NBS has significant impacts on hydrodynamics, sediment transport and morphological changes. Variation of water levels within the saltmarsh area showed that NBS delayed rising and falling of water levels, and the latter is prominent. Therefore, it can be generally expected to have more sedimentation as there is more time for settling of sediments. However, this process depends on the storm severity as well as the locations within the saltmarsh area. During the low severity event (Herwart), water levels were completely damped in the middle of the saltmarsh area, whereas at the seaward edges, showed a similar rising and falling trend. Wave height, velocity and bed shear stress followed the similar trend for events of different severity and locations within the saltmarsh. For example, at the seaward saltmarsh edge, both mean velocity and mean bed shear stress during Xaver decreased by about 85% and 100% respectively. Sediment transport within the saltmarsh area notably occurred only during the high severity event, and it was mainly dominated by the suspended-load transport. Furthermore, it was found that the sediment transport outside the saltmarsh area decreases, particularly along the saltmarsh edge. Bed evolution significantly decreased within the saltmarsh area, resulting in low volume of sediments from erosion and sedimentation depending on the severity of a storm event. During both storm events, saltmarsh area supplied sediment into Ley Bay causing erosion therein, which remarkably decreased in the application of NBS.

These preliminary results clearly indicate that the selected NBS, application of saltmarsh, is a potential agent for coastal protection, which enables the resistance against the adverse impacts during storm events. A previous project of NLWKN, A-KUEST (Niemeyer et al., 2014; Kaiser et al., 2010), revealed that increased sedimentation in the saltmarsh areas of the Ems-Dollard estuary improves the adaptation to sea level rise. Furthermore, the higher the saltmarshes the lower the wave heights during storm surges resulting in the reduction of wave runup and overwash. Ongoing work further investigates this NBS to increase the credibility

of the outcome using different modeling techniques (e.g., 2DH vs 3D, improving formulations for stabilization by plant roots) and future climate change scenarios (e.g., sea level rise).

3.5.2.German Bight model (Hereon)

Hereon has assessed large-scale erosion risk reduction implicitly with SCHISM, examining kinematic attenuation and sediment mobilization reduction in response to seagrass vegetation. Different restoration scales and focal areas (high- or low-energy zone) were considered in the selected experiments (section 3.3.1). The scenarios were statistically analyzed based on differences in the monthly average and 95th percentile for various hydrodynamic variables relative to the reference run for the month of October 2017, when Storm Herwart occurred. These differences show the hydrodynamic engineering capacities of seagrass on average and under more dynamic conditions.

The results show that the effect of seagrass on sea level is quite limited and varies locally, reaching only a few mm to cm with respect to average conditions (Figure. 3.28a). For the 95th percentile (Figure. 3.28b), the presence of seagrass generally reduces the sea level elevation and, in the case of the maximum seagrass expansion scenario, also affects the ungreened tidal flat area, and shoreward the reduction can be as much as more than 15 cm (10-15%). However, as long as seagrass does not cover the majority of the mudflat area, the overall direct impact on sea level remains neglectable.

In contrast to sea level changes, seagrass has a very pronounced effect on the current velocity within the meadow (Figure. 3.29). The reductions within the meadows compared to the same areas in the scenario without seagrass are assumed to be potentially 10-30 cm/s (30% to nearly 80%). The widespread decrease in flow velocity is moderately offset by partially increased flow velocities in portions of a few seagrass-free intertidal channels.

This localized increase in current velocity occurs primarily in the maximum Vegetation scenario, and to a lesser extent in the VegHE scenario with seagrass at the edge of the channels. The differences in quantiles indicate a maximum reduction in flow velocity of 25 cm/s or more (up to 0.8 m/s). The presence of seagrass results in similar overall relative changes for the quantile compared to the changes in monthly average velocity (up to 20% in the deeper zones and up to more than 80% in the shallowest zones).

Seagrass restoration appears to be a similarly effective measure for reducing significant wave height. The simulated significant wave heights (HS) at the barrier island level correspond to approximately 1 to 1.5 m compared to the monthly average, and the 95th percentile of significant wave heights is about 1.5 to 2 m. Wave heights continue to decrease as they enter the back tidal flats in response to the shallow bathymetry, which favors wave refraction and friction, causing the Hs value to drop below 0.5 m and approaching 0 m. The presence of seagrass contributes to wave attenuation, which additionally increases HS reduction by a few cm up to more than 20 cm and on average up to more than 40 cm locally with respect to the quantiles (Figure. 3.30).

The seagrass restoration scenarios indicate a further reduction of a few cm in the shallow areas, and reductions of over 40 cm on average and over 60 cm with respect to the 95th percentile for the locations where seagrass would occur in deeper areas, where still relatively high waves occur. Generally, where seagrass is located, HS is reduced by over 20% in the deeper reaches and more than 50% in regions shallower than 1 m, approaching almost complete attenuation for the shallow most regions that are still vegetated.

Naturally, the attenuation of currents and waves in the Wadden Sea results in lower stresses that can drive coastal erosion via the mobilization of bottom sediments. This is finally reflected by decreased monthly

average bottom concentrations on the order of a few centi to maximum deci g/l, when introducing, respectively increasing the amount of seagrass. This denotes a reduction widely over 80% compared to the REF scenario. During strong current conditions sediment mobilization seen from the 95th quantiles is reduced by up to more than half a g/l (Figure 3.31b).

Overall, the results from the experiments with the SCHISM setup illustrate that seagrass can significantly influence hydro-morphodynamic conditions bv effectively reducing both currents and waves ., This promotes sediment accumulation and via the attenuated bottom stresses, effectively reduces erosion potential, especially during extreme events. The effects within a meadow are larger for a higher density of vegetation. Attenuation mainly occurs locally within the vegetated area and partially in the landward sheltered area, consequently, different scenarios suggest that the area protected from erosion increases roughly in proportion to the extent of vegetated coverage. While the results provide a positive first-order approximation of the protective role of seagrass, there are notable limitations. The model assumes a unidirectional interaction—seagrass affects flow, but not vice versa—and represents seagrass as rigid, neglecting the bending behavior that, in reality, reduces drag and limits wave attenuation. This simplification leads to an overestimation of current attenuation and does not account for seasonal or storm-driven changes in seagrass dynamics. These factors highlight areas where future model improvements are needed.

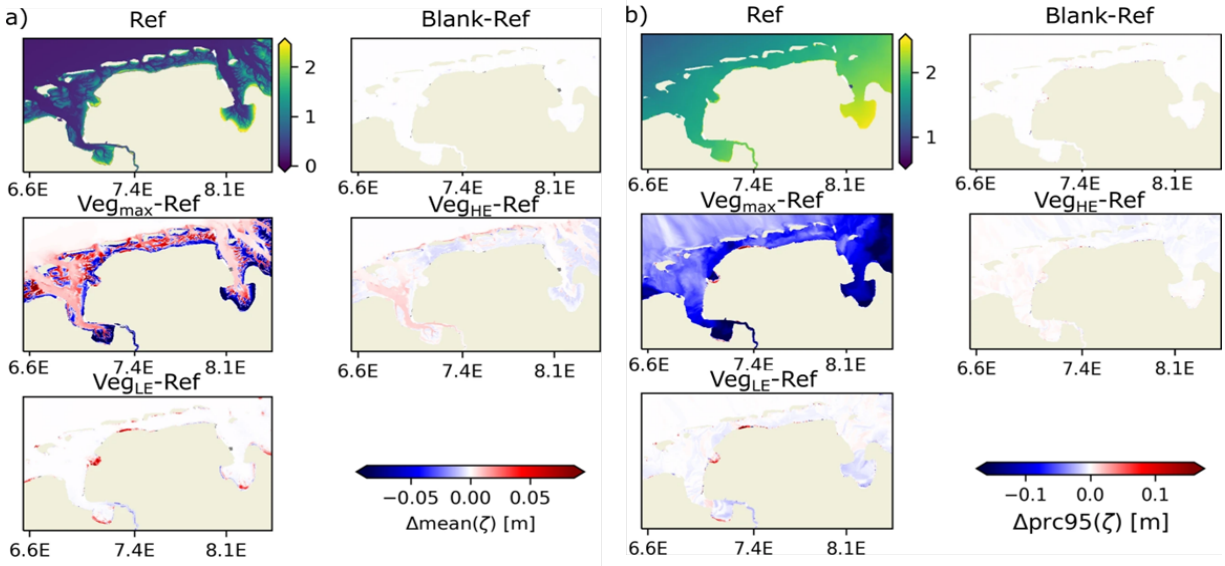

Figure 3.28. Differences in monthly average (a) and 95th percentile (b) sea surface height between seagrass scenarios and reference run.

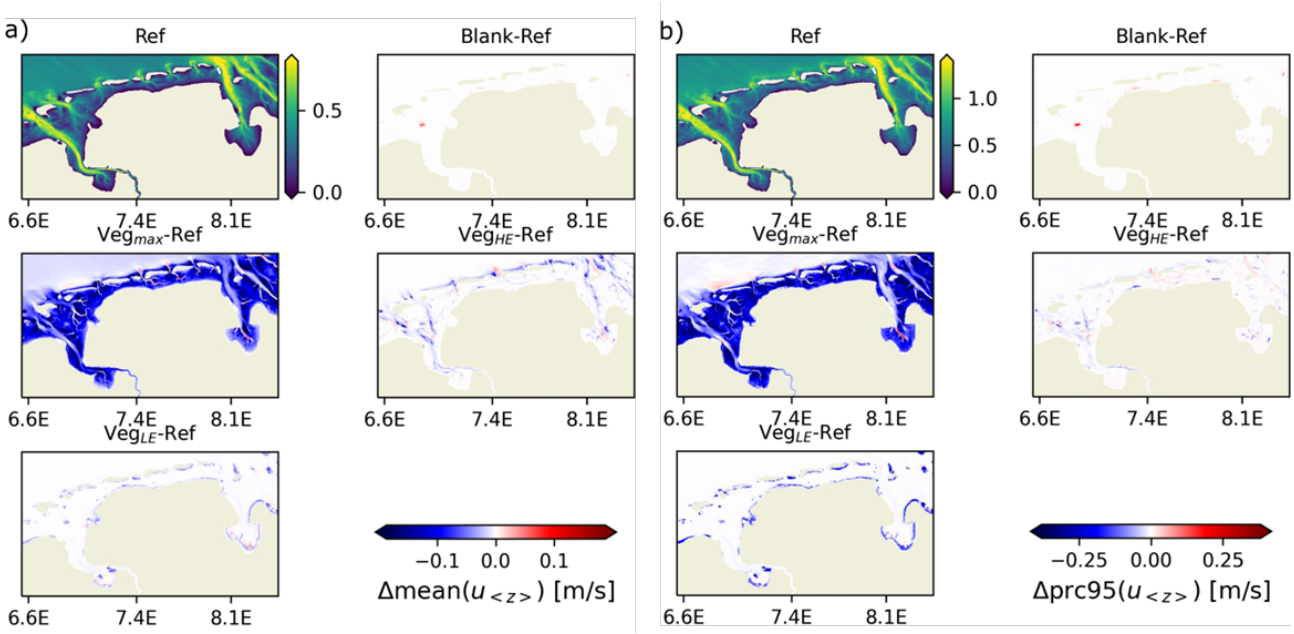

Figure 3.29. Differences in monthly average (a) and 95th percentile (b) of depth averaged velocity between seagrass scenarios and reference run.

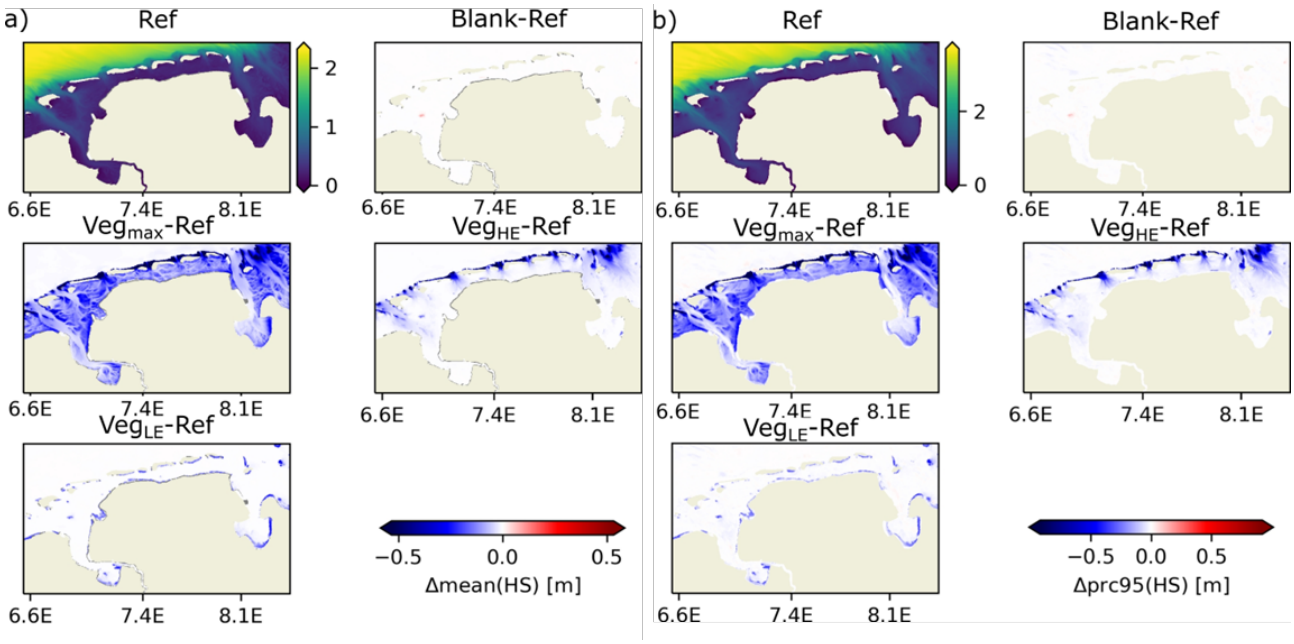

Figure 3.30. Differences in monthly average (a) and 95th percentile (b) of significant wave height between seagrass scenarios and reference run.

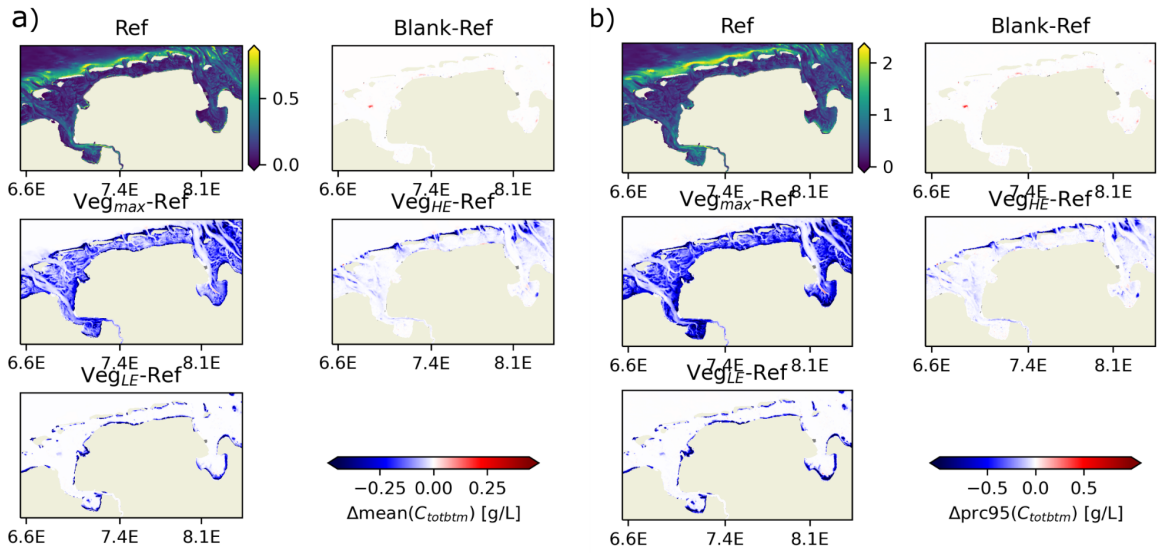

Figure 3.31. Differences in monthly average (a) and 95th percentile (b) of bottom layer suspended sediment concentration between seagrass scenarios and reference run .

The seagrass ESS of coastal erosion protection is directly assessed through quantifying the Norderney nearshore morphological evolution during a specific storm event.

As shown in Figure. 3.32, the seagrass meadow is able to effectively reduce wave height and roller energy, particularly when located in the wave-breaking region. Specifically, when the seagrass meadow is placed in this area, wave height is reduced from 1.5 m to less than 0.5 m and roller energy drops to approximately zero within the seagrass domain. This suggests that seagrass is able to preserve the beach behind the meadow by reducing the roller energy, which is strongest at a water depth of approximately 3 m.

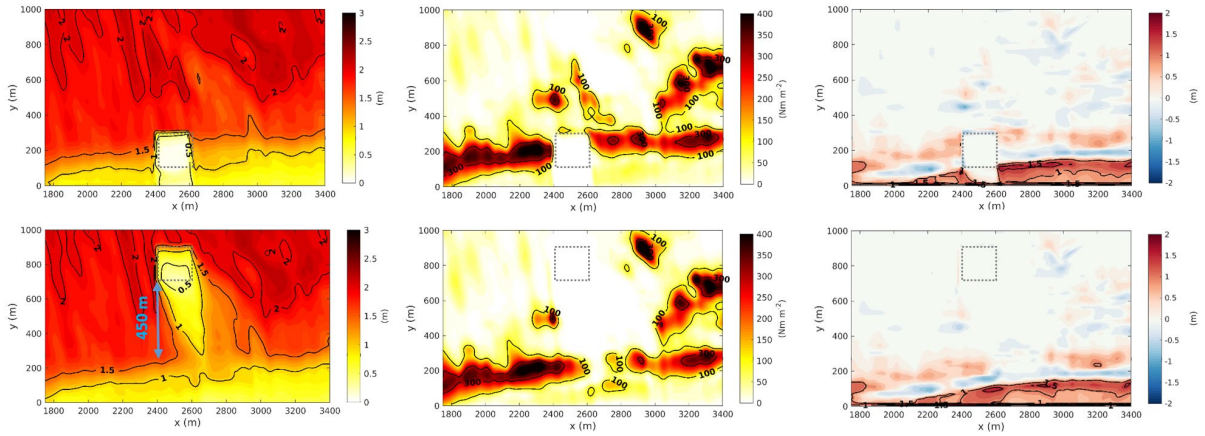

Figure 3.32. Sensitivity of (left column) the time mean wave height, (middle column) roller energy on Day 3 (storm day), and (right column) bathymetric differences before and after the storm for the locations of seagrass placement. Positive values in bathymetric changes denote erosion. The gray dashed square indicates the area of the seagrass meadow.

In general, a wider range of depths requires a larger area of seagrass (Figure. 3.33a). However, since the slope of the shoreface varies in the alongshore direction, the area and distribution of seagrass change when the plantings start at different depths and have different sizes (Figure. 3.33b and c). The seagrass area reaches an extreme when the combination of the two parameters intersects the white dashed line shown in Figure. 3.33a. The largest seagrass area was obtained when seagrass was planted with hs=1.6 m and hr=1.4 m.

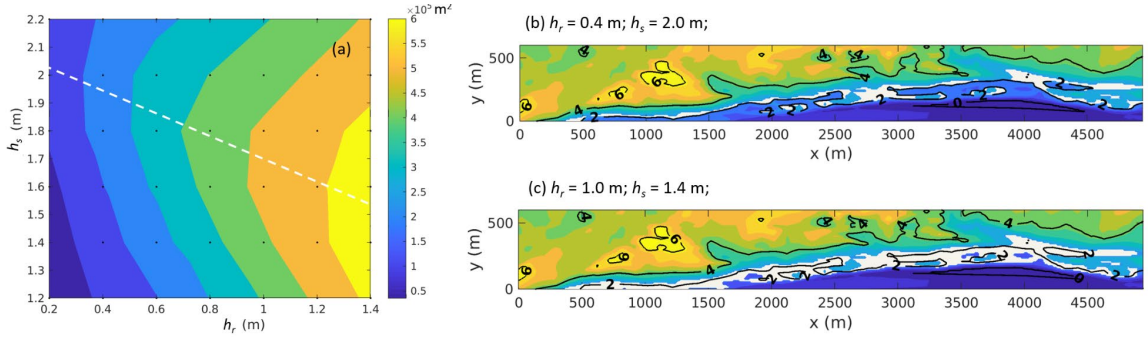

Figure 3.33. (a) Seagrass meadow area for experiments as a function of hr and hs. The black dots indicate experiments with different hr and hs combinations. Panel (b) illustrates the seagrass distribution (in white colour) for the 'deep start-narrow range' scenario (i.e.,hr = 0.6 m and hs = 2.0 m); (c) is the same as (b) but for the 'shallow start-wide range' scenario (hr = 1.0 m and hs = 1.4 m).

The reduced volume of erosion was compared with the eroded volume from the reference run, with the relative value E shown in Figure. 3.34. Even for the minimum seagrass planting scenario (i.e., hr=0.2 m and hs=1.2 m), the amount of erosion was found to be reduced by approximately 40%. For the same hr, when the seagrass meadow starts from deeper depths, it yields a greater reduction of erosion. In the case of hs=2.2 m, the reduced erosion reaches approximately 60%. Comparatively, the reduction in sediment erosion was found to be more sensitive to the increasing depth range of the seagrass plantings, hr, rather than increasing the starting depth hs. However, the relation between the reduction in erosion and seagrass location/size is not monotonic. An opposite relation was found between the starting depth of the seagrass plantings and the reduction in seabed erosion when the depth range increased. The white dashed curve in Figure. 3.34a illustrates the combinations of hr and hs when the reduced erosion reaches the extrema.

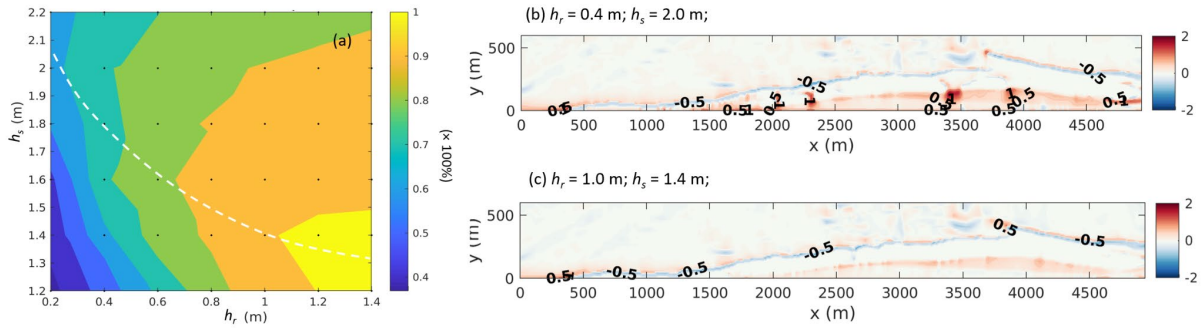

Figure 3.34. (a). The reduction of erosion with respect to the erosion (E) for experiments as a function of hr and hs. (b) and (c) are the results corresponding to experiments Figure. 3.34 (b) and Figure.3.34 (c).

A ratio, R, between relative erosion reduction E (Figure. 3.34a) and normalized seagrass area A (Figure. 3.33a) indicates the efficiency of erosion reduction for different seagrass area outcomes that result from the corresponding hr and hs combinations. The maximum efficiency rate of R equal to 6.5 is obtained when hr = 0.2 m and hs = 1.2 m (Figure. 3.35). This combination reduces erosion by approximately 40% while utilizing only approximately 6% of the maximum seagrass area. The steepest increase in R occurs along the direction of the normal, as represented by the grey dashed line. Along this line, the `optimal' combination is found at point `i', where hr=0.85 m and hs=1.35 m, which yields the maximum E of approximately 0.9 and is furthest from the maximum seagrass area. At this point, R is approximately 2. The grey line further crosses with the maximum seagrass area curve at `ii' (hr=1.25 m, hs=1.6 m), which yields the `potential' combination, where R ~ 1.

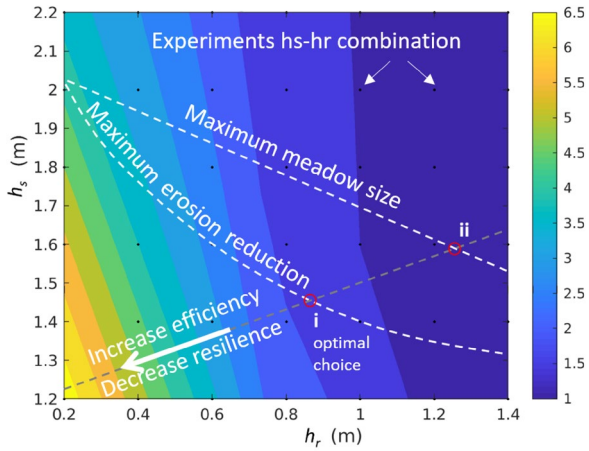

Figure 3.35. The ratio R between the relative erosion reduction E and the normalized seagrass area A for different combinations of hr and hs. The grey dashed line denotes the normal direction in which R decreases with increasing hr and hs.

Seasonal dependence

To gain insight into the intra-annual variability of the beneficiary effects of seagrass for coastal protection, the maximum area seagrass scenario, Veg_max has been contrasted with the Ref scenario during a summer and a winter period.

The current seagrass configuration in the model framework is time-invariant. Attenuation capabilities for different seasons were as well explored by contrasting the 95th quantiles of various variables from the summer and winter months of the present-day reference simulation for the year 2017.

Although maximum sea levels in winter appeared higher, the number of strong wind events was insufficient to significantly raise the 95th percentile, leaving both summer and winter periods relatively unchanged (Figure. 3.36). The statistics for wave quantiles showed slightly higher waves in the back barrier of the Wadden Sea. On average, the quantiles for velocities and bottom stress remained similar, but in winter, they tended to increase in the tidal flat area and decrease in the channels.

As shown in Figure. 3.36, the reduction capabilities at the scale of multi-monthly quantiles do not change significantly for most variables (see the strong agreement of figures in the first and second columns). Due to higher waves, the absolute reduction in HS is enhanced in winter and appears almost uniform. The velocity quantile reduction in the flat areas increases by roughly 10% in winter, with a difference in the seagrass-induced reductions of about 2-5 cm/s. Analogously, stress reductions at the bottom are enhanced in tidal flat areas, with a minor opposing trend for the channels that are free of vegetation. The greater erosive potential during the winter months is sufficiently buffered by the seagrass, leading to additional reductions of bottom layer quantiles approaching 0.25 g/l. Overall, seagrass remains an effective buffer against meteorological conditions corresponding to the winter season.

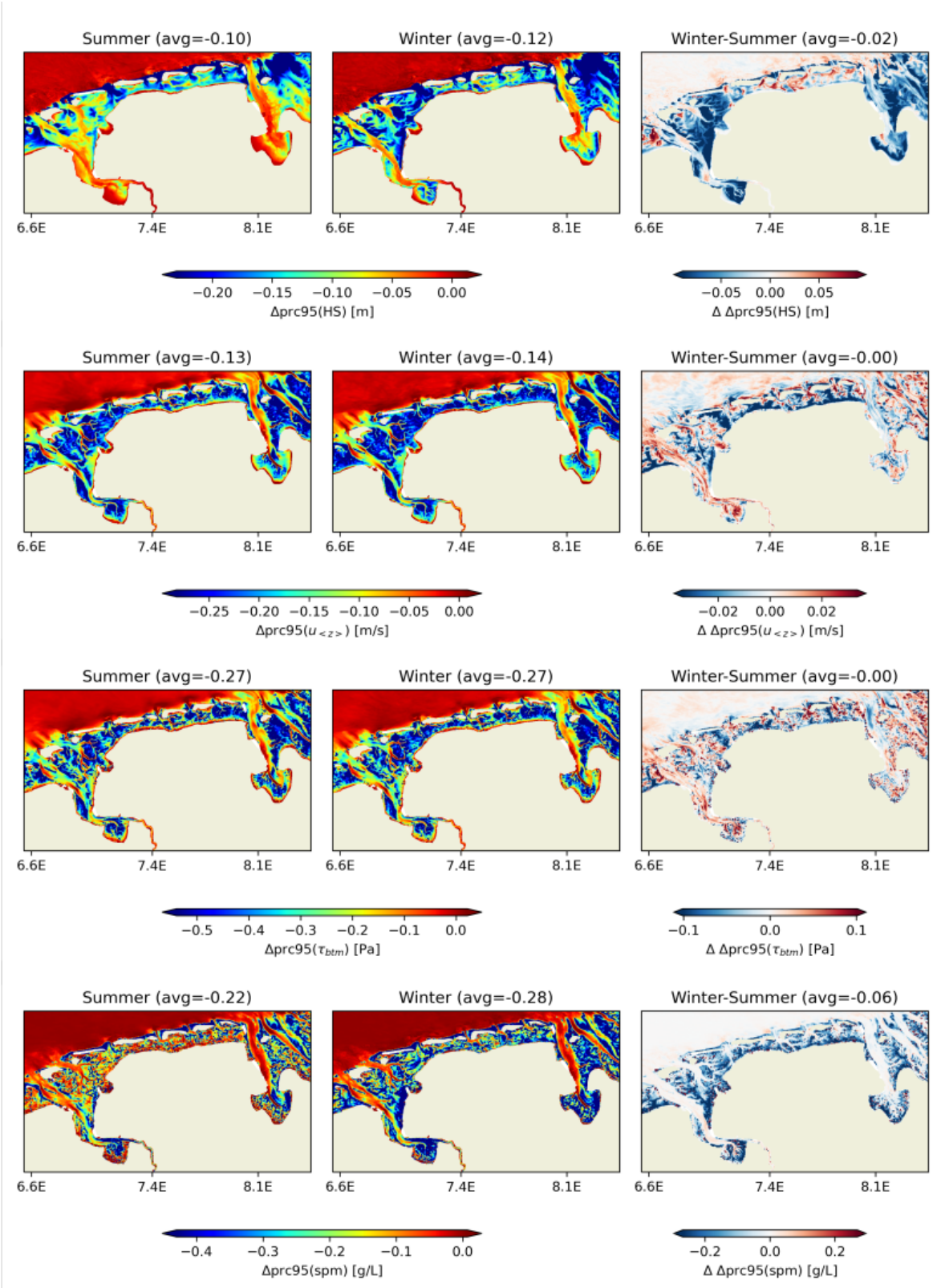

Figure 3.36. Reductions in 95th seasonal percentiles in Veg_max scenario with respect to Veg_CNTRL scenario during summer (first column) and winter season (second column, difference in third column). From top to bottom this is with respect to the variables significant Wave Heights, depth averaged velocity, bottom stress, and bottom layer total suspended sediment concentration. Number in the respective title denotes the spatial average for the depicted domains the spatial average for the depicted domain.

Extreme events with different return periods

Under storm conditions, wave and current attenuation appeared slightly increased compared to that under calm weather conditions. However, this attenuation was reduced in relative terms. To compare the effectiveness of attenuation during severe and calm weather, we compared two tidal cycles (from October 28th until October 30th) during the storm event to the tidal cycles 10 days prior to the storm (October 18th–October 20th) using the previous statistical measures (mean and 95th percentile). Overall, the hydrodynamic values increased during the storm, causing a corresponding increase in the attenuation due to the seagrass. The reductions compared to the realistic scenario with sparse seagrass (Ref) remained relatively similar for significant wave height, bottom stress, TKE, and SPM concentrations. For the variables referenced at the bottom, reductions of over 90% are found in areas shallower than 2m, and decreases of over 10% occur within areas up to 4m depth for the Veg_max scenario.

To investigate how the reduction potential of seagrass changes depending on the magnitudes reached during the extreme event, the impact on kinematics is compared for the Herwart and Xaver events for different variables based on the maximum levels reached during the respective storms.

Within the EFWS study area, peak sea levels during Xaver exceed those during Herwart by more than 1m, as shown in Figure. 3.37. The highest sea levels occur in the eastern part of the study area and increase with the tidal range along the coast. Seagrass has a minimal effect on reducing peak sea levels, with a maximum reduction of about 10 cm, which is equivalent to 3 to 4% during Herwart. During Xaver, the sea level reduction

for Xaver is similarly low, even 2 to 3 cm lower, resulting in a relative sea level reduction of 1% or less. In some parts of the supra littoral area, seagrass even increases the maximum observed sea levels.

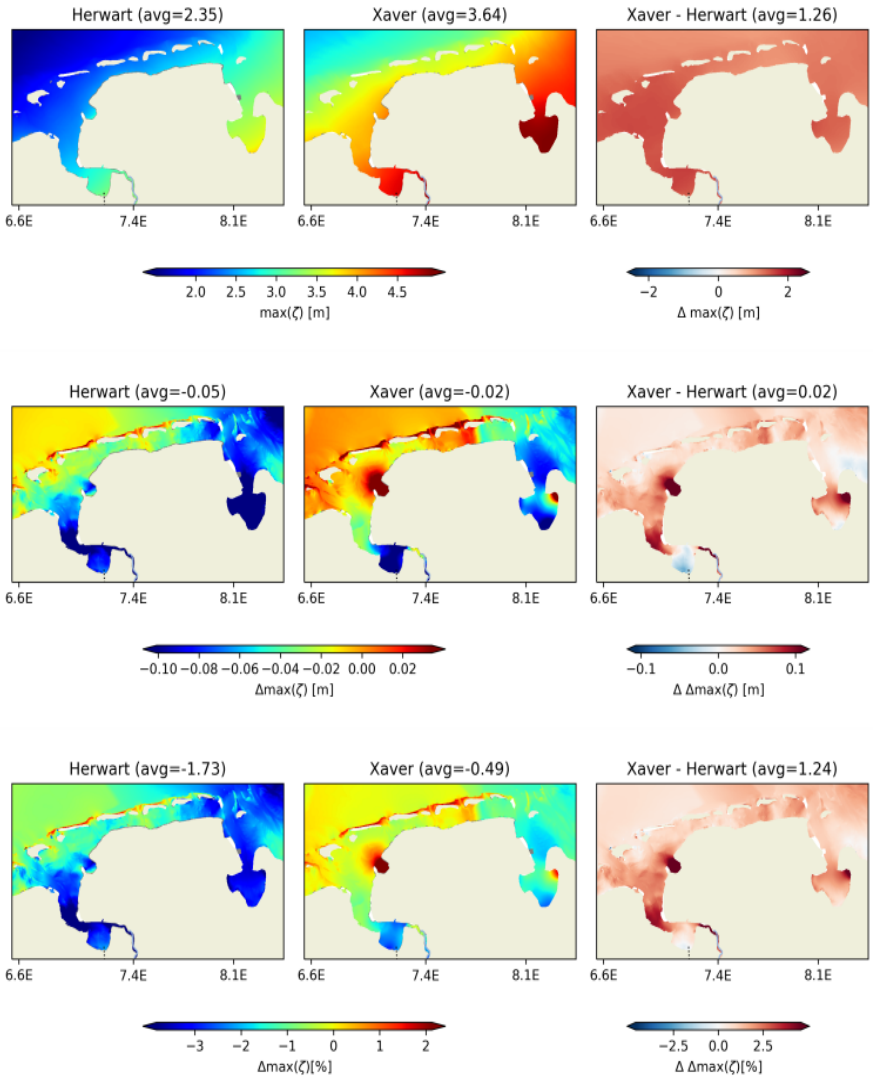

Figure 3.37. Maxima in Sea Surface Height and their reduction due to seagrass (Veg_max scenario): Top row shows peak values during Herwart and Xaver and the differences. The middle row depicts the respective difference for the maximum coverage seagrass scenario - the no seagrass scenario, and the difference in differences (positive values in the 3rd column denote a weaker reduction during Xaver). The bottom row is analogous to the middle row comparing reductions relative to the absolute values without seagrass instead. Number in the respective title denotes the spatial average for the depicted domain.

Wave Heights

During Xaver, simulated maximum significant wave heights are approximately 1 metre higher directly in front of the Barrier islands (see Figure. 3.38). Beyond the Barrier Islands, waves are significantly reduced due to breaking on the shallow bathymetry, but still remain at slightly higher levels during Xaver. The shallow Wadden Sea bathymetry efficiently breaks and dampens the waves. The wave trains passing by the barrier islands via the tidal channels are reduced by around 0.2 to 0.4 metres in the tidal flat area. During Xaver, peak waves in the back barrier Wadden Sea were slightly dampened by 5 to 10 cm, except for the sea ward channels of Ems and Jade Bay, where Xaver resulted in lower maximum wave heights. The overall peak wave height reduction reached about 20-40 percent among the tidal flats and between 0 and 10% within the

channels. While wave damping tends to increase with larger waves during severe storms, it causes a similar reduction across the tidal flats, with a tendency to be lower by around 5%.

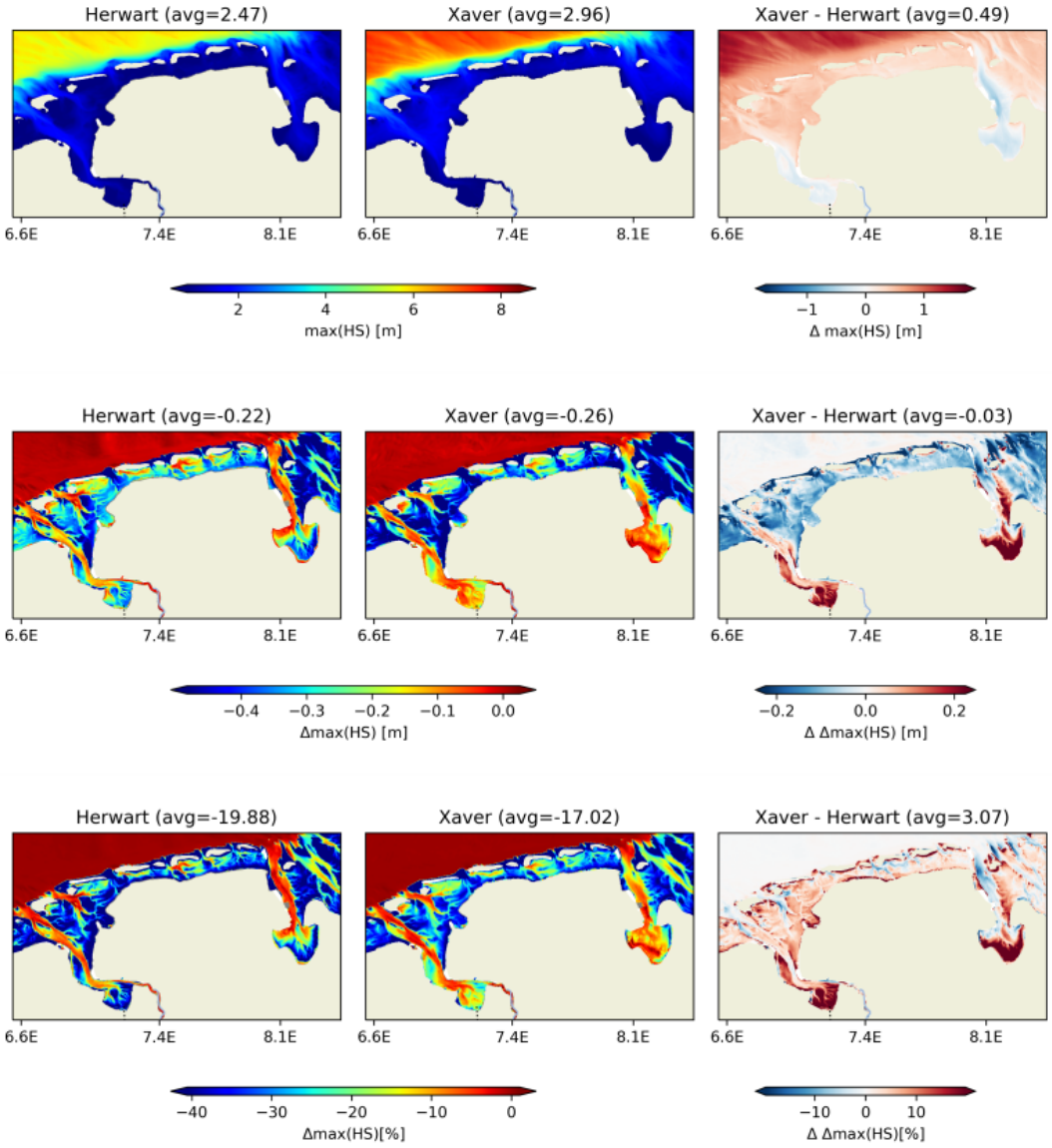

Figure 3.38. Maxima in Significant Wave Height and its reduction due to seagrass (Veg_max scenario): Top row shows peak values during Herwart and Xaver and the differences. The middle row depicts the respective difference for the maximum coverage seagrass scenario - the no seagrass scenario, and the difference in differences (positive values in the 3rd column denote a weaker reduction during Xaver). The bottom row is analogous to the middle row comparing reductions relative to the absolute values without seagrass instead. Number in the respective title denotes the spatial average for the depicted domain.

Current Velocities

Vertically averaged velocities reach up to 1 m/s in the narrow tidal channels during Herwart and below 0.6 in the shallow Wadden Sea. The largest values are found in Jade Channel, reaching up to 1.5 m/s (see Figure. 3.39). During Xaver, peak velocities are approximately 0.5 m/s higher in front of the islands and within the tidal basin centers. They are also increased in the tidal flat area due to higher water levels and reduced friction damping. The average depth velocities during Xaver were reduced compared to Herwart. This reduction is due to the effective dampening of seagrass in the vegetated layer above the ground, which is

approximately 20 cm. Although the reduction during Xaver is higher in this layer, the much larger sea level setup results in a higher water column in the Wadden Sea. As a result, the upper layers of the water column are less affected by the bottom frictional damping.

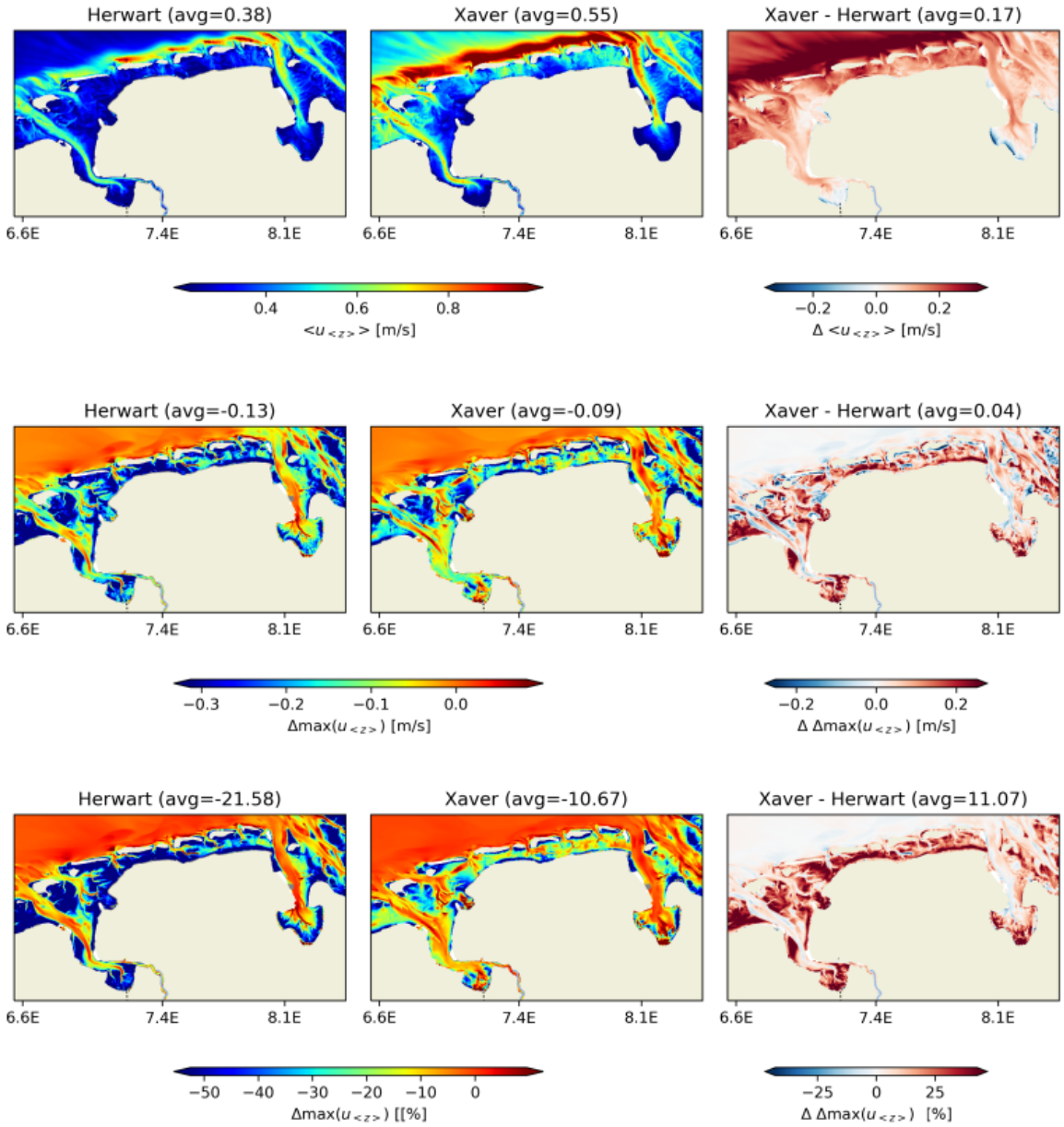

Figure 3.39. Maxima in depth averaged velocity and its reduction due to seagrass (Veg_max scenario): Top row shows peak values during Herwart and Xaver and the differences. The middle row depicts the respective difference for the maximum coverage seagrass scenario - the no seagrass scenario, and the difference in differences (positive values in the 3rd column denote a weaker reduction during Xaver). The bottom row is analogous to the middle row comparing reductions relative to the absolute values without seagrass instead. Number in the respective title denotes the spatial average for the depicted domain.

Bed shear stress and sediments

The increase in velocities among secondary channels and tidal flat areas caused bottom stress maxima during Xaver to exceed those during Herwart by a few centipascal (refer to Figure. 3.40). In the majority of regions where bottom stress during Xaver significantly exceeds bottom stress during Herwart, the reduction in bottom stress during Xaver is predominantly more pronounced in absolute values compared to Herwart.

However, the relative reductions do not scale proportionally with the increase in absolute value. As a result, the relative reduction in the tidal flat areas is less and closer to 30-40%, as opposed to more than 50% across the tidal flat regions surrounding the channels.

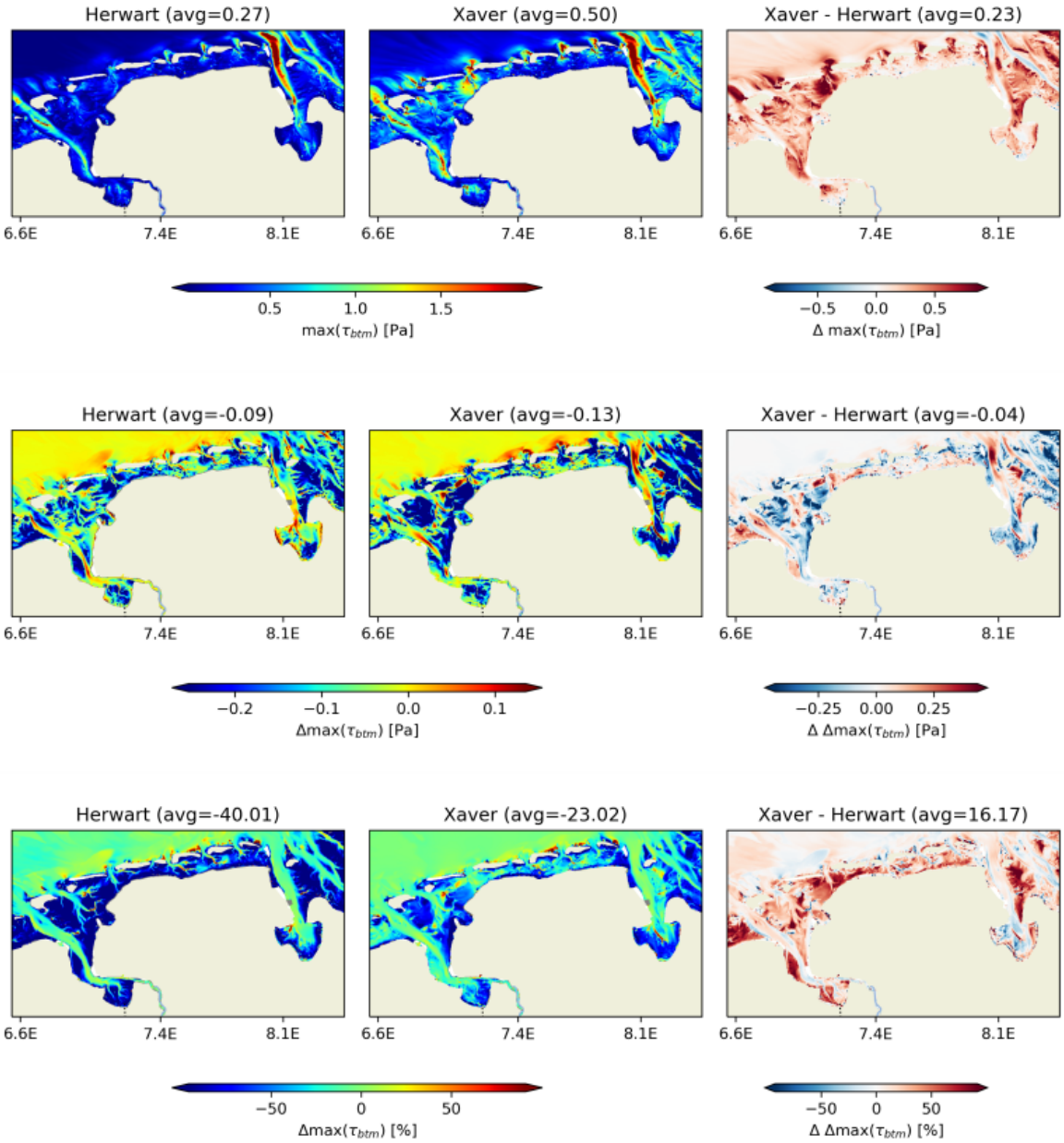

Figure 3.40. Maxima in Bottom Stress and its reduction due to seagrass (Veg_max scenario): Top row shows peak values during Herwart and Xaver and the differences. The middle row depicts the respective difference for the maximum coverage seagrass scenario - the no seagrass scenario, and the difference in differences (positive values in the 3rd column denote a weaker reduction during Xaver). The bottom row is analogous to the middle row comparing reductions relative to the absolute values without seagrass instead. Number in the respective title denotes the spatial average for the depicted domain.

The maximum concentration of bed layer sediment increased by 30% during Xaver over Herwart. The presence of seagrass resulted in a reduction of peak concentration, ranging from 0.2 to 0.4g near the channel edges and 0.6 to 0.8 on the tidal flats (refer to Figure. 3.41). This reduction was more than 80% during Herwart and between 60% and 80% during Xaver, compared to the tidal flats. During heavier storms, there

is a higher level of stress on the soil, resulting in increased sediment erosion from unprotected areas. Despite this, erosion reduction is still effective during stronger storms, although it appears to be 20% less effective.

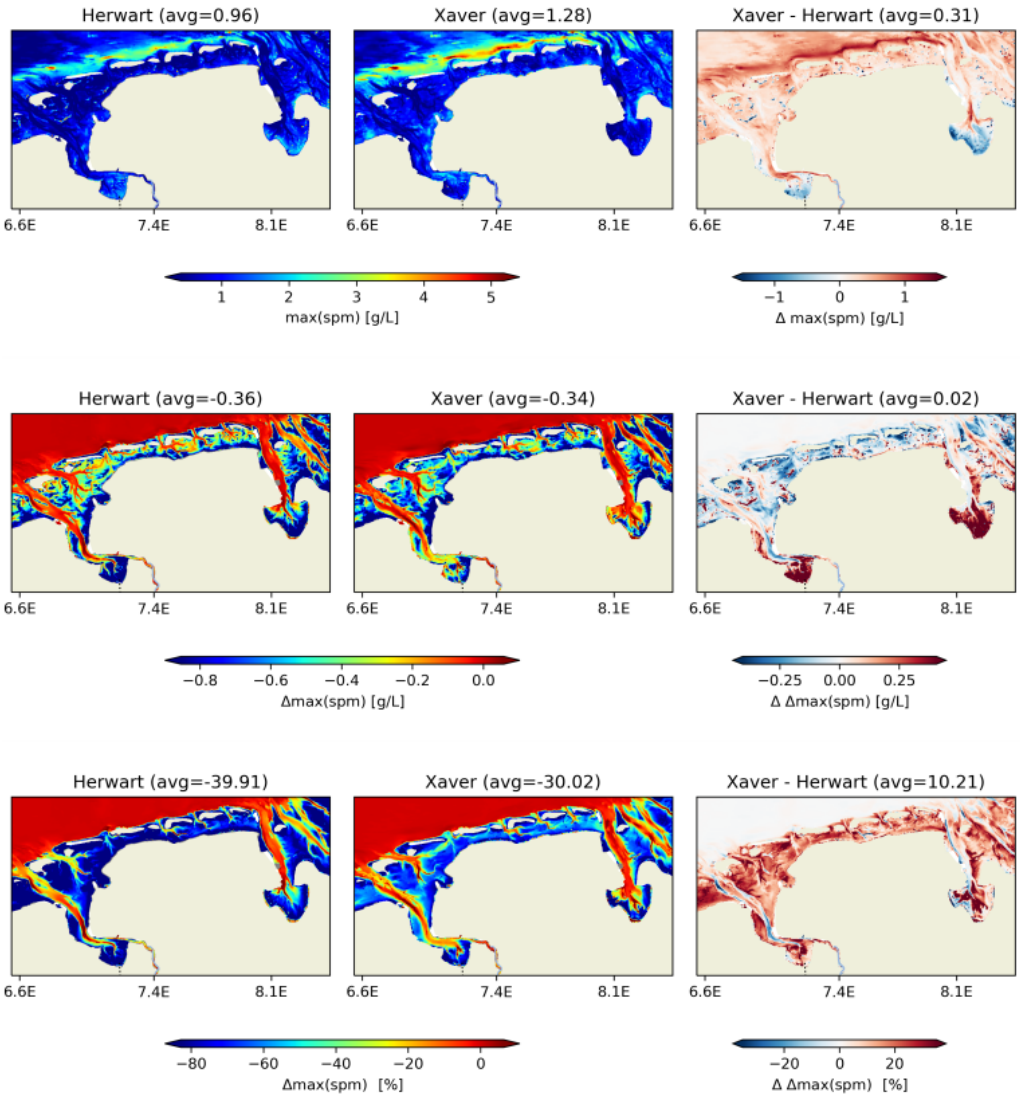

Figure 3.41. Maxima in Bottom layer total suspended matter concentration and its reduction due to seagrass (Veg_max scenario): Top row shows peak values during Herwart and Xaver and the differences. The middle row depicts the respective difference for the maximum coverage seagrass scenario - the no seagrass scenario, and the difference in differences (positive values in the 3rd column denote a weaker reduction during Xaver). The bottom row is analogous to the middle row comparing reductions relative to the absolute values without seagrass instead. Number in the respective title denotes the spatial average for the depicted domain.

Overall baseline values in hydrodynamics were significantly higher during Xaver compared to Herwart. Under these amplified circumstances, seagrass is suggested to maintain its attenuation capabilities. It tends to lead to an increased reduction in absolute terms. Therefore, it remains beneficial for coastal protection. However, it becomes less effective in relative terms as the attenuation capacities do not scale linearly with the magnitude of currents and waves.

3.6. Conclusions

Preliminary results of NLWKN indicate that the existing sediment transport trend is enhanced by SLR, and the area close to the mainland of the basin is subjected to sedimentation. Both these observations appear to increase as the rate of SLR increases.

The results from Hereon indicate a negligible direct contribution of seagrass towards flood risk reduction, but a significant reduction of currents and waves, and also of the resulting mobilization of sediments. Thereby and via the general alteration of hydrodynamic conditions towards sediment accumulation it could indirectly contribute to flood risk reduction at long time scales supporting the vertical height growth in the Wadden Sea with respect to SLR. Wave and current attenuation under storm conditions appeared slightly increased compared to that under calm weather conditions, but this attenuation was reduced in relative terms.

The seagrass meadow is able to effectively reduce wave height and roller energy, particularly when located in the shore-breaking region. Specifically, when the seagrass meadow is placed in this area, wave height is reduced from 1.5 m to less than 0.5 m, and roller energy drops to approximately zero within the seagrass domain. As the seagrass meadow is placed further away from the coast, the erosion of the shoreface gradually decreases.

The layout of seagrass meadows has a significant impact on the efficiency they have of mitigating onshore sediment erosion. As the starting position of the planting moves towards shallow water and the depth range of the planting increases, the area covered by the seagrass meadow continues to expand. This leads to a greater reduction in coastal erosion as a function of seagrass planting. However, the study discovered that for a specific depth range, the most significant reduction in erosion is not achieved by starting at the depth that results in the largest meadow size. In terms of reducing erosion per unit area of seagrass, the most efficient combination of depth ranges and start locations is that the size of the meadow is minimized. However, the small size of these seagrass meadows may not provide adequate protection against damage caused by storms. The results overall suggest seagrass expansion to be a useful addition to engineered coastal protection measures and lore the risk of coastal erosion.

4. Multi-hazard forecasting (including a multidisciplinary calibration) and application limits Venice Lagoon Pilot (CMCC, COR)

4.1 Introduction

The Venice Lagoon, located in the Northern Adriatic Sea, is the largest transitional environment in the Mediterranean Sea. Its total surface is ca. 549 km^2 but, excluding islands and tidal marshes, ca. 432 km^2 are free waters. The lagoon is divided into three main hydrological basins (southern, central, and northern basins) by the Lido and Pellestrina watersheds, the edges of which depend on tidal excursions and winds. Three inlets, situated at the eastern boundary of the lagoon, ensure a water exchange between the Northern Adriatic Sea and the lagoon. These inlets are called, from north to south, Lido, Malamocco, and Chioggia. They are 500 to 1000 m wide and up to 15 m deep (Umgiesser et al., 2004).

The lagoon is a very polymorphous environment, exhibiting a mean depth of ca. 1.0-1.2 m, but with depth ranges between 10 and 20 m in the main canals and in the lagoon inlets with the exception of the Malamocco inlet, which is the deepest site of the Northern Adriatic Sea (ca. 50 m). The tidal sea-water exchange through the three inlets is approximately 1.46 x 10^9 m^3 in each tidal cycle (12 hr), which is more than half of the entire water loading, although the water renewal in the inner areas may take ca. 10-20 days. The mean annual freshwater input from 24 tributaries is ca. 35.5 m^3 s^{-1}, but under particularly adverse conditions, freshwater discharges can increase up to 344 and 273 m^3 s^{-1} on an hourly and daily basis, respectively (Zuliani et al., 2005). In the past, other authors had measured outflows of up to 600 m^3 s^{-1} (Cavazzoni 1973). The lagoon exhibits an annual mean water level difference of ± 31 cm (Pirazzoli 1974) but, under particular tidal events and/or meteorological conditions, the water fluctuations can be remarkably higher: from -80 cm to +160 cm (up to +196 cm in 1966) on the mean tide level.

Two major wind regimes are present, the Bora from north–east and the Scirocco from south–east. These wind regimes superimpose a strong circulation on top of the tidal pumping action inside the lagoon, important for mixing and transport. They also create wind waves locally that are then responsible for the resuspension of sediments in the shallow parts of the lagoon (Umgiesser et al., 2004). These wind regimes impact erosion of the different hydrological basins in different manners, where due to the geographical distribution of salt marshes and islands in the central-southern lagoon the Bora wind is free to generate fetch unlimited wave fields, thus adversely influencing the erosive trends in these basins (Carniello et al., 2009).

Apart from the tidal and wind-induced water level changes, the city of Venice has had problems with global sea level rise. This rise, together with the well documented phenomenon of subsidence (Carbognin et al., 1995), is threatening the treasures of art contained in the old city. Moreover, human intervention like the dredging or creation of artificial channels, the creation of the railway bridge or the building of the industrial Port Marghera inside the lagoon have altered the natural equilibrium and evolution of the Venice Lagoon seen as a dynamical system, leading to the progressive degradation of the lagoon.

Due to the complicated morphology and bottom topography of the lagoon, the hydrodynamics of the lagoon can be understood only by use of mathematical modeling.

Increased frequency/ intensity of coastal risks and sea level rise related to climate change require fit-for-purpose and improved nearshore protection (Hanley et al., 2020; Ondiviela et al., 2020; Lobeto et al., 2021). In this context, the application of Nature Based Solutions (NBS) has gained great attention, mainly due to its ability to address social, environmental and climate concerns (Nesshöver et al., 2017; Kumar et al., 2020; Stankovic et al., 2021; Gómez Martín et al., 2021, Pillai et al., 2022). Since the 70s, the national and local Italian governments started to systematically address the safeguarding of Venice and its lagoon (Munaretto

& Huitema, 2012). Since the 90s, a variety of mitigation and adaptation interventions have been implemented, including the mobile barrier system MOdulo Sperimentale Elettromeccanico (MOSE), Piano di Azione per il Clima del Comune di Venezia, Piano Europe, Piano Morfologico and a variety of LIFE projects. These interventions aim to improve the morphological, ecological and hydrological functioning of the lagoon by focusing on, for instance, saltmarsh restoration and seagrass transplantation.

In the Venice lagoon, the saltmarsh extension has reduced over 76% in the last two centuries, decreasing from 180 km^2 to 43 km^2 in the present day (Carniello et al., 2009). Saltmarsh disappearance is governed by a variety of physical and biological processes that drive their evolution in both the vertical and horizontal directions (Tommasini et al., 2019). Saltmarsh restoration in the Venice lagoon is carried out under the Piano Morfologico based on historical analysis of the morphological changes and hydraulic optimisation, and aims to protect from flooding and erosion, re-establish the hydro-geo-morphological equilibrium of the lagoon and abate pollution, while promoting the socio-economic development of the Venice area (Munaretto & Huitema, 2012).

Over the past 25 years various lagoon authorities have carried out seagrass transplantations both for the purpose of technical experiments and environmental restoration (Tagliapietra et al., 2018). In recent decades, a global decline in seagrass meadows has been observed due to numerous environmental activities (Waycott et al., 2009; Donatelli et al., 2019; McKenzie et al., 2020). Furthermore, the European Union (EU) supports ecological quality levels in coastal regions and has established principles for the use of seagrasses as indicators of the health of the ecosystem.

Many studies have reported that seagrasses enable “wave damping” (Koch and Gust, 1999; Méndez and Losada, 2004; Paul and Amos, 2011), and modify local hydrodynamics (Fonseca and Fisher, 1986; Zhang and Nepf, 2019). Water waves which propagate through submerged vegetation lose energy by performing work on the plant which directly results in smaller wave heights (Dalrymple et al., 1984).

In the Venice Lagoon, five marine and freshwater angiosperms are present, three of which are common species and exhibit abundant biomasses: *Cymodocea nodosa, Zostera marina, Zostera noltii*, where *Z. marina* shows the highest coverage. The other two species, *Ruppia cirrhosa* (Petagna) *Grande* and *Ruppia maritima Linnaeus* are rare and rarely studied. Angiosperm meadows play an important role in the ecology of the Venice Lagoon, in that they provide habitats for many species (den Hartog 1977, Fonseca 1990), favour the stabilization of sediments, enhance their deposition, and prevent their resuspension (Sfriso et al., 2004, 2005).

In the RESTCOAST project, for the Venice pilot site, we investigate seagrass and wetland as NBS by assessing their role in coastal protection, with a particular focus on ecosystem services (ESS) related to wave attenuation and current damping. To quantify their contribution, we adopted a numerical modelling approach based on the WAVEWATCH III and SHYFEM models to simulate the hydrodynamic conditions of the lagoon.

4.2. High-resolution coupled coastal models

The main objective of this study is the development of an operational forecasting system to serve as an Early Warning System (EWS) capable of forecast and identify storm events. The operational modelling framework is downscaled using open lateral boundary conditions derived from Copernicus products and is forced by atmospheric fields from ECMWF hi-resolution datasets (IFS dataset). Each component of the modelling framework is described in detail in the following sections. The accuracy of the model has been thoroughly

evaluated through hindcast simulations, using historical periods for which observational data are available, and these data have been used to validate and calibrate the models.

4.2.1. Wave Model

The wave core of the modelling system is based on WAVEWATCH III (hereafter, WW3) (Tolman et al., 2019), a community wave modeling framework that includes the latest scientific advancements in the field of wind-wave modeling and dynamics. This model solves the random phase spectral action density balance equation for wavenumber-direction spectra. The implicit assumption of this equation is that properties of medium (water depth and current) as well as the wave field itself vary on time and space scales that are much larger than the variation scales of a single wave. The model includes options for shallow-water (surf zone) applications, as well as wetting and drying of grid points. Propagation of a wave spectrum can be solved using regular (rectilinear or curvilinear) and unstructured (triangular) grids, individually or combined into multi-grid mosaics.

Source terms for physical processes include parameterizations for wave growth due to the actions of wind, exact and parameterized forms accounting for nonlinear resonant wave-wave interactions, scattering due to wave-bottom interactions, triad interactions, and dissipation due to whitecapping, bottom friction, surf-breaking, and interactions with mud and ice. The model includes several alleviation methods for the Garden Sprinkler Effect and computes other transformation processes such as the effects of surface currents to wind and wave fields, and sub-grid blocking due to unresolved islands. Wave energy spectra are discretized using a constant directional increment (covering all directions), and a spatially varying wavenumber grid. First-, second- and third-order accurate numerical schemes are available to describe wave propagation. Source terms are integrated in time using a dynamically adjusted time stepping algorithm, which concentrates computational efforts in conditions with rapid spectral changes. The model is used worldwide by several institutions to simulate waves of several systems in many regions of the world, from global to coastal scale.

The wave modelling approach is based on downscaling CMEMS Marine products released at the regional scale of the Mediterranean Sea. The current Med_Waves-CMEMS (Korres et al., 2021) (https://data.marine.copernicus.eu/product/MEDSEA_ANALYSISFORECAST_WAV_006_017/description) implementation is based on WAM cycle 6 model with an horizontal resolution of 1/24° (~4.6km). The model solutions are corrected by an optimal interpolation data assimilation scheme of along-track significant satellite wave height observations. The scalar fields from Med-Waves-CMEMS (significant wave surface height, peak wave period and mean direction) are treated at the boundary nodes of the nested system through the Yamaguchi (1984) approximation, to rebuild local wave spectra. The model is initialized using the fetch limited approach: the local JONSWAP spectrum is calculated using the local wind speed and direction, using the spatial grid size as fetch.

Meridional and zonal wind components at 10-m height (U10M and V10M) of well-consolidated atmospheric products from ECMWF (6.5 km resolution and 3h frequency) are adopted as forcing. The atmospheric fields are corrected by land-contaminated points following (Kara et al., 2007) and horizontally interpolated at each ocean grid node by means of linear interpolation.

The wave model has been implemented following WAM Cycle 4 model physics (Günther et al., 1992). The propagation scheme used is a third order scheme (Ultimate Quickest) with the Garden Sprinkler Effect alleviation method of spatial averaging. Wind input and dissipation are based on (Ardhuin et al., 2010), in which the wind input parameterization is adapted from Janssen's quasi-linear theory of wind-wave generation (Janssen, 1991; Chalikov and Belevich, 1993), following adjustments performed by (Bidlot et al., 2005; Bidlot 2008). Nonlinear wave-wave interaction have been modelled using the Discrete Interaction

Approximation (DIA) (Hasselmann et al., 1986, Hasselmann et al., 1985). The model system includes shallow water physics for coastal processes as nonlinear triad interactions, modelled using the LTA-model of Eldeberky (1996). Depth-induced breaking has been implemented using the approach of Battjes and & Janssen, (1978). Ripple-induced bottom friction has been parameterized according to SHOWEX formulations from Ardhuin et al., 2003). The wave spectra for the Venice implementation have been discretized in 24 directions (covering the full circle) and 32 frequencies, from 0.05 Hz to 0.96 Hz.

4.2.2.Circulation model

The circulation modelling system is based on the SHYFEM model, which is a 3-D finite element hydrodynamic model (Umgiesser et al., 2004) solving the Navier–Stokes equations by applying hydrostatic and Boussinesq approximations. The unstructured grid is Arakawa B with triangular meshes (Bellafiore and Umgiesser, 2010; Ferrarin et al., 2013), which provides an accurate description of irregular coastal boundaries. The scalars are computed at grid nodes, whereas velocity vectors are calculated at the center of each element. Vertically a z layer discretization is applied and most variables are computed in the center of each layer, whereas stress terms and vertical velocities are solved at the layer interfaces (Bellafiore and Umgiesser, 2010). The peculiarity of unstructured meshes is the ability of representing several scales in a seamless fashion, reaching higher resolution where necessary.

The model uses a semi-implicit algorithm for integration over time, which has the advantage of being unconditionally stable with respect to gravity waves, bottom friction and Coriolis terms, and allows transport variables to be solved explicitly. The Coriolis term and pressure gradient in the momentum equation, and the divergence terms in the continuity equation are treated semi-implicitly. Bottom friction and vertical eddy viscosity are treated fully implicitly for stability reasons, while the remaining terms (advective and horizontal diffusion terms in the momentum equation) are treated explicitly.

The model has been already applied to simulate hydrodynamics of several systems in many regions of the world, proving its quality and accuracy. Exploiting the variable mesh approach, the model has been successfully applied to several scales, from the open sea (e.g., Mediterranean Sea, Black Sea, Gulf of Mexico) to the coastal seas and estuaries (e.g., coastal areas of Adriatic Ionian and Western Mediterranean Seas in Italy, Kotor Bay in Montenegro, Danube Delta in Romania) to open-sea islands (e.g., Malta) to the fjords (e.g., Roskilde, Denmark, Oslo) to the lagoons (e.g., Venice, Menor in Spain, Nador in Morocco, Dalyan in Turkey, Curonian in Lithuania, Tam Giang in Vietnam) to the ports (e.g., Apulian ports in Italy) to the rivers (e.g., Po river in Italy, Savannah river in Georgia, US) to the lakes (e.g., Geneva in Switzerland, Garda in Italy).

The modelling approach is based on the downscaling of CMEMS Marine products released at the regional scale of the Mediterranean Sea. The current Med-CMEMS-PHY (https://data.marine.copernicus.eu/product/MEDSEA_ANALYSISFORECAST_PHY_006_013/description) implementation is based on the Nucleus for European Modelling of the Ocean (NEMO) (Madec, 2008) finite-difference code with a horizontal resolution of 1/24 of a degree (4–5 km approximately) and 141 unevenly spaced vertical levels. The results are corrected with a data assimilation system based on the 3D-VAR scheme developed by Dobricic and Pinardi (2008). The modelling system is three-dimensionally downscaled from Med-CMEMS-PHY both in terms of initialization and open boundaries. The scalar fields from Med-CMEMS-PHY (sea level, temperature, and salinity) are treated at the boundary nodes of the nested system through a clamped boundary condition. The velocity fields are imposed as nudged boundary condition from the parent model in the barycentre of the triangular elements using a relaxation time of 3600 s.

Three basic surface boundary conditions are used:

a) For temperature, the air-sea heat flux is parameterized by bulk formulas described in Pettenuzzo et al., (2010).

b) For momentum, surface stress is computed with the wind drag coefficient according to Hellermann and Rosenstein, (1983).
c) For the vertical velocity and the salinity, the salt flux boundary condition is adopted and the water flux advected through the air-sea interface is given by precipitation minus evaporation.

For the atmospheric fields, well-consolidated products from ECMWF (10 km resolution and 1h frequency) are adopted as forcing. The atmospheric fields are corrected by land-contaminated points following Kara et al. (2007) and horizontally interpolated at each ocean grid node by means of Cressman's interpolation technique (Cressman, 1959).

The atmospheric variables used for the parametrization are 2 m air temperature (T2M), 2 m dew point temperature (D2M), total cloud cover (TCC), mean sea level atmospheric pressure (MSL), and meridional and zonal 10 m wind components (U10M and V10M) and total precipitation (TP).

About the main numerical settings, we use a total variation diminishing (TVD) scheme for both the horizontal and vertical advection in the transport and diffusion equation for scalars, with constant diffusivity.

Horizontal advection of momentum is discretized by an upwind scheme and horizontal eddy viscosity is computed by the Smagorinsky's formulation.

For the computation of the vertical viscosities and diffusivities, a k–ε turbulence scheme is used, adapted from the GOTM (General Ocean Turbulence Model) model described in Burchard et al. (1999).

The bottom drag coefficient is computed using a logarithmic formulation via bottom roughness length, set homogeneous over the whole system to a value of 0.01 m (Ferrarin et al., 2017).

4.2.3. Bathymetry and grid generation

In REST-COAST a specific and hyper-resolution configuration for the Venice lagoon has been developed. The system covers the entire lagoon and a portion of open-sea shallow water of the Northwestern Adriatic Sea (Figure 4.1). The horizontal resolution ranges from 1 km at open-sea to 50 m in the coastal waters to 10-30 m in the lagoon. Figure 4.1 shows the grid and bathymetry. A single open boundary is created connecting the Po River delta and Lido di Jesolo (see Figure 4.1). The horizontal grid has been created adopting advanced and customized tools (mainly python-based) of meshing based on GMSH (http://gmsh.info/) and BLENDER (https://www.blender.org/) software.

The bathymetry of the gulf was derived from the EMODnet (https://www.emodnet-bathymetry.eu/) product at a resolution of 1/8 x 1/8 arcminutes (approx. 230 x 230 meter), resolution for open sea and coastal waters and integrated with higher-resolution bathymetry (resolutions of order of half meter) for lagoon, inlets, and near-inlet coastal areas (Provveditorato Interregionale per le Opere Pubbliche per il Veneto, Trentino Alto Adige e Friuli Venezia Giulia).

WW3 and SHYFEM share the same unstructured meshes.

.

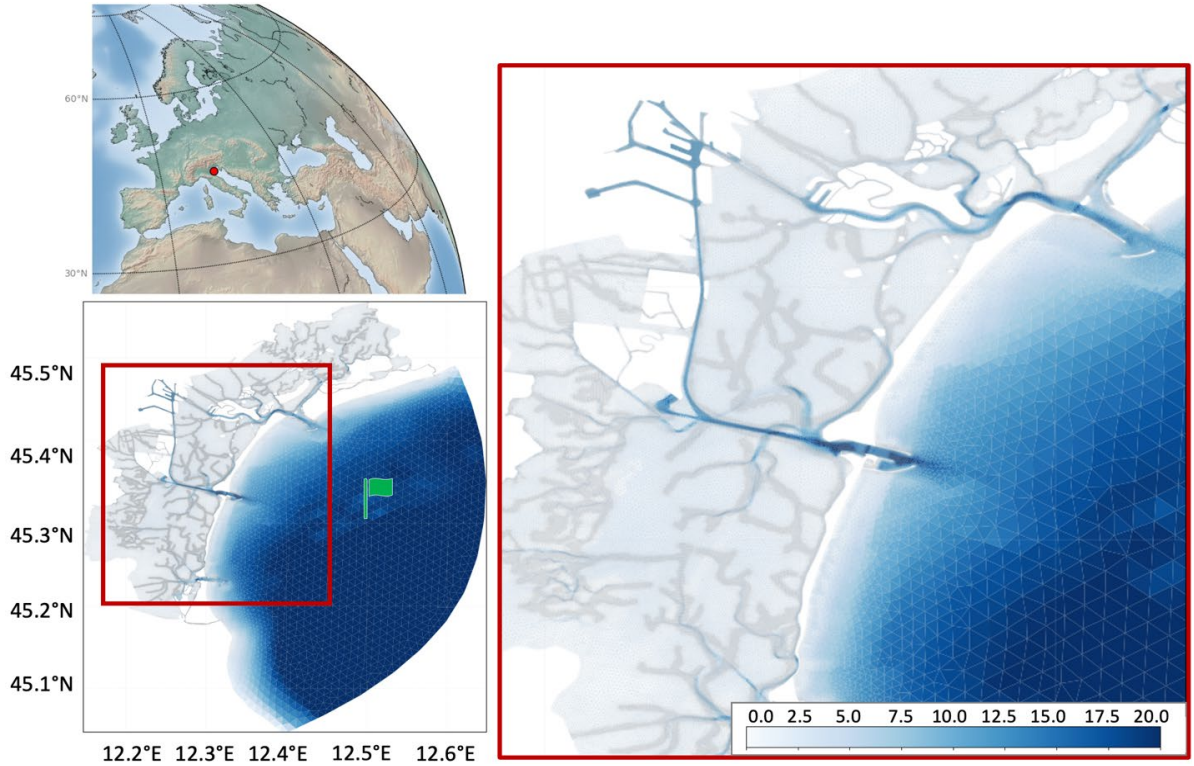

Figure 4.1.Numerical grid and bathymetry [m] for REST-COAST Venice pilot (left panel), and magnification (right panel). Green flag shows the CNR "Acqua alta" platform location.

4.2.4. Inclusion of vegetation in the wave model

To account for vegetation-induced dissipation, we modify the SHOWEX bottom friction equation by incorporating the wave damping due to vegetation (Sds,veg; Dalrymple et al., 1984; Mendez and Losada, 2004) as indicated below;

$$S_{ds,veg} = -\sqrt{\frac{2}{\pi}}\; g^2 \widetilde{C_D}\; b_v\, N_v \left(\frac{\tilde{k}}{\tilde{\sigma}}\right)^3 \frac{sinh^3 \tilde{k}\alpha h \;+\; 3\, sinh\, \tilde{k}\alpha h}{3k\; cosh^3 \tilde{k}h} \sqrt{E_{tot}}\, E(\sigma,\theta) \tag{4.1}$$

where $\widetilde{C_D}$ is the bulk drag coefficient that may depend on the wave height, bv is the plant stem diameter, Nv is the number of plants per square meter, αh is the vegetation height, h is the water depth, $\tilde{k}$ is the mean wave number, $\tilde{\sigma}$ is the mean frequency, E_{tot} is the total wave energy, and E(σ, θ) is the wave variance spectrum.

Afterwards, the total bottom friction (*St*) is redefined by adding SHOWEX bottom friction (*Sbot*), with the *Sds,veg*.

$$S_t = S_{bot} + Maskveg \times S_{ds,veg} \tag{4.2}$$

where *Maskveg* is the mask file which specifies the location of the vegetation.

4.2.5.Inclusion of vegetation in the circulation model

In SHYFEM, seagrass was implemented in the governing equations following an approach similar to the one described in Beudin et al. (2017), and Zhang et al. (2019). The seagrass form drag was written as:

$$F_{veg,x} = \frac{1}{2} C_{Dv} D_v N_v \left|\vec{u}\right| u$$

$$F_{veg,y} = \frac{1}{2} C_{Dv} D_v N_v \left|\vec{u}\right| v \qquad \text{(4.3) and (4.4)}$$

where C_{Dv} is a plant drag coefficient, with values that can vary from close to zero to 3 (Nepf and Vivoni, 2000; Tanino and Nepf, 2008), D_v is the stem diameter, N_v is the vegetation density (number of stems per m^2), u and v are the zonal and meridional components of the velocity, respectively, and $\vec{u}$ is the velocity vector.

4.3. Parameterization of hydro-morpho-eco interactions to simulate ESS.

The Venice pilot of REST-COAST project implements two morpho-ecological structures in the numerical models:

- Wetlands;
- Seagrasses.

In our numerical implementation, wetlands are considered as small islets. A wave approaching the coast (in general) and thus an islet, is affected by several processes such as shoaling, refraction, dissipation of wave energy by depth-induced breaking and reflection at the coast. The spatial distribution of the wetlands has been defined according to the shapefiles obtained from the the open source Atlante della laguna (https://www.atlantedellalaguna.it) and commissioned by the Venice Water Authorities.

In the REST-COAST Venice wave model implementation, we considered a mono-species distribution of the most common angiosperm for the Venice lagoon, *Zoostera marina.* The related vegetation parameters (Table 4.1) have been set following Mazzella et al. (1998).

Figure 4.2 shows the spatial map of both the structures in the lagoon, and highlights that the Northern lagoon is the poorest in vegetation and wetlands presence, on the contrary, Southern lagoon has a large presence of vegetation and several wetlands.

Table 4.1: Seagrass parametrization included in the wave model, from Mazzella et al. (1998).

Wave Model parameters				
Seagrass Type	**Seagrass distribution**	**Stem diameter of plant (Bv in m)**	**No. of plants per square meter (Nv)**	**Length of seagrass (Lv in m)**
Zostera marina	**According to open source Atlante della laguna**	0.0032	270	0.213

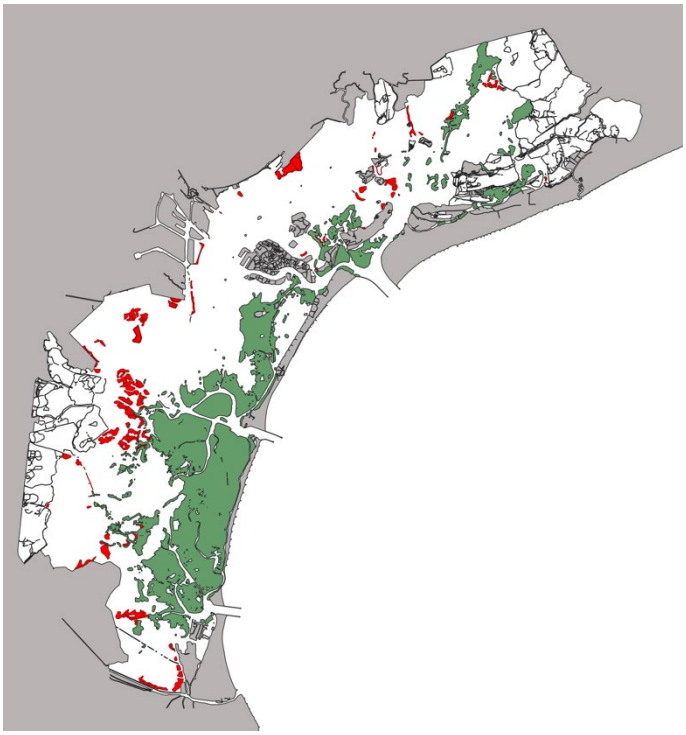

Figure 4.2. Morpho-ecological structures adopted for the Venice lagoon: in red wetlands, while in green seagrass are highlighted.

4.4. Target operational period for testing the EWS nested into CMEMS products

Calibration and validation of the wave model was carried out according to the availability of data from the CNR "Acqua alta" platform (http://www.ismar.cnr.it/infrastrutture/piattaforma-acqua-alta). Installed in March 1970 about 8 miles off the coast of Venice, on a water depth about 16 m (GPS 45° 19' N, 012° 30' E), the Acqua Alta Oceanographic Platform is one of the main research infrastructures managed by the National Research Council. It consists of a laboratory module, as well as sophisticated distribution systems for management and data transfer in real time from numerous measuring stations and sensors such as: sea level, sea state, sea currents, salinity, temperature, oxygen and nutrients.

Particular attention has been paid to represent extreme events such as storm surges and waves. The simulation used for validation has been carried out using the same infrastructure developed for the operational system that supports the EWS. For this phase, the system was run in hindcast mode, meaning the same modelling framework was applied to past periods for which observational data is available for validation.

The WW3 model for the REST-COAST Venice pilot has simulated 3 years (2020-2022), and Figure 4.3 shows the averaged Significant Wave Height (SWH) for the lagoon. Northern lagoon represents the calmest area of the domain, with an average SWH approximately of 4 cm maximum. Central and Southern lagoons showed higher SWH on average, reaching 10 cm maximum close to the Malamocco channel. In all the three mouths, the wave height is higher than 10 cm on average, because of the swell approaching the lagoon from the Adriatic Sea; however, due to shallow depths, waves are promptly dissipated.

Due to the lack of observational data, the model accuracy could be assessed only for 10 months, from March to December 2022. Figure 4.4 compares the time series of hourly values from model (in black) and observation (in red), at the "Acqua Alta platform" location. The WW3 implementation can reproduce wave statistics with high confidence, well describing the wave pattern. On average, the model has a slight general tendency to underestimate the measurements, both during calm and rough conditions. Table 4.2 shows the

validation statistics for the available time. The qualitative underestimation highlighted by the time series is quantified by a negative bias of ~12 cm. A high correlation is shown, with a Pearson correlation of 0.93 and a RMSE of approximatey 20 cm.

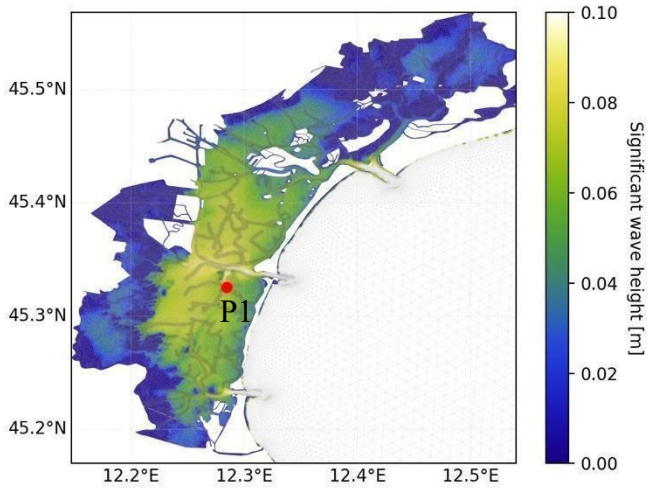

Figure 4.3. Three-years averaged significant wave height for the Venice lagoon. Red dot (P1) indicates the location selected for the time series comparison.

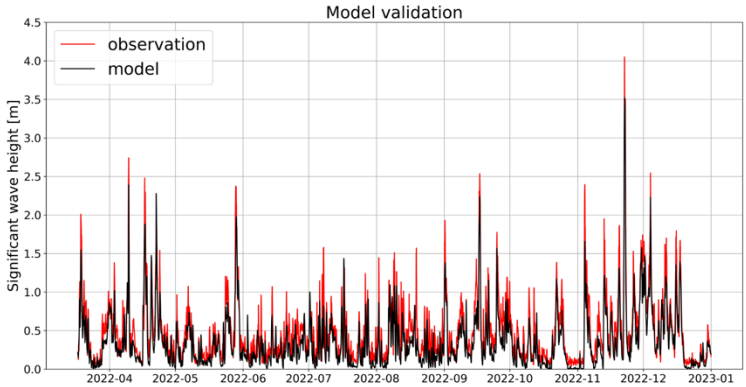

Figure 4.4. Timeseries plot of significant wave height (m) from model, in black, and CNR "Acqua alta platform", in red.

Table 4.2: Skill scores for the wave model

Statistics	Score
Bias [m]	-0.124
RMSE [m]	0.198
Pearson correlation	0.93

4.5. Hazard reduction from ESS as a function of restoration scale.

In this section the ESS provided by the inclusion of wetlands and seagrass in the modelling framework was investigated. The ESS has been quantified comparing the simulation (named ESS-run) with a reference run showing the same configuration but with the exception of seagrass and wetlands. In particular, the seagrass and wetlands, i.e., the NBS, have been altered to explore the influence on the ESS they provide. The skills assessment has been carried out for an extreme event that occurred in 2022. Both the runs were also compared over a one-year period at point P1 (Figure 4.3), with coordinates 45.35 °N, 12.27 °E. This position has been selected because it is located in one of the roughest areas of the lagoon, and it lays on the seagrass pattern.

As anticipated in the previous section, the average SWH in the Central lagoon is approximately 10 cm. This value has been confirmed by observing the SWH timeseries in Figure 4.4; however the hourly plot helped in the assessment of the extremes during the 2022. At P1, SWH rarely exceeded 0.6 m, while 0.5 m occurred in all the seasons, except for Summer. As a general rule, the SWH has fast fluctuations, with higher values reaching for a few hours and rapidly dropping. Only during Autumn and Winter did longer storms occurr.

The difference between the reference run and the ESS-run is reported by the red line in Figure 4.5. In few cases SWH is higher in ESS-run than the reference, this is probably related to the direction of the wave approaching the point which begin to shoal before breaking. In almost all the cases ESS-run has lower SWH than the reference, from approximately 1 to 9 cm maximum. The highest dissipation we observed was on 11th November with a reference wave of 62 cm and 53 cm in the ESS-run (~17%).

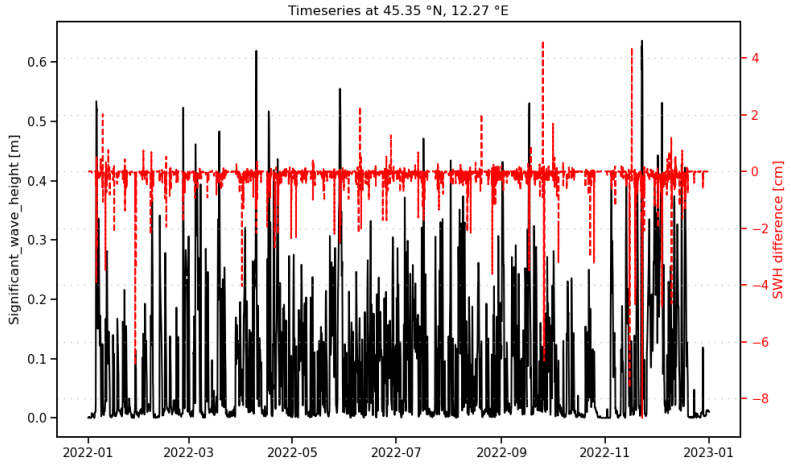

Figure 4.5. Significant wave height at P1 for the 2022 for the reference run (in black). Red line indicates the difference between reference run and simulation including ESS.

The SWH spatial map (Figure 4.6) of the storm event showed that the highest waves are located at the lagoon mouths because of the swell from the Adriatic Sea, and along the largest channels because of the deeper water. However, SWH rarely exceeds 0.6 m inside del lagoon, and the roughest area is represented by the Southern part.

The difference between the reference and the ESS-run is shown in Figure 4.6 and allows to quantify the ESS (dissipation of SWH) due to NBS (seagrass and wetlands). The negative difference indicated lower waves in the ESS-run with respect to the reference, and the spatial pattern fits well the vegetation distribution. This is quite evident in the Southern and Central lagoons where most of the vegetation is located, and waves are higher. Reduced SWH can be found even at the Northernmost part where some wetlands and vegetation are

present. From the difference map we can distinguish 2 patterns, the first related to the vegetation dissipation, with smoothed large patches and reduction of SWH around 2-5 cm, the second one related to wetlands where the SWH reduction is localized, slightly extended down-wave, and exceeding 10 cm in some cases.

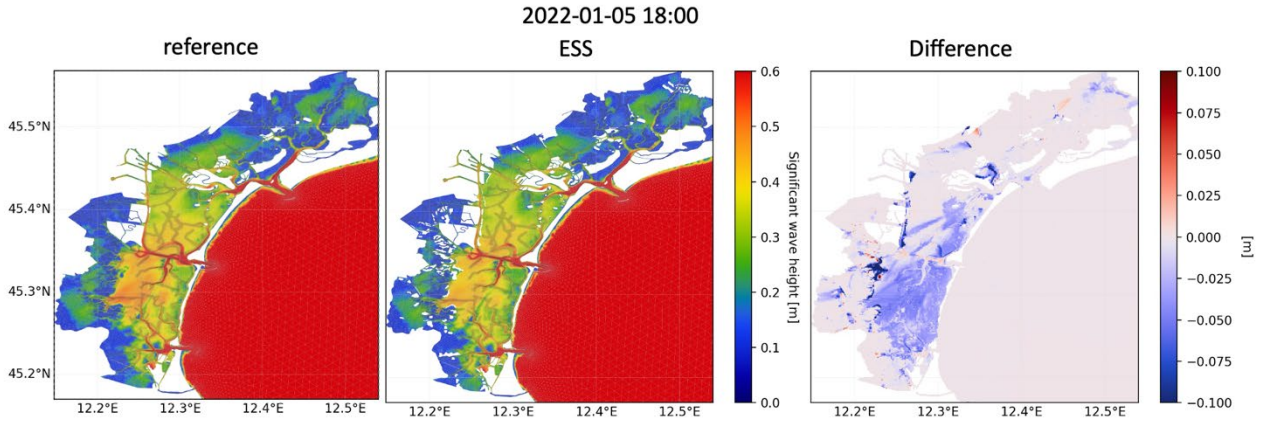

Figure 4.6. Significant wave height (m) during a storm at the Venice lagoon. Left panel shows the reference run (without wetlands and seagrass), middle panel shows the simulation including wetlands and seagrass, right panels show the difference between the simulations.

Hydrodynamics and ESS itself are shown here, considering one of the worst storms that hit the Venice lagoon, in November 2019. In Figure 4.7 a snapshot of the event is presented. The hour was chosen to have the highest water level in the Southern lagoon, where most of the vegetation and wetlands are located. In detail, the Southern lagoon has a sea-level approx. 140-150 cm, which decreased down to 110-120 cm in the Northernmost part. Observing the difference map (Figure 4.7c) almost al the lagoon has a lower sea-level in the ESS-run compared to the reference, with a minimum of approx. -2.5 cm in the Northern part, and a maximum of -6 cm in the Southern one, up to a maximum decrease of -5%. An increase of the water level is evident in the ESS-run along the three lagoon mouths and nearby. We assumed that this pattern could be related to the reduced circulation inside the lagoon of the incoming water, due to the increased bottom stress.

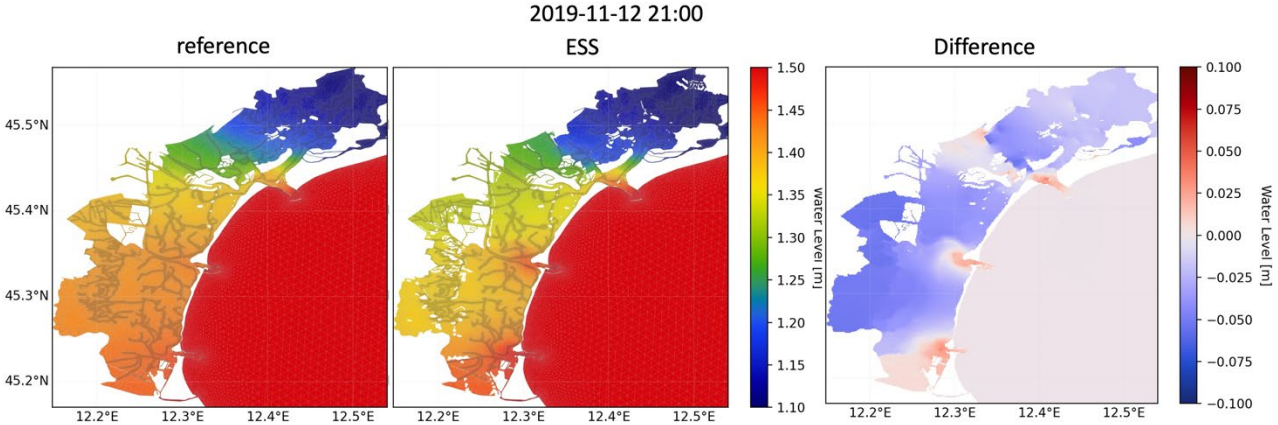

Figure 4.7. Water level (m) during a storm at the Venice lagoon. Left panel shows the reference run (without wetlands and seagrass), middle panel shows the simulation including wetlands and seagrass, right panels show the difference between the simulations.

In Figure 4.8 we report the time series of sea level for the reference and ESS-run configurations at point P1. For the entire period (and simulation), the ESS-run exhibited a smaller amplitude than the reference run, revealing that seagrass and wetland presence mitigate both high and low extremes. On average, the difference between the two runs has been quantified as approx. 2 cm, while the maximum difference was 9 cm.

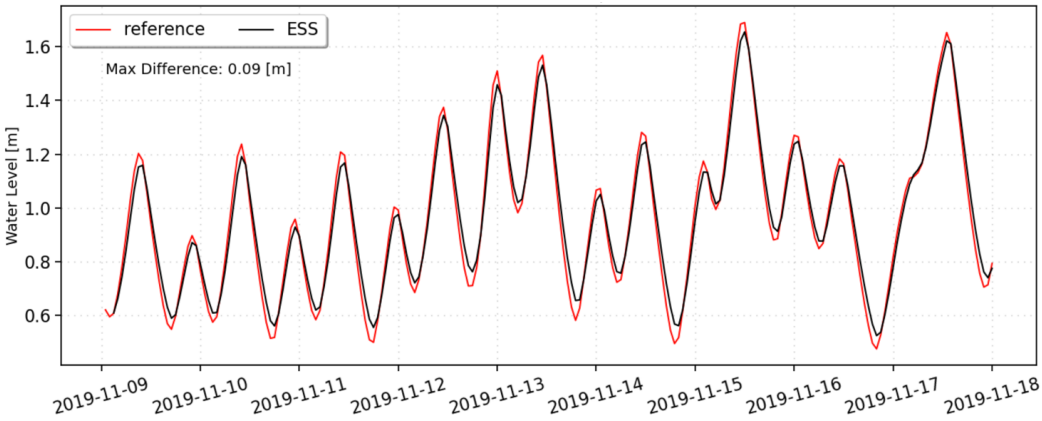

Figure 4.8. Water level (m) time series during the extreme event of November 2019 at P1 showed in Figure 4.3. Red line refers to the reference run (no seagrass, no wetlands), black line shows the ESS-run (inclusion of seagrass and wetlands).

The presence of wetlands and vegetation has a significant impact on the bottom stress, thus on erosion and deposition processes. For this reason, Figure 4.9 shows the spatial maps of bottom velocity for the reference and ESS-run simulations. All over the lagoon, excluding deeper channels, bottom velocity reached 20 cm/s maximum. The reduction of velocity in the ESS-run well reproduced the spatial distribution of the seagrass throughout the lagoon, although, due to the larger spatial vegetation covering is more evident in the Southern and Central lagoons.

The increase of bottom velocity, in some areas, related to the presence of wetlands and vegetated bottom is also appreciable. It is evident that wetlands reduce the section through which water flows, increasing the velocity, as shown at North of the Murano Island in the ESS-run. In addition to this, bottom velocity is also increased along the deeper unvegetated channels, more evident in the Southern lagoon, where water flows through lower resistance.

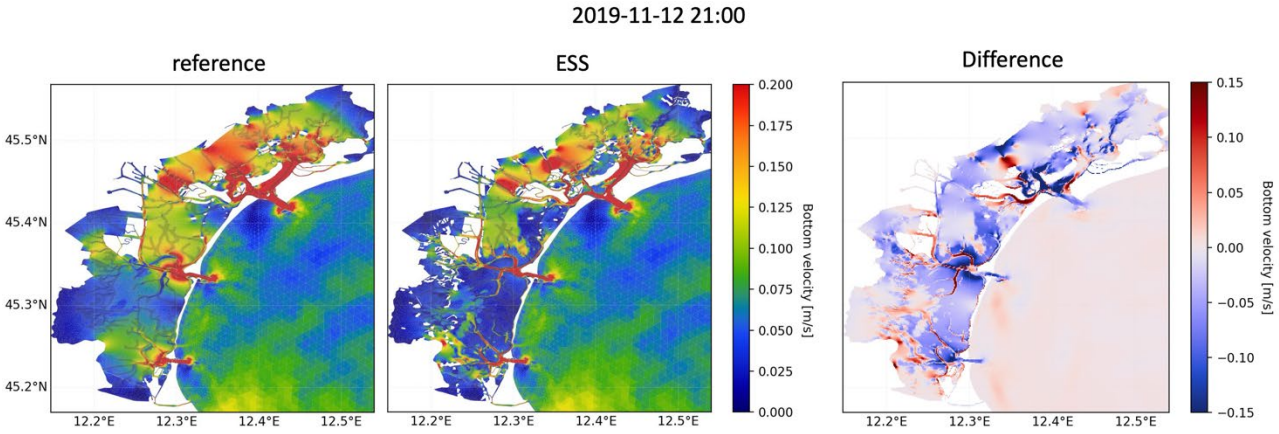

Figure 4.9. Water velocity at bottom (m/s) during a storm at the Venice lagoon. Left panel shows the reference run (without wetlands and seagrass), middle panel shows the simulation including wetlands and seagrass, right panels show the difference between the simulations.

4.6. Conclusions

In Task 2.1, CMCC developed an operational forecasting circulation-wave modelling system to serve as EWS in the Venice lagoon. The validation of the numerical results has been carried out simulating near past conditions at the Venice lagoon. The models have been validated using data from the CNR “Acqua alta platform”, providing high accuracy and precision.

The hincast was also used to assess ESS related to coastal protection, specifically the attenuation of wave and currents provided by NBS such as seagrass and wetlands in the pilot area. Two configurations have been implemented: with wetlands and seagrasses, and without them. The comparison between the different configurations allowed to appreciate and quantify the ecosystem services due to the inclusion of wetlands and seagrass in the lagoon. Their role has been assessed both for hydrodynamics, through water level and water velocity at bottom, and waves through the significant wave height.

In detail, the comparisons carried out highlighted the following ESS:

- a reduction of wave height due to the presence of seagrass (on average -15%, in some cases above 30%) and, as expected, on a greater extent, wetlands;
- a reduction of water level (up to 5%) in the vegetated zones;
- a general reduction of water velocity at the bottom in the vegetated zones.

The work also identified a side-effect given by the inclusion of wetlands and vegetation in the lagoon which could be considered during planning of restoration activities. In particular, the increased bottom friction brought in some cases to the increasing water level along the main mouths during the flooding phase. Even currents at the bottom showed an increase along the unvegetated deeper channels and where the wetlands presence reduced the section through which water flows.

5. Multi-hazard forecasting (including a multidisciplinary calibration) and application limits Rhone Delta Pilot (TDV)

5.1. Introduction

The Rhone Delta Pilot, namely the "Former Saltworks", located in the south-eastern part of the Rhone delta (Figure 5.1), is an area of 6,527 ha which was acquired by the Conservatoire du Littoral (French "Coastal Protection Agency") between 2008 and 2012. For about 50 years, and until its sale in 2008 for industrial and economic reasons, this site was devoted to industrial salt production. The acquisition of this site by the Conservatoire du Littoral involved changes in management, compared to that implemented in an industrial salt production model. Water management by means of hydraulic pumps, as well as continuous maintenance of the dikes of the former salt production site in the context of sea level rise, was no longer economically sustainable without the financial benefits of salt production. In addition, with the existing dikes of the former salt production site, and without the use of hydraulic pumps to generate water flows, the Former Saltworks site would have been with no change in management a very confined site with long residence times. Due to the high evaporation rates in Mediterranean areas, this site would have been exposed to very high salinity and water absence for several months of the year, which would have been problematic for several plant species, birds and fish. In addition, the reconnections with the sea allow new biological connections on this site.

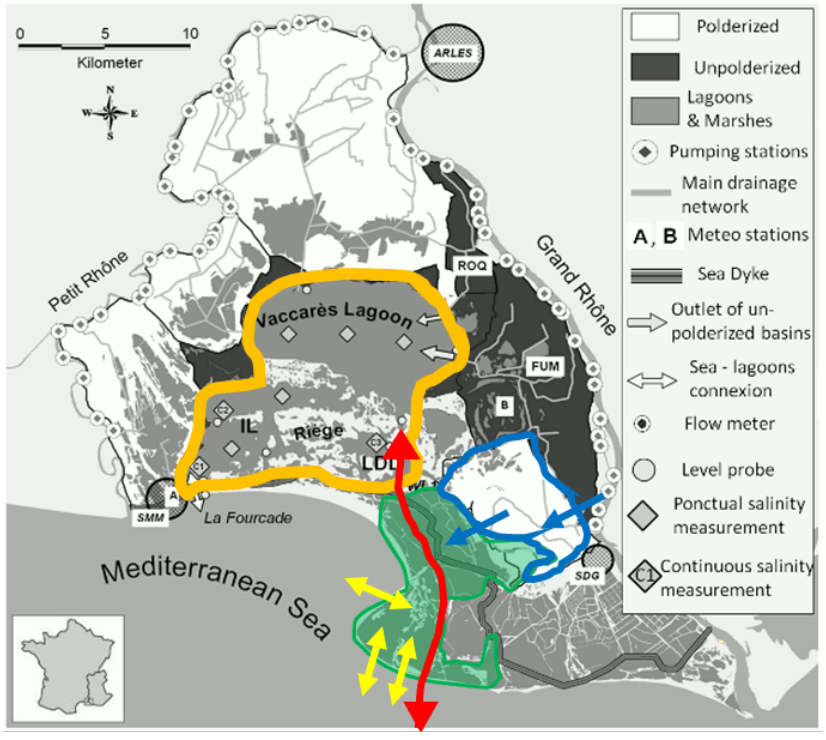

Figure 5.1. Location of the Fellow Pilot in the Rhone delta (in green). Also shown in blue is the agricultural catchment area reconnected to the Pilot Site, and in orange the central lagoons of the Rhone delta, which can be connected to the Pilot Site via a hydraulic structure. The new connections between the Pilot Site and the sea resulting from the choice to no longer maintain the historic dykes are indicated in simplified form by yellow arrows. The red arrow indicates the path of the main flows targeted by the restoration of the site.

It was therefore decided since 2010 to implement a realignment strategy on the site, by re-establishing gravity flows and no longer depending on pumping stations:

- The sea-dikes protection of the former salt production site are no longer maintained, and the protection effort is now focused on a maintained dike which is located about 7 km inland, resulting in a new 4600 ha “Climate change buffer area” between the former and the inland dikes.
- Several works have been carried out (opening of dikes, dredging works, etc.) to create connections between the various former salt production basins.
- Hydraulic works have reconnected the site to a nearby agricultural catchment, itself irrigated from the Rhone river, allowing new fresh water flows in the site.
- A new hydraulic structure was created to have the possibility to hydraulically connect the site to the central lagoons of the Rhone delta, namely the Vaccares Lagoon Hydrosystem, thus creating a reconnected whole of over 16,000 hectares.

Within REST-COAST, restoration projetc for this site is pursued through a Nature based solutions (NBS) implementation, with the following two types of measures:

- passive restoration, with the continued non-maintenance of the sea-dikes protection of the former salt production site and restablishment of natural coastal dynamic.

- active restoration, which consists in accompanying the site managers in the implementation of a management of the remaining hydraulic works of the site which i) favours at the same time the biodiversity, the restoration of the habitats, the 5 Ecosystem Services (ESS) considered in REST-COAST and the economic activities and ii) that adapts to the effects of the non-maintenance of the sea-dikes protection (e.g. continuous modification of hydro-saline exchanges with the sea with the non-maintenance of the former sea-dikes protection) and iii) that anticipates the effects of climate change.

The habitats targeted in REST-COAST for the Rhone Delta Fellow Pilot are: Coastal lagoons (N 1150); Beach areas (N 1140); Mediterranean and thermo-Atlantic halophilous scrubs (N 1420); Salicornia and other annuals colonising mud and sand (N 1310), and the associated plant species.

5.2. High-resolution coupled coastal models

In WP2, several models are developed for the Rhone Delta Fellow Pilot, in particular to study the consequences of restoration and NBS implementation on ESS “Water quality purification” (through hydro-saline regulation), “Reduction of coastal flooding risk” and “Reduction of coastal erosion risk” (through hydro regultation and restoration of natural coastal processes). Furthermore, the results of these models will be used, in combination with data acquired in WP1 on Green House Gases (GHG) emission and sequestration, and historical data on fish populations, to study the consequences of the restoration on ESS “Climate change regulation”, and “Food (fish) provisioning”.

The models developed consist of three TELEMAC-2D hydro-saline models, one XBEACH morphodynamic model, and one model of the evolution of the coastline using DSAS.

5.2.1. Hydro-saline models

The three hydro-saline models used in REST-COAST for the Rhone Delta are implemented with the two-dimensional hydrodynamics code TELEMAC-2D.

Two models are specific to the Rhone Delta Fellow Pilot. Their objective is to show the influence of the restoration implemented on the hydro-saline dynamics of the site, with a particular focus on the ESS "Water quality purification" and "Reduction of coastal flooding risk". The first model simulates the hydro-saline dynamics of the site that would have occurred without the implementation of restoration and NBS. The second model simulates the hydro-saline dynamics of the site following restoration and NBS implementation. These two models use the same mesh, but with different topo-bathymetric data. An example of the interpolated topo-bathymetry for the pre-restoration site is shown in Figure 5.2.

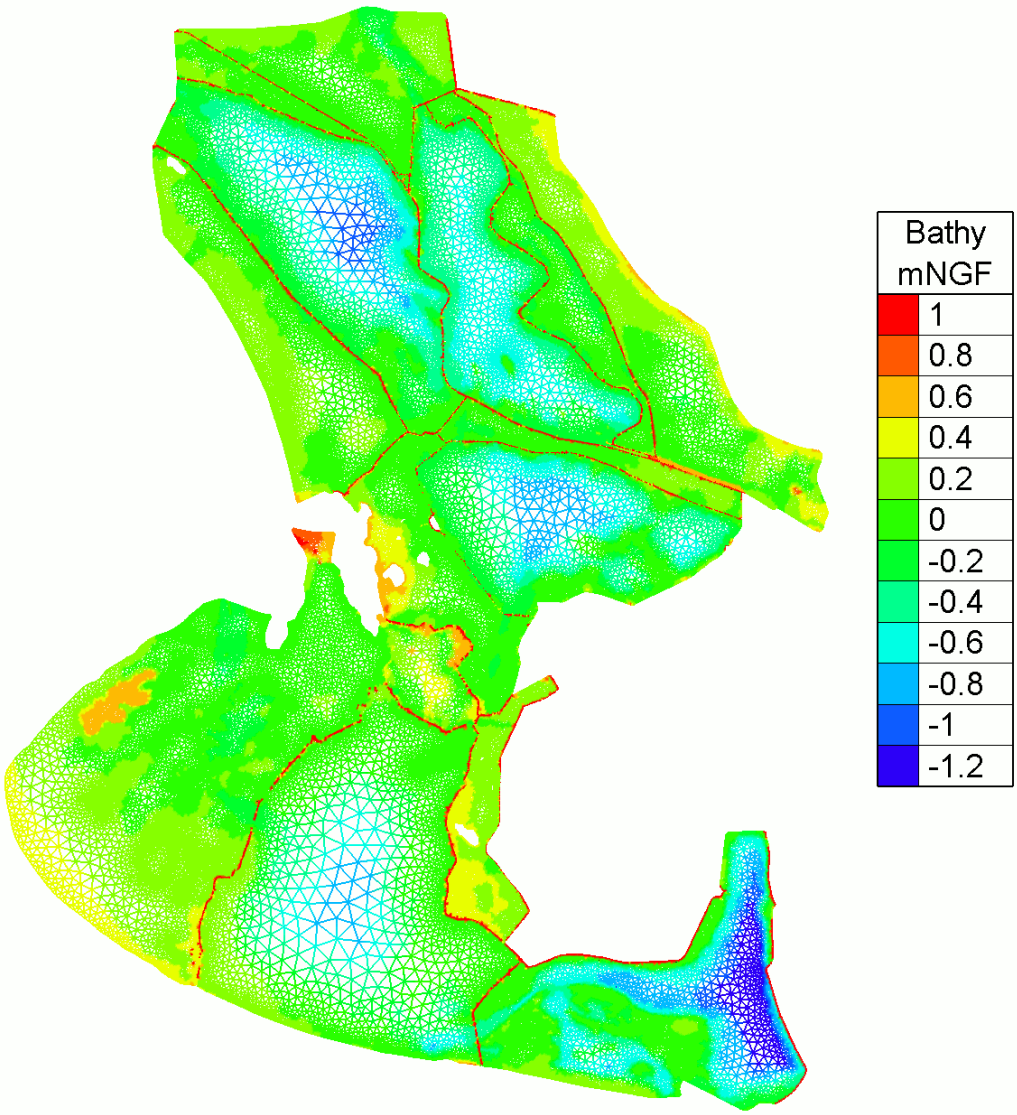

Figure 5.2. TELEMAC-2D mesh of the Rhone Delta Fellow Pilot, and interpolated topo-bathymetry for the configuration without restoration.

The third model (Figure 5.3) aims to study the influence of the restoration of the pilot site on the surrounding ecosystems, in the upscaling stage studied in REST-COAST. This model encompasses the Pilot site, and the

system of lagoons located in the centre of the Rhône delta and the National Reserve of Camargue, in orange in Figure 5.1.

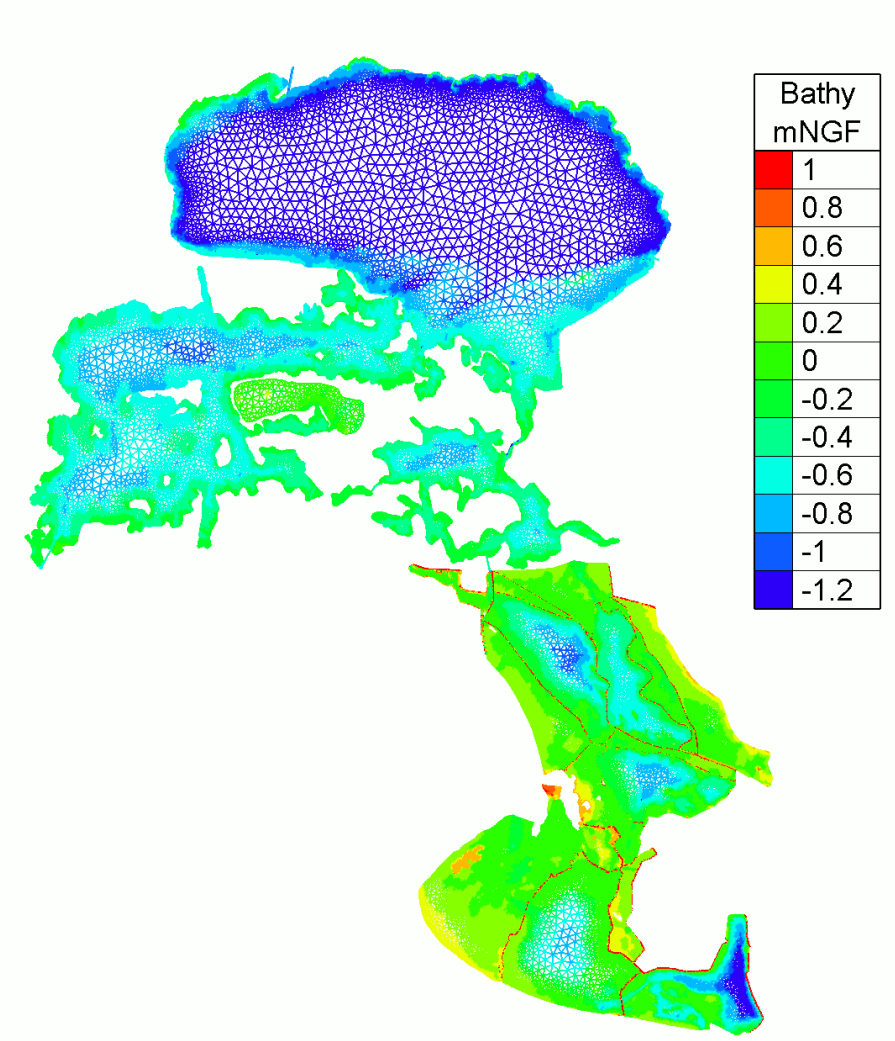

Figure 5.3. TELEMAC-2D mesh and interpolated topo-bathymetry of the Rhone Delta Fellow Pilot and the main lagoons of the central part of the Rhone Delta.

For the three models, we use the hydrodynamic model TELEMAC-2D to simulate the hydrodynamics, water temperature and salinity dynamics. The choice of using a two-dimensional model is justified by the very shallow depths of the systems studied, the absence of water over a large part of the site for a good part of the year, and measurements of salinity and temperature carried out vertically at several points of the site, showing no notable difference in these two variables.

The TELEMAC-2D software solves the second-order partial differential equations for depth-averaged fluid flow derived from the full three-dimensional turbulent Navier-Stokes equations (Hervouet, 2007, 2000). This provides a system consisting in an equation for mass continuity and two force-momentum equations. The equations are averaged over the vertical by integrating from the bottom to the water surface by considering the assumption of the Shallow Water equations (hydrostatic pressure and vertical velocity negligible).

The averaged form of the continuity equation is:

$$\frac{\partial h}{\partial t} + \vec{u}.\vec{\nabla}(h) + h.div(\vec{u}) = S_h \qquad (5.1)$$

The averaged form of the momentum equations are:

$$\frac{\partial u}{\partial t}+\vec{u}.\vec{\nabla}(u)=-g\frac{\partial Z}{\partial x}+S_x+\frac{1}{h}div\left(h\nu_t\vec{\nabla}u\right) \quad (5.2)$$

$$\frac{\partial v}{\partial t}+\vec{u}.\vec{\nabla}(v)=-g\frac{\partial Z}{\partial y}+S_y+\frac{1}{h}div\left(h\nu_t\vec{\nabla}v\right) \quad (5.3)$$

with u and v the depth-averaged velocity components (m.s-1) in the x and y Cartesian directions, h the water depth (m), S_h the point injection or removal of fluid (m.s-1), ν_t the coefficient of turbulent momentum diffusion (m2.s-1), g the gravitational acceleration (m.s-2), t the time (s), Z the free surface elevation (m), S_x and S_y (m.s-2) the source terms of the momentum equation in u and v, respectively, including the Coriolis force, bottom friction, surface wind shear and source/sink of momentum in the domain.

Salinity and temperature are modeled as tracers, with equation 5.4:

$$\frac{\partial T}{\partial t}+\vec{u}.\vec{\nabla}(T)=S_T+\frac{1}{h}div\left(h\nu_T\vec{\nabla}T\right) \quad (5.4)$$

where T is the tracer (in this study the salinity or temperature in psu and °C, respectively), ν_T the tracer diffusion coefficient (m2.s-1), and S_T the source or sink of tracer (psu.s-1 or °C.s-1). The influences of rain, evaporation and wind are taken into account in the model.

Equations 5.1 to 5.4 are solved using a finite element method on an unstructured mesh, made with more than 107,190 triangular elements of varying size and 55,081 nodes for the Rhone Delta Fellow Pilot (Figure 5.2), and 160,000 elements and 85,500 nodes for the model encompassing the lagoon in the central part of the Rhone delta. The advection of h (equation 1) is solved applying the conservative PSI (Positive Streamwise Invariant) scheme (Hervouet, 2007). The advections of u and v (equations 2 and 3) are solved applying a PSI distributive scheme with a locally implicit predictor-corrector and a full implicitation only in the dry zones (Hervouet et al., 2015). To solve the advections of T (salinity or temperature) we use the N distributive scheme with a locally implicit predictor-corrector and a full implicitation only in the dry zones (Hervouet et al., 2015). These numerical schemes, although time consuming, have the advantage of greatly limiting the numerical diffusion in the presence of dry zones, which can be temporarily covered by water.

For the temperature of water, the term S_T in equation 4 is the heat source $Q/\rho_w c_w h$, with Q the heat flux (W.m-2) between the atmosphere and the water, ρ_w is the water density, and c_w the specific heat of water. Q is computed by the following thermal radiative model (Ata, 2017):

$$Q=RS-RE-CV-CE+RA \quad (5.5)$$

with RS the sunray flux, RE the free surface radiation, CV the advection heat flux, CE the evaporation heat flux and RA the atmospheric radiation.

5.2.2. Morphological models

To study the morphodynamics of the site in relation to restoration, two types of modelling are used. The first, applied to the entire pilot site, is based on the use of the USGS DSAS tool. A study of the dynamics of shoreline change has been carried out from 1936 (date of the first usable data) to 2020 (Figure 5.4). Over this period, the results generally indicate a zone of accretion to the west of the site, and a zone of erosion to the south (Figure 5.4). Following this initial analysis with the available data, we will study the consequences of the passive restoration strategy implemented on the site by comparing, with DSAS, the dynamics of change before and after 2008, the date on which maintenance of the dikes in the south of the site stopped.

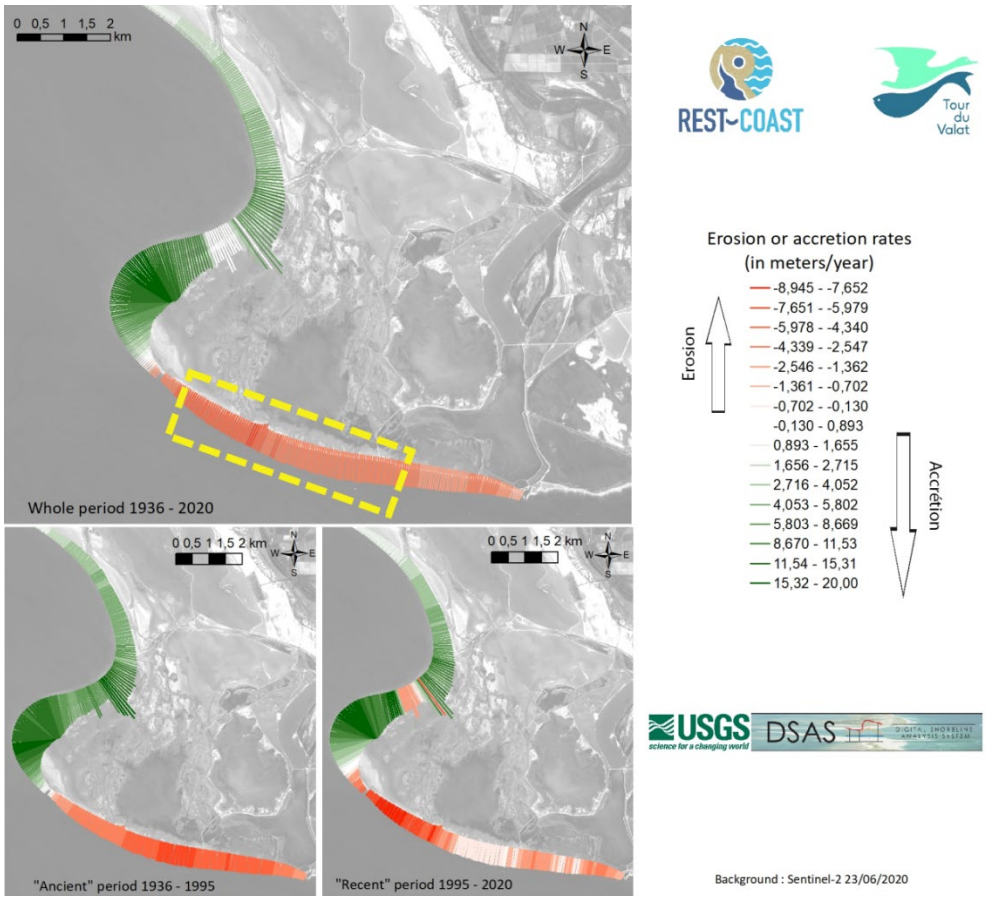

Figure 5.4. Results of DSAS: dynamics of the shoreline for several periods.

In addition to this analysis of the entire site, specific modelling using XBeach and TOMAWAC was carried out on one of the site's erosion zones, indicated by the yellow dotted lines in Figure 5.4, where a beach area was reconstituted to the north of the unmaintained dykes by overwash phenomena, and several new connections with the sea were formed during storms (Figure 5.5).

Figure 5.5. Aerial drone views highlighting the geomorphological dynamics observed in the southern part of the Rhone Delta Fellow Pilot with the non-maintenance of sea-dikes protection of the former salt production site. To the left: formation of new connections to the sea. To the right: creation of beaches areas. On both views the sea is on the left and the Fellow Pilot is on the right.

The TOMAWAC numerical model (Benoit et al., 1996) is made up of a triangular mesh (Figure 5.6). The cell sizes range from 500 m offshore to 20 m at the coast. The boundary conditions on the coast correspond to wave absorption conditions. On the other boundaries, Hs, T and directions were prescribed via ERA5 and the flow velocities were left free i.e. calculated by the model. The offshore domain extension corresponds to the location of the ERA5 model grid extraction point. The topo-bathymetry corresponds to a linear interpolation between different data sets (topo-bathymetric LiDAR with the Optech Titan DW600 of Nantes and Rennes French Universities, and bathymetry from the European Marine Observation Data Network, EMODnet).

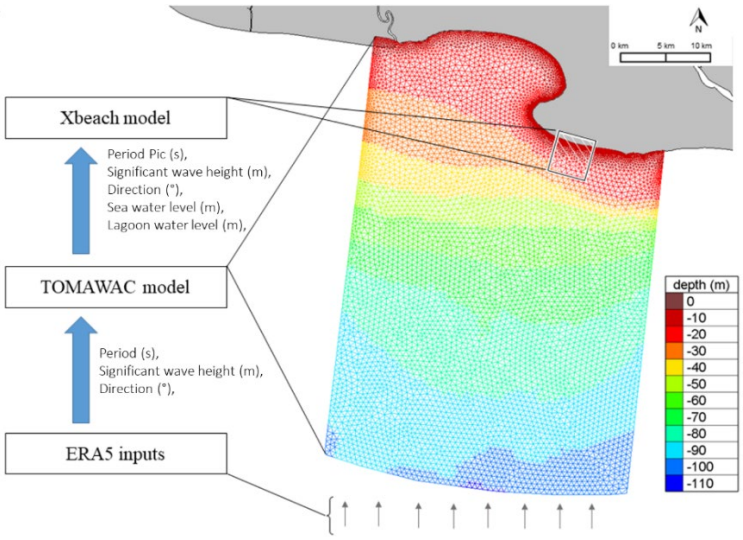

Figure 5.6. XBeach and TOMAWAV models used to investigate the qualitative geomorphological evolution of the southern part of the Former Saltworks during storm events.

The XBeach numerical model (Roelvink et al., 2010) is made up of a regular mesh comprising 280x201 cells of size 20m x 20m (Figures 5.6 and 5.7). The offshore domain extension corresponds to the location depth where the TOMAWAC model was validated. Short waves are generated from the JONSWAP spectrum using the peak wave period, Hs and direction from TOMAWAC model simulations at the boundaries of the Xbeach offshore domain (Figures 5.6). Temporarily varying water levels were applied in the lagoons and in the sea. Water levels in the lagoon and in the sea correspond to the data recording every 5 min from two probes, one being located in the lagoon directly north to the non-maintained dike, and the other (sea level) being located

at la Fourcade, see Figure 5.1. The topo-bathymetry corresponds to a linear interpolation of the same data sets as those used for the TOMAWAC model.

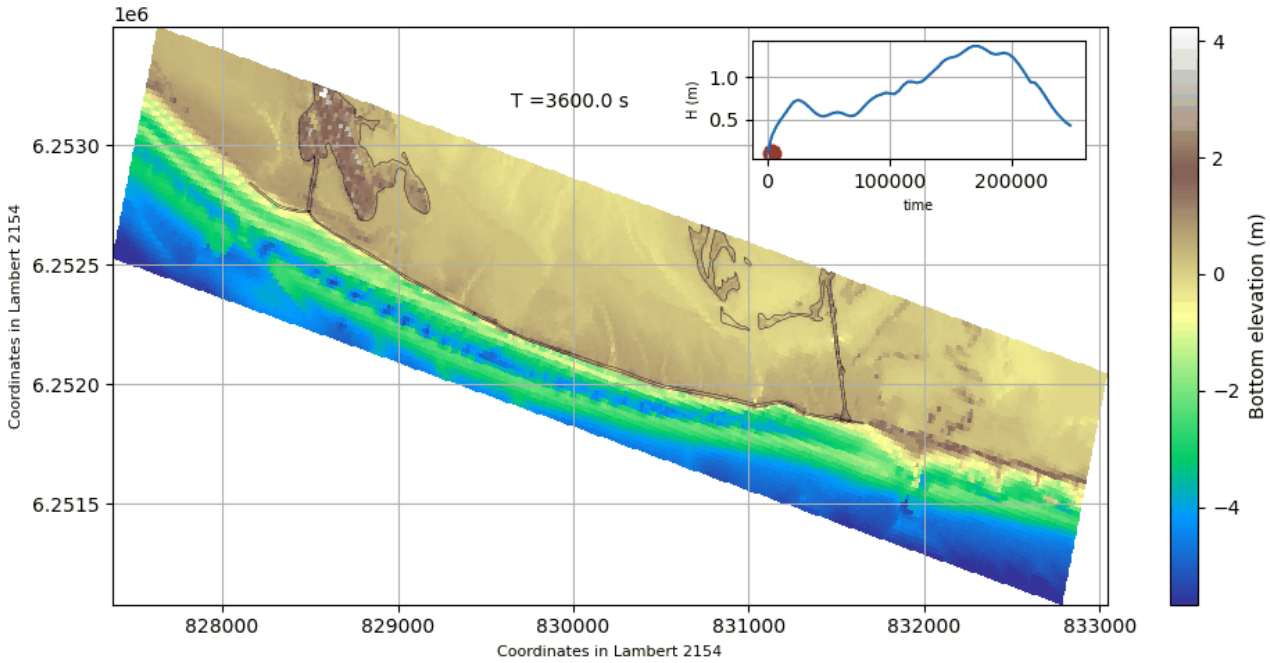

Figure 5.7. XBeach model used to investigate the qualitative geomorphological evolution of the southern part of the Former Saltworks during storm events. The location of the model is shown in Figure 5.6.

5.3. Parameterization of hydro-morpho-eco interactions to simulate ESS.

During REST-COAST, the TOMAWAC and XBeach models did not require any specific developments, but rather classic calibration and validation stages by comparison with existing experimental data or data specifically acquired during REST-COAST.

On the contrary, the TELEMAC-2D models used to estimate the impact of restoration on ESS “Water quality purification” required significant development work. Thus, within REST-COAST, several code modifications had to be made to be able to simulate the hydro-saline dynamics of the Pilot Site, and quantify the benefits of the restoration on ESS “Water quality purification”, through hydro-saline regulation, and through improved water circulation in the site (decrease in residence time).

Due to the high evaporation on the Rhone delta, the overall shallowness of the pilot site, and the limited connection with the sea, a large part of the site is subject to periods of drying, with salt crystallisation/dissolution phenomena, as illustrated in Figure 5.8.

Figure 5.8.Illustration of the potential for prolonged drying out and crystallization of salts on the Rhone Delta Fellow Pilot.

Taking into account these phenomena of crystallisation/dissolution of the salts contained in the water is essential to correctly model the hydro-saline dynamics of this site, and thus study the consequences of the restoration of the site on ESS "Water quality purification".

Furthermore, the predominance of evaporation on the evolution of water levels in these environments makes the methodologies based on concentration evolutions classically used to estimate the residence time of this type of environment not applicable.

Finally, the influence of salinity on evaporation is very often not taken into account in the models classically implemented on such sites.

In view of all these limitations of the current models, we have made the following changes to TELEMAC-2D within REST-COAST:

- Modification n°1: a simplified formalism has been implemented for taking into account crystallisation/dissolution of the salts
- Modification n°2: a new approach has been defined for simulating residence times in these hypersaline and choked wetlands
- Modification n°3: several terms have been added in the equations to take into account influence of salinity on evaporation rates.

To account for the possibility of precipitation and dissolution of salts, a source or sink term S_{salt} has been added to equation 5.4.

The rate of salt crystallization or dissolution S_{salt} is modelled with equation 5.6, as described by (Lionberger et al., 2004; Manganaro and Schwart, 1985):

$$S_{salt} = k_1 A_d \left(c_1 - c_1^* \right) \qquad (5.6)$$

Where k_1 is the average mass-transfer coefficient for salt dissolution (m.s^{-1}), A_d is the wetted area of the considered mesh element (m^2), c_1 is the concentration of salt in solution (kg.m^{-3}), c_1^* is the saturated concentration of salt in solution at the considered temperature (kg.m^{-3}). S_{salt} is expressed in kg.s^{-1}.

The hydro-saline dynamics of the site involve a large number of different salts. Indeed, when the seawater that has entered the site evaporates, it deposits its detrital particles and the ions it contains precipitate in the form of salts. The deposited materials constitute an evaporitic sequence. The order of precipitation of the salts is as follows: first *CaCO3*, then *CaSO4*, then *NaCl*, then *MgSO4* and finally salts of *Br* and *K.*

The phenomena of precipitation and dissolution of all these salts are complex. Their modelling is possible thanks to models such as PHREEQC (Parkhust and Appelo, 2013), but it requires the modelling of all the solid and aqueous phases of these salts, which, in the context of a coupling with a hydrodynamic model such as TELEMAC-2D solving the classical transport equations for each tracer, would lead to computation times that would be prohibitive for an application on a site of the size of the Rhone Delta Fellow Pilot. In the context of REST-COAST, a simplified approach has therefore been adopted, in which c_1 in the equation has been taken to the salinity (kg.m^{-3}). With this assumption, c_1^* in equation is the maximum salinity that can be reached in the system.

Acknowledging that *NaCl* is the major salt in the seawater entering the site, it was considered to be representative of the overall salt dynamics at the Pilot Site regarding the values of solubility, precipitation and dissolution rates, and the dependence of these quantities on temperature. This assumption allows only one tracer to be considered for salt dynamics, making it possible to use hydrodynamic modelling to the site with acceptable calculation times.

To estimate whether there is precipitation of the salts contained in the water column, or dissolution of the salts deposited on the bottom, we then decided to base ourselves on the solubility product of Sodium Chloride in water, equal to 358.5 g.L^{-1} at 20°C. As the solubility of sodium chloride varies little with temperature over the range of temperatures observed at the site (approximately 0 to 40°C), we also assumed that this solubility product was independent of temperature. In equation 5.6, c_1^* is then considered as independent of water temperature and is equal to 358.5 g.L^{-1}.

Increasing water salinity reduces evaporation since the dissolved salt ions lower the free energy of the water molecules, i.e., reduce the water activity, and hence reduce the saturation vapor pressure above the saline water at a given water temperature (Harbeck, 1955; Lee, 1927; Salhotra et al., 1985; Stumm & Morgan, 1981). The reduced latent heat flux of evaporation from saline water increases the surface water temperature, which promotes evaporation, yet, the effect of salinity overcomes the effect of temperature rise and the evaporation is eventually reduced (Salhotra et al., 1985).

Given the very high salinities that can be reached on the Pilot Site, leading to possible salt crystallization, the effect of salinity on evaporation must be taken into account. In our approach, it was decided to calculate in TELEMAC-2D this effect by adding the new equations 5.7 and 5.8 (Kokya and Kokya, 2008; Martínez-Alvarez et al., 2011):

$$e_s^* = \beta . e_s \tag{5.7}$$

$$\beta = 1 - 571.10^{-6} S \tag{5.8}$$

With β the water molar fraction, S the water salinity, e_s^* the the saturated vapour pressure for saltwater, and e_s the saturated vapour pressure above pure liquid water. The salinity-corrected e_s^* is then used in the various terms of equation 5.5.

Within REST-COAST, the benefits of the restoration on ESS “Water quality purification” is also estimated for the Rhone delta through improved induced water circulation in the site, which we study through the notion of residence time.

In lagoons, residence time is classicaly assessed through the mathematical expression given by (Takeoka, 1984a, 1984b), known as the remnant function. The remnant function $r(t)$ of the concentration is given as $r(t) = c(t)/c_0(t)$, where $c(t)$ is the concentration at time t of the passive tracer in the lagoon basin and $c_0 = c(t=0)$ is its initial value. The local residence time $\tau(x,y)$can then be defined for every mesh node (coordinates x,y) as:

$$\tau(x,y) = \int_0^\infty r(x,y,t)dt \qquad (5.9)$$

2D or 3D hydrodynamic models are typically used to estimate local residence times: the tracer is released into the lagoon basin with an initial concentration corresponding to a given value and zero elsewhere, and its evolution is computed for each element of the grid domain, the computation being carried out till the ratio between c(t) and c_0 becames lower than 5% for all the elements of the mesh. The global residence time is defined as the highest value of all the local residence times. However, a major assumption made during these simulations is that the water level in the lagoons does not vary, so c(t) can only decrease over time, as the water in the lagoon is replaced by 'outside' water. This assumption is not applicable to choked sites subject to very high rates of evaporation, which may exceed the site's exchanges with the outside systems. In such sites, such as the Rhone Delta Fellow Pilot, the concentration $c(t)$ may increase over time due to evaporation.

Within REST-COAST, we had to adapt the formalism described above in order to calculate the residence time.

It was therefore decided to calculate for each node the local residence time $\tau_{Evap}(x,y)$ for these highly evaporative systems as follows:

$$\tau_{Evap}(x,y) = \int_0^\infty \frac{M(x,y,t)}{M_0(x,y,t_0)}dt \qquad (5.10)$$

With $M(x,y,t)$ the mass at time t of the passive tracer, and $M_0(x,y,t_0)$ its initial value.

To assess $\tau_{Evap}(x,y)$, we used TELEMAC-2D: a tracer is released into the Pilot Site with an initial concentration of 1kg/m^3 and zero elsewhere, and the evolution of its mass is calculated for each element. The global residence time has been defined as the time required for all the elements of the mesh to replace 95% of the mass of the conservative tracer originally released, with a volume of ”new” water at least equal to the initial one. In other words, calculations are carried out until equations (5.11) and (5.12) have been verified for all the mesh elements of the site:

$$\begin{cases} \dfrac{M(x,y,t)}{M(x,y,t_0)} < 0.05 \\ Vol(x,y,t) \geq Vol(x,y,t_0) \end{cases} \qquad (5.11) \text{ and } (5.12)$$

The global residence time is defined as the highest value of all the local residence times.

All the modifications required to calculate the residence time for these confined sites subject to heavy evaporation have been implemented in TELEMAC-2D for the purposes of REST-COAST.

5.4. Target operational period for testing the EWS nested into CMEMS products

For the Rhone delta, the EWS considered are linked to the risk of very high salinity levels on the site, closely related to the risk of prolonged drying out of the site, as well as to the risk of flooding.

In consultation with local stakeholders, the identified variables on which the EWS is based are:

- for the risks of very high salinity levels and prolonged drying out of the site:
  - for each location of the site, average, minimum or maximum local salinity thresholds during more than YYY days of for specific months
  - range of average water levels in different areas of the pilot for different months
  - drying of specific areas, i.e. nil water depth for more than XXX days.
  - residence times greater than ZZZ days in specific areas

- for the risk of flooding, the considered variables are:
  - water depth during flooding higher than XXX m and lasting more than YYY hrs at the foot of the inland dyke on which the protection effort is now focused
  - loss of xxx ha of beach south of the Fellow Pilot (wave damping)

Regarding the EWS linked to the risk of very high salinity levels and prolonged drying out of the site, the target operational period for testing the EWS must cover a sufficiently long period to have contrasting conditions of precipitation and evaporation, sea levels and flows at the outlets of the agricultural catchment areas connected to the site, over a period when all these data must exist and be usable (i.e. be of sufficient quality). Although flow data at the outlets of agricultural catchments only exist since 2015, when their connection to the Fellow Pilot was created, the period chosen for testing the EWS is 2001-2022, for which several sub-periods will be studied.

Regarding the EWS linked to the risk of flooding, the period chosen for testing the EWS is 1959-2022, for which data of significant wave heights (Hs) and wave periods (T), are available from the ERA5 model at longitude 4.4° and latitude 42.9°, relevant for the Rhone Delta Fellow Pilot.

5.5. Hazard reduction from ESS as a function of restoration scale.

Where the dikes to the south of the site were not maintained, beaches appeared in some areas as a result of overwash, and in other areas new connections with the sea were formed (Figure 5.5). These restored natural coastal dynamics have consequences for the ESS considered in REST-COAST.

To study the hazards reduction from the ESS induced by the implemented restoration, the modelling tools developed to simulate the hydro-saline dynamics of the site before and after the restoration are being used. For each of the ”before/after” restoration configurations, the simulations' results are analyzed regarding the variables identified on which the EWS are based, as described in paragraph 5.4. This enables to quantify the impact of the restoration implemented on these hazards, through the considered ESS “Water quality purification”, “Reduction of coastal flooding risk” and “Reduction of coastal erosion risk”.

Furthermore, the results of these ”before/after” restoration simulations will be used, in combination with data acquired in WP1 on GHG emission and sequestration, and historical data on fish populations, to study the consequences of the restoration on ESS “Climate change regulation”, and “Food (fish) provisioning”.

The effect of restoration scale will also be studied: between the Rhone Delta Fellow Pilot (in green in Figure 5.1) and the central lagoons of the Rhone delta (in orange in Figure 5.1) there is a hydraulic structure that provides a possible connection between the two systems, but which is closed most of the time. The impact that the restoration of the Rhone Delta Fellow Pilot (new connections with the sea) could have on reducing the risk of very high salinity in these central lagoons, if this hydraulic connection was permanent, will be demonstrated using the REST-COAST modelling tools.

5.6. Conclusions

For the Rhone Delta Fellow Pilot, five models are used in the WP2 of REST-COAST. The DSAS tool did not necessitate any particular development or calibration. The XBeach model developed for the southern part of the Pilot Site did not require the development of new functions to study the consequences of restoration on the ESS considered, but it did require calibration and validation stages. The three hydro-saline models developed using TELEMAC-2D required the development of new functions, in particular to study the consequences of the restoration on ESS “Water quality purification”.

In addition to making it possible to study the impact of restoration on ESS “Reduction of coastal erosion risk” and “Reduction of coastal flooding risk”, the DSAS tool and XBeach model will make it possible to provide, in a prospective phase, possible scenarios for the evolution of the site's connections with the sea, which will be used in the hydro-saline modelling under TELEMAC-2D, enabling us to focus on the risk of flooding and the risk of excessive salinity over the whole site.

6. Multi-hazard forecasting (including a multidisciplinary calibration) and application limits Arcachon Bay Pilot (EGIS)

6.1. Introduction

Seagrass beds are present throughout all European coastlines and serve many critical ecological functionalities and ecosystem services (ESS) amongst which: coastal inundation mitigation, erosion control and coastal stabilization, habitats for a high diversity of marine species and support of coastal fisheries, carbon capture and storage. As stated in the latest IPBES report (2019), these key habitats are declining rapidly worldwide including in Europe. Urgent large-scale actions must be undertaken for their preservation and restoration in order to enhance coastal resilience and tackle rapidly declining marine biodiversity. The EU Biodiversity Strategy for 2030 specifically mentions these habitats as crucial carbon-rich ecosystems to protect and the need to anticipate the climatic effects, which will trigger spatial shifts.

Following the REST COAST rationale, Egis contribution is proposed to be on the restoration of the functional coastal dynamics for large-scale Zostera recolonization at Arcachon Bay pilot site. Indeed, Zostera species show the most potential for rapid large-scale restoration given both their ecological traits and the current technology readiness of restoration methods. The specific contribution of Egis to WP2 is the preparation of a risk assessment suite based on a coupled hydro-morpho-eco model. ESS will be expressed as a function of restoration scale and climatic conditions.

6.1.1. Geographical and physical context for the simulation domain

Arcachon Bay is a semi-confined triangular-shaped lagoon, located in the southeast of the Bay of Biscay (the Aquitaine and Landes coast; Figure 6.1). Offshore of the Bay, the narrowness of the shelf and the local topography lead to the generation of very weak barotropic tidal currents as well as weak tidal (Eulerian) residual currents (Lazure and Dumas, 2008). The mixed layer depth ranges typically from 10 to 20 m during spring, when thermal stratifications are more frequent than salinity stratification. Nonetheless, under particular conditions of winds (northwesterly), the Gironde river plume can reach that area (Puillat et al., 2006). Hence, water mass circulation in this area is governed mainly by winds and, secondarily, by density currents (Lazure and Jegou, 1998 ; Puillat et al., 2006 ; Lazure and Dumas, 2008).

The surface of Arcachon Bay is about 174 km2 at high tide, and about 65% of this surface emerges at low tide. The tidal cycle is semi-diurnal with a weak diurnal inequality; tidal amplitude ranges between 0.8 and 4.6 m for neap and spring tides, respectively, whilst the mean depth is 4.6 m. The Bay communicates with the sea through two main mouths, separated by the Arguin Bank. Many little streams run into the lagoon, but the two main rivers, the Eyre and the Porges Canal, contribute for more than 95% (73% and 24%, respectively) of the total annual freshwater inflows (Plus et al., 2009). The mean monthly flows range, respectively, from 8.4 to 38.6 m3 s-1 and from 1.8 to 12.9 m3 s-1 , for the Leyre and the Porges canal, with the maxima occurring in February and the minima in August.

The wind generates wind-waves as the second main hydrodynamic forcing in the Bay after tidal forcing (Parisot et al., 2008). The propagation of offshore waves within the Bay is limited due to the configuration and associated bathymetry at the entrance of the Arcachon Bay. Within the Bay, the main waves are generated by wind-induced processes. This process is nonetheless largely controlled by the tide which influences the water height and the length of the fetch.

Several types of sediments are present within the Bay. On the main entrance and in the channels, mainly medium sand (between 320 and 500 µm) and gravels are found. The secondary channels are mainly

composed of sand and muddy sand (mix between 175 and 365 µm). The intertidal flats correspond to sandy mud ad muddy sands (Cayocca, 1996; Bouchet et al., 1997).

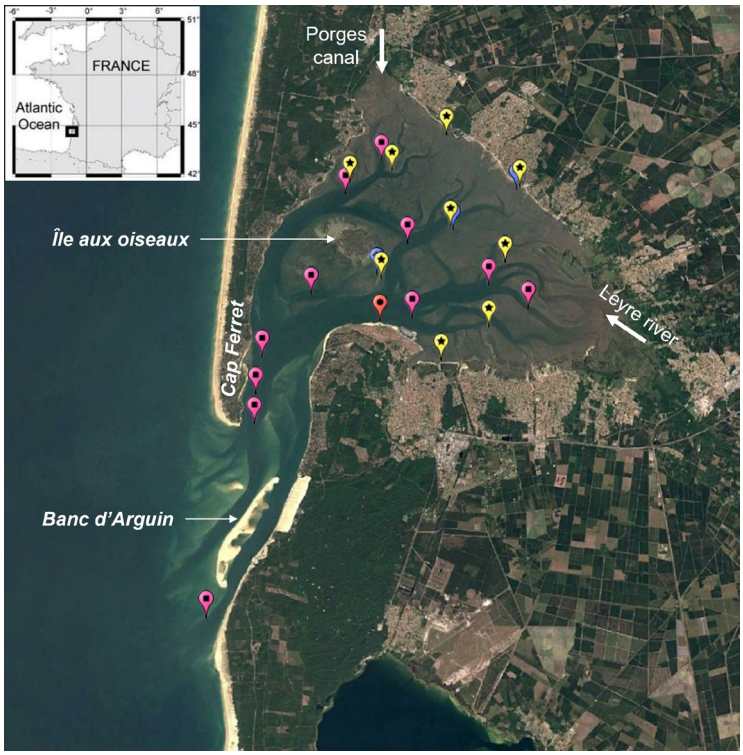

Figure 6.1. Overview of the Arcachon Bay area showing freshwater inputs and locations of the observations sampling stations used for validation. The map shows observation stations for hydrodynamics (yellow), waves parameters (blue) and sediment parameters (pink).

6.1.2. ESS provided by seagrass meadows

Ecosystem services (ESS) are widely used among scientists and policy makers to highlight the importance of the environment (including biodiversity) in sustaining human livelihoods (Convention on Biological Diversity, 2010, 1998; Costanza and Kubiszewski, 2012; Maes et al., 2016; La Notte et al., 2017). An important milestone of ecosystem service research was the Millenium Ecosystem Assessment (MA, 2005) which made prominent the idea that human well-being depends on ecosystems, and that such linkages can be tracked and framed through the notion of ecosystem services. The MA found that more than 60% of ecosystem services is being degraded or transformed endangering future human well-being. ESS research has since progressed at different levels—from theoretical conceptualization to practical applications (see Braat and de Groot, 2012; Egoh et al., 2012; Seppelt et al., 2011; Potschin et al., 2016 for a review).

The Zostera meadows located in the Arcachon Bay also provide ESS. Balle-Beganton et al. (2015) gives an overview of this ESS linked with anthropogenic forcings and activities, including: stabilization of soil in favorizing sediment deposition, improve water clarity, feed fishes and other species, improve biodiversity, stock carbon into sediment, etc.

In the Arcachon Bay, two species of Zostera meadows co-exist: Zostera noltii – mainly located in intertidal parts –, and Zostera marina – located in submerged areas on the edges of the channels –. However, a large regression of these seagrass species has been observed since the beginning of the 21st century, leading to an increase of fine sediment concentration inside the Bay and changing tidal dynamics as well (Cognat, 2019 ;Figure 6.2). The reasons for this regression are not clear but main hypotheses link the regression to climatic events, water pollution and/or the set-up of feedback loops processes (Cognat, 2019). In the Arcachon Bay,

the total surface of Zostera meadows has decreased by 38% and 85% for Z.noltii and Z.marina respectively between 1989 and 2012.

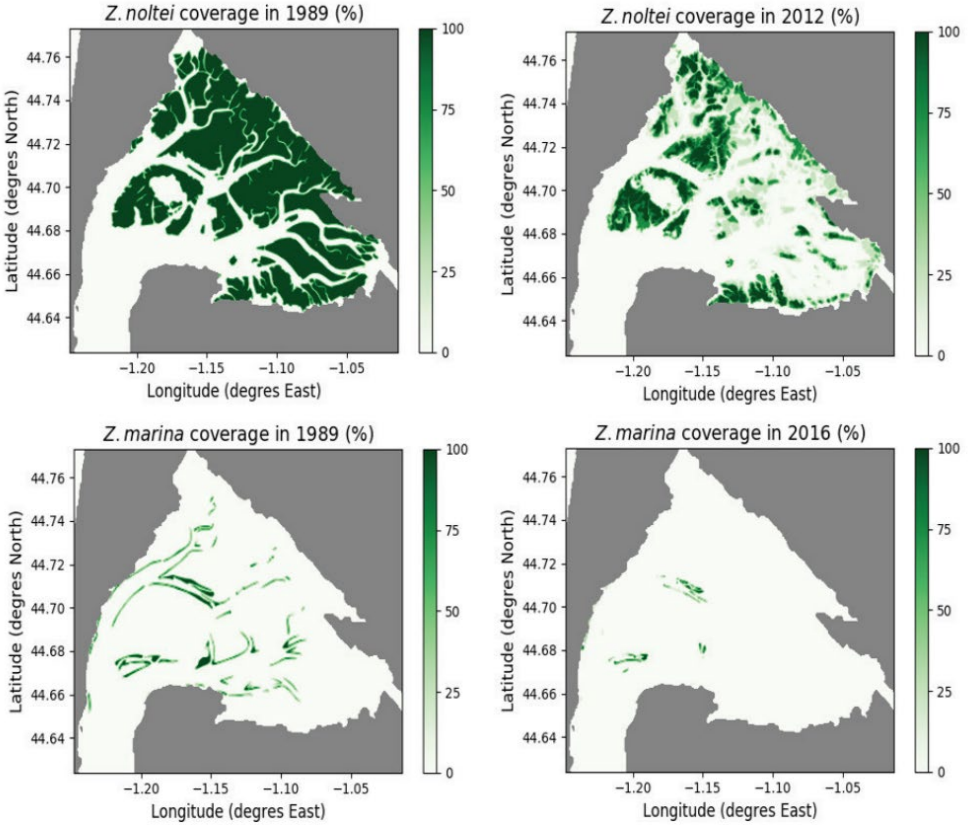

Figure 6.2. Map showing Zostera meadows decline (normalized area coverage) between 1989 (pre-regression state) and actual state : 2012 for noltii and 2016 for marina. From Cognat (2019).

6.1.3. Objective

Within the WP2 scope at the Arcachon Bay, the two main objectives are the assessment of (1) a potential reduction of coastal inundation risk and (2) coastal erosion risk due to the restoration actions. The species targeted by the restoration actions are the Zostera noltii seagrass meadows. The Nature-Based Solution (NBS) at Arcachon Bay refers to the restoration of seagrass within the Bay. The improvement of water quality, carbon sequestration and food production can then be considered as secondary objectives for the Arcachon Bay pilot. Those objectives define the main ESS targeted for the pilot site.

Taking into account physical, social and economic contexts of the Arcachon Bay, the coastal erosion hazards refer to (1) the sedimentation of fine sediments within the Arcachon Bay – increasing the requirements for dredging activities within the harbors –, (2) the erosion of the intertidal areas, and sedimentation and migration of the channels – affecting the location of oyster natural reefs and thus the health of the biodiversity. The coastal flooding hazard refers to the coastal inundation extent in areas bordering the Arcachon Bay with impacts on population and infrastructures.

6.1.4. Methodology

In order to estimate those hazards, a coupled model is developed, describing wind-induced waves propagation, hydrodynamics and morphodynamics. Based on the Delft3D Flexible Mesh suite (DFM), the model also includes the effect of marine vegetation in dampening wave energy and current velocities, as well

as reducing turbidity levels and sediment transport rates. The effects of seagrass meadows are now implemented in the coupled model and have a non-neutral impact on the assessment of coastal flooding and erosion hazards (M2.1). The wave propagation and hydrodynamics are simulated and the coupled model is validated (M2.2) using in situ observations. At this stage, further improvements are required for the validation of the morphodynamics.

This chapter therefore presents activities and modelling results as follows:

- Presentation of the modelling tools and how the vegetation is implemented in the coupled model in sections 6.2 and 6.2.1,
- Sensitivity analysis for the definition of vegetation parameters in section 6.3,
- Validation of the coupled hydro-sedimentary model in section 6.3.3,
- Description of operational period for testing the coupled morphodynamic model in section 6.4,
- Results concerning hazard assessment in section 6.5

6.2. High-resolution coupled coastal models

6.2.1. Modelling platform presentation

Within this project, the DFM platform is chosen to address the different objectives in term of hazard assessment. Therefore, the coupled model is set-up to simulate wave generation and propagation, hydrodynamics, sediment transport and morphodynamics. Different modules are coupled (Figure 6.3) with the effect of the vegetation on hydrodynamics taken into account.

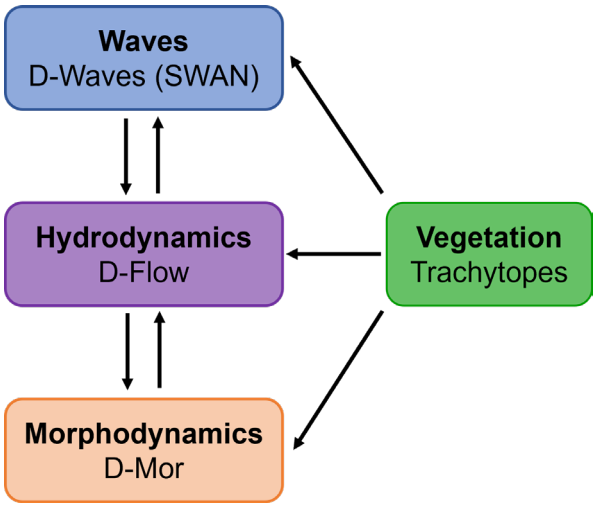

Figure 6.3.Diagram representing DFM coupled modules. Arrows are indicating interactions between modules. The vegetation module affects waves propagation, dampen currents and decrease sediment erosion.

The main module is the D-Flow module, computing hydrodynamics resulting from tidal, meteorological and continental inflows perturbations. It solves non-linear shallow water equations in two dimensions, following Boussinesq assumptions on Navier-Stokes equations. D-Waves is based on a third-generation SWAN model, computing generation and propagation of waves, accounting for non-linear wave-wave interactions and wave dissipation. Sediment transport and bed updating (morphological changes), varying from erosion/sedimentation fluxes, is calculated by D-Mor module. Both bedload and suspended sediment transport are calculated, due to waves and currents. In addition, different types of sediments can be defined, following non-cohesive and cohesive sediment transport formulations. To take into account the complex

sand-mud mixtures present within the Bay, the formulation of Van Ledden (2003) is followed, coupled with Van Rijn (1993) transport formula for sand.

In practice, two models are used: (1) a flooding hazard model (FH model) including wave propagation, hydrodynamics, and vegetation, and (2) a coastal erosion hazard model (CEH model) including hydrodynamics, morphodynamics and vegetation.

6.2.2. Model configuration

The model is implemented on a 2D curvilinear grid (6.4), with a resolution ranging from about 300 m near the offshore boundaries to 100 m in the Arcachon Bay. The bathymetry is based on bathymetric surveys processed by Ifremer in 2016. The coupled model is forced by: meteorological data (coming from reanalysis model ERA5 by ECMWF), tidal harmonic components (deducted from tidal gauge timeseries located in Arcachon harbor), freshwater inputs from the Leyre river, and offshore waves from IOWAGA database (waves characteristics products coming from large-scale model; Ardhuin et al., 2014). The vegetation is initialized with the actual cover, measured in 2012 for Zostera noltii and in 2016 for Zostera marina.

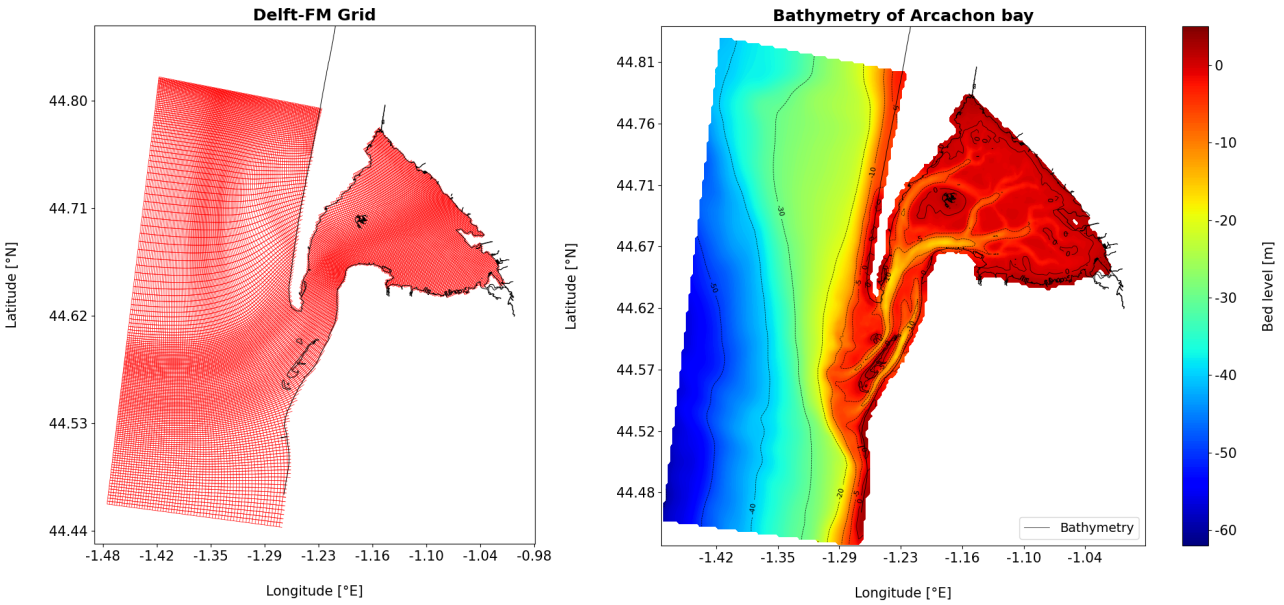

Figure 6.4. DFM curvilinear grid (left). Initial bathymetry applied in the model (m with respect to MSL ; right).

Depending on the modelling purpose, different time scales are considered. A first aim is to calibrate and validate the hydrodynamic model. To that end, in-situ observations available at different sampling stations located within the Arcachon Bay (Figure 6.1) are used. Those stations measured water levels (m ; 9 sampling stations), wave characteristics (Hs in m, Tp in s, Direction in °N, etc. ; 3 stations), and sediment characteristics and concentrations (11 stations) during the 2015-2016 period. Data collected in 2015 are used to calibrate both FH model and CEH model. Then, the FH model is validated against data collected in 2016. The CEH model is validated against sediment concentration data collected in 2016 and morphological changes occurring between 2016 and 2019 (from new bathymetric surveys made by SIBA, Syndicat Intercommunal du Bassin d'Arcachon).

6.3. Parameterization of hydro-morpho-eco interactions to simulate ESS.

6.3.1. Including vegetation module

The effect of seagrass meadows is implemented in the coupled model in order to have a non-neutral impact on the assessment of coastal flooding and erosion hazards (M2.1).

Following the formulations of Baptist (2005), the effect of the vegetation on flow resistance and bed roughness are separated. Actually, some formulations only consider the calculation of the flow resistance by means of the increase of the bed roughness (James et al., 2012). However, it leads to higher bed shear stress and larger sediment transport rates in case of morphological modelling. This is typically the opposite to what is expected. In the trachytopes formulations used in DFM, a $-\frac{\lambda u^2}{2}$ term is included in the momentum equation where λ represents the flow resistance of the vegetation, and u the flow velocity.

The vegetation is also dampening the energy of waves. It is expressed with the formulation of Mendez and Losada (2004) following the work of Dalrymple et al. (1984) on cylinders, which was implemented in SWAN by Suzuki et al. (2012):

$$S_{d,\ veg} = -\sqrt{\frac{2}{\pi}} g^2 \widetilde{C_D} b_v n_v \left(\frac{\tilde{k}}{\tilde{\sigma}}\right)^3 \frac{\sinh^3(\tilde{k}l_v)+3\sinh(\tilde{k}l_v)}{3\tilde{k}\cosh^3(\tilde{k}h)} \sqrt{E_{tot}}\, E(\sigma,\theta) \quad (6.1)$$

Where $\widetilde{C_D}$ is a bulk drag coefficient, $\tilde{k}$ is the mean wave number, $\tilde{\sigma}$ is the mean wave frequency, h is the water depth, E_{tot} is the total wave energy, and E is the wave energy at frequency σ and direction θ. The vegetation is defined by b_v the width of individual plants, n_v the number of stems per unit area, and l_v the height of the vegetation. Beudin et al. (2017) schematically represents the effect of vegetation on hydrodynamics (Figure 6.5), highlighting vertical current profiles and turbulence schemes.

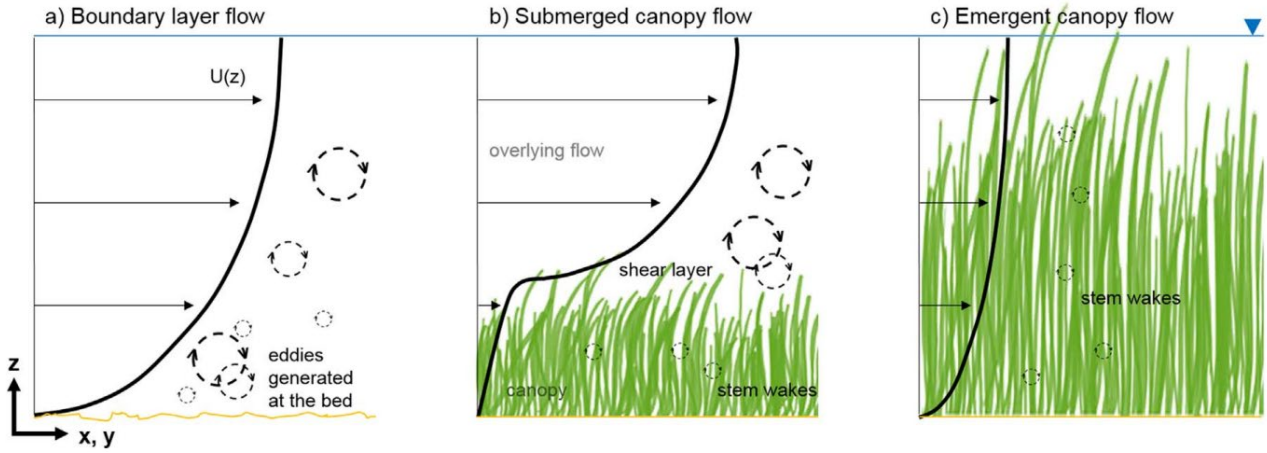

Figure 6.5. Sketch of different flow regimes showing the dominant source of turbulence (left: bed, center: the top of canopy, right: stem wakes). From Beudin et al. (2017).

In the simulations, the vegetation is spatially fixed and its parameters are not changing over time. A summer configuration is considered and a sensitivity analysis is conducted on vegetation parameters (see next section). Table 6.1 lists the parameters used for representing the vegetation in the coupled model.

Table 6.1: Vegetation parameters used in coupled modelling. They correspond to summer configuration (Mütterlein et al., 2016).

Normalized cover(-)	Leaf length l_v (m)	Leaf width b_v (m)	Leaf density n_v (n.m^{-2})	Drag coefficient C_D (-)

< 0.25	0.13	1.1	20 000	0.7
$0.25 \leq \ . \ < 0.75$	0.14	1.1	40 000	0.7
≥ 0.75	0.20	1.1	80 000	0.7

6.3.2. Sensitivity analysis concerning vegetation parameters

In order to better understand the influence of vegetation on hydrodynamics components, different vegetation configurations are used. In particular, Mütterlein et al. (2016) suggested parameter values for coverage, leaf length, leaf width and leaf density used in the MARS3D model and representative of the Arcachon Bay. The latter model is developed by Ifremer and integrate vegetation as well (e.g. Kambiadou et al., 2014 ; Cognat, 2019). They suggested different configurations depending on the season, as it is known that those parameters have higher values in summer than in winter.

With the aim to assess the impact of vegetation on hydrodynamics components, Figure 6.6 shows the vertically averaged currents anomaly (m.s-1), averaged on an entire tidal cycle, between with and without vegetation and between summer and winter configurations. On the left panel of Figure 6.6, the current velocities are reduced all over the areas where vegetation is established. On intertidal areas, the reduction in current velocities is greater than 0.14 m.s-1. Along the decrease on the tidal flats, current velocities are greater in the channels. This should lead to larger erosion of the channels and higher sedimentation on the tidal flats with vegetation. On the right panel of Figure 6.6, a clear decrease of currents in vegetated areas can be observed when differentiating between summer and winter configurations, but it does not affect the whole Arcachon Bay.

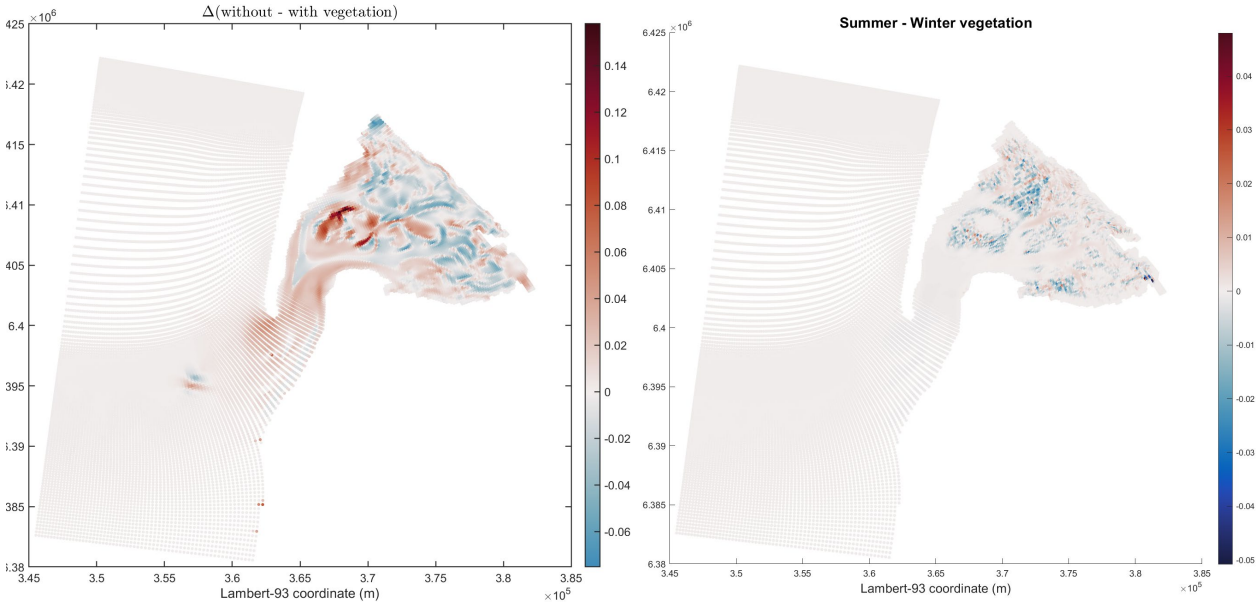

Figure 6.6. Vertically averaged currents anomaly (m/s) for the difference between with and without vegetation (left), and between summer and winter vegetation configurations (right).

On Figure 6.7, the different configurations are compared in terms of water levels, in several stations located within the Arcachon Bay. Tide propagation within the Bay is affected by the presence of vegetation. The asymmetry between ebb and flood is more pronounced, in particular on tidal flats areas. In the presence of vegetation, water levels are generally higher at high tide on those stations, with about 20 cm gap at high tide. However, no notable difference between the summer and winter configurations is observed.

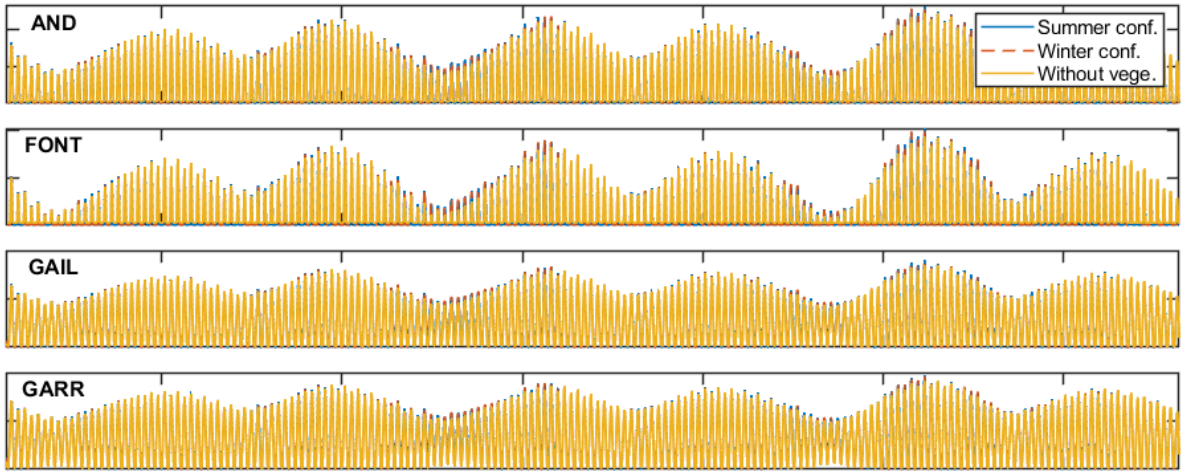

Figure 6.7. Water levels (m) during several tidal cycles for different vegetation configurations: without (yellow), winter (blue), summer (red).

To evaluate the effectiveness of restoration scenarios, the summer configuration is used for the next steps.

6.3.3. Validation of the coupled model using in-situ measurements

In-situ observations for water levels and wave characteristics were available for the period 2015-2016. Those data were collected and exploited by Cognat (2019) and Le Pevedic (PhD in progress). The hydrodynamic part is validated against water level observations (Figure 6.8). The model results show a good agreement with in-situ data with a slight over-estimation of the water levels at stations closer to the coastline (about 10 cm).

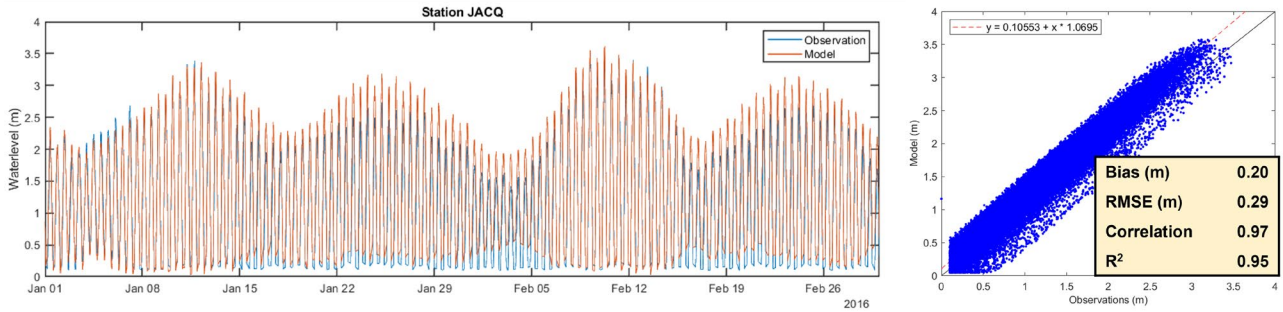

Figure 6.8. Water levels (m) for JACQ station over months Jan. and Feb. 2016 (left). Regression diagram comparing observations of the 9 sampling stations within the lagoon, and model results for the entire period of simulation (right). The equation of the linear regression is indicated.

With respect to the wave characteristics, the model results are compared to in-situ observations at 3 sampling stations. Observations of significant wave heights (H_s), wave period at peak (T_p) and spectra are compared to model results (Figure 6.9). Waves within the Arcachon lagoon are mainly induced by wind processes. Therefore, meteorological forcing schematization and good representation of wind processes in the model are very important to assess waves characteristics within the bay. The applied meteorological forcings are hourly estimates from ERA5 products, although over-estimation of wind velocities has been noticed (Molina et al., 2021), leading to discrepancies in wave characteristics estimations. Furthermore, spectral analysis of waves components from in-situ observations hold some uncertainties. Still, taking into account those uncertainties, the model results show good agreement with in-situ observations. The determination coefficient reaches 0.6 for GARR station, located within the Arcachon Bay, near intertidal areas. The wave heights are thus under-estimated by the model with gaps between observations and model results increasing with higher values of H_s. With hourly forcing for winds, it is acceptable not to catch every

peaks measured at observation stations but this should be taken into account in assessing coastal flooding hazard.

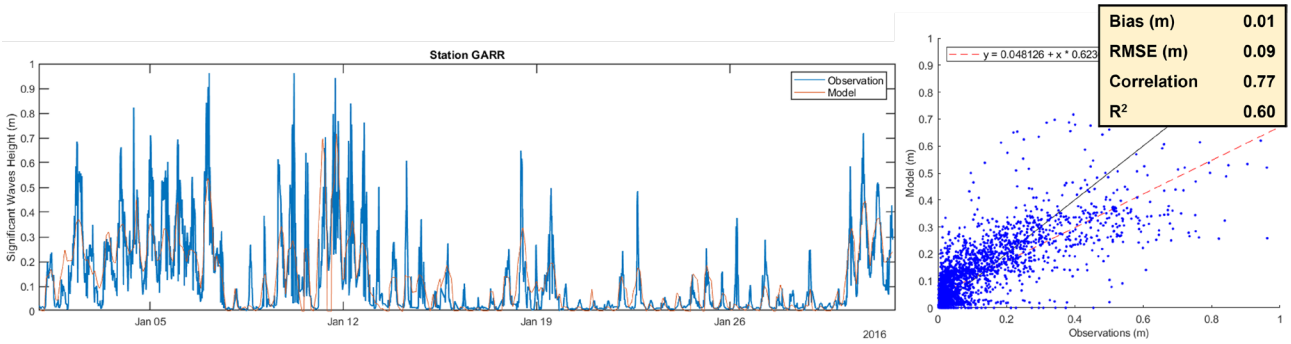

Figure 6.9. Significant waves height (m) for GARR station over the period 2015-2016. Regression diagram for the entire period of simulation (right). The equation of the linear regression is indicated.

In terms of current velocities, no in situ observations were available over the studied period. However, the validated modelling platform MARS3D, implemented by Ifremer on the Arcachon Bay (Lazure and Dumas, 2008 ; Ganthy, 2011 ; Kombiadou et al., 2014 ; Cognat, 2019), provides current velocities estimates for the 2015-2016 period. Results obtained with the D-FM coupled model are then compared to MARS3D results over an entire tidal cycle (Figure 6.10). Within the Arcachon Bay, the currents are shown to be very close to those calculated by MARS3D. The highest discrepancies between the two models are located around the entry of the Bay, in the channels, still at locations where MARS3D model has not been calibrated.

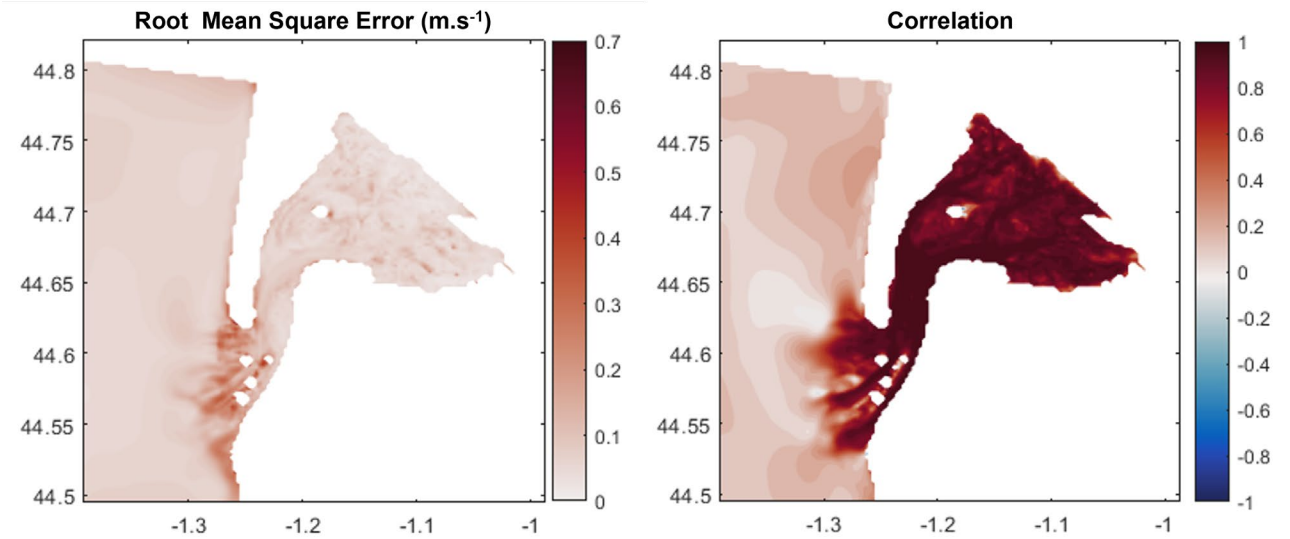

Figure 6.10. Map of Root Mean Square Error (m/s), averaged over one tidal cycle, between the coupled DFM model results and MARS3D results (left). Map of correlation coefficient, averaged over one tidal cycle, between the two models results (right).

In addition to hydrodynamics parameters detailed above, sediment characteristics were also available on the 2015-2016 period. The aim of the WP2 at Arcachon Bay is also to work on erosion/sedimentation and water quality linked to sediment dynamics. To ensure addressing these objectives, the CEH model is validated against sediment concentrations collected in 2016 and morphological changes occurring between 2016 and 2019 (from new bathymetric surveys made by SIBA). On the 2015-2016 period, bi-monthly sediment concentration measurements were available within the Arcachon Bay. Figure 6.11 shows the comparison between model results and in situ observations.

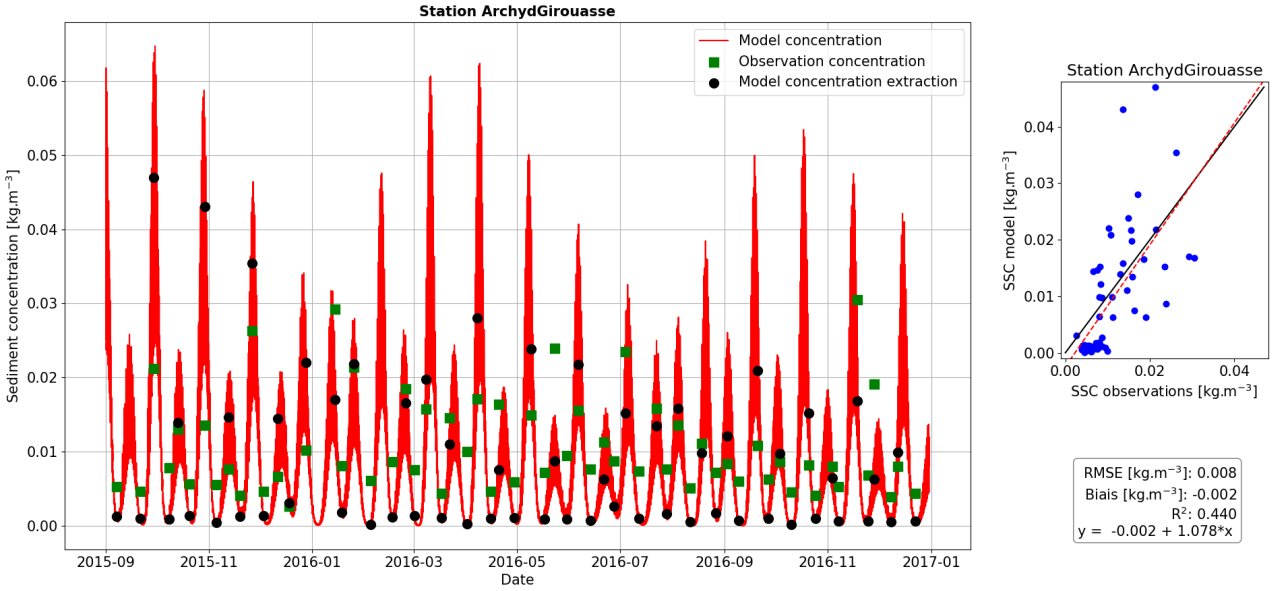

Figure 6.11. Suspended sediment concentration (kg.m-3) for Girouasse station over 2015-2016 period. Regression diagram for the entire period of simulation (right). The equation of the linear regression is indicated.

Model results are in the same order of magnitude than in-situ observations. For low sediment concentrations, model results tend to under-estimate the observed concentrations. The determination coefficient remains satisfactory with 0.44 at the Girouasse station.

The validated coupled model enables to : (1) include wave generation and propagation from wind forcing; (2) correctly represent hydrodynamics due to meteorological forcing, tidal processes and with wave coupling; (3) adequately represent sediment transport and resuspension, including 3 types of sediments; (4) include the effect of vegetation on waves, hydrodynamics and erosion/sedimentation patterns.

6.4. Target operational period for testing the EWS nested into CMEMS products

In the context of assessing coastal flooding and erosion hazards for present climatic conditions, but for different storm conditions, and in order to test the developed coupled model, including sediment morphodynamics, operational periods are defined.

After the implementation, development and calibration of the sediment transport and morphodynamics module, the concept of morphological factors is applied aiming at: (1) reducing the computational time of coupled simulations, and then (2) applying the coupled model to simulate longer period of time. A morphological factor is an acceleration factor for morphological changes that should occur during an interval of time (called 'Morfac'; Roelvink, 2006). For example, if one month is simulated, and Morfac is set to 12, then the obtained morphological changes correspond to a one-year evolution. To do that, representative forcings of the entire considered period are determined and reduced to the simulated period. Only tidal forcing is considered given the tide is the main process for sediment transport in the Arcachon Bay.
A model calibration is currently ongoing with aim at defining the appropriate tidal forcing reduction and associated morphological factor. To do so, a sensitivity analysis is carried out for assessing the influence on these two aspects (work in progress).

To validate the implementation of the morphological module in the coupled DFM model, a simulation will be then conducted over the period 2016 to 2019 (work in progress), given that two bathymetric surveys of the

Arcachon Bay are available in 2016 and 2019. The results obtained using the morphological factor approach will be additionally compared to the results obtained based on a real-time simulation and covering the 3-years period.

The assessment of coastal erosion hazard will then follow, with new possibilities in terms of long-term morphological application. For instance, the consideration of several scenarios of future bathymetric changes due to sea level rise could be envisioned.

6.5. Hazard reduction from ESS as a function of restoration scale.

The aim of this study is to assess coastal flood and erosion hazards for the Arcachon Bay, considering potential restoration scenarios, for present climatic conditions and different storm conditions.

6.5.1. Definition of restoration scenarios

In this study, two restoration scenarios (S0 and S1) are considered. Two additional scenarios (S2 and S3) are envisioned but the delimitation of potential restored vegetation extent is still a work in progress (WP1). S0 corresponds to the present state of vegetation, considering that restoration actions will maintain the actual extent. S1 corresponds to the pre-regression state, defined from observations made in 1989. S2 and S3 correspond to two strategies of deployment of Roselière devices within the Arcachon Bay. This device aims at reducing flow velocities, recreating favorable hydro-sedimentary conditions for the spontaneous recovery of vegetated areas. The first considered deployment consists of settling Roseliere devices along the secondary channels, around the intertidal areas, limiting strong currents that could possibly affect vegetated areas. The second deployment consists of iterated actions: place Roseliere near vegetated areas, wait for a natural recolonization of vegetation towards Roseliere devices, move the devices further away from re-vegetated areas and then start a new iteration. The second one will certainly need more maintenance and tracking than the first one. Figure 6.12 shows the normalized cover for scenarios S0 and S1.

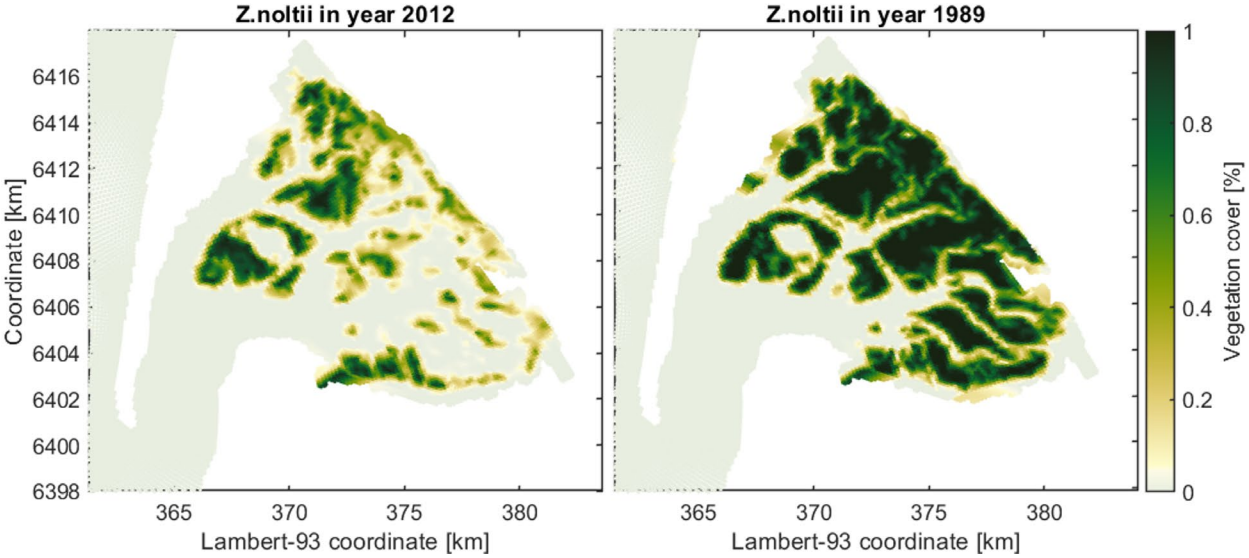

Figure 6.12. Map of vegetation cover for present state scenario (S0, left) and pre-regression state scenario (S1, right).

6.5.2. Coastal flooding hazards

The coastal flooding hazard refers to the coastal inundation extent in areas bordering the Arcachon Bay with impacts on population and infrastructures. To assess this hazard, the model outputs targeted are the water levels reaching the coastal areas inside the Bay and the corresponding current velocity components.

In order to define different flooding scenarios, a statistical analysis of environmental forcings is carried out. The water levels inside the Arcachon Bay are influenced by tidal processes, waves, and meteorological components such as atmospheric pressure during storm events. Inside the Bay, prevailing waves are wind-induced waves (Parisot et al., 2008). Then, the definition of flooding scenarios has been led by the analysis of wind forcings, more than offshore waves. Figure 6.13 shows the results from statistical analysis on wind data coming from Météo-France observations in Cap Ferret meteorological station. An extreme values analysis has been followed, determining extreme values using block maxima on 1-year window. On the right panel, wind speed values can be linked with return period. The theorical Gumbel distribution is correctly fitting extreme values selected.

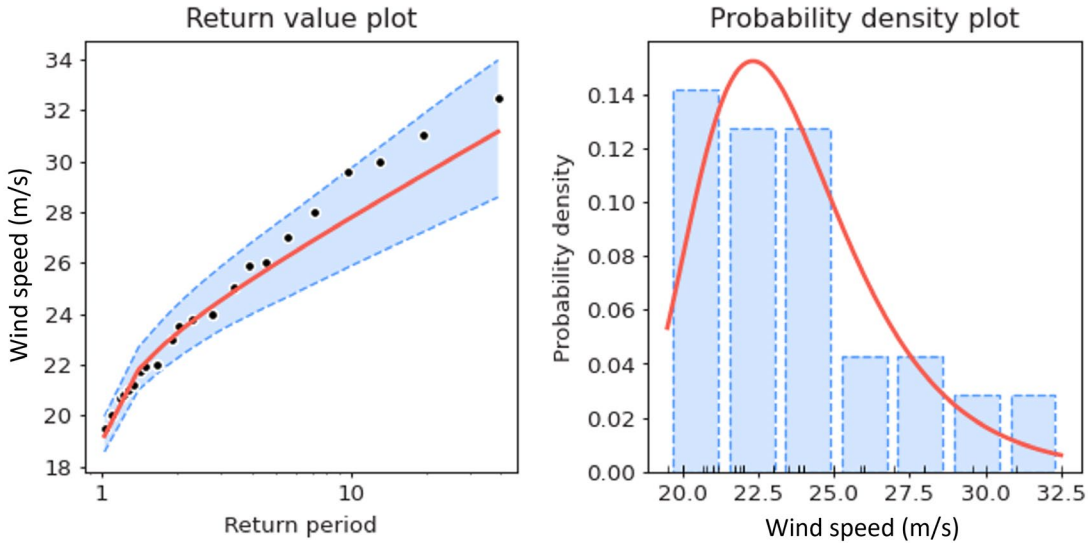

Figure 6.13. Return value plot (left) and probability density plot (right) for wind velocity extreme values (m.s-1), determined by block maxima method on one year window. Météo-France observations in Cap Ferret station over 1985-2022 period are used.

The same approach was followed for water levels measured by SHOM (Service Hydrographique et Océanographique de la Marine) at the Eyrac station, located in the Arcachon habor. The Gumbel distribution is also used for assessing return values (Figure 6.14; location = 2.46 and scale = 0.14).

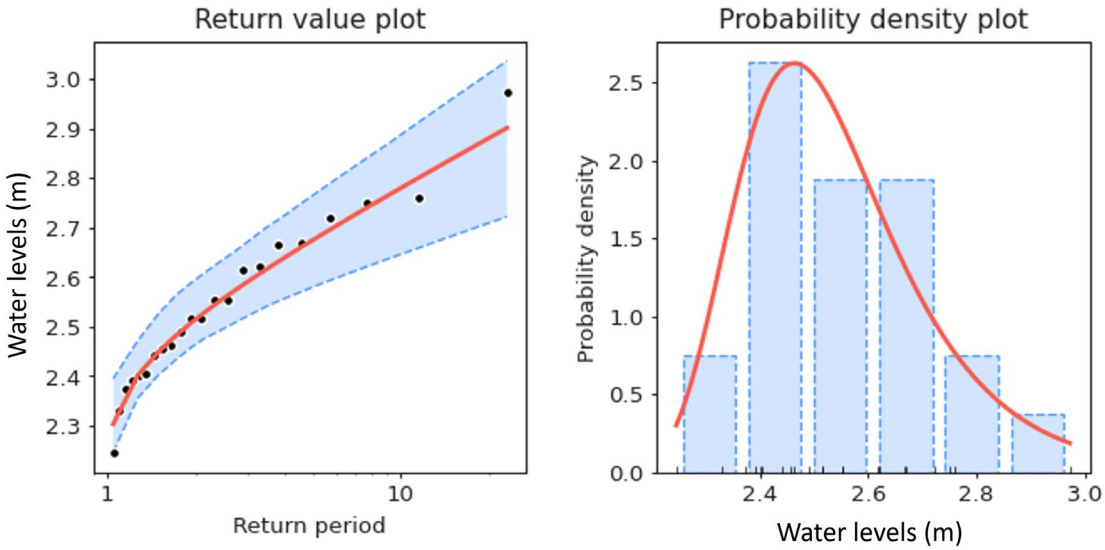

Figure 6.14. Return value plot (left) and probability density plot (right) for water levels extreme values (m.s-1), determined by block maxima method on one year window. SHOM observations in Eyrac station over 2001-2023 period are used.

The univariate statistical analysis is a first step in defining storm conditions for flooding scenarios. A multi-variate analysis is needed to take into account the possibility of having concomitant events of extreme water levels (1 value) and extreme winds (speed and direction, 2 values). Following the JOIN-SEA approach, Mugica et al. (2014) assessed 100-year return period of concomitant events for the Arcachon Bay. The same approach is followed here and the results are presented in Table 6.2. Directions of wind follow the results of Mugica et al. (2014) and are considered as the most unfavorable in terms of coastal flooding.

Table 6.2. Definition of flooding events for different return periods, based on joint analysis of water levels and wind characteristics.

Return period (year)	Water level (m MSL)	Wind speed (m.s-1)	Wind direction (°N)
1	1.92	10.6	[270°, 215°]
5	2.18	12.4	[270°, 215°]
10	2.42	16.6	[270°, 215°]
100	2.65	22.6	[270°, 215°]

6.6. Conclusions

A D-FM coupled wave-hydro-morpho-eco model is developed for the Arcachon Bay. It includes the effect of the vegetation on wave propagation, hydrodynamics, and morphodynamics. Using in-situ observations available within the Bay over the 2015-2016 period, the coupled model is calibrated and validated, leading to an optimized parameterization of the vegetation module, based on a sensitivity analysis of key parameter settings. Furthermore, the development and implementation of the sediment transport and morphodynamics module offer good perspectives for application under current and climatic forcing for testing various seagrass restoration scenarios. Consolidated modelling results will be presented in the following deliverable.

7. Multi-hazard forecasting (including a multidisciplinary calibration) and application limits Sicily Lagoon Pilot (UC)

7.1. Introduction

The University of Catania (UC) leads the research activities related to the evaluation of the effectiveness of a range of coastal restoration measures within the REST-COAST Sicily pilot site: the Cuba-Longarini coastal lagoon system, belonging to the Natura 2000 site of the Lagoons of the South East of Sicily. The region is subject to a twofold source of risk: a flooding and erosion threat to the village of Granelli, built over the dune-belt in between the lagoons and the sea; and the anthropic pressures on the lagoon biodiversity, induced by human activities in the surrounding area (intensive agriculture and tourism, mostly), which led to a reduction in both extension and quality of the local habitats and water resources. In collaboration with the local managers of the site, UC is assessing a range of solutions to both improve biodiversity value, by protecting the environment, and increase the provision of ecosystem services related to flooding and erosion risk mitigation. Presently, two solutions, additional to the ones currently carried out as pro-biodiversity measures (i.e. construction of artificial islands within the lagoons and new hydraulic connections between the different areas of the two lagoons), are investigated, (i) a revegetation of the dunebelt in between the Granelli village and the beach, (ii) an extension of the present seagrass meadow in front of the Granelli coast, (iii). The performance assessment of these solutions is pursued by means of numerical modelling, aimed to evaluate the response of the system to extreme events, under present and climate change conditions, therefore including impact of sea level rise as well as modification of the wave climate. Hereunder, the investigated hydrodynamic scenarios, the input data employed, and the model setup/validation are described.

7.1.1.Case study

The "Pantani della Sicilia Sud-Orientale" (South-East of Sicily lagoons, Figure 7.1a) is a saline lagoon and wetland system in close connection with the adjacent coastal environment. The area hosts important breeding populations of rare and endangered species, representing a crucial migration hot-spot for bird species along the central Mediterranean migration flyway. Due to its naturalistic and biodiversity value, these region is included in international environmental protection frameworks (RAMSAR, Natura 2000), Special Protection Areas and regional nature reserves.

The Cuba-Longarini lagoons is the largest complex of wetlands in the area (Figure 7.1b), covering an area of approximately 240 ha. They are separated from the sea by a narrow coastal fringe, consisting of a dunestrip and a sandy beach, and are intermittently connected to the sea by a small estuary channel, depending on the actual lagoon water level. The lagoons are characterized by shallow waters, with depth generally smaller than one meter.

The construction of the small town of Granelli in the 1970s, over the narrow fringe between the sea and the lagoons, has led to a reduction of hydraulic connectivity between the wetlands and the sea, alongside the degradation of the coastal dunebelt, over which the urbanized area is built. As a consequence, the area is subject to flooding due to intense runoffs from the lagoon side, and from wave storms from the side.

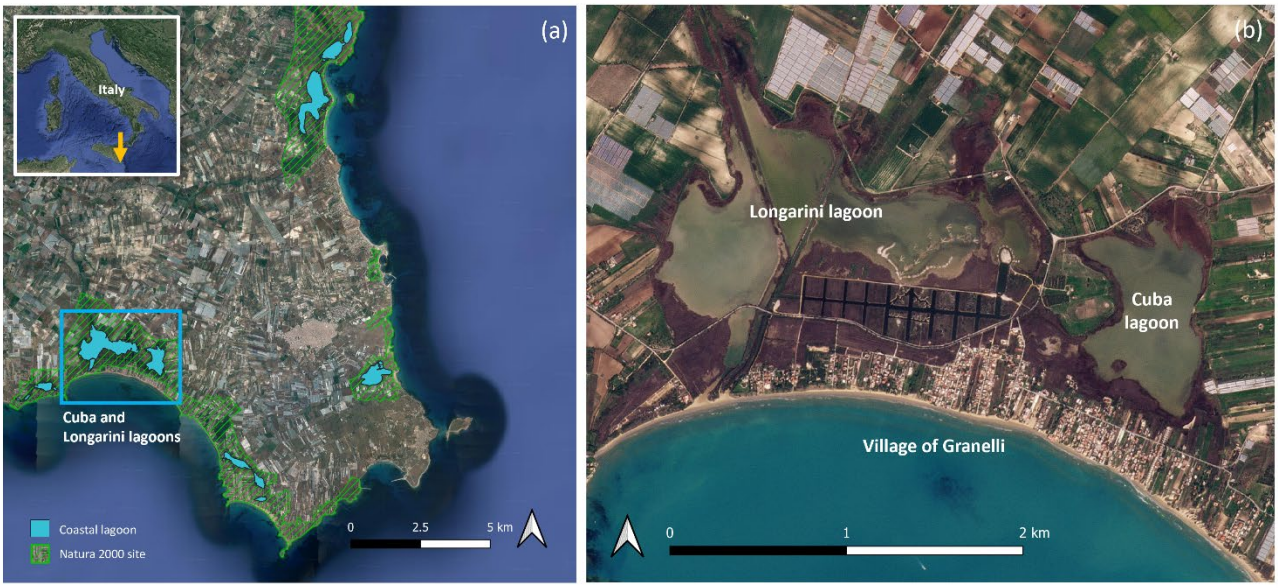

Figure 7.1. a) Aerial view of the lagoons of the South-East of Sicily. b) aerial view of the Sicily lagoon pilot site area: the Cuba-Longarini lagoons.

With the aim to mitigate coastal risk and restore biodiversity value, a range of Nature-based Solutions are investigated considering a current state (with actual active restoration measures) and proposed additional restoration measures. Indeed, as previously mentioned, the town of Granelli was built over a coastal dune strip, with consequences on the reduction of the sediment fluxes and the natural protection capabilities of the environment. A full dune reconstruction would rather be feasible due to the narrow space remaining in between the beach and the urbanized area. Instead, a revegetation to stabilize the dune and improve wave dissipation capabilities of the system could be envisaged. The chosen species is the endemic Ammophila arenaria, which is already marginally present on-site. The proposed intervention entails expanding the dune habitat by an area of about 0.043 km^2, stretching along the shoreline for a length of 3.30 km and extending across a width of 13 m (average). Furthermore, a replantation of the seagrass meadow in front of the town is also investigated. Specifically, an extension of the existing meadow of *Posidonia oceanica*, which is a protected marine plant, is designed to evaluate its capabilities to dissipate wave energy and reduce storm-induced erosion. The investigated replantation of the seagrass extends for 1.04 km^2, distributed around the existing meadow (0.77 km^2).

7.2. Materials and methods

In order to assess the performance of the solutions, a SWAN+XBeach modelling chain is setup. In the present chapter, the input data, the model setup and the pursued simulations are described.

7.2.1.Input data description

7.2.1.1. Topographic and beach data

In order to build the SWAN numerical grid, bathymetric contours were taken from nautical charts (Istituto Idrografico della Marina, 2019). In order to build the Xbeach numerical grid, a Digital Elevation Model (DEM) of the study area was obtained from the Regional Geographic Information System of Sicilia Region. The DEM was recovered through LiDAR flights in 2013 and has an horizontal resolution of 2x2 m and vertical resolution of 0.01 m. The DEM was combined with bathymetric data obtained through a multi-beam survey, previously carried out by the University of Catania, that covered the entire nearshore part of the domain in 2019. The

dataset is integrated with data obtained by means of satellite images, drone data and field surveys, to include small artificial islands and channels built in 2023 to improve biodiversity value of the site.

The shoreline was obtained through PlanetScope satellite imagery (having 3x3 m resolution) by tracking the wet/dry boundary. Elevations from DEM, bathimetry and shoreline position were combined to assign elevation at the XBeach grid nodes through linear interpolation. The beach is made up by fine sand, with d50=0.27mm, estimated based on several field samples collected at the Granelli beach.

7.2.1.2. Marine climate and sea level rise data

Present wave conditions were obtained from the MEDSEA MULTIYEAR WAV 006 012 reanalysis dataset (Korres et al., 2021) provided by the Copernicus Marine Service. The dataset spans the years 1993-2022 and includes hourly time series of marine climate, with a spatial resolution 4.66 × 4.66 km.

Climate change projected wave conditions were taken from Ocean surface wave time series for the European coast from 1976 to 2100 derived from climate projections dataset (Caires et al., 2020). The dataset provides hourly time series on the marine wave climate derived from ocean surface wave parameters calculated across a European-wide domain. The ocean surface wave fields are generated through ECMWF's Wave Model (SAW), driven by surface wind and incorporating considerations for ice coverage at polar latitudes based on IPCC AR5 climate projections. The year timespan of the dataset is 2041-2100, with hourly temporal resolution and a spatial resolution of 30 x 30 km.

The dataset includes projected wave conditions for two IPCC AR5 Representative Concentration Pathway (RCP) scenarios: one aligns with a more optimistic emission trajectory, wherein emissions begin to decline beyond 2040 (RCP4.5), and the other represents a pessimistic scenario where emissions persistently increase throughout the century, often referred to as the business-as-usual scenario (RCP8.5).

For both present and future projection datasets, significant wave height H_s, peak period T_p and mean wave direction θ were extracted for present, RCP4.5 and RCP8.5 scenarios. The data were extracted in the correspondence of the grid point closest to our model offshore boundary (latitude 36.69°N, longitude 15.00°E - EPSG 32633).

The categorization of events based on their H_s and θ was also carried out to identify the prevailing direction and the direction associated with the most energetic sea states. This analysis involved subdividing the directional sector from which waves originate into eight sub-sectors. Considering the geographical fetch of the site under investigation, the directional sector for wave propagation spans from 150°N to 270°N, covering a total width of 120°. Therefore, the whole sector was subdivided into eight sub-sectors, each spanning 15° (Figure 7.2).

For each sub-sector, an extreme value analysis was conducted to obtain Hs associated with storms with given return period T_r. In order be consistent among the present and future scenarios, the extreme value analysis was conducted considering the same length of for the time window of analysis. For the historical timeseries the time window corresponds to the actual extension of the dataset time series, namely 1993-2022 (present condition). For the RCP scenarios two-year windows were considered instead, namely the 2041-2070 and the 2071-2100. Thus doing, the extreme value analysis is carried out considering a dataset 30 years long, for each scenario.

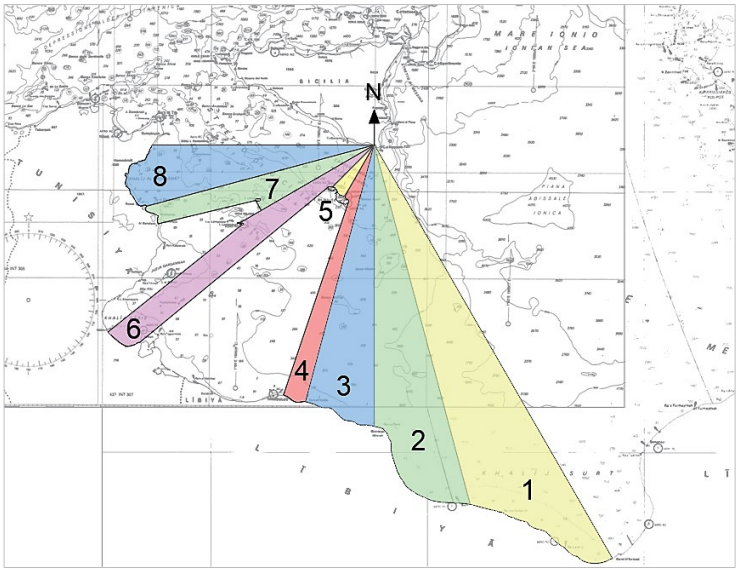

Figure 7.2. Geographical fetch and wave directional sub-sectors.

Extreme value analysis was conducted as follows. First, a Peak-Over Threshold method was used to identify peaks associated with storms within the extracted Hs timeseries, given an Hs threshold of 2.0 m and a minimum temporal distance between independent events equal to 12 hours (Boccotti, 2004). Then, a range of probability distributions (Weibull, Gumbel, LogNormal and Generalised Pareto) were tested against the storm H_s timeseries to check which one best-fits with the sample. The goodness-of-fit was tested by means of the Kolmogorov-Smirnov test. The Generalised Pareto distribution was identified as the best-fitting one for the extreme values of H_s for each one of the directional sub-sectors.

Finally, for each subsector Hs value for a return period T_r of 5, 50, 100 years was extracted from the adapted Pareto distribution. From a preliminary analysis of both the storms per each subsector and the geographical fetch, it was noted that a predominant occurrence of events came from the western directions. Consequently, the subsequent analysis was focused on the eighth subsector corresponding to the West (θ = 262.5°N).

Concerning the peak period, the following site-specific correlations between T_p and H_s were defined by applying the least squares method to the available datasets:

$$T_p = 6.6301 H_s^{0.2593} \quad (7.1)$$

$$T_p = 6.3327 H_s^{0.2867} \quad (7.2)$$

$$T_p = 6.3224 H_s^{0.2892} \quad (7.3)$$

for present, RCP4.5 and RCP8.5 scenarios, respectively.

Sea level rise projections based on IPCC AR6 for the years 2020-2100 were obtained from the NASA Sea Level Change projection tool at the closest geographical coordinates to our site (latitude 36.00° and longitude 14.00°). In IPCC AR6, the RCP scenarios have been replaced with Socioeconomic Pathways (SSP). Since there is no direct one-to-one correspondence between specific RCP and SSP scenarios, a combination of RCP and

SSP scenarios can be chosen depending on the projected storyline to be investigated. Since considerations about future socio-economic projections at our study case are not available, we decided to combine RCP and SSP scenarios based on the same radiative forcing value. Therefore, wave conditions for RCP4.5 scenarios were matched with sea level rise projections for SSP2-4.5 scenario (radiative forcing equal to 4.5 W/m^2). Similarly, data projected for RCP8.5 wave scenarios are associated with sea level rise corresponding to SSP5-8.5 scenario (radiative forcing equal to 8.5 W/m^2). The sea level rise projection is the one corresponding to the last year of the examined year window, i.e. 2070 and 2100, for the 2041-2070 and 2071-2100 windows respectively.

In the end, we investigated 5 climatic scenarios, a present scenario (SP) based on the analysis of the hystorical re-analysis dataset, two climate change projection scenarios associated with a radiative forcings equal to 4.5 W/m^2 with 2070 and 2100 time horizons (S4.5-2070 and S4.5-2100 respectively), and two scenarios for radiative forcing equal to 8.5 W/m^2 scenarios (S8.5-2070 and S8.5-2100).

Considering the abovementioned, a range of hydrodynamic scenarios were investigated, based on combination of sea level rise and wave conditions at different return period (Table 7.1).

Table 7. 1. Present and future hydrodynamic scenarios investigated for the Sicly pilot site.

Return Period [years]	Climatic scenario	Year window	H_S [m]	T_P [s]	SLR [m]
5	Present (SP)	1993 - 2022	4.26	9.65	0.00
	S4.5-2070	2041 - 2070	5.68	10.42	0.37
	S4.5-2100	2071 - 2100	5.16	10.14	0.57
	S8.5-2070	2041 - 2070	5.22	10.20	0.48
	S8.5-2100	2071 - 2100	5.48	10.34	0.78
50	Present (SP)	1993 - 2022	5.61	10.37	0.00
	S4.5-2070	2041 - 2070	8.06	11.52	0.37
	S4.5-2100	2071 - 2100	7.21	11.16	0.57
	S8.5-2070	2041 - 2070	6.67	10.95	0.48
	S8.5-2100	2071 - 2100	8.36	11.68	0.78
100	Present (SP)	1993 - 2022	6.01	10.56	0.00
	S4.5-2070	2041 - 2070	8.70	11.77	0.37
	S4.5-2100	2071 - 2100	7.75	11.39	0.57
	S8.5-2070	2041 - 2070	6.97	11.09	0.48
	S8.5-2100	2071 - 2100	9.18	12.00	0.78

7.2.1.3. Vegetation data

The XBeach model allows to simulate the wave dissipation due to the presence of vegetation. To do so, characteristics of vegetation and spatial distribution of the vegetation must be given as input to the model. The spatial distribution of vegetation was obtained by EUNIS2019 habitat maps (Chytry et al., 2020) integrated with field surveys.

7.2.2. Modelling setup

The SWAN computational domain extends for 2068 km^2, encompassing approximately 90 km of coastline (Figure 7.3.a). The numerical grid consists of 17141 nodes. The unstructured grid resolution (i.e. distance between nodes) is variable and bathymetry-dependent. For depths greater than 100 m, the elements have a side of 1 km. For depths between 100 m and 30 m, the size gradually changes from 1 km to 400 m. For depth less than 30 m, the elements maintain a size of 400 m. A higher resolution (100 m) was adopted in the proximity of the XBeach domain.

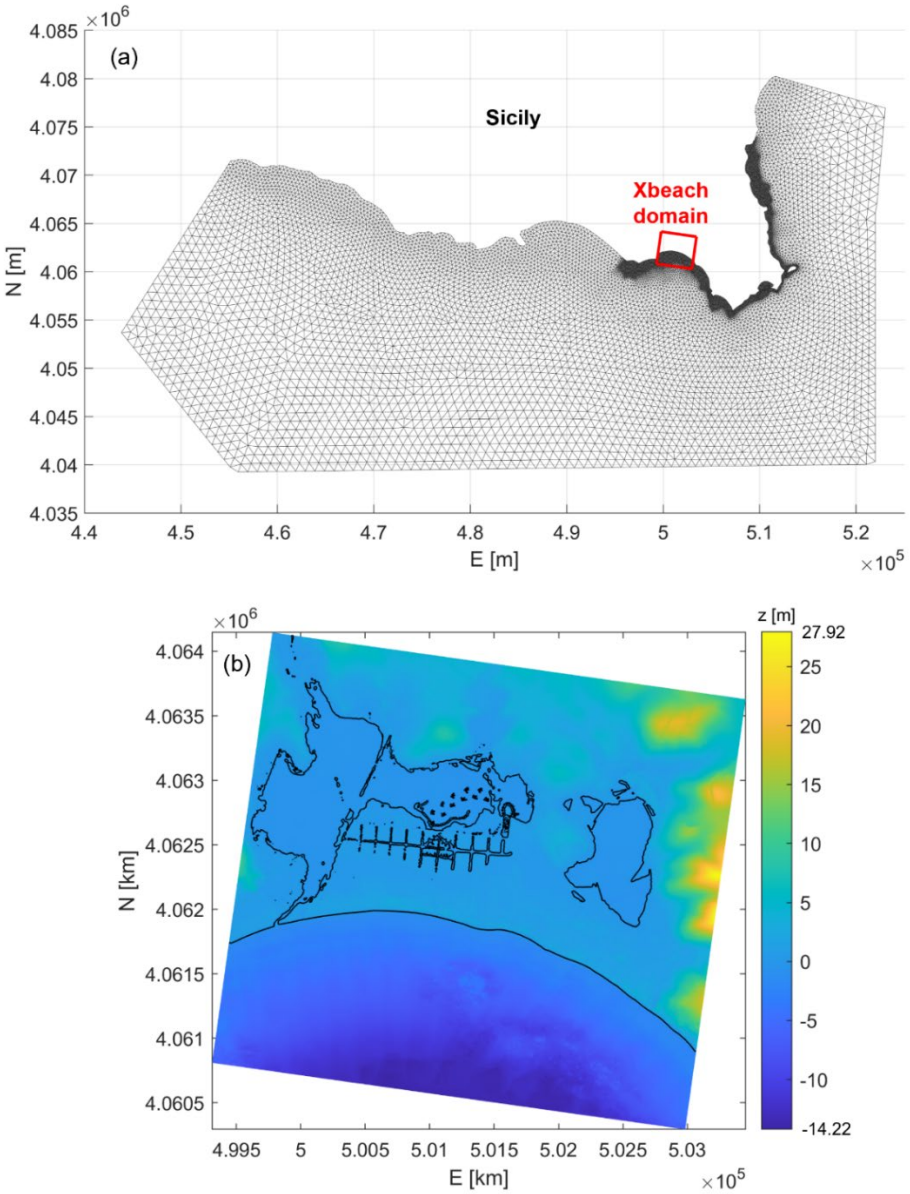

Figure 7.3. a) SWAN numerical grid. The red rectangle shows the nested Xbeach domain. b) XBeach numerical grid with associated elevation values in color scale.

The XBeach computational domain (Figure 7.3.b) is nested into the SWAN domain and consists of a 3.36 km cross-shore and 3.69 km long-shore tile, consisting of a total surface of 12,398 km2, enclosing the Cuba-Longarini lagoon system, Granelli town and beach. A structured grid with variable resolution was built within the domain, ranging 2.5 - 10 m cross-shore and 5 - 10 m longshore. The grid is made up by 1150 (cross-shore)

x 544 (long-shore) cells, for a total of 625,600 nodes. To each cell node, an elevation value is associated based on the topographical data mentioned in Section 2.1.

The XBeach model allows to simulate wave dissipation due to presence of vegetation by implementing a dissipative term in the short-wave action balance equation (Holthuijsen et al., 1989):

$$\frac{\partial A}{\partial t}+\frac{\partial c_x A}{\partial x}+\frac{\partial c_y A}{\partial y}+\frac{\partial c_\theta A}{\partial \theta}=-\frac{D_b+D_f+D_v}{\sigma} \quad (7.4)$$

where A is the wave action, c_x, c_y and c_θ are the propagation speeds in the x-, y- and θ- domains respectively, D_b is the wave energy dissipated by breaking, D_f is the wave energy dissipated by bottom friction, σ is the wave angular frequency and

$$D_v=\sum_{i=1}^{n_{sec}} D_{v,i} \quad (7.5)$$

is the wave energy dissipated by vegetation, where n_{sec} is the number of vegetation vertical sections and $D_{v,i}$ is the short-wave energy dissipation due to the vegetation layer i

$$D_{v,i}=\frac{1}{2\sqrt{\pi}}\rho\widetilde{C_d}b_v N_v\left(\frac{kg}{2\sigma}\right)^3\frac{(\sinh^3 k\alpha_i h-\sinh^3 k\alpha_{i-1}h)+3(\sinh k\alpha_i h-\sinh k\alpha_{i-1}h)}{3k\cosh^3 kh}H_{rms}^3 \quad (7.6)$$

where $\widetilde{C_d}$ is the drag coefficient, ρ is the water density, bv is the vegetation stem diameter, Nv is the number of vegetation stems per m2, k is the wave number, h is the water level, αi is the relative vegetation height for layer i (Mendez & Losada, 2004; Suzuki et al., 2012, van Rooijen et al., 2015)

For each habitat within the study area, a representative vegetation species is assigned based on a cross-comparison between EUNIS habitat mapping and field surveys. The pertinent characteristics of the vegetation, such as the number of vertical sections (n_v), vertical section height (αh), drag coefficient ($\widetilde{C_d}$), stem diameter (b_v), and vegetation density (N) were sourced from relevant literature (Knutson et al., 1982; Garzon et al., 2019; Fernández-Montblanc et al., 2020; van Loon-Steensma et al., 2016) and local expert approach. The specific values employed in the study are presented in Table 2. Vegetation maps for current state (including already performed restoration), dune revegetation, and seagrass revegetation used in XBeach are shown in Figure 7.4a,b, and c respectively.

Table 7.2. Vegetation characteristics associated with EUNIS habitat codes

Species	Associated habitat (EUNIS code)	n_{sec}	αh [m]	$\widetilde{C_d}$ [-]	b_v [m]	N_v [stems/m²]
Ammophila arenaria	Shifting coastal dunes (N14)	1	1	0.7	0.0025	260
Spartina alterniflora	Coastal saltmarshes and saline reedbeds (MA25)	1	0.625	1	0.003	400
Phragmites australis	Reedbeds normally without free-standing water (Q51)	2	0.25 2	0.86 0.86	0.006 0.026	110 110

Posidonia oceanica	Biocenosis of Posidonia oceanica (MB252)	1	0.50	1	0.01	280

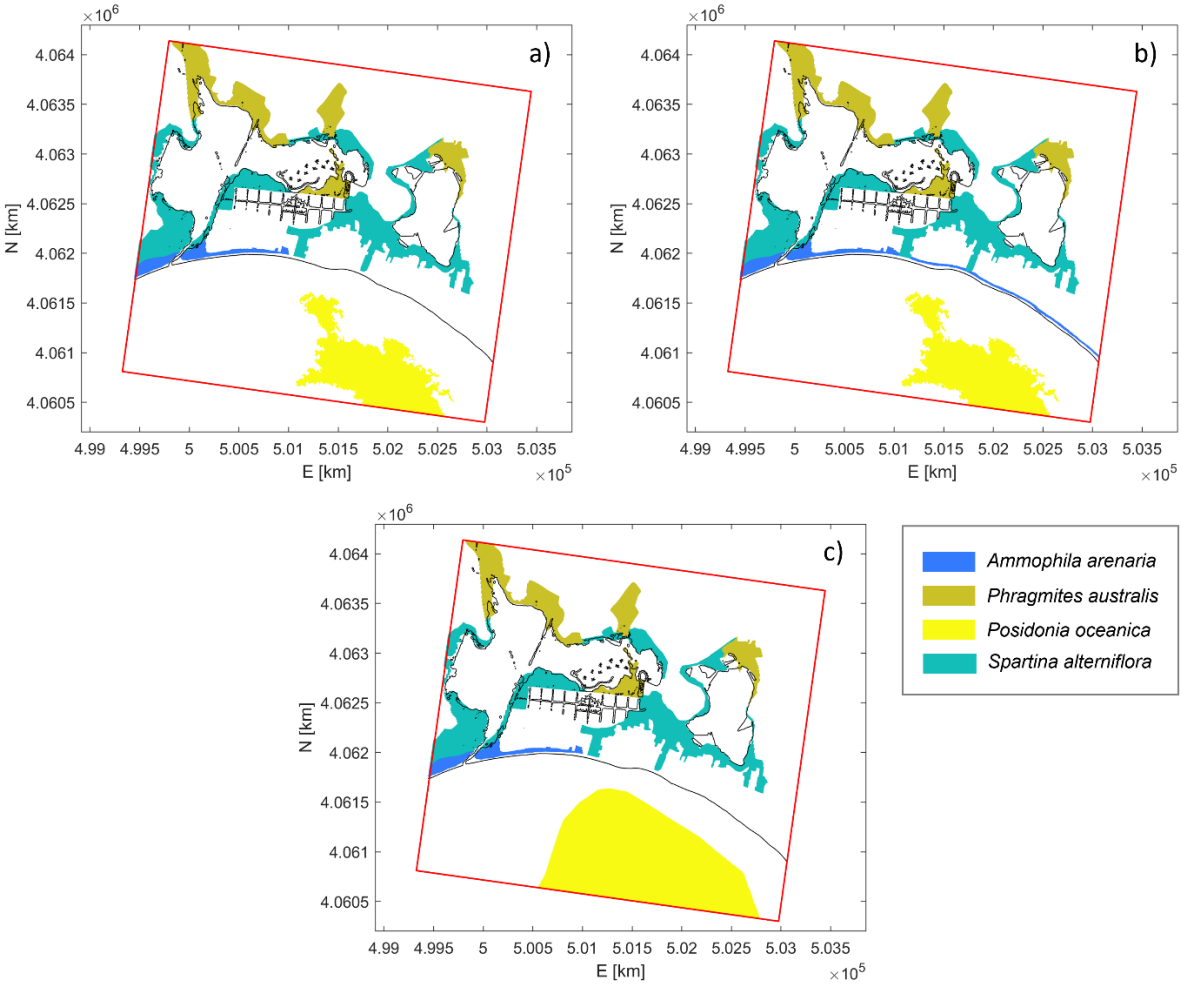

Figure 7.4. Vegetation maps used as inputs in XBeach for: (a) current state, (b) dune revegetation, (c), seagrass revegetation.

7.2.3.Model validation

The model validation is carried out for both SWAN and XBeach, to evaluate hydrodynamic and morphodynamic accuracy of the modelling chain. The model is validated considering a real storm event occurred from 21st of April 2022 06:00 UTM+1 to 22nd April 2022 07:00 UTM+1. The storm lasted 25 hours and reached a Hs at the peak of the storm equal to 4.19 m, measured in the correspondence of a wave buoy, installed by the University of Catania in front of the beach of Granelly in the framework of the INTERREG Italia-Malta Project NEWS. The storm was chosen because its energy was high enough to produce a significant modification of the shoreline, which was clearly detectable from PlanetScope satellite images. Therefore, the shoreline on the 19th of April 2022 was taken as the initial one.

The storm is propagated by the SWAN-Xbeach modelling chain, then the estimated post-storm coastline is compared with the one measured from the first clear available satellite image following the storm, corresponding to the 4th of May 2022. No other storms occurred between the end of the chosen storm event and the 4th of May.

.

In particular, hourly wave data from 20th of April 2022 00:00 UTM+1 to 25th of April 2022 00:00 UTM+1 (120 hours) were extracted from MEDSEA MULTIYEAR WAV 006 012 reanalysis dataset. Data are extracted in the correspondence of the reanalysis model grid point closest to the SWAN offshore boundary (36.4792 lat, 15.0000 lon). Then, each hourly seastate was simulated, for a total of 120 SWAN simulations. Figure 7.5 shows the significant wave height measured by the wave buoy (blue line) and the model prediction (black dots).

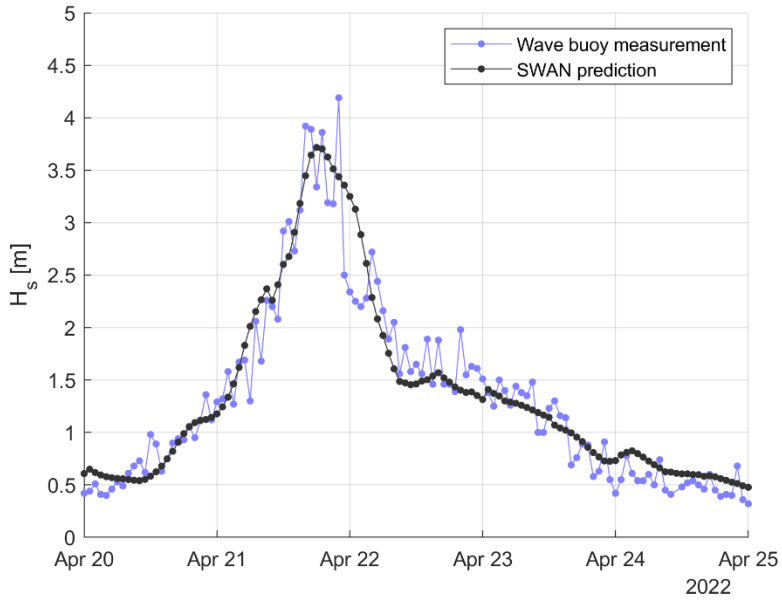

Figure 7.5. Significant wave height of the storm used for validation of the model, measured by local wave buoy (blue) and SWAN prediction at the grid node closest to buoy position (black).

To assess SWAN model prediction performance, the following metrics are computed:

$$B = \frac{1}{N}\sum_{i=1}^{N}(H_{s,mod,i} - H_{s,obs,i}) \qquad (7.7)$$

where B stands for Bias, and it is an indicator of the tendency of the model to over- or under-predict observed values, N is the number of samples, and $H_{s,obs,i}$ and $H_{s,mod,i}$ are the i-th observed and modelled significant wave heights respectively;

$$RMSE = \sqrt{\frac{1}{N}\sum_{i=1}^{N}\left(H_{s,obs,i} - H_{s,mod,i}\right)^2} \tag{7.8}$$

where $RMSE$ stands for root-mean square error and it is a dimensional metric to quantify accuracy of the model to reproduce observed values, and

$$WSS = 1 - \frac{\sum_{i=1}^{N}\left(H_{s,obs,i} - H_{s,mod,i}\right)^2}{\sum_{i=1}^{N}\left(\left|H_{s,mod,i} - \langle H_{s,obs}\rangle\right| + \left|H_{s,obs,i} - \langle H_{s,obs}\rangle\right|\right)^2} \tag{7.9}$$

where WSS is the Willmott Skill Score, also known as Willmott agreement index (Willmott, 1981), which is a nondimensionalized indicator of the agreement between predicted and observed values, ranging from 0 (complete disagreement) to 1 (perfect agreement).

Bias resulted equal to 0.02 m, resulting in the model not having a strong tendency to over- or under-estimate observed values. RMSE resulted equal to 0.37 m, whereas WSS is equal to 0.95, showing a highly satisfactory agreement between model and measured values.

In the following, the validation of the capabilities of XBeach to correctly predict storm morphodynamics is illustrated. Preliminarly, it should be recalled that XBeach allows to decouple hydrodynamic and morphodynamic time by means of morphodynamic acceleration. In other words, morphological changes can be accelerated by a certain morphodynamic factor (up to 10), by keeping the same duration of the hydrodynamic event. Given the above, the following procedure is carried out:

(i) Five sea states have been chosen from the selected storm, with each sea state being 5 hours apart from the next one.
(ii) Five runs have been performed to simulate the above mentioned five sea states, with XBeach simulating 0.5 hours of hydrodynamic time and 5 hours of morphodynamic time, with a morphodynamic acceleration factor equal to 10.
(iii) After the first simulation is run (simulating sea state no.1), the final bed elevation of simulation n.1 is extracted and given as a bed elevation input to simulation no.2 (simulating sea states no.2).
(iv) The procedure is repeated up to simulation no. 5.
(v) The location of the computed shoreline after simulation no. 5 (sea state no.5), corresponding to 25 hours after the beginning of the storm, is extracted and compared with the post-storm coastline obtained from satellite image after the storm, corresponding to the 4th of May 2022.

Figure 7.6 shows the sea-states generated in XBeach with the abovementioned methodology.

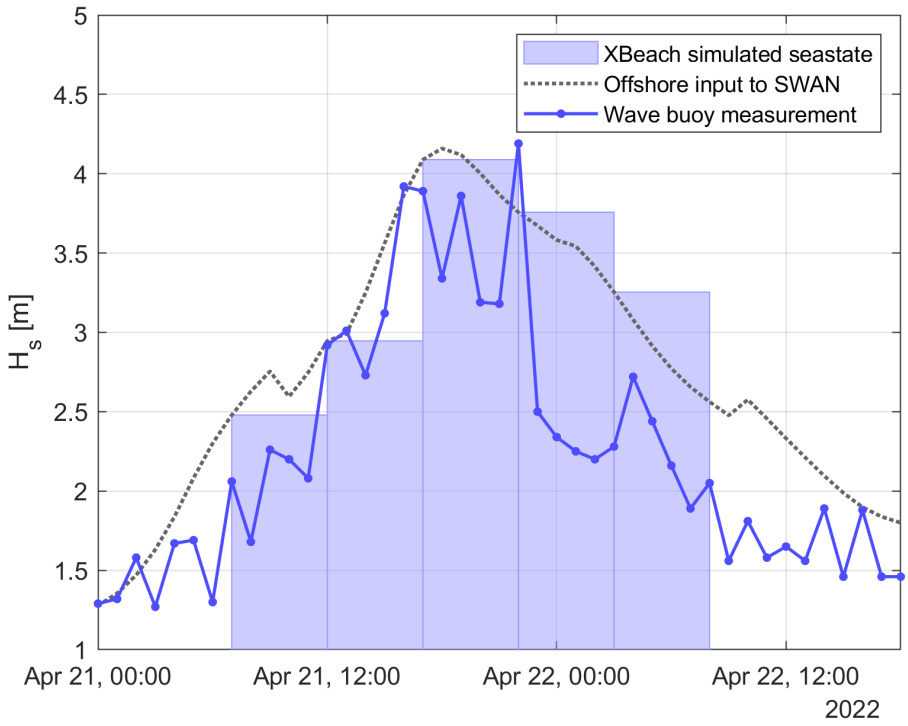

Figure 7.6. Storm seastates generated for validation

Figure 7.7 shows the pre-storm (blue line), post-storm (green line) shorelines obtained from satellite imagery and post-storm shoreline predicted by the model (red line). To evaluate the performance of the model setup in reproducing correctly storm morphodynamics of the site, the post-storm shoreline obtained from satellite imagery is compared with the one resulted from the model simulations. In order to quantify the comparison, 30 transects orthogonal to the pre-storm shoreline are considered. For each transect, the distance between observed pre-storm and observed (d_{obs}) and modelled (d_{mod}) post-storm shorelines is measured. To assess prediction skill of the model, the following metrics are computed

$$B = \frac{1}{N}\sum_{i=1}^{N}(d_{mod,i} - d_{obs,i}) \qquad (7.10)$$

where B stands for Bias, N is the number of samples, and $d_{mod,i}$ and $d_{mod,i}$ are the i-th observed and modelled significant wave heights respectively; and the RMSE

$$RMSE = \sqrt{\frac{1}{N}\sum_{i=1}^{N}\left(d_{mod,i} - d_{obs,i}\right)^2} \qquad (7.11)$$

Bias resulted equal to 0.91 m, i.e. 6.7% of the average beach observed retreat at each transect (14.28 m), revealing only a minor tendency of the modelled shoreline to retreat, i.e. over-predicting erosion, whereas RMSE resulted equal to 2.55 m.

Moreover, the Brier Skill Score, or BSS (Sutherland, 2004) is computed. The BSS is a commonly used score in coastal modelling to validate morphodynamic modelling by comparing modelled and observed post-storm beach profiles with a pre-storm baseline. In this application, since data pre- (nor post-) storm observations

of beach profiles are not available, BSS is applied to shoreline change. BSS is calculated according to the Murphy-Epstein decomposition (Murphy and Epstein, 1989):

$$BSS = \frac{\alpha-\beta-\gamma+\varepsilon}{1+\varepsilon} \tag{7.12}$$

where

$$\alpha = r^2 \tag{7.13}$$

$$\beta = \left(r - \frac{\sigma_{d,mod}}{\sigma_{d,obs}}\right)^2 \tag{7.14}$$

$$\gamma = \left(\frac{\langle d_{mod}\rangle - \langle d_{obs}\rangle}{\sigma_{d,obs}}\right)^2 \tag{7.15}$$

$$\varepsilon = \left(\frac{\langle d_{obs}\rangle}{\sigma_{d,obs}}\right)^2 \tag{7.16}$$

where r is the correlation coefficient between d_{obs} and d_{mod}, $\sigma_{d,obs}$ and $\sigma_{d,mod}$ indicate the standard deviation of d_{obs} and d_{mod} respectively, and angular brackets denote the mean of a set of observations/predictions. Perfect modelling would lead to $\alpha = 1$, $\beta = 0$ and $\gamma = 0$, and therefore to a BSS = 1. Results from our model give $\alpha = 0.79$, $\beta = 0.09$ and $\gamma = 0.04$, leading to a BSS equal to 0.97, therefore resulting in an excellent satisfactory shoreline change prediction skill of our model.

Largest discrepancies were observed in the proximity of the lagoon-sea channel, up to 6.42 m at transect V3. This is due to the inherent morphological dynamic of the estuarine region, which is also influenced by the river discharges, which are not integrated in the model yet. In any case, since the focus of the present study is to assess the capability of the NBS to reduce erosion and flooding risk in the city area, their influence on the evolution of the estuarine mouth is presently not taken into account in the investigation.

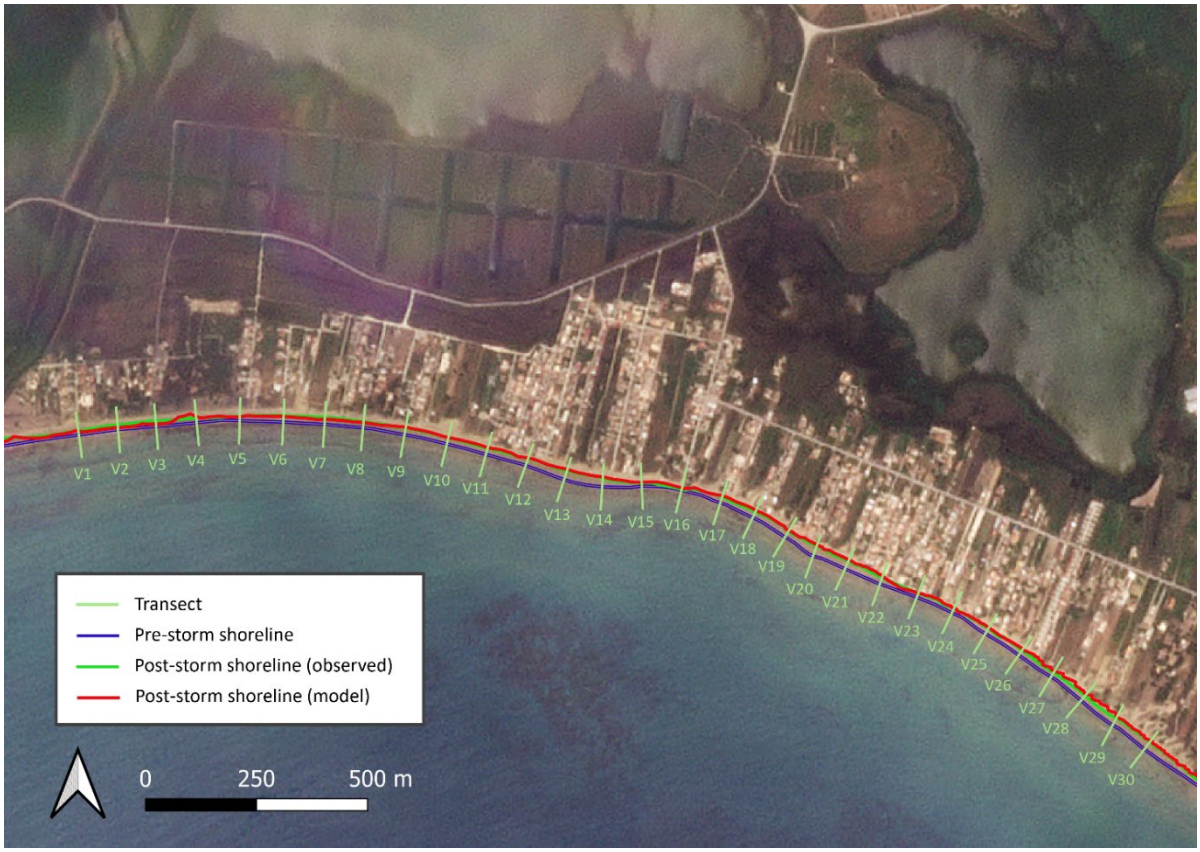

Figure 7.7. Pre-storm (blue line), post-storm (green line) shorelines obtained from satellite imagery and post-storm shoreline predicted by our model (red line). The figure shows the position of the 30 transects along which shoreline observed and predicted

8. Multi-hazard forecasting (including a multidisciplinary calibration) and application limits Vistula Lagoon (IBW).

8.1. Introduction

Vistula Lagoon is generally isolated from direct effects of sea level rise and increasing storminess. It is separated from the Baltic Sea by a very robust wide coastal barrier (about 1.5 km) and several swathes of high dunes (up to 20 m high). The dunes are additionally stabilized by forestation. Being located inside the Gulf of Gdańsk, the barrier is protected from the most powerful storms. Thus, even the most pessimistic climatic scenarios (RCP 8.5) do not anticipate breaching events of that barrier. The Vistula Lagoon has a very mild wave climate itself, being a very shallow water body (ca. 2.5 m depth on average). The main hydrodynamic phenomenon are wind driven storm surges, which can be very high and exceed 1.5m. The most exposed areas are located in the SW corner of the Lagoon, see Figure 8.1. This area is heavily protected, and remains outside the REST-COAST project. In all, the effects of sea level rise will be generally static for most banks of the Lagoon. As they are largely uninhabited and pristine, the ensuing permanent flooding will be acceptable. Another issue is the winter ice action; ice sheets often develop due to very shallow depths of the Lagoon and the associated rapid cooling of the water column in winter. Ice usually exerts tremendous forces on any man-made structures. In this context, studies on multi-hazard forecasting and application limits are mainly associated with the limits of application of NbS during design, erection and operation of the currently constructed artificial island – Vistula Lagoon pilot in the REST-COAST project, intended to serve as biodiversity restoration effort by creating a habitat for birds hatching on meadows, water birds and waders, see Figure 8.1.

Figure 8.1. Location of artificial island – study site in the Polish part of Vistula Lagoon: source – public domain, adapted by G. Różyński.

8.1.2. Coastal and marine environments of Vistula Lagoon simulations.

High end IPCC sea level rise predictions along the Polish coast, located at the southernmost part of the Baltic Sea Baltic, are in the range of 0.7 – 0.9 m by the end of 21st Century, incl. the glacial isostatic adjustment. It

will impact the western corner of the Lagoon - depression pertaining to Vistula Lagoon River Delta – cf. Figure 8.1. This vast issue is beyond the REST-COAST project – dikes securing the delta are being refurbished now and will have to be elevated further to secure future safety and ensure sustainable farming in the delta. Hence, IBW does not plan any studies related to remediation of sea lever rise aftermaths in the delta. Second, breaching of the barrier separating the Lagoon from the Baltic Sea is very unlikely as well, incl. the highest seawater levels. Thus, this problem is also beyond the scope of the studied pilot site.

The criteria that determine the efficiency of multi-hazard forecasting and application limits at Vistula Lagoon pilot are concentrated on: (1) minimization of impact of the placement of the island on hydrodynamics that controls local sediment transport patterns and adjacent morphodynamics, which is aimed at respecting the NbS approach, (2) maximization of the use of natural materials during the construction of the rim of the island, also being consistent with NbS paradigm, and (3) harnessing secondary by-effects, resulting from the erection of the island, namely gradual, spontaneous appearance of reed fields around the rim (aimed at creation of additional spawning grounds for local fish populations) and partial denitrification of water returning to the Lagoon after deposition of dredged sediment. The main criterion regarding the rim is the required resilience against ice action. The main rationale regarding the island location is minimum change of wave and current fields forced by winds blowing from directions producing the largest fetch, i.e. NE and SW. The harnessing of by-effects is also consistent with the NbS approach.

8.2. High resolution coupled coastal models

Hydrodynamic simulations were executed to evaluate the change of wave and current fields in the Lagoon after construction of the island. The DELFT3D package was used for this purpose.

Figure 8.2 presents the adopted numerical grid for DELFT3D simulations. It covers the entire Vistula Lagoon (both Polish and Russian part) to reproduce the wave and current fields with utmost precision.

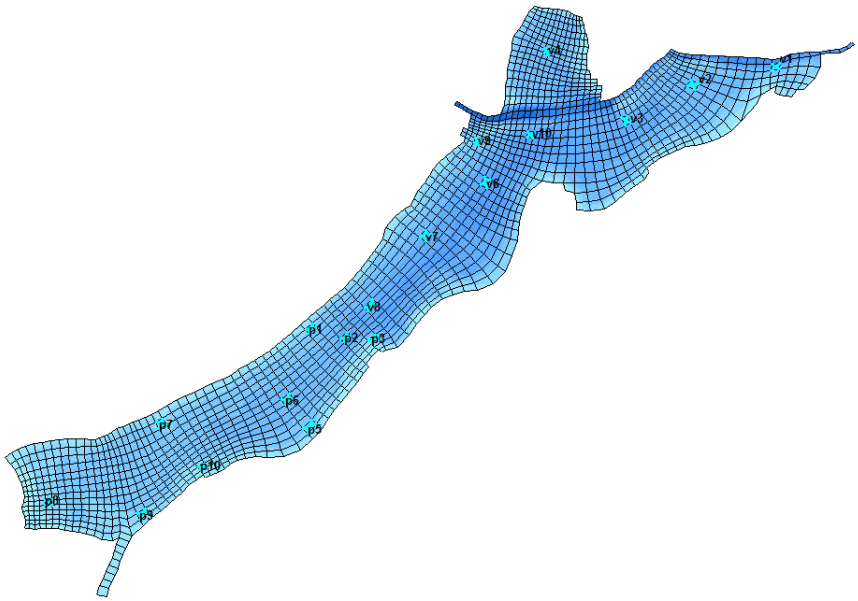

Figure 8.2. Curvilinear numerical grid adopted for DELFT3D simulations of wave and current fields in Vistula Lagoon; source IBW PAN.

Consequently, Figure 8.3 presents a detailed bathymetric map of the Lagoon – hi-res bathymetric data (consistent with hi-res numerical grid) was used in all simulations to include local seabed relief, particularly near the anticipated area of the placement of the artificial island. Interestingly, a generally shallow character of the Lagoon (especially the Polish part) is evident – we can also see artificial navigation channel in the Russian side leading to the main harbor in Kaliningrad.

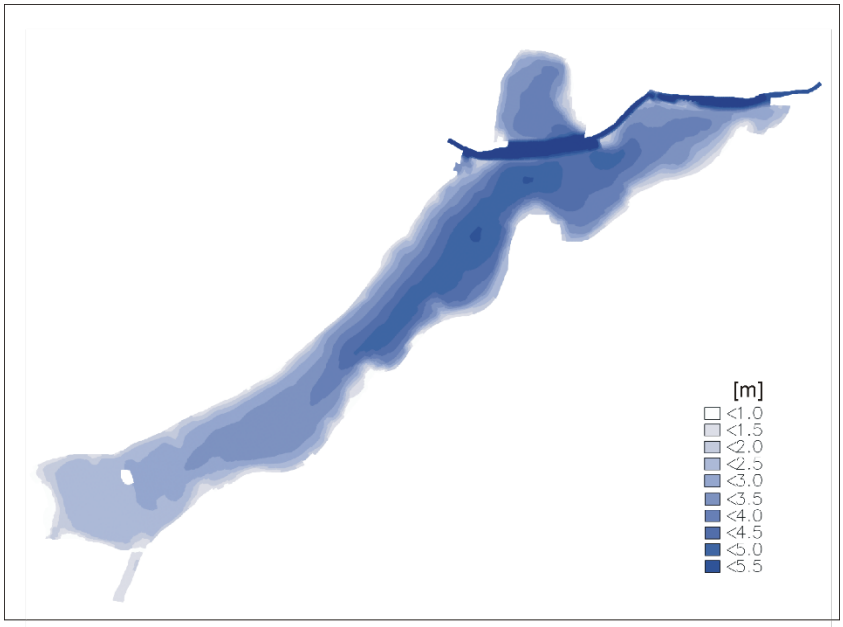

Figure 8.3. Bathymetry of Vistula Lagoon used in simulations of wave and current fields before and after construction of the artificial island: source IBW PAN.

Finally, Figure 8.4 presents the main purpose of the modeling, i.e. determination of the placement of the new island. It could be done after determination of the location of offshore approach harbor, which was entirely beyond the scope of the REST-COAST project. Approximate placement of the island was determined bearing in mind minimization of costs of dredging operations, while respecting integrity of the adjacent spawning grounds. Hence, optimization of the ultimate placement with the DELFT3D modeling was based on minimization of alterations of hydrodynamics (waves and currents) near the island after its completion.

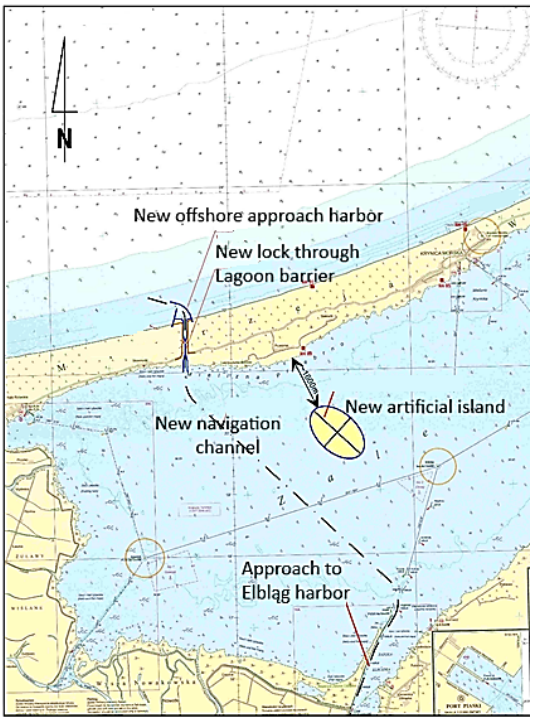

Figure 8.4. Placement of artificial island serving as biodiversity restoration site in Vistula Lagoon: source – IBW PAN.

The investigations of possible NbS solutions of the rim required execution of consolidation tests of sediment samples from the Lagoon seabed. They featured clays and silts with sizable admixtures of organic material (ca. 3% – 5%). Consequently, their natural water content is very high (between 50% - 120%) resulting in very low strength parameters against structural loads. Figure 8.5 shows the results of edometric tests of one of sediment samples with organic matter content in the range of 2.5%. The curves demonstrate the change of sample height in time for a given load – in each next step the load is doubled. Although edometric analyses are not hi-res coastal models, Figure 8.5 demonstrates their time consuming aspect: each test required about 7 days to obtain a curve for a given load range – in all 6 tests consumed almost a month and a half to be complete the tests for just 1 sample.

The results of edometric analyses were used for determination of strength parameters of lagoon sediments; those parameters were then used to establish the feasibility of NbS approach to the construction of the rim, see next section.

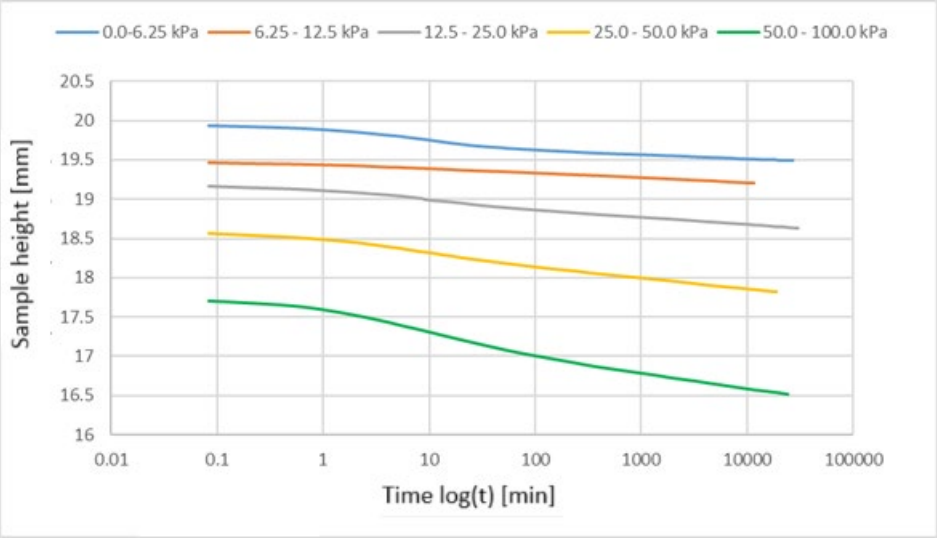

Figure 8.5. Edometric curves describing time needed for stabilization of standard sediment sample under given loads: source IBW PAN.

8.3. Parameterization of hydrodynamic-morphological and ecological interactions to simulate ESS impacts.

As mentioned before, the placement of artificial island on Vistula Lagoon was primarily dictated by protection of existing spawning grounds in the area considered for the placement. The main ecological premise was dictated by minimization of local hydrodynamic fields (waves and surface currents). DELFT3D simulations were forced by winds blowing from NE and SW, that is along the longer axis of the Lagoon, producing the longest fetches. Figure 8.6 demonstrates the results for the sustained wind speed of 15 m/s (corresponding to the return period of 50 years) blowing from NE, that is along the whole Lagoon from the Russian part down to the Polish one. The corresponding Figure 8.7 exhibits the concomitant fields of surface currents. In all, it can be concluded that indeed the impact of the island on adjacent hydrodynamic fields is negligible. In other words, the island will not impair local ESS for even the most powerful winds. Moreover, it will be providing habitat for birds, predominantly those hatching of meadows, whose populations have been declining in recent years due to general land use changes in Vistula Lagoon region. Furthermore, it is expected that the rim of the island will gradually transform into a new spawning ground (ca. 10 ha) contributing to local biodiversity.

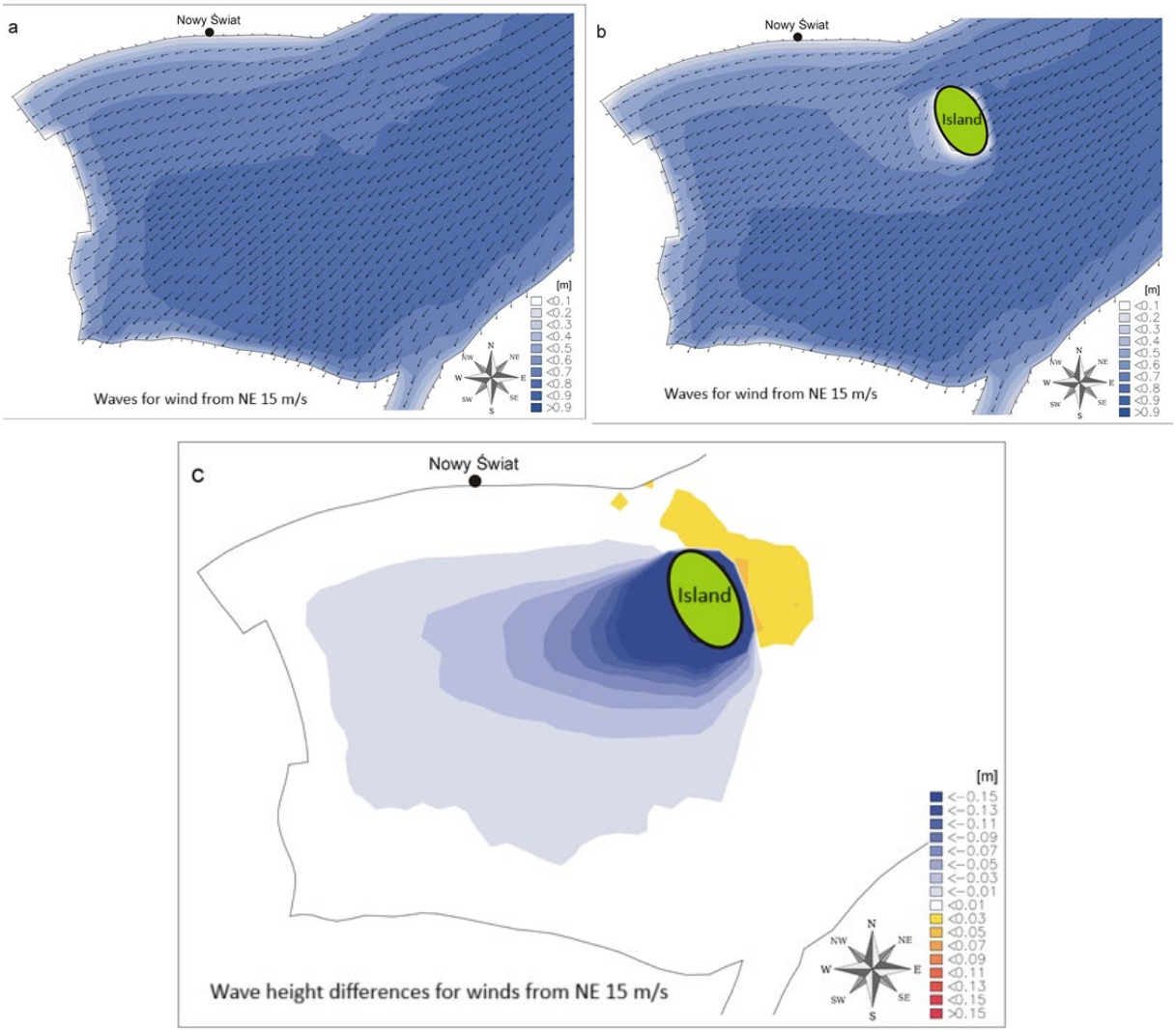

Figure 8.6. Wave fields for wind from NE 15 m/s with and without artificial island.

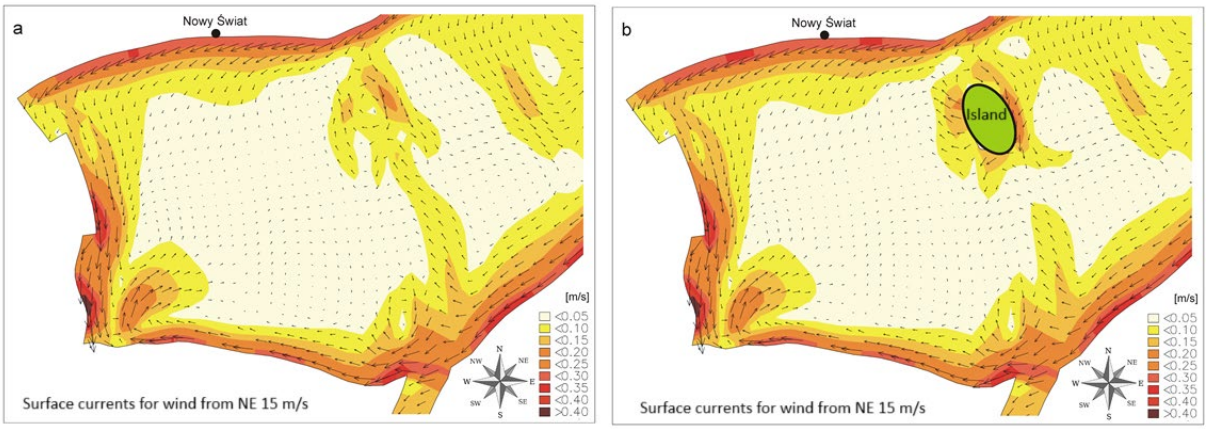

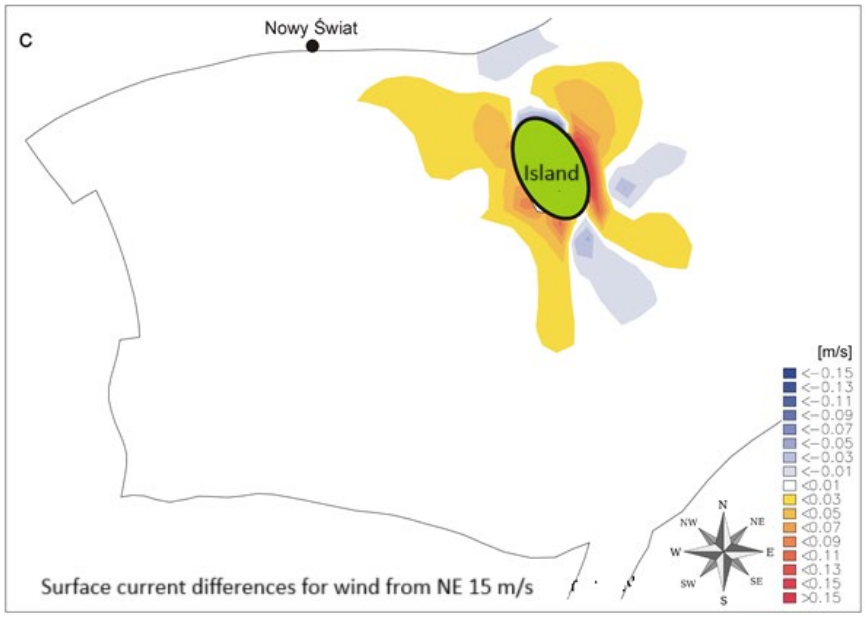

Figure 8.7. Surface current fields for wind from NE 15 m/s with and without artificial island.

In brief the parameterization of interactions between hydro- and morphodynamic forcings and ecological response was aimed at minimum interference of ESS in Vistula Lagoon. Here, this minimization was achieved by achieving minimum disturbances to hydrodynamics (and the resulting morphodynamic response) by induced by new artificial island, serving as safe habitat for birds, predominantly those hatching on meadows.

Construction of the rim encircling interior of the artificial island also underwent vast considerations regarding ESS. The initial concept, presented in Figure 8.8, favored natural materials for the rim. It demonstrates geo-tubes, located at the inner and outer foot and on the top of the rim. Their cores are composed of sand and the whole structure is topped with a heavy stone armor resisting ice action.

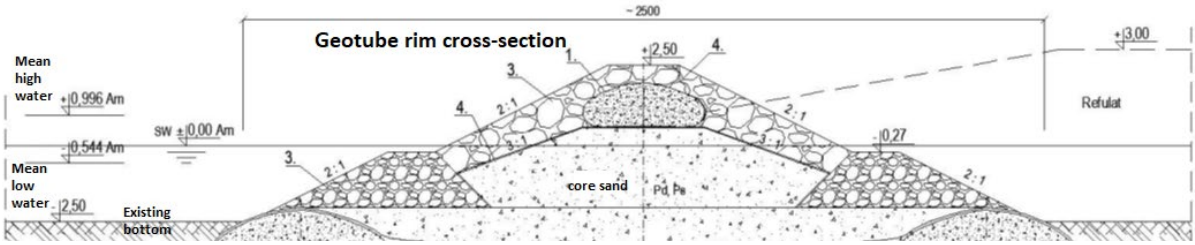

Figure 8.8. Initial concept of rim employing geo-tubes with local sediment, source Maritime Office Gdynia.

This concept had to be discarded after the execution of strength tests of lagoon bed soil samples, cf. Figure 8.5. They revealed clays and silts with sizable admixtures of organic material (ca. 3% – 5%). Consequently, their natural water content was found to be very high (between 50% - 120%) resulting in very low strength parameters against structural loads. Therefore, implementation of the concept shown in Figure 8.8 would certainly trigger very high and uneven subsidence of the rim. Thus, traditional engineering methods had to be used to construct the rim, cf. Figure 8.9. The rim is ca. 5000 m long. It consists of two rows of Larsen sheet piles (each unit is 13 m long: 9 m driven through organic soils down to a stable sand layer, 2 m across the water column and 2 m above mean water level in Vistula Lagoon). Both rows are braced together on top and

filled with stone armor to resist ice action. The length of units demonstrates difficulties related to ultra-low strength parameters of the Lagoon's bed; they had to be driven to a depth securing safe contact with sand underlying thick organic sediments to ensure structural stability of the rim. The completed rim is presented in Figure 8.10. Heavy stone armor provides safety from sea level rise, and predominantly, from tremendous forces generated by ice in winters. In this way, limitations of NbS solutions in basins where the bed is composed of thick layers of organic sediments were identified and could be highlighted. Simultaneously, we could parameterize the ESS for such sedimentary conditions, very common in many lagoons. Here, minimization of the impacts on ESS consists in minimization of maintenance works of the rim had its the geo-bag variant been selected.

Figure 8.9. Rim under construction, made of two rows of sheet piles with stone armor gradually forming the crest between them: source - courtesy NDI group.

Figure 8.10. The rim of artificial island, Sept. 2023: source - REST-COAST.

The lessons learned during implementation of the artificial island vis a vis parameterization of ESS included two important by-effects. First, upon consultations with ichthyologists it was determined that reeds will gradually appear spontaneously around the island rim. Given its length of ca. 5000 m and conservatively assuming the width of 20 m we can expect additional spawning grounds of 5000·20 = 100000 m^2 (10 ha). Other associated ESS will include formation of habitat for insects on which both juvenile fish and birds living on the island will feed. Parameterization of this ESS will be possible when spontaneous development of reed field is initiated.

Second, in extra denitrification of effluent returning to the Lagoon after delivering sediment to the island provides another positive by-effect. This benefit is occurring in sedimentation tanks for the effluent, where it passes through jute rollers containing vegetation capable of its partial denitrification, see Figure 8.11. Upon trial-and-error the following plants were found suitable for this task: sweet flag (Acorus calamus L.), greater tussock-sedge (Carex paniculata L.), great manna grass (Glyceria maxima [Hartm.] Holmb.), common rush (Juncus effuses L.), lesser bulrush (Typha angustifolia L.) and common bulrush (Typha latifolia L.). Further works are needed to determine the efficiency of denitrification by evaluation of nutrient concentrations in the effluent vis a vis those in the water column.

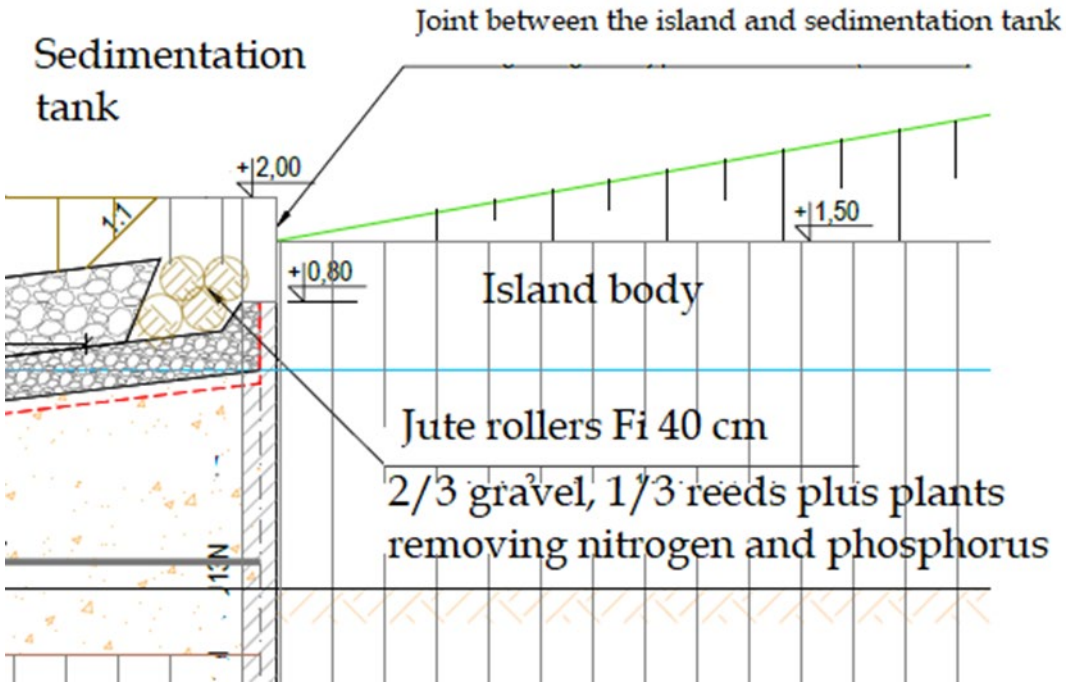

Figure 8.11. Denitrification by jute rollers containing reeds that denitrify effluent returning to Vistula Lagoon after deposition of sediment.

8.4. Hazard reduction from ESS as a function of restoration scale.

As Vistula Lagoon is generally sheltered from the effects of climate change (sea level rise and increased storminess) the focus of analyses presented herein was concentrated on the limits of NbS applied in shallow coastal lagoons (minimization of impacts on hydro- and morphodynamics by artificial island, minimization of maintenance works of the rim). It can be crudely (but safely) assumed that in sheltered areas there should be a general linear dependence between the physical scale of restoration and its impacts on ESS (in the absence of sea level rise). Linear relationships mean that greater physical scales imply greater ecological

effects (in Vistula Lagoon the number of specimen of restored bird populations). Greater scales also dictate greater hydro- and morphodynamic impacts (despite their minimization criterion). Therefore, each site will require studies on maximum 'carrying capacity' of hard restoration efforts. In other words, maximum permissible dimensions of such structures will be defined by the maximum permissible hydro- and/or morphodynamic impacts. The only exception is the by-effect related to denitrification of water returning to the lagoon; it can be used for general improvement of water quality in highly eutrophicated basins (like Vistula Lagoon) by installation of a large number of floating islands extracting nutrients during the vegetation season (spring, summer), see concept in Figure 8.12. In autumn the harvest is physically removed and dumped outside the Lagoon. The floating islands bear little negative ecological impacts, so their restoration scales can be very large. However, their main prohibitive element is related to high operating costs of such schemes – the islands must be towed to ports for wintering to avoid damages by ice.

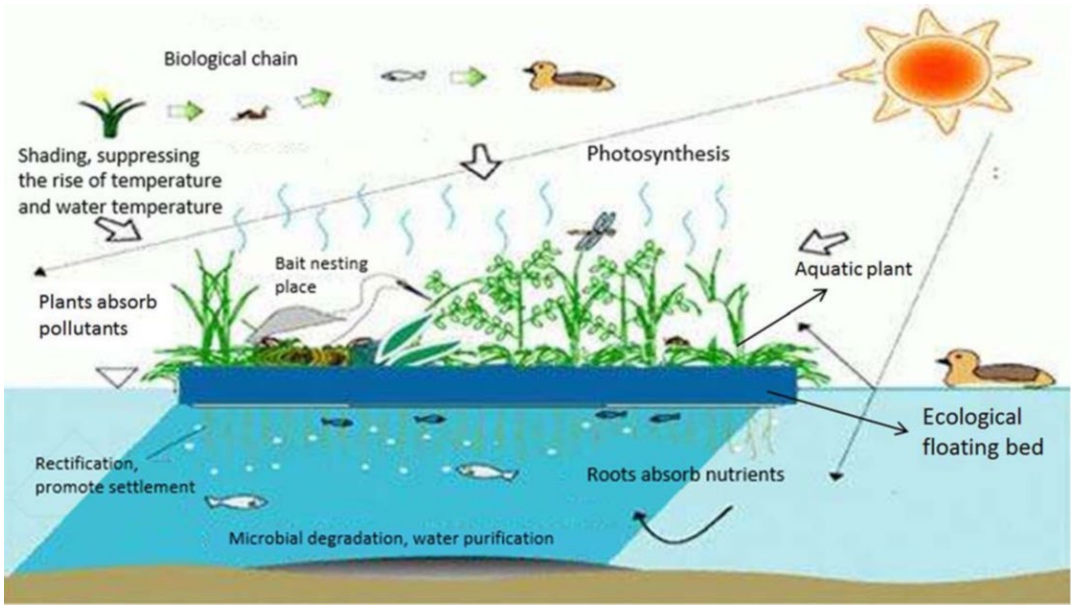

Figure 8.12. Concept of artificial island: source – Environ. Sci. Pollut. Res. (2021) 28:40075–40087.

8.5. Conclusions

This pilot site is primarily aimed and biodiversity restoration and conservation of birds deemed important elements of the local ecosystem. Vistula Lagoon is both NATURA 2000 area for both birds (PLB280010) and habitats (PLH280007). This explains the efforts aimed at biodiversity restoration. Simultaneously, one of key characteristics of the Lagoon is its almost perfect sheltering from climate change consequences, apart from its south western corner, which is entirely outside the REST-COAST project. Therefore, climate change consequences are of secondary importance at the study site. The general lesson learned are the limitations of NBS in terms of maximum permissible alterations to local hydro- and morphodynamics induced by hard artificial structures serving as habitat for targeted species (birds in case of Vistula Lagoon). The term 'maximum permissible alterations' means that (theoretically) there are maximum physical dimensions of an artificial island to be located in the Vistula Lagoon. Such considerations can serve as blueprint for similar analyses elsewhere. The second issue is minimization of maintenance costs of the island's rim and the resulting choice of hard engineering structures at a site with thick organic layers forming the seabed. Again, the work done here (determination of strength parameters of the lagoon bed) can serve as a blueprint for similar studies. Finally, utilization of by-effects can be recommended in future (biodiversity) restoration

efforts. The vision of artificial islands can become materialized to meet the WFD targets at highly eutrophicated basins. In this context ice appears to be the main impediment, yielding high operational costs. However, such installations are plausible in warmer areas, where forces generated by ice do not exist.

9. Integrated conclusions

This section presents the integrated conclusions of Deliverable D2.1, highlighting the outcomes of modelling-supported risk reduction across the pilot sites addressed in Task 2.1. The results focus on multi-hazard assessments under present-day conditions, based on the implementation and validation of coupled hydro-morpho-eco models that incorporate ecosystem services (ESS). These modelling efforts enable a rigorous evaluation of the capacity of nature-based solutions to mitigate coastal risks such as flooding, erosion, and salinisation across diverse geomorphological and socio-ecological contexts

Contribution of the Ebro Delta Pilot

In the Ebro Delta Pilot, the modelling approach combines fluvial and coastal processes to evaluate the potential of nature-based solutions (NbS) in reducing erosion and flood risks during storm events. The work focuses on sediment fluxes along the Ebro River and their interaction with deltaic dynamics, particularly under controlled flood conditions aimed at re-establishing sediment continuity disrupted by upstream dams.

A 2D river sediment transport model was validated using continuous discharge and water level data from the SAIH network, as well as field measurements of turbidity and velocity collected during the May 2022 controlled flood. These controlled releases—temporarily halted due to the ongoing drought—were designed to test sediment bypassing strategies and inform future large-scale restoration interventions. Complementary assessments, including sediment carrying capacity under varying hydrological regimes, were presented at the Coastal Sediments 2023 conference.

Downstream, coastal dynamics were simulated using a nested suite of hydro-morphodynamic models based on COAWST and XBeach, which were validated using storm Gloria (2020), the most extreme event recorded in the region. The modelling chain downscales CMEMS forecasts through COAWST to high-resolution XBeach grids, using MPI-enabled parallelisation and automated post-processing tools (Python and MATLAB) to optimise computational performance.

The model suite demonstrated a high level of accuracy, with RMSE for significant wave height reduced to 0.3 m at storm peak. Current simulations focus on storm sequences between 2020 and 2023, using remote sensing data from ICGC (satellite, LiDAR and orthophotos) to assess the effectiveness of existing NbS—such as dune recovery and sediment redistribution—in mitigating erosion and coastal flooding.

This integrated modelling approach supports both operational forecasting and restoration planning, providing a science-based framework to quantify the benefits and trade-offs of sediment management and ecosystem restoration in a dynamic deltaic environment.

Contribution of the Wadden Sea Pilot

In the Wadden Sea Pilot, partners have developed and validated high-resolution coupled hydro-morphodynamic models to assess risk reduction through nature-based solutions (NbS) under storm conditions. The modelling contributions from Deltares, NLWKN, and Hereon cover the Ems-Dollard estuary, Ley Bay, and the broader German Bight, respectively, with a shared focus on key ecosystem services (ESS) such as reduction of coastal flooding, wave attenuation, erosion mitigation, sediment retention, and water quality improvement.

Deltares focused on morphodynamic modelling of the Ems-Dollard estuary using Delft3D Flexible Mesh, applying a nested modelling approach to simulate sediment transport and morphological evolution during extreme events. Calibration was supported by bathymetric data (vaklodingen, EMODnet, and DGM) and boundary conditions from the Dutch Continental Shelf Model. Validation was carried out using storms Xaver (2013) and Herwart (2017), with the best wave calibration achieved using the Schiermonnikoog Noord station. The model chain simulated wave and tide conditions using synthetic spring-neap cycles, and was

tested for its capacity to reproduce water levels and sediment redistribution during high-energy conditions. The modelling strategy also included the computation of turbidity and blue carbon changes, with outputs classified into EUNIS biotopes to support habitat-based planning.

NLWKN developed a high-resolution Delft3D model in Ley Bay (Oster-Ems) to analyse the effect of saltmarshes as NbS on hydrodynamic attenuation and sediment trapping during storm events. The model incorporated five open boundaries and was calibrated using LiDAR bathymetry and in-situ observations from 2015. Performance was validated for multiple storm scenarios, including Xaver and Herwart, using a classification based on wave height and tidal anomaly (Hs + TA > 3.4 m). Comparative runs with and without NbS showed that saltmarshes significantly reduce wave heights and promote sediment deposition. These effects were analysed for different storm intensities and saltmarsh configurations, with statistical agreement (e.g., $R^2 = 0.95$ for water level prediction and RMSE = 0.22 m) confirming model reliability.

Hereon applied a coupled SCHISM-XBeach framework to evaluate the protective effect of seagrass meadows on coastal dynamics in the German Bight. The system includes advanced modules for vegetation (rigid cylinder approximation), sediment (SED3D), and waves (WWM III). More than 110 restoration scenarios were simulated, testing variations in seagrass extent, density, and spatial configuration. The results, focused on the October 2017 storm (Herwart), showed that seagrass reduces current velocities by up to 80% in shallow zones and significantly attenuates wave heights—by more than 40 cm in some areas. These effects were strongest in shallow intertidal zones and barrier island fronts. Simulations also highlighted the importance of meadow placement and structure in maximising protection and enhancing sediment stability.

Overall, the Wadden Sea modelling confirms that well-designed NbS—saltmarshes and seagrass meadows—can substantially reduce wave energy, flow velocities and erosion under storm conditions. The comprehensive validation with storm events ensures that the predicted ESS performance is robust and applicable to planning and decision-making in this dynamic coastal region.

Contribution of the Venice Lagoon Pilot

In the Venice Lagoon Pilot, a high-resolution operational modelling system was developed to assess the impact of nature-based solutions (NbS)—specifically seagrass meadows and wetlands—on wave attenuation and current reduction during storm events. The modelling framework couples the SHYFEM hydrodynamic model with the WAVEWATCH III (WW3) wave model, both implemented on a shared unstructured-grid mesh covering the entire lagoon and adjacent coastal waters. Bathymetric data were obtained from EMODnet and local high-resolution LIDAR surveys, with grid generation carried out using GMSH and BLENDER-based tools.

Vegetation effects were explicitly included in both circulation and wave modules. In SHYFEM, seagrass-induced form drag was parameterised following established approaches (Beudin et al., 2017; Zhang et al., 2019), while WW3 included vegetation-based wave dissipation terms based on the formulation of Dalrymple et al. (1984) and Mendez & Losada (2004). The dominant species modelled was Zostera marina, with vegetation parameters derived from the Atlante della Laguna and literature values (Mazzella et al., 1998). Wetlands were represented as islets, introducing hydraulic roughness and flow constriction effects.

The model was validated in hindcast mode using multi-year data (2020–2022) and observations from the CNR “Acqua Alta” oceanographic platform. Simulated storm conditions were used to quantify ecosystem services (ESS) through comparisons of configurations with and without NbS. Key results include:

1. Reduction of wave heights by 15% on average due to seagrass, with local reductions exceeding 30% in vegetated sectors; wetlands contributed an even larger damping effect.
2. Decrease in bottom water velocity in vegetated zones, particularly in the southern and central lagoon where NbS are more extensive.

3. Lower water levels by up to 5% in NbS-covered areas during storm surges.

However, the inclusion of vegetation also introduced redistribution effects: increased bottom velocities were observed in deeper unvegetated channels and in areas where wetlands reduced flow cross-section, such as north of Murano. This highlights the importance of detailed spatial planning in restoration design.

These results confirm that NbS significantly enhance storm resilience in the Venice Lagoon, while also pointing to trade-offs that must be considered in the planning of restoration strategies integrated with MOSE barrier operations.

Contribution of the Rhone Delta Pilot

In the Rhone Delta Pilot, a comprehensive modelling framework has been developed to assess the impact of restoration interventions on coastal hazards and key ecosystem services (ESS) under storm conditions. The site, a 6,527 ha former industrial saltwork area, has undergone passive and active restoration measures, including the deliberate non-maintenance of sea dikes, reconnection with agricultural catchments, and the establishment of hydraulic connectivity with the Vaccarès Lagoon system. These interventions promote natural coastal dynamics while enhancing biodiversity, habitat recovery and ESS delivery.

To support the assessment of ESS such as coastal flood and erosion risk reduction, water quality regulation, and fish provisioning, five numerical models were applied:

1. Three TELEMAC-2D hydro-saline models simulate salinity, water temperature and hydrodynamic behaviour under “before” and “after” restoration conditions using identical grids with updated topo-bathymetry. One model focuses on the pilot site, another on its surrounding lagoon system, and a third explores upscaling effects under different hydraulic connection scenarios.
2. The XBeach model, coupled with TOMAWAC, simulates storm-driven morphological dynamics (e.g., overwash and breaching) in the southern section of the site, where new beach formations and sea connections have developed. Storm scenarios showed the capacity of these restored areas to absorb wave energy and reduce erosion risk, supporting the viability of passive NbS approaches.
3. The DSAS tool was used to reconstruct shoreline evolution from 1936 to 2020. The analysis highlights a shift in accretion and erosion patterns following dike removal, offering insight into long-term site response to restoration.

The models revealed that restored connectivity and wetland expansion contribute to improved hydro-saline regulation, supporting both water quality and fish habitat conditions. The hydro-saline simulations suggest that if the hydraulic connection with the central lagoons were permanently open, it could help reduce the risk of hypersalinity during dry periods. This potential benefit is critical for adaptive water management under increasing climate variability.

Together, these models confirm that the implemented nature-based strategies can enhance resilience to coastal hazards while restoring ecological function. The work provides a robust evidence base to support the planning and scaling of restoration efforts across the Rhone Delta system.

Contribution of the Arcachon Bay Pilot

In the Arcachon Bay Pilot, partners have implemented and validated a high-resolution coupled hydro-morpho-eco modelling suite to assess the role of seagrass restoration in mitigating coastal flooding and erosion risks under storm conditions. The main ecosystem services (ESS) targeted include coastal protection, water quality improvement, carbon sequestration, and food provisioning.

The modelling system is based on the Delft3D Flexible Mesh (DFM) platform, integrating the D-Flow, D-Waves, and sediment transport modules. Two models were configured: a flooding hazard (FH) model and a coastal erosion hazard (CEH) model. The models include the effect of Zostera noltii and Zostera marina through a trachytopes formulation, which separates vegetation-induced flow resistance from bed roughness. This approach avoids artificial increases in shear stress and sediment transport rates, ensuring realistic morphological response.

Model forcing was derived from ERA5 meteorological reanalysis, CMEMS tidal boundary data, freshwater inflows from the Leyre River, and offshore waves from the IOWAGA dataset. Initial bathymetry was based on 2016 Ifremer surveys, and vegetation cover was initialized using 2012 and 2016 mappings for Z. noltii and Z. marina, respectively.

Calibration and validation were carried out using in situ observations from 2015–2016, including water levels, wave parameters and sediment concentrations. Additional validation against the MARS3D platform confirmed consistent current velocity fields. Sediment dynamics were assessed by comparing model outputs to bi-monthly concentration measurements and morphological changes between 2016 and 2019 from SIBA bathymetric surveys.

Restoration scenarios simulated different configurations of seagrass extent, including a reference state (S0), a pre-regression condition (S1, from 1989 data), and conceptual deployment strategies using Roselière devices. These scenarios enabled quantification of ESS benefits such as:

1. Reduced wave height and current velocities in vegetated areas, lowering erosion and flood risk;
2. Sediment stabilisation in intertidal flats, contributing to water clarity and habitat recovery;
3. Buffering of hydrodynamic energy with clear implications for coastal infrastructure and tourism resilience.

This modelling effort provides a robust tool to support planning and implementation of large-scale seagrass restoration, confirming that such nature-based solutions are effective in mitigating storm-induced hazards in the Arcachon Bay context.

Contribution of the Sicily Pilot

In the Sicily Pilot, the modelling work led by the University of Catania focuses on assessing nature-based solutions (NbS) for flood and erosion risk mitigation in the Cuba-Longarini lagoon system. This wetland complex, part of the Natura 2000 network and the “Pantani della Sicilia Sud-Orientale”, faces increasing pressures from urban development and agriculture, especially in the Granelli coastal village, which was built atop the dune belt separating the lagoons from the sea.

The pilot explores the effectiveness of two NbS strategies: (i) the revegetation of the coastal dunes using the endemic species Ammophila arenaria, and (ii) the expansion of the Posidonia oceanica seagrass meadow in front of Granelli beach. These interventions aim to improve biodiversity and stabilise sediment while reducing wave impact and flood risk during extreme storm events.

To evaluate performance under present-day conditions, a coupled SWAN + XBeach modelling system was implemented. Input datasets included high-resolution topography from 2013 LiDAR surveys, bathymetric data from multibeam campaigns (2019), and shoreline positions extracted from satellite imagery. A detailed characterisation of beach sediment (d50 = 0.27 mm) was included to accurately represent morphological response.

Vegetation effects were explicitly represented in the XBeach model using parameterisations aligned with EUNIS habitat types. For the dune system, Ammophila arenaria was modelled across a 3.3 km stretch (0.043 km²), while seagrass expansion was simulated over an area of 1.04 km² around the existing Posidonia

meadow (0.77 km²). Each habitat was assigned specific drag coefficients, stem diameters and vegetation densities based on literature and field data.

Model results under storm forcing demonstrated that both NbS significantly enhance coastal resilience: the dune vegetation reduces wave run-up, while the seagrass acts as an effective energy buffer, lowering wave heights and stabilising sediment. These findings provide solid evidence for the role of ecosystem-based interventions in mitigating hazard exposure, while simultaneously supporting habitat recovery and ecological connectivity.

Contribution of the Vistula Lagoon Pilot

In the Vistula Lagoon Pilot, the modelling activities focus on the hydrodynamic and morphodynamic implications of constructing a new artificial island in the Polish sector of the lagoon. The primary goal is to evaluate the island's function as a biodiversity restoration measure under a Nature-based Solutions (NbS) framework, while ensuring minimal interference with existing ecosystem services (ESS) and maintaining local hydro-morphological stability.

The site, located in a shallow inland lagoon separated from the Baltic Sea by high dunes and a robust coastal barrier, is largely sheltered from direct impacts of sea level rise and severe storm surges. Instead, the key hazards to be addressed are wind-induced storm surges and ice-related mechanical stress during winters. Given these characteristics, the pilot is designed to explore the limits of NbS in physically constrained lagoon environments, with particular attention to sediment strength, ice pressure and long-term sustainability of hard-structure-based NbS.

A Delft3D hydrodynamic model was implemented to simulate wave and current fields before and after the island's construction. The model covers the entire lagoon—including the Russian sector—to ensure accurate reproduction of wave fetches and current circulation patterns under dominant wind directions (NE and SW). Simulations confirmed that the island would have negligible impact on surrounding hydrodynamics, preserving existing ESS and avoiding disturbance to sediment transport and morphodynamics.

The project also assessed different design options for the island's perimeter (rim), initially favouring soft engineering alternatives (geo-tubes filled with local sand). However, geotechnical analyses of seabed sediments—composed of organic-rich silts and clays with low bearing capacity—revealed that such options would be prone to excessive and uneven subsidence. Consequently, a hybrid solution was adopted: a rim formed by two rows of steel sheet piles filled with stone armour, designed to withstand ice pressure and ensure long-term stability over weak substrates.

Secondary NbS effects are also expected: spontaneous development of reed fields along the island's rim, supporting fish spawning grounds and water quality improvement through denitrification. These by-effects, though not originally intended, represent additional ecosystem benefits consistent with the NbS approach.

This case study exemplifies how engineering constraints can shape the feasible application of NbS, and offers a blueprint for implementing ecosystem-based restoration in shallow lagoons with soft sediments and harsh winter conditions.

Final integrated conclusion

The modelling activities presented in this deliverable demonstrate the maturity and robustness of the coupled hydro-morpho-eco systems developed across the pilot sites. By focusing exclusively on present-day storm conditions, these models provide a scientifically sound foundation for evaluating the effectiveness of nature-based solutions in reducing multiple coastal hazards. The consistent implementation of ecosystem services (ESS) and their validation under real events reinforce the applicability of these tools for risk-informed decision-making and operational planning. Together, these efforts contribute to advancing a shared methodology for coastal restoration, grounded in both scientific rigor and site-specific realities.

10. References

Anderson, R.S. (2002). Modeling the tor-dotted crests, bedrock edges, and parabolic profiles of high alpine surfaces of the Wind River Range, Wyoming. Geomorphology, 46, 35–58.

Ardhuin, F., Accensi, M., Roland, A., Girard, F., Filipot, J. F., Leckler, F., & Le Roux, J. F. (2014). Numerical wave modeling in PREVIMER: multi-scale and multi-parameter demonstrations. Editorial–Apr 2014–The Pre-operational PREVIMER system, 2017.

Ardhuin, F., O'Reilly, W.C., Herbers, T.H.C., Jessen, P.F., 2003. Swell transformation across the continental shelf. Part I: attenuation and directional broadening. J. Phys. Oceanogr. 33 (9), 1921–1939.

Ardhuin, F.; Rogers, E.; Babanin, A.V.; Filipot, J.F.; Magne, R.; Roland, A.; Collard, F. Semiempirical dissipation source functions for ocean waves. Part I: Definition, calibration, and validation. J. Phys. Oceanogr. 2010, 40, 1917–1941.

Ballé-Béganton, J., J. Herry, M. Philippe, R. Pasco, B. Angst, M. Urien, D. Bailly, M. Cassé. Les services écosystémiques en soutien à la gestion des herbiers de zostères du golfe du Morbihan, Projet Interreg IVA Manche VALMER, 14p, 2015.

Baptist, M., 2005. Modelling floodplain biogeomorphology, PhD Dissertation, TU Delft library, http://resolver.tudelft.nl/uuid:b2739720-e2f6-40e2-b55f-1560f434cbee.

Baptist, M.J., van der Wal, J.T., Folmer, E.O., Gräwe, U., Elschot, K., 2019. An ecotope map of the trilateral Wadden Sea, Journal of Sea Research 152, 101761.

Battjes, J.A., Janssen, J.P.F.M., 1978. Energy loss and set-up due to breaking of random waves. Proc. 16th Int. Conf. Coastal Eng. ASCE, pp. 569–587.

Bellafiore, D., Umgiesser, G., 2010. Hydrodynamic coastal processes in the north Adriatic investigated with a 3D finite element model, Ocean Dynam., 60, 255–273.

Beudin, A., Kalra, T. S., Ganju, N. K., & Warner, J. C. Development of a coupled wave-flow-vegetation interaction model. Computers & Geosciences, 100, pp. 76-8, 2017.

Bidlot, J, S Abdalla, and PAEM Janssen (2005). A revised formulation for ocean wave dissipation in CY25R1. In: Internal Memorandum Research Department.

Bidlot, JR (2008). Intercomparison of operational wave forecasting systems against buoys: Data from ECMWF, MetO

Bladé, E.; Cea, L.; Corestein, G.; Escolano, E.; Puertas, J.; Vázquez-Cendón, E.; Dolz, J.; Coll, A. (2014). Iber: Herramienta de simulación numérica del flujo en ríos. Rev. Int. Métodos Numér. Cálc. Diseño Ing., 30, 1–10.

Boccotti, P. (2004). Idraulica marittima. Utet.

Bouchet, J.-M., J.-P. Deltreil, F. Manaud, D. Maurer, and G. Trut. Etude intégrée du bassin d'arcachon. 1997. L.C. Braat, de Groot, R. The ecosystem services agenda: bridging the worlds of natural science and economics conservation and development, and public and private policy. Ecosyst. Serv. 1, 4–15, 2012.

Burchard, H., Bolding, K., Villarreal, M.R., 1999. GOTM—a general ocean turbulence model. Theory, applications and test cases. Technical Report EUR 18745 EN, European Commission.

Caires, S., & Yan, K. (2020). Ocean surface wave time series for the European coast from 1976 to 2100 derived from climate projections. Copernicus Climate Change Service (C3S) Climate Data Store (CDS).

Carniello L., Defina, A., & D'Alpaos, L. (2009). Morphological evolution of the Venice lagoon: Evidence from the past and trend for the future. *Journal of Geophysical Research: Earth Surface*, *114*(F4), 4002. https://doi.org/10.1029/2008JF001157

Cavazzoni, S. 1973. Acque dolci in laguna di Venezia. Rapporto No. 64. Laboratorio per lo Studio della Dinamica delle Grandi Masse, Venezia.

Cayocca, F Modélisation morphodynamique d'une embouchure tidale: Application aux passes d'entrée du Bassin d'Arcachon. PhD thesis, Bordeaux 1, 1996.

Cea, L.; Puertas, J.; Vázquez-Cendón, M.E. (2007). Depth Averaged Modelling of Turbulent Shallow Water Flow with Wet-Dry Fronts. Arch. Comput. Methods Eng., 14, 303–341.

Chalikov, D. V., and M. Y. Belevich (1993), One-dimensional theory of the wave boundary layer, Bound. Layer Meteor., 63, 65–96.

Cognat, M. Rôles des facteurs environnementaux et des interactions biomorphodynamiques sur l'évolution spatio-temporelle des herbiers de zostères dans une lagune mésotidale. PhD thesis, Université de Bordeaux, 2019.

Convention on Biological Diversity. COP Decision X/2, 2010.

Costanza, R., Kubiszewski, I. The authorship structure of ecosystem services as a transdisciplinary field of scholarship. Ecosyst. Serv. 1, 16–25, 2012.

Cressman, G.P., 1959. An operational objective analysis scheme, Mon. Weather Rev., 87, 367–374.

Dalrymple, R.A., Kirby, J.T., Hwang, P.A., 1984. Wave diffraction due to areas of energy dis- sipation. ASCEJ. Waterw. Port Coast. Ocean Eng. 110 (1), 67–79.

Den Hartog, C. 1977. Structure, function and classification in seagrass communities. In: (C.P. McRoy and C. Helfferich, eds) Marine Science Volume 4: Seagrass Ecosystems, A Scientific Perspective. Marcel Dekker, Inc., New York, U.S.A. pp. 89-122.

Dissanayake, P., & Wurpts, A. (2013). Modelling an anthropogenic effect of a tidal basin evolution applying tidal and wave boundary forcings: Ley Bay, East Frisian Wadden Sea. *Coastal engineering*, *82*, 9-24.

Dobricic, S., Pinardi, N., 2008. An oceanographic three-dimensional variational data assimilation scheme, Ocean Model., 22, 89–105.

Donatelli, C., Ganju, N.K., Kalra, T.S., Fagherazzi, S., Leonardi, N., 2019. Changes in hydrody- namics and wave energy as a result of seagrass decline along the shoreline of a microtidal back-barrier estuary. Adv. Water Resour. 128, 183–192.

Egoh, B., Drakou, E.G., Dunbar, M.B., Maes, J., Willemen, L. Indicators for Mapping Ecosystem Services: A Review. Publications Office of the European Union, Luxembourg. 2012.

Eldeberky, Y. (1996), Nonlinear transformations of wave spectra in the nearshore zone, Ph.D. thesis, Delft University of Technology, Delft, The Netherlands, 203 pp.

Escudier, R., Clementi, E., Cipollone, A., Pistoia, J., Drudi, M., Grandi, A., Lyubartsev, V., Lecci, R., Aydogdu, A., Delrosso, D., Omar, M., Masina, S., Coppini G., Pinardi, N. (2021). A High Resolution Reanalysis for the Mediterranean Sea. Frontiers in Earth Science, 9, 1060,

Esselink, P., van Duin, W.E., Bunje, J., Cremer, J., Folmer, E.O., Frikke, J., Glahn, M., de Groot, A.V., Hecker, N., Hellwig, U., Jensen, K., Körber, P., Petersen, J., Stock, M., 2017. Salt marshes, In: Wadden Sea Quality Status Report 2017. Eds: Kloepper, S. et al., Common Wadden Sea Secretariat, Wilhelmshaven, Germany. Last updated 21.123.2017.

Fernández-Montblanc, T., Duo, E., & Ciavola, P. (2020). Dune reconstruction and revegetation as a potential measure to decrease coastal erosion and flooding under extreme storm conditions. Ocean & Coastal Management, 188, 105075.

Ferrarin, C., Roland, A., Bajo, M., Umgiesser, G., Cucco, A., Davolio, S., Buzzi, A., Malguzzi, P., Drofa, O., 2013. Tide-surge-wave modelling and forecasting in the Mediterranean Sea with focus on the Italian coast, Ocean Model., 61, 38–48.

Ferrarin C, Maicu F, Umgiesser G., 2017. The effect of lagoons on Adriatic Sea tidal dynamics. Ocean Model., 119:57–71.

Fonseca, M.S., Fisher, J.S., 1986. A comparison of canopy friction and seagrass movement be- tween four species of seagrass with reference to their ecological restoration. Mar. Ecol. 29, 15–22.

Ganthy, F. Rôle des herbiers de zostères (Zostera noltii) sur la dynamique sédimentaire du Bassin d'Arcachon. PhD thesis, Universté de Bordeaux 1, 2011.

Garzon, J. L., Maza, M., Ferreira, C. M., Lara, J. L., & Losada, I. J. (2019). Wave attenuation by Spartina saltmarshes in the Chesapeake Bay under storm surge conditions. Journal of Geophysical Research: Oceans, 124(7), 5220-5243.

Gómez Martín, E., Costa, M.M., Egerer, S., Schneider, U.W., 2021. Assessing the long-term ef- fectiveness of nature-based solutions under different climate change scenarios. Sci. Total Environ. 794, 148515.

Gorria, H. (1877). Desecación de las marismas y terrenos pantanosos denominados de Los Alfaques. Techical Report. Ministerio de Agricultura, Madrid, España.

Günther, H., Hasselmann, S., & Janssen, P. A. E. M. (1992). The WAM model Cycle 4 (revised version). Klim. Rechenzentrum. Techn. Rep, (4), 23-40.

Hanley, M.E., Bouma, T.J., Mossman, H.L., 2020. The gathering storm: optimizing management of coastal ecosystems in the face of a climate-driven threat. Ann. Bot. 125 (2), 197–212.

Hasselmann, D.; Bösenberg, J.; Dunckel, M.; Richter, K.; Grünewald, M.; Carlson, C. Measurements of wave-induced pressure over surface gravity waves. In Wave Dynamics and Radio Probing of the Ocean Surface; Springer: Boston, MA, USA, 1986; pp. 353–368.

Hasselmann, S.; Hasselmann, K.; Allender, J.K.; Barnett, T.P. Computations and parameterizations of the nonlinear energy transfer in a gravity-wave specturm. Part II: Parameterizations of the nonlinear energy transfer for application in wave models. J. Phys. Oceanogr. 1985, 15, 1378–1391.

Hellermann, S., Rosenstein, M., 1983. Normal wind stress over the world ocean with error estimates, J. Phys. Oceanogr., 13, 1093–1104.

Holthuijsen, L. H., Booij, N., & Herbers, T. H. C. (1989). A prediction model for stationary, short-crested waves in shallow water with ambient currents. Coastal engineering, 13(1), 23-54.

Houwing, E. J., Tanczos, I.C., Kroon, A., De Vries, M.B., 2000. Interaction of submerged vegetation, hydrodynamics and turbidity; analysis of field and laboratory studies, Conference Proc. INTERCOH2000.

Ibàñez, C., Prat, N., Canicio, A. (1996). Changes in the hydrology and sediment transport produced by large dams on the lower Ebro river and its estuary. Regulated Rivers: Research & Management, 12(1), 51-62.

IPBES. Global assessment report on biodiversity and ecosystem services of the Intergovernmental Science-Policy Platform on Biodiversity and Ecosystem Services (Version 1). 2019.

James, C. S., A. L. Birkhead, A. A. Jordanova & J. J. O'Sullivan. Flow resistance of emergent vegetation, Journal of Hydraulic Research, 42:4, 390-398, 2004.

Janssen, P. A. E. M. (1991), Quasi-linear theory of of wind wave generation applied to wave forecasting, J. Phys. Oceanogr., 21, 1,631–1,642.

Kaiser, R.; Knaack, H.; Miani, M.; Niemeyer, H.D. (2010). Examination of Climate Change adaptation strategies for Coastal Protection. In: MCKEE SMITH, J. and LYNETT, P. (ed.): Proceedings of the 32nd International Conference on Coastal Engineering, 2010, Shanghai. http://journals.tdl.org/icce/index.php/icce/issue/view/154/showToc

Kambiadou, K., Ganthy F., Verney R., Plus M., Sottolichio A. Modelling the effects of Zostera noltei meadows on sediment dynamics: application to the Arcachon lagoon. Ocean Dynamics 64, pp. 1499-1516, 2014.

Kara, B. A., Wallcraft, A. J., Hurlburt, H. E., 2007. A Correction for Land Contamination of Atmospheric Variables near Land–Sea Boundaries, *J. Phys. Oceanogr.*, 37, 803–818.

Knutson, P. L., Brochu, R. A., Seelig, W. N., & Inskeep, M. (1982). Wave damping in Spartina alterniflora marshes. Wetlands, 2, 87-104.

Koch, E.W., Gust, G., 1999. Water flow in tide and wave dominated beds of the seagrass Thalassia testudinum. Mar. Ecol. Prog. Ser. 184, 63–72.

Korres, G., Ravdas, M., Zacharioudaki, A., Denaxa, D., & Sotiropoulou, M. (2021). Mediterranean Sea Waves Analysis and Forecast (CMEMS MED-Waves, MedWAM3 system) (Version 1) set. Copernicus Monitoring Environment Marine Service (CMEMS). https://doi.org/10.25423/CMCC/MEDSEA_ANALYSISFORECAST_WAV_006_017_MEDWAM3

Kumar, P., Debele, S.E., Sahani, J., Aragão, L., Barisani, F., Basu, B., Bucchignani, E., et al., 2020. Towards an operationalisation of nature-based solutions for natural hazards. Sci. Total Environ. 731, 138855.
La Notte, A., D'Amato D., Mäkinen H., Paracchini M.L., Liquete C., Egoh B., Geneletti D., Crossman N.D. Ecosystem services classification: A systems ecology perspective of the cascade framework. Ecological indicators 74, pp. 392-402, 2017.

Lazure, P., Jegou, A.-M. 3D modelling of seasonal evolution of Loire and Gironde plumes on Biscay Bay continental shelf. Oceanologica Acta 21, 165–177, 1998.

Lazure, P. and Dumas, F. An external-internal mode coupling for a 3D hydrodynamical model for application at regional scale (MARS). Advances in Water Ressources, 31: 233-250, 2008.

Lobeto, H., Menendez, M., Losada, I.J., 2021. Future behavior of wind wave extremes due to climate change. Sci. Rep. 11, 7869.

Longuet-Higgins, M., and R. Stewart (1964), Radiation stresses in water waves; a physical discussion, with applications, Deep Sea Res. Oceanogr. Abstr., 11, 529–562

MA. Millennium Ecosystem Assessment. World Resources Institute, Washington, DC, 2005.

Maes, J., Teller, A., Erhard, M., Murphy, P., Paracchini, M., Barredo, J., Grizzetti, B., Cardoso, A., Somma, F., Petersen, J. Mapping and Assessment of Ecosystems and Their Services—Indicators for Ecosystem Assessments Under Action 5 of the EU Biodiversity Strategy to 2020. European Commission, ISBN, pp. 978–992, 2014.

Mascioli, F., Piattelli, V., Cerrone, F., Gasprino, D., Kunde, T., Miccadei, E., 2021. Feasibility of objective seabed mapping techniques in a coastal tidal environment (Wadden Sea, Germany), Geosciences, 11(2), 49.

Mazzella, L., Guidetti, P., Lorenti, M., Buja, M.C., Zupo, V., Scipione, M.B., Rismondo, A., Curiel, D., 1998. Biomass partioning in Adriatic Seagrass ecosystems (Posidonia Oceanica, Cymodoces Nodosa, Zostera Marina). Rapp. Comm. Int. Mer Medit. 35, 562–563.

McKenzie, L.J., Nordlund, L.M., Jones, B.L., Cullen-Unsworth, L.C., Roelfsema, C., Unsworth, R.K.F., 2020. The global distribution of seagrass meadows. Environ. Res. Lett. 15, 074041.

Méndez, F.J., Losada, I.J., 2004. An empirical model to estimate the propagation of random breaking and nonbreaking waves over vegetation fields. Coast. Eng. 51, 103–118.

Mudd, S.M.; Furbish, D.J. (2004). Influence of chemical denudation on hillslope morphology. J. Geophys. Res. Earth Surf., 109.

Mugica, J., Bulteau T., Paris F. et Pedreros R., avec la collaboration de Delvallee E. Caractérisation de l'aléa submersion marine dans le cadre des PPRL du Bassin d'Arcachon (Gironde), Détermination de l'évènement naturel de référence. Rapport intermédiaire BRGM/RP-61408-FR, 73 p., 2014.

Munaretto, S., & Huitema, D. (2012). Adaptive comanagement in the Venice lagoon? An analysis of current water and environmental management practices and prospects for change. *Ecology and Society*, *17*(2). https://doi.org/10.5751/ES-04772-170219

Mütterlein, S., Ganthy F., Sottolichio A. Effect of small seagrass Zostera noltei on tidal asymmetry in a semi-enclosed shallow lagoon: the Arcachon Bay (SW France). International Coastal Symposium, 6-11 March 2016.
Nesshöver, C., Assmuth, T., Irvine, K.N., Rusch, G.M., Waylen, K.A., Delbaere, B., et al., 2017. The science, policy and practice of nature-based solutions: an interdisciplinary perspective. Sci. Total Environ. 579, 1215–1227.

Niemeyer, H. D., Berkenbrink, C., Ritzmann, A., Knaack, H., Wurpts, A., Kaiser, R. (2014). Evaluation of Coastal Protection Strategies in Respect of Climate Change Impacts. In: Die Küste 81. Karlsruhe: Bundesanstalt für Wasserbau. S. 565-577.

Oberrecht, D., 2020. Development of a numerical modeling approach for large-scale fluid mud flow in estuarine environments. Hannover: Gottfried Wilhelm Leibniz Universität, Diss. (2020), xvi, 118 S. DOI: https://doi.org/10.15488/10488

Paola, C.; Voller, V.R. (2005). A generalized Exner equation for sediment mass balance. J. Geophys. Res. Earth Surf., 110

Parisot,J.-P., J. Diet-Davancens, A. Sottolichio, E. Crosland, C. Drillon, and R. Verney. Modélisation des agitations dans le bassin d'arcachon. Xèmes Journées Sophia Antip, pages 435–444, 2008.

Paul, M., Amos, C.L., 2011. Spatial and seasonal variation in wave attenuation over Zostera noltii. J. Geophys. Res. 116, C08019.

Pettenuzzo, D., Large, W. G., and Pinardi, N., 2010. On the corrections of ERA40 surface flux products consistent with the Mediterranean heat and water budgets and the connection between basin surface total heat flux and NAO, J. Geophys. Res., 115, C06022

Pirazzoli, P. 1974. Dati storici sul medio mare a Venezia. Atti Acc. Sci. Istituto Bologna 13(1): 125-148.

Plus, M., D. Maurer, J.-Y. Stanisiere, and F. Dumas. Caractérisation des composantes hydrodynamiques d'une lagune mésotidale, le bassin d'arcachon. 2006.

Potschin, M., Haines-Young, R., 2016. Defining and measuring ecosystem services. In: Potschin, M., Haines-Young, R., Fish, R., Turner, R.K. (Eds.), Routledge Handbook of Ecosystem Services. Routledge, Taylor & Francis Group, London; New York, p. 2016.

Pranavam Ayyappan Pillai, U., Pinardi, N., Federico, I., Causio, S., Trotta, F., Unguendoli, S., & Valentini, A. (2022). Wind-wave characteristics and extremes along the Emilia-Romagna coast. Natural Hazards and Earth System Sciences, 22(10), 3413-3433.

Proveditorato for the Public Works of Veneto, Trentino Alto Adige and Friuli Venezia Giulia, n.d. Progetto Venezia2021.

Puillat, I., Lazure, P., Jégou, A.-M., Lampert, L., Miller, P. Mesoscale hydrological variability induced by north-westerly wind on the French continental shelf of the Bay of Biscay. Scientia Marina 70S1, 15–26, 2006.

Roelvink, J.A. Coastal morphodynamic evolution techniques. Coastal Engineering, 53(2), 277–287, 2006.
C. Rhodes. National ecosystem services classification system. 2015.

Roland, A., Zhang, Y. J., Wang, H. V., Meng, Y., Teng, Y. C., Maderich, V., ... & Zanke, U. (2012). A fully coupled 3D wave-current interaction model on unstructured grids. *Journal of Geophysical Research: Oceans*, *117*(C11).

Santillán, D., Cueto-Felgueroso, L., Sordo-Ward, A., Garrote, L. (2020). Influence of Erodible Beds on Shallow Water Hydrodynamics during Flood Events. Water, 12(12), 3340.

Schrijvershof, R. A., Van Maren, D. S., Torfs, P. J. J. F., & Hoitink, A. J. F. (2023). A synthetic spring-neap tidal cycle for long-term morphodynamic models. *Journal of Geophysical Research: Earth Surface*, *128*(3), e2022JF006799.

Secretariat, C. W. S. (2008). Nomination of the Dutch-German Wadden Sea as world heritage site. *Wadden Sea Ecosystem*, *24*, 200.

Seppelt, R., Dormann, C.F., Eppink, F.V., Lautenbach, S., Schmidt, S. A quantitative review of ecosystem service studies: approaches, shortcomings and the road ahead. J. Appl. Ecol. 48, 630–636, 2011.

Sfriso, A., C. Facca and M. Tibaldo. 2005. Macrophyte biomass updating in the lagoon of Venice. In: Lagoons and Coastal Wetlands in the Global Change Context: Impacts and Management Issues. IOC Integrated Coastal Area Management (ICAM), Dossier N° 3. UNESCO. Cap. 29, pp. 224-231.

Sfriso, A., C. Facca and S. Ceoldo. 2004. Growth and production of Cymodocea nodosa (Ucria) Ascherson in the Venice Lagoon. In: (P. Campostrini, ed.) Scientific Research and Safeguarding of Venice. CoRiLa. Research Programme 2001-2003. 2002 Results. Multigraf, Spinea. Vol II. pp. 229-236.

Shields, A. (1936) Anwendung Der Aehnlichkeitsmechanik Und Der Turbulenzforschung Auf Die Geschiebebewegung. Ph.D. Thesis, Technical University Berlin, Berlin, Germany.

Soulsby, R.L., Whitehouse, R.J.S. (1997). Threshold of sediment motion in coastal environments. In Pacific Coasts and Ports' 97: Proceedings of the 13th Australasian Coastal and Ocean Engineering Conference and the 6th Australasian Port and Harbour Conference; Volume 1 (pp. 145-150). Christchurch, NZ: Centre for Advanced Engineering, University of Canterbury.

Stanev, E. V., Jacob, B., & Pein, J. (2019). German Bight estuaries: An inter-comparison on the basis of numerical modeling. *Continental Shelf Research*, *174*, 48-65.

Stankovic, M., Ambo-Rappe, R., Carly, F., Dangan-Galon, F., Fortes, M.D., et al., 2021. Quan- tification of blue carbon in seagrass ecosystems of Southeast Asia and their potential for climate change mitigation. Sci. Total Environ. 783, 146858.

Suzuki, T., Zijlema, M., Burger, B., Meijer, M. C., & Narayan, S. (2012). Wave dissipation by vegetation with layer schematization in SWAN. Coastal Engineering, 59(1), 64-71.

Tagliapietra, D., Baldan, D., Barausse, A., Buosi, A., Curiel, D., Guarneri, I., Pessa, G., Rismondo, A., Sfriso, A., Smania, D., & Volpi Ghirardini, A. (2018). *Protecting and restoring the salt marshes and seagrasses in the lagoon of Venice*. http://journal.um-surabaya.ac.id/index.php/JKM/article/view/2203.

Tolman, H.; Accensi, M.; Alves, J.H.; Ardhuin, F.; Bidlot, J.; Booij, N.; Bennis, A.C.; Campbell, T.; Chalikov, D.; Chawla, A. Usermanual and System Documentation of WAVEWATCH III R Version; NOAA/NWS/NCEP/MMAB: Baltimore, MD, USA, 2019; 465p.

Tommasini, L., Carniello, L., Ghinassi, M., Roner, M., & D'Alpaos, A. (2019). Changes in the wind-wave field and related salt-marsh lateral erosion: inferences from the evolution of the Venice Lagoon in the last four centuries. *Earth Surface Processes and Landforms*, *44*(8), 1633–1646. https://doi.org/10.1002/esp.4599.

Van Ledden, M.. Sand-mud segregation in estuaries and tidal basins. University of Technology Sydney, 2003.

Van Ledden, M., Wang, Z. B., Winterwerp, H., & Vriend, H. D. (2004). Sand–mud morphodynamics in a short tidal basin. *Ocean Dynamics*, *54*, 385-391.

Van Leer, B. (1979). Towards the Ultimate Conservative Difference Scheme, V. A Second Order Sequel to Godunov's Method. J. Comput. Phys., 32, 101–136.

Van Loon-Steensma, J. M., Hu, Z., & Slim, P. A. (2016). Modelled impact of vegetation heterogeneity and salt-marsh zonation on wave damping. Journal of Coastal Research, 32(2), 241-252.

Van Rijn, L.C. (1984a). Sediment Transport, Part I: Bed Load Transport. J. Hydraul. Eng., 110, 1431–1456

Van Rijn, L.C. (1984b). Sediment Transport, Part II: Suspended Load Transport. J. Hydraul. Eng., 110, 1613–1641

Van Rijn, L.C. (1987). Mathematical modelling of morphological processes in the case of suspended sediment transport. Delft: Delft Hydraulics Communications #382.

Van Rijn, L. C., Nieuwjaar, M. W., van der Kaay, T., Nap, E., & van Kampen, A. Transport of fine sands by currents and waves. Journal of waterway, port, coastal, and ocean engineering, 119(2), 123-143, 1993.

Van Rooijen, A. A., Van Thiel de Vries, J. S. M., McCall, R. T., Van Dongeren, A. R., Roelvink, J. A., & Reniers, A. J. H. M. (2015, June). Modeling of wave attenuation by vegetation with XBeach. In E-proceedings of the 36th IAHR World Congress (Vol. 28). Netherlands: IAHR.

Vanoni, V. A., Brooks, N. H. (1987). Laboratory Studies of the Roughness and Suspended Load of Alluvial Streams, Sedimentation Laboratory, California Institute of Technology, Report E-68, Pasadena, CA, USA.

Warner, J. C., Sherwood, C. R., Signell, R. P., Harris, C. K., & Arango, H. G. (2008). Development of a three-dimensional, regional, coupled wave, current, and sediment-transport model. *Computers & geosciences*, *34*(10), 1284-1306.

Waycott, M., Duarte, C.M., Curruthers, T.J.B., Orth, R.J., Dennsion, W.C., Olyarnik, S., Callandine, A., Fourqurean, J.W., Heck Jr., K.L., Hughes, A.R., Kendrick, G.A., Kenworthy, W.J., Short, F.T., Williams, S.L., 2009. Accelerating loss of seagrass across the globe threatens coastal ecosystems. Proc. Natl. Acad. Sci. 106 (30), 12377–12381.

Umgiesser, G., Canu, D. M., Cucco, A., Solidoro, C., 2004. A finite element model for the Venice lagoon: Development, set up, calibration and validation, J. Marine Syst., 51, 123–145.

Yamaguchi, M. (1984). Approximate expressions for integral properties of the JONSWAP spectrum. Doboku Gakkai Ronbunshu, 1984(345), 149-152.

Zhang, Y. J., Gerdts, N., Ateljevich, E., & Nam, K. (2020). Simulating vegetation effects on flows in 3D using an unstructured grid model: model development and validation. *Ocean Dynamics*, *70*, 213-230.

Zhang, Y., Nepf, H., 2019. Wave-driven sediment resuspension within a model eelgrass meadow. J. Geophys. Res. Earth Surf. 124 (4), 1035–1053.

Zhang, Y. J., Ye, F., Stanev, E. V., & Grashorn, S. (2016). Seamless cross-scale modeling with SCHISM. *Ocean Modelling*, *102*, 64-81.

Zuliani, A., L. Zaggia, F. Collavini and R. Zonta 2005. Freshwater discharge from the drainage basin to the Venice Lagoon (Italy). Environ. Int. 31: 929-938.